
UNIVERSIDAD DE VALLADOLID

ESCUELA TÉCNICA SUPERIOR DE INGENIEROS INDUSTRIALES



DEPARTAMENTO DE INGENIERÍA ENERGÉTICA Y FLUIDODINÁMICA

DOCTORAL THESIS

**“HIGH TEMPERATURE FIXED POINTS: INVESTIGATION OF INFLUENCE
PARAMETERS ON THE TEMPERATURE UNCERTAINTY BY THERMAL
MODELLING”**

Author:

Pablo Castro Alonso

Director:

Prof. Miguel Angel Villamañán Olfos

Co-director:

Prof. Graham Machin

Valladolid, February 2011

Abstract

In the field of temperature standards and calibration, accurate determination of the high temperature eutectic melting point is very important. However due to the difficulty in performing experimental measurements at such high temperatures thermal modelling is an essential tool to understand the sources of uncertainty in the realisation of these fixed points. Once the temperatures of these fixed points is established, they can easily be used in any laboratory that has suitable facilities as reliable high temperature fixed points (HTFP).

The difference between the ideal fixed point temperature at the liquid-solid interface and the temperature measured by the radiation thermometer is caused by several factors: heat loss to the surroundings, thermal resistance of the crucible walls, temperature profile in the furnace, design of crucible and furnace and the nominal temperature of the fixed point. It is these factors that are most easily investigated through thermal modelling.

In this work the uncertainties of these factors for radiation thermometry of high temperature eutectic fixed points is estimated. In particular, this modelling is applied to the melting temperature of the Co-C, Pt-C and Re-C alloys which are the subject of intense research by the world metrology community to form the basis of new temperature references. These uncertainties (in terms of a temperature difference) has been evaluated by numerical simulation using the FLUENT (finite volume method) computational package to specific crucible-furnace configurations designed by the National Metrology Institute of Japan (NMIJ), the National Physical Laboratory (NPL, UK) and Laboratoire National D'Essais (LNE, France). There have also been studies undertaken with the National Institute of Metrology of China (NIM), the Spanish Metrology Institute (CEM) and the National Institute of Standards and Technology (NIST, United States of America) all with the aim of understanding uncertainty contributions to facilitate the accurate realisation of high temperature fixed points.

The first chapters deal with general aspects about thermometry and the analysis and validation of the approach of numerical modelling. The next chapters are focused in modelling and evaluating the uncertainty factors in the temperature drop associated with the HTFP.

As a result of this work, the influence of cracks and holes inside imperfectly formed metal-ingots is evaluated, uncertainties associated with the values of emissivity and thermal conductivity of graphite are calculated and also the influence of the blackbody tube length and the back-wall thickness or the use of different furnaces and temperature profiles is estimated.

Resumen

En el campo del calibrado térmico, la determinación de puntos fijos de fusión de materiales eutécticos a alta temperatura es muy importante. Sin embargo, debido a la dificultad para realizar medidas experimentales a altas temperaturas, el modelado térmico es una herramienta esencial para comprender las fuentes de incertidumbre en la obtención de estos puntos fijos. Una vez determinados dichos puntos, son fácilmente reproducibles en cualquier laboratorio que tenga las instalaciones adecuadas, pudiendo servir de patrón para el calibrado de instrumentos térmicos de medida.

La diferencia entre la temperatura medida con el termómetro y la temperatura de la interfase líquido-sólido es causada por varios factores: Las pérdidas de calor al entorno, la resistencia térmica del metal y de las paredes del crisol, la distribución de temperatura en el horno, el diseño del crisol y del horno y la temperatura nominal del punto fijo.

En este trabajo se estiman las incertidumbres asociadas a los factores anteriores en la calibración de termómetros de radiación mediante puntos fijos eutécticos de alta temperatura. En particular, se realiza el modelado sobre las aleaciones eutécticas Co-C, Pt-C y Re-C que son objeto de una intensa investigación por parte de la comunidad de metrología como base para nuevas referencias en la escala de temperaturas. Estas incertidumbres (en términos de diferencia de temperatura) se evalúa mediante simulación numérica empleando el software FLUENT, basado en el método de volúmenes finitos, a configuraciones específicas de hornos y crisoletas diseñados por el Instituto Nacional de Metroología de Japón (NMIJ), el Laboratorio Nacional de Física de Inglaterra (NPL) y el Laboratorio Nacional de Metroología Francés (LNE). También se han realizado estudios para el Laboratorio Nacional de Metroología de China (NIM), el Centro Español de Metroología (CEM) y el Instituto Nacional de Estándares y Tecnología de Estados Unidos (NIST), todos ellos con el objetivo de entender las

contribuciones de las distintas incertidumbres y así facilitar la implementación de los puntos fijos de alta temperatura con la suficiente precisión.

Los primeros capítulos se refieren a aspectos generales sobre la termometría y el análisis y la validación de la simulación numérica. Los siguientes capítulos se centran en la evaluación de los factores de incertidumbre asociados a estos puntos fijos.

Como resultado de este trabajo, se ha evaluado la influencia de grietas y poros en aleaciones eutécticas con defectos de formación, se han calculado las incertidumbres asociadas a los valores de la emisividad y la conductividad térmica del grafito y se ha estimado tanto la influencia de la longitud del crisol y el espesor de sus paredes como el uso de hornos y perfiles de temperatura diferentes.

PART I

English version



Acknowledgements

I am deeply indebted to Prof. Miguel Ángel Villamañán Olfos, Dr. Pieter Bloembergen and Dr. Graham Machin for giving me the opportunity to work on this project. Their words of encouragement and motivation came a long way in bringing this work to fruition.

I would like to acknowledge the contribution that CEM and in particular M. José Martín and M. Dolores del Campo have made to the progress of this research.

I would like to acknowledge all the members of HIMERT consortium, without their contribution this work could not have been done. Special thanks are given to Dave Lowe, Jonathan Pearce and L. Wright from NPL, Ronan Morice, Veronique Le Sant and G. Failleau from BNM-LNE, Mohamed Sadli from BNM-INM, and Klaus Anhalt from PTB.

I am very much indebted to Leonard Hanssen from NIST for his willingness in providing experimental data, for sharing his knowledge and for his cooperation.

Finally, I am very much indebted to the contribution that NMIJ and in particular Yoshiro Yamada for sharing their knowledge and for their cooperation.

TABLE OF CONTENTS

TABLE OF CONTENTS

<i>Abstract / Resumen</i>	<i>i</i>
---------------------------	----------

PART I: English version

<i>Acknowledgements</i>	<i>v</i>
<i>Table of Contents</i>	<i>vii</i>
<i>List of Symbols</i>	<i>xi</i>
<i>List of Acronyms</i>	<i>xiii</i>

Chapter 1. Introduction and objectives

1.1. Introduction	3
1.2. Objectives	7

Chapter 2. Fundamentals of thermometry: temperature, thermometers and temperature scales

2.1. Historical notes	11
2.2. Temperature concept	14
2.3. Concept of thermometer and temperature scale	16
2.4. International temperature scale (ITS)	19
2.4.1. Temperature units	20
2.4.2. ITS principles	20
2.4.3. Current thermometry developments in the ITS	24

Chapter 3. Analysis of thermal modelling methods

3.1. Introduction	31
3.2. Characteristics of Computational Fluid Dynamics (CFD)	31
3.2.1. Introduction	31
3.2.2. Advantages and disadvantages of the CFD	33

3.2.3. Methodology	33
3.3. Working with FLUENT	35
3.3.1. The heat transfer equation	35
3.3.2. Radiative Transfer Equation	36
3.3.3. Description of the different types of radiation models for FLUENT 6.1	38
3.3.3.1. DTRM model (discrete to transfer radiation model)	38
3.3.3.2. P-1 model	39
3.3.3.3. Rosseland model	40
3.3.3.4. DO model (Discrete Ordinates)	40
3.3.3.5. S2S model (surface to surface)	41
3.3.4. Choosing the Radiation Model	42
3.4. Summary	43

Chapter 4. Preliminary studies and validation of the approach of numerical modelling

4.1. Introduction	47
4.2. An equilateral triangular enclosure	47
4.3. An axisymmetric cylindrical enclosure with participating media	50
4.4. A three zone high temperature furnace for thermocouples	53
4.4.1. Description of the high temperature furnace	53
4.4.2. Finite volume simulations	54
4.4.3. Results	56
4.5. Comparison between FLUENT and ANSYS software packages for the numerical resolution of HTFP	58
4.5.1. Description of the simulated system	58
4.5.2. Numerical models	59
4.5.3. Results	60
4.5.4. Conclusions	62
4.6. Conclusions	63

Chapter 5. Uncertainty factors in the temperature drop I: temperature effects of imperfectly formed metal-ingots

5.1. Introduction	67
5.2. Construction and implementation of thermal model	68
5.3. Simulation results	69
5.3.1. Results with the holes	69
5.3.2. Results with the cracks	72
5.4. Discussion	74
5.5. Conclusions	76

Chapter 6. Uncertainty factors in the temperature drop II: emissivity, thermal conductivity and effect of Nagano-M furnace temperature profile

6.1. Introduction	79
6.2. Systems to be modeled	80
6.3. Calculations	83
6.3.1. Model structure and material properties	83
6.3.2. Quantities to be calculated	83
6.4. Results	85
6.5. Discussion	92
6.6. Conclusions	94

Chapter 7. Uncertainty factors in the temperature drop III: blackbody tube length, backwall thickness and Thermogage furnace temperature profile

7.1. Introduction	97
7.2. Description of the model	98
7.3. Simulation results	103
7.3.1. Temperature drop	103
7.3.2. Effect of back-wall thickness	104
7.3.3. Effect of the crucible length	106
7.4. Discussion	108
7.4.1. Furnace conditions	108

7.4.2. Back-wall thickness	110
7.4.3. Crucible length	111
7.4.4. Graphic data presentation	112
7.5. Conclusions	115

Chapter 8. Thermal modelling of the eutectic fixed points Co-C, Pt-C and Re-C as input for the determination of the cavity effective emissivity

8.1. Introduction	119
8.2. Thermal modeling of the temperature distributions within the cavity	120
8.3. Attained results of effective emissivity and radiance temperature from the thermal modeling	123
8.4. Summary and conclusions	125

Chapter 9. Investigation of influence parameters for contact thermometry HTFP cell

9.1. Introduction	129
9.2. Description of the model	129
9.3. Simulation results	131
9.4. Conclusions	137

Chapter 10. Final conclusions

10.1. Conclusions	141
10.2. Future research lines on this field	142

<u>Annex I. Bibliography</u>	145
<u>Annex II. Glossary of key metrological terms</u>	155
<u>Annex III. Published papers and contributions to International Conferences from this work</u>	177

PART II: Spanish Thesis Summary / Resumen en castellano

List of Symbols

T_{90} : International Kelvin Temperature of 1990

ρ : Density

h : Sensible enthalpy

K : Conductivity

ε : Emissivity

C_p : heat capacity

T : Temperature

S_h : Volumetric heat source

θ : Tilt angle of the cavity bottom

r : Cavity-aperture radius

L : Cavity length

d : Thickness of the cavity bottom

ε_g : Wall emissivity of graphite

K_g : Thermal conductivity of graphite

σ : Stefan-Boltzmann constant

ΔT : Temperature drop

$u(K_g)$: Standard uncertainty in the thermal conductivity of graphite

$u(\varepsilon_g)$: Standard uncertainty in the wall emissivity of graphite

$u(\Delta T; K_g)$: Uncertainty in ΔT due to the uncertainty $u(K_g)$

$u(\Delta T; \varepsilon_g)$: Uncertainty in ΔT due to the uncertainty $u(\varepsilon_g)$

$u(\Delta T; K_g, \varepsilon_g)$: Uncertainty in ΔT due to the combined uncertainties $u(K_g)$ and $u(\varepsilon_g)$

$u(\Delta T; \text{FTP})$: Uncertainty in ΔT due to the uncertainty in the furnace temperature profile

$u(d)$: Standard back-wall thickness variation for different crucible configurations

$u(L)$: Standard crucible length variation for different crucible configurations

$u(\Delta T; d)$: Standard uncertainty in ΔT due to the uncertainty $u(d)$

$u(\Delta T; L)$: Standard uncertainty in ΔT due to the uncertainty $u(L)$

$u(\Delta T)$: Overall standard uncertainty in ΔT

List of Acronyms

HTFP: high temperature fixed point
M-C: metal-carbon eutectic
MC-C: metal carbide-carbon eutectic
CCT : Comité Consultatif de Thermométrie
CCT-WG5: Comité Consultatif de Thermométrie – working group on radiation thermometry
NMI: National Measurement Institute
NMIJ: National Metrology Institute of Japan
NPL: National Physical Laboratory
PTB: Physikalisch-Technische Bundesanstalt
BNM-INM: BNM-Institut National de Metrologie/CNAM
BNM-LNE: BNM-Laboratoire National D'Essais
VNIIIFI: All-Russia Institute for Measurements in Optics and Physics
NIM: National Institute of Metrology of China
NML: National Measurement Laboratory of Australia
KRISS: Korea Research Institute of Standards and Science
BIPM: Bureau International des Poids et Mesures
NIST: National Institute of Standards and Technology of the USA
CEM: Spanish National Metrology Institute
HIMERT: Novel, High temperature, Metal-carbon Eutectic fixed points for Radiation Thermometry, Radiometry and Thermocouples
IS: International System
ITS: International Temperature Scale
ITS-90: International Temperature Scale of 1990
CFD: Computational Fluid Dynamics
RTE: Radiative Transfer Equation
DTRM: Discrete transfer radiation model
S2S: Surface-to-surface radiation model
DO: Discrete ordinates radiation model
FTP: Furnace Temperature Profile
RP: Real Profile
LP: Linear Profile

Sin P: Sine shaped Profile

CP: Constant Profile

HP: High Profile

NF: No Furnace

SCK: Sensitivity Coefficient for thermal conductivity of graphite K_g

SCE: Sensitivity Coefficient for the wall Emissivity of graphite ϵ_g

CHAPTER 1

Introduction and objectives



Chapter 1. Introduction and Objectives

1.1. Introduction

In the field of temperature measurement and calibration, the determination of the melting temperature of high temperature fixed points¹ has become the subject of intense research by the world temperature metrology community. This is because, once temperatures of these high temperature fixed points are determined, they will be used as easily reproducible radiance sources in any laboratory. In effect they will serve as stable temperature references for the calibration of thermal instruments of measurement (such as radiation thermometers and radiometers).

When characterising high temperature fixed points (HTFPs) there is a difference between the temperature measured with the radiation thermometer and the temperature of the liquid-solid interface. This difference is caused by several factors:

- The heat losses to the surroundings
- The thermal resistance of the metal and the walls of the crucible
- The material properties of the fixed point
- The temperature distribution in the furnace
- The design of the crucible and the furnace
- The nominal temperature of the fixed point
- The presence of impurities in the alloy
- How well the metal ingot is formed

Investigating and quantifying the effect of these parameters on the realised temperature of HTFPs of different designs and implementations is at the heart of this thesis.

¹ Most fixed points are temperatures at which a substance changes its phase, for example from solid to liquid or vice versa. During the phase change a significant amount of heat is absorbed or liberated, the latent heat of melting or fusion, and while this is happening the temperature remains almost constant, i.e. it is ‘fixed’. If a thermometer is used to measure this temperature during the phase change, its calibration at this point can be performed. A full calibration can be obtained by using a series of fixed points over the range of interest.

There are several motivations for this work. Firstly, high level metrology, where the Comité Consultatif de Thermométrie (CCT) in 1996 recommended National Measurement Institutes (NMIs) work towards developing high temperature fixed points above 2300 K having a reproducibility better than 0.1 K [1]. Secondly from a practical standpoint, there is an increasing need of improved accuracy measurements at high temperatures (in aerospace, nuclear, metals and material industries for instance). Because of these requirements several attempts have been made to construct high temperature fixed points above the copper point, which until recently was the highest temperature reliable fixed-point.

Studies have been performed on pure metal fixed points such as the freezing point of nickel (1728 K), cobalt (1768 K), iron (1811 K), palladium (1828 K), platinum (2041.3 K), rhodium (2236 K), iridium (2719 K), molybdenum (2895 K) and tungsten (3687 K). These have all been recommended as secondary reference points above the freezing point of copper [2]. However the problem of constructing these fixed points, it was supposed, is that graphite can not be used as the crucible material since it would diffuse in the pure metal contaminating it, and thus modifying the transition temperature. To avoid this contamination problem alumina crucibles have been used for the nickel [3], platinum [4, 5] and the palladium [6, 7] fixed points. However alumina crucibles are too fragile for long term practical use and if used for radiation thermometry they have the intrinsic problem of a much lower emissivity than those made with graphite [8], leading to large corrections required to the radiometric temperature. In the case of thermocouples, this problem is not so severe in that calibration at high temperatures can be performed using the wire bridge method [9] or miniature cells (which are intrinsically more robust) at the points of palladium (in argon atmosphere) and platinum. However both the wire-bridge and the use of mini-ingots lead to large calibration uncertainties in the national measurement institutes. Additionally alumina itself has also been studied as a possible fixed point material [10], around 2320 K, using tungsten to construct the crucible, but the results were at best inconclusive.

More recently a new series of high temperature fixed point materials that would allow the use of graphite crucibles was reported by Yamada *et al.* [11, 12] from the National Metrology Institute of Japan (NMIJ). This new idea consists in the use of metals that have a eutectic reaction with carbon, the resulting eutectic

alloy is the fixed point material. The usage of such materials, metal-carbon (M-C) eutectics, metal-carbide-carbon eutectics (MC-C) and metal-carbide carbon peritectics M(C)-C avoids the contamination problem when using graphite crucibles because graphite is one of their components, and thus enables the use of graphite to construct high temperature crucibles. The advantages of using graphite crucibles are their much better robustness and higher emissivity compared to alumina crucibles.

Moreover there is a significant intrinsic advantage through using M-C fixed points in graphite crucibles.

First, the M-C eutectic transition temperature is independent of the amount of carbon present in the alloy, provided that the solid solubility of carbon in the metal is exceeded. Even this latter condition is not true if realised in a graphite crucible for the metal dissolves graphite from the crucible itself until it attains the eutectic composition. Similarly, when the concentration of carbon in the alloy is hypereutectic (i.e. too high a concentration of graphite to be at the eutectic composition), primary graphite will form (i.e. will be precipitated) during freezing until the remaining liquid reaches the eutectic composition along the liquidus line. At this point the transition will occur at the eutectic temperature. The precipitated graphite has no noticeable effect on the measured transition temperature.

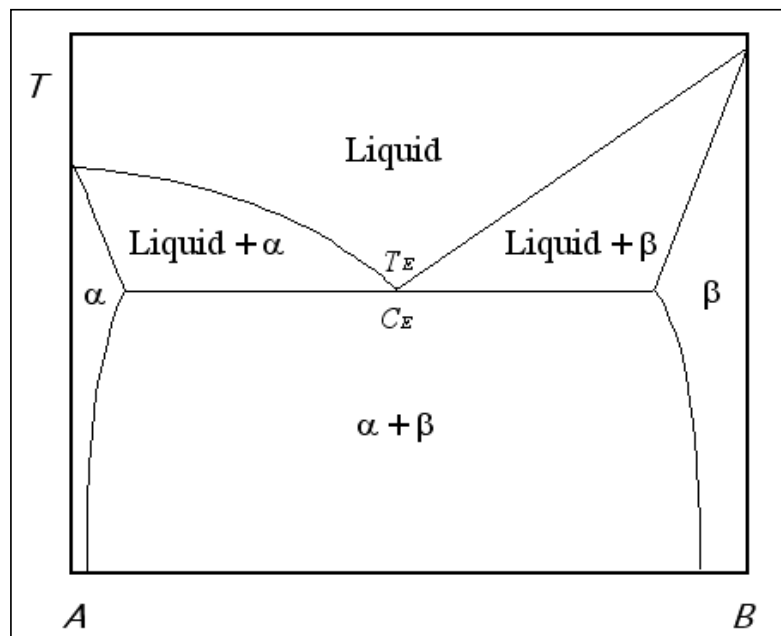


Figure 1.1. Binary eutectic phase diagram.

Second, M-C eutectics provide a large number of possible high temperature fixed points ranging from the Fe-C eutectic fixed point (1153 °C) up to the Re-C eutectic fixed point (2474 °C). This temperature range can even be increased above 2500 °C by the use of metal carbide-carbon (MC-C) eutectic fixed points [13, 14]. MC-C eutectic fixed points are based upon metals that form carbides, having an eutectic reaction between these carbides and carbon. As a result graphite crucibles do not contaminate MC-C eutectics either. Finally an important extra class of materials based on the peritectic reaction have been discovered [15], these are important because of the WC-C peritectic which has very good performance nearly 300 K above that of the Re-C (2749 °C).

Since the initial paper on M-C eutectics [11], several NMIs have initiated studies on these new high temperature fixed points both for radiation and contact thermometry. Development and research on M-C eutectic fixed points started at the National Measurement Institute of Japan (NMIJ) but quickly spread to the National Physical Laboratory (NPL, UK), the BNM-Institut National de Metrologie/CNAM (BNM-INM, FR), the BNM-Laboratoire National D'Essais (BNM-LNE, FR) and the Physikalisch-Technische Bundesanstalt (PTB, DE) within the frame of a cooperative Euromet project (no. 550, Study and realization of metal-carbon eutectic fixed points for radiation thermometry purposes) [16]. The first blackbodies for radiation thermometry developed at the NPL were Co-C, Pd-C, Pt-C, Ru-C and Ir-C eutectic fixed points. The first prototype developed at the BNM-LNE for contact thermometry used Pt-C eutectic as the fixed point material.

Later within Europe the number of interested partners increased to include direct industrial participation (Thermocoax and Land Instruments International) and a University (Universidad de Valladolid). A proposal was put to the European Commission fifth Framework “GROWTH” Programme whose objective was to develop a significant knowledge base in M-C eutectic technology within Europe. This proposal Novel High temperature, Metal-carbon Eutectic fixed points for Radiation Thermometry, Radiometry and Thermocouples (HIMERT) was accepted and successful in its objectives – making Europe the centre for HTFP research [17]. During the HIMERT project there was close cooperation between the consortium members and NMIJ.

Other NMIs apart from the ones already cited have also done research studies and have participated on comparisons on M-C and MC-C eutectics. The All-Russia Institute for Measurements in Optics and Physics (VNIIIOFI) has developed MC-C eutectic fixed points for implementation in radiometry [18]. The VNIIIOFI, the National Institute of Metrology of China (NIM), the Spanish Metrology Centre (CEM), the National Measurement Laboratory of Australia (NML), the Korea Research Institute of Standards and Science (KRISS), the Bureau International des Poids et Mesures (BIPM) and the National Institute of Standards and Technology of the USA (NIST) have all participated in comparisons with members of the HIMERT consortium and the NMIJ [19-24].

A good review of M-C and MC-C eutectic temperatures as measured by six NMIs (NMIJ, NPL, BNM-INM, PTB, VNIIIOFI and NIST) which have done studies on these high temperature fixed points can be found in reference [25] and a good introduction to HTFP is found in [15].

This work is a continuation of the results presented in the thesis of Pablo Jimeno Largo [26], from Valladolid University.

1.2. Objectives

There are many parameters that influence the realised temperature of a high temperature fixed point. The work undertaken in this thesis is to provide definitive quantitative answers to the influence of those parameters. Specifically the objectives of this thesis are:

- To confirm that a good numerical analysis to simulate radiation heat transfer inside high temperature furnaces is possible.
- To better understand the behaviour of the high temperature fixed points inside the furnace, e.g. model a) the effect of the furnace and the crucible design on the resultant temperature and also b) to evaluate the influence of the furnace temperature profile on the melting point.
- To determine the uncertainty due to the heat losses from the furnace aperture to the surroundings, the so called temperature drop effect.

- To estimate the uncertainty in the resultant temperature due to the graphite thermal conduction and to the emissivity of the radiation walls inside the high temperature furnace.

In order to undertake this study, a numerical analysis approach with the Computational Fluid Dynamics (CFD) software FLUENT was performed. Numerical analysis was used in this study because experimental investigation of these parameters is impossible in some cases and too costly in others.

CHAPTER 2

Fundamentals of thermometry: temperature, thermometers and temperature scales



Chapter 2. Fundamentals of Thermometry: Temperature, Thermometers and Temperature Scales

2.1. Historical notes

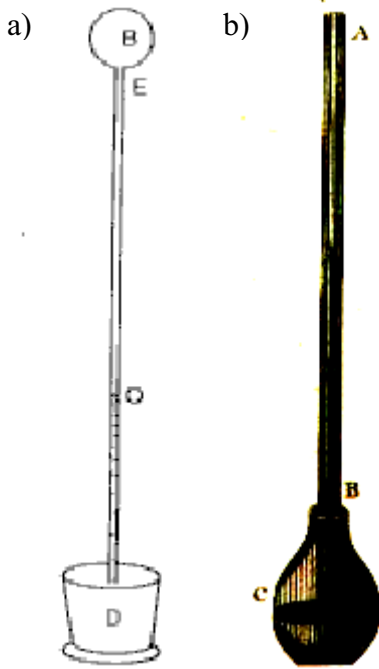
Temperature has been, from antiquity, a well-known and yet not-understood concept. Everyone knew what the subjective terms “hot” and “cold” means but quantification was elusive. Other measurement quantities, like mass, length and time¹ being extensive quantities were better understood and hence quantified. In fact a good understanding of temperature did not begin to emerge until the XVIII century, and even then it was only in terms of practical, if arbitrary, scales and did not grasp at the fundamental meaning of temperature as a measure of thermal energy. It was not until the mid-19th Century with the work of Kelvin, Boltzmann and others that a true understanding of temperature began to emerge, this was bound up with the development of the physical discipline of thermodynamics.

It is not so strange to think that the intuitive temperature concept is difficult. It is an intensive quantity, and not directly related to any extensive quantity. In addition, it is necessary to consider that a loose concept of temperature idea is arrived at through the senses which are not very reliable.

Therefore, to introduce a quantitative concept of temperature the first thing to do is to exactly define the quantity, which then gives a starting point to begin measuring it. Once the concept has been established then apparatus will be needed, as well as scales and units.

In the daily life different scales are generally used mainly the Celsius, °C, and (in the US) the Farenheit, °F. However it should be noted that the scale in use throughout the world (including the US) is the ITS-90 which uses Kelvin, K. With respect to the apparatuses, the alcohol and mercury thermometers are familiar. It

¹ These four quantities are part of the seven fundamental quantities of SI. The others are electric current, amount of substance and luminous intensity, www.bipm.org/en/si/base_units.



is known that the length of the liquid column changes with the temperature (due to the expansion of the liquid) and a relation between column length and temperature is derived. These aren't, of course, fundamental scales but initially at least arbitrary and practical. In fact a thermometer can be constructed from any quantity that varies with the temperature if the relation is known (for example the variation of the electrical resistance of a wire or piece of semi-conductor with temperature).

Figure 2.1 a) Air t. **b)** Florentine t. With respect to the use of thermometers, the first reference is to Santorio Santorre (Italian) who invented the air thermometer (1612). He used his thermometer to measure a variety of temperatures ranging from medicine to meteorology.

The air in bulb B (figure 2.1.a) contracts or expands in proportion to the temperature and moves the meniscus O of the liquid (water, alcohol or oil). D is a reservoir for the liquid.

By the middle of XVII century sealed glass thermometers began to be used with liquid instead of air as the working fluid. At the outset water and alcohol ("spirit thermometer") were used but latterly mercury. In the development of these thermometers the advances in the art of glass-blowers in Northern Italy were very important. They made very sensitive thermometers, but they were still marked with a practical arbitrary scale and as such a universal scale had not yet been established.

In 1661 Robert Hooke (England) made an important step forward. He modified the Italian design and showed that comparable thermometers could be constructed with no need to have the same dimensions. In addition he introduced the idea of a fixed point for the first time, another important innovation (although Hooke thought there were two fixed points for the freezing of the water possibly due to the anomalous expansion of water to 4°C where it has the maximum density). He established a -7 scale degrees to 13 degrees and these were used as

the standard in the Royal Society until 1709 and with which a large number of weather recordings were made. These values were chosen as the first fixed points and showed the main importance that they would have in the future.

Until now, independence of the scale with the thermometric quantity does not exist, since an appreciation of the differences between the properties of the fluid did not exist. It was Reaumur (1739) who showed that the scales of alcohol and mercury were different because both liquids do not expand uniformly with temperature (as indicated above the liquid column of a water thermometer would decrease between 0°C and 4°C as the density of the water increases between these two values).

At the beginning of XVIII century the contributions of Fahrenheit and Amontons appear, who worked in two different aspects of thermometry that now are distinguished between primary (or absolute) and practical thermometry.

- Fahrenheit:

He was the first person to make reliable mercury thermometers. In addition, after discussions with the astronomer Römer he established a scale with two fixed points and a regular number of divisions. He accepted the calibration methods of Römer and settled on fixed points of a water mixture with ice (32°F) and the temperature of the healthy human body to 96°F. (He divided the degrees of Römer in 4 to have more resolution and set as zero the temperature of the coldest day of the year - 7 January of 1709 - in Copenhagen).

- Amontons:

He made a very significant contribution to the understanding of thermometry as he developed a gas thermometer with constant volume. He used air as the thermometric fluid and concluded that the lowest possible temperature was that corresponding to zero pressure gas. He indicated that the temperature was proportional to the pressure and therefore considered it was only necessary for one fixed point to define the scale. His proposal in this regard was not considered as practical at the time which is a pity because his work foreshadowed the proposals of Kelvin and others of an absolute temperature scale by more than a century.

However from that point the history of thermometry followed two paths, that today are known as practical and primary thermometry.

In the first case practical scales based on arbitrary fixed points were developed. In this sense, Celsius (1742) established a scale in a mercury thermometer with two fixed points, the ice point and that of boiling water. He assigned 100 degrees to the ice point and 0 degrees to the steam. It was his disciple, Strömer that inverted the scale to the familiar one we know today. In addition the thermometers of platinum resistance and the Rhodium/platinum thermocouple were introduced at the end of XIX century. The culmination of the work in practical thermometry was the adoption of an international temperature scale in 1927 (ITS-27) and its successors.

In the second case, the gas thermometer and thermodynamics are developed. The works of Boyle, Dalton, Gay-Lussac, Charles, etc. on the properties of the gases, reached the conclusion that all the gases had almost the same coefficient of expansion. This realised a scale with effectively only one fixed point. This was not accepted completely until in 1960 the kelvin was defined assigning an only fixed point the triple point of water.

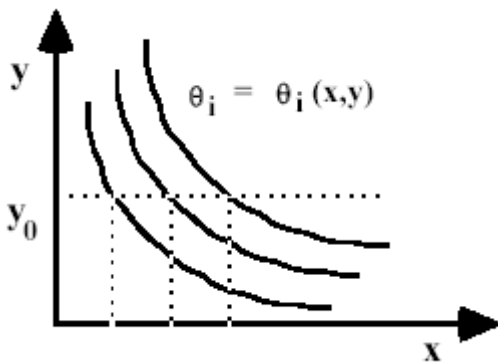
2.2. Temperature concept

In this section the theoretical basis of temperature and temperature measurement are briefly outlined.

“Temperature is a quantity that takes the same value in all systems that are in thermal contact and have arrived at thermal equilibrium”.

The idea of a parameter (i.e. temperature) that characterizes the internal state of the system comes from the Zeroth law: “if two systems are in thermal equilibrium with a third system then they are also in thermal equilibrium with each other”. This allows to “imagine” a system, called a thermometer, that can be put in thermal contact with other systems to discover if they are or not in the same thermal state. This law is arguably the most fundamental of the four numbered laws of thermodynamics. It was called the zeroth law because the need to state it explicitly was not understood until after the first, second, and third laws had been named and found common acceptance in the physics community.

Starting from the idea that thermal equilibrium exists and therefore a functional relation between the state variables of the systems exists -a state

**Figure 2.2. State function.**

of all points with the same value of that function is an isotherm (constant T).

The First law of thermodynamics, an expression of the principle of conservation of energy, states that energy can be transformed (changed from one form to another), but cannot be created or destroyed: “The internal energy of an isolated system is constant”:

$$dU = \delta Q - \delta W \quad (2.1)$$

Where dU is an infinitesimal (differential) change in internal energy, δQ and δW are infinitesimal amounts of heat supplied to the system and work done by the system, respectively.

The Second law of thermodynamics, which can be expressed as: “Heat cannot spontaneously flow from a colder location to a hotter location”, is an observation of the fact that over time, differences in temperature, pressure, and chemical potential tend to even out in a physical system that is isolated from the outside world.

In addition, the Second law allows the definition of another important quantity in thermodynamics, entropy S , which is intimately related to the temperature. Entropy is a measure of how much the evening-out process has progressed. The entropy of an isolated system which is not in equilibrium will tend to increase over time, approaching a maximum value at equilibrium.

variable is one of the set of variables that describe the "state" of a thermodynamic system, such as temperature, pressure, internal energy, enthalpy, and entropy- it can be mathematically justified the existence of a function $\Theta=\Theta(x, y)$ (figure 2.2) with the same value in all the systems in thermal equilibrium. The geometric place

$$\delta Q/T = dS \text{ (reversible process)} \quad (2.2)$$

An important application of the Second law is the heat engine, which performs the conversion of heat energy to mechanical work by exploiting the temperature gradient between a hot "source" and a cold "sink".

The theoretical maximum efficiency of any heat engine depends only on the temperatures it operates between. This efficiency is usually derived using an ideal imaginary heat engine such as the Carnot heat engine. Mathematically, this is because in reversible processes, the change in entropy of the cold reservoir is the negative of that of the hot reservoir, keeping the overall change of entropy zero.

In classical thermodynamics, the Second law is a basic postulate applicable to any system involving heat energy transfer, however the statistical thermodynamics approach is also important in understanding temperature. In this the microscopic behaviour of the particles that constitute the system is analyzed. In particular the kinetic theory for ideal gases indicates that for a molecule of mass m , the average value of the square of the speed for the particles in the gas is $\langle v^2 \rangle = 3 K_b T m^{-1}$. In this approach the temperature, T , allows to estimate the average speed, v , of the ideal gas particles provided the molecular mass, m , is known, where K_b is the Boltzmann constant. Alternatively and more fundamentally the temperature is an indication of the average kinetic energy of the particles that constitute the gas.

2.3. Concept of thermometer and temperature scale

In thermometry both primary and practical thermometers are used. Generally primary thermometers are used for determining thermodynamic temperatures on which practical temperature scales are based. These two classes are defined below.

Primary thermometers: Those in which the equation of state can be explicitly written and solved without the need to introduce any empirical or arbitrary constants. Correction terms for solving practical problems are allowed - such as virial coefficients in gas thermometry - to allow for two and three particle interactions. *Examples:*

- Gas thermometry: All kinds of gas thermometry are based on simple relations between the properties of an ideal gas and thermodynamic temperature:

$$pV = nR.T \quad (2.3)$$

Where p is the gas pressure, V the volume of the gas, n the number of moles, R the universal gas constant and T the thermodynamic temperature.

Though many gases exhibit a nearly ideal behaviour at and above the triple point of water, the small departures from the ideal behaviour must be carefully considered for the highest level of accuracy even at these temperatures. This is done by measuring the dependence of the relevant property on gas density (measurement of isotherms). The ideal behaviour is then deduced by fitting an appropriate virial expansion to the measured isotherm and extrapolating to zero. The range of applicability is defined in terms of the vapour-pressure temperature relations of ${}^3\text{He}$ and ${}^4\text{He}$ between 0.65 K and 5.0 K and by means of a helium gas thermometer between 3.0 K and the triple point of neon (24.5561 K).

- Acoustic thermometry: Acoustic thermometry exploits the simple relationship between the speed of sound of a monatomic gas, v , (such as argon) and the thermodynamic temperature of the gas, T :

$$v = \sqrt{(\gamma RT)/M} \quad (2.4)$$

Where γ is the adiabatic dilatation coefficient, R is the universal gas constant, and M is the molar mass of the gas.

The frequencies of acoustic resonances within a nearly spherical, gas-filled cavity are proportional to the speed of sound or the square root of thermodynamic temperature. Although numerous corrections must be applied to the raw data, the corrections are well documented and theoretically well understood. Acoustic thermometry has excellent demonstrated reproducibility in the range of 150 K to 300 K.

- Electrical noise thermometry: Noise thermometry exploits Nyquist's relationship between thermodynamic temperature and the variance of the thermally induced fluctuations in noise current or voltage generated by a resistor. Noise thermometers are appealing because they are entirely electronic and have a simple and accurate equation of state. However, noise thermometers have the disadvantage of a small and easily corrupted noise signal spread across a wide

bandwidth. Johnson noise thermometry works well at temperatures <1 K. The equation of Nyquist's theorem is given by:

$$S_v = 4K_b T r \quad (2.5)$$

Where S_v is the voltage noise power spectral density, K_b is the Boltzmann constant, T is the temperature and r is the resistance.

- Total radiation thermometry: Total radiometry is so-called because it seeks to accurately measure the total power emitted from a blackbody of uniform and stable temperature. The equation is given by the Stefan–Boltzmann law:

$$E^0(T) = \int_0^{\infty} E^0(\lambda, T) d\lambda = \sigma T^4 = 5,67 \cdot 10^{-8} \cdot T^4 (W \cdot m^{-2}) \quad (2.6)$$

In which the total emittance, E^0 , integrated for all the wavelengths, λ , is proportional to the fourth power of the temperature T .

The lowest uncertainty implementation of the method is through the use of a cryogenic electrical substitution radiometer. The recommended range of applicability is above the freezing point of silver (961.78 °C).

- Spectral band thermometry: Absolute spectral band radiometry is a method underlying the measurement of the spectral radiance or irradiance of a blackbody radiator. This requires the construction of a filter radiometer. In principle, these are simple devices composed of a well characterized aperture, a spectrally selective filter, and a silicon photodiode. Although simple in concept, in practice, significant precautions need to be taken in both radiometer design and implementation to obtain optimum performance. Absolute spectral-band radiometry is highly appropriate for temperatures above 1200 K.

Practical thermometers: Those that are not primary, i.e. where an explicit equation of state cannot be written down nor solved. *Examples:*

- Platinum resistance thermometers: Also called resistance temperature detectors (RTDs), are temperature sensors that exploit the predictable change in electrical resistance of some materials with changing temperature. As they are almost invariably made of platinum, they are often called platinum resistance thermometers (PRTs).

- Thermocouples: In 1821, the German-Estonian physicist Thomas Johann Seebeck discovered that when any conductor (such as a metal) is subjected to a thermal gradient, it will generate a voltage. This is now known as the

thermoelectric effect or Seebeck effect. In electronics, thermocouples are a widely used type of temperature sensor and can also be used as a means to convert thermal potential difference into electric potential difference. They are cheap and interchangeable, have standard connectors, and can measure a wide range of temperatures.

- Thermistors: A thermistor is a type of resistor used to measure temperature changes, relying on the change in its resistance with changing temperature. Thermistor is a combination of the words thermal and resistor. The thermistor was invented by Samuel Ruben in 1930.

- Radiation thermometers: They use the Planck's law, which relates the radiation emitted by a body to its temperature. The most important characteristic of these thermometers is that there is no physical contact between the sensor and the system whose temperature is desired to measure. They receive the generic name of pyrometers.

In order to use practical thermometers they must be calibrated, ideally against sources of known temperature to determine the form of unknown temperature dependent terms². The known temperature sources are determined *a priori* by primary thermometry. These known temperature sources can be fixed points or isothermal regions whose temperature is determined by primary methods.

PRI[□]ARY THER[□]O[□]ETRY \rightarrow THER[□]ODYNA[□]IC TE[□]PERATURE
(variable of the state function)

PRACTICAL THER[□]O[□]ETRY \rightarrow E[□]PIRICAL TE[□]PERATURE²
(Bound to a thermometric property, that varies with the temperature)

2.4. International temperature scale (ITS)

The International Temperature Scale of 1990 (ITS-90) was adopted by the International Weights and Measures Committee in its meeting of 1989, in agreement with the resolution of the General Conference of 1987. This scale replaces the Practical International Temperature Scale of 1968 (edition reviewed in 1975) and the Provisional Scale of 1976 between 0.5 and 30 K. The purpose of

² Of course they could be calibrated against an arbitrary scale – as in the past and could still be used as thermometers but the temperatures would have no fundamental significance apart from the arbitrary scale.

the ITS-90 was to generate a scale that was easy to realise, precise and reproducible whilst at the same time generate values that were close to thermodynamic temperatures. So whilst it is a practical scale in that it relies on practical thermometers (the platinum resistance thermometer) nevertheless because of its formulation it generates, very closely, thermodynamic temperatures. Temperature units, and in particular the ITS-90, is described below [27].

2.4.1. Temperature Units

The unit of the fundamental physical quantity known as thermodynamic temperature, symbol T , is the kelvin, symbol K, defined as the fraction 1/273.16 of the thermodynamic temperature of the triple point of water.

Due to the form in which the previous scales were defined, it is common to express the temperature from its difference with respect to the ice point, 273.15 K. A thermodynamic temperature, T , expressed in this form is known as Celsius temperature, t , defined by:

$$t \text{ } (\text{°C}) = T \text{ } (\text{K}) - 273.15 \quad (2.7)$$

The unit of the Celsius temperature is the degree Celsius, whose symbol is °C, which has the same size as the kelvin by definition. A temperature difference can be expressed in kelvin or Celsius.

The International Temperature Scale of 1990 (ITS-90) defines the International Kelvin Temperature, T_{90} , and the International Celsius Temperature, t_{90} .

2.4.2. ITS principles

The formal stated purpose of the ITS was:

"The intention of the International Temperature Scale is to allow measurements of temperature to be made precisely and reproducibly and with temperatures measured on these scales being as close an approximation as possible to the corresponding thermodynamic temperatures" [28].

Significant numerical differences between the values of T_{90} and the corresponding ones of T_{68} measured in the International Practical Temperature Scale of 1968 (IPTS-68) were found to exist at the time of the redefinition. The largest deviation amounting to above $0.3\text{ }^{\circ}\text{C}$ at about $800\text{ }^{\circ}\text{C}$, was due to the use of a Pt/Rh thermocouple being used as the scale realisation sensor in IPTS-68, this was replaced with the high temperature platinum resistance thermometer in the ITS-90.

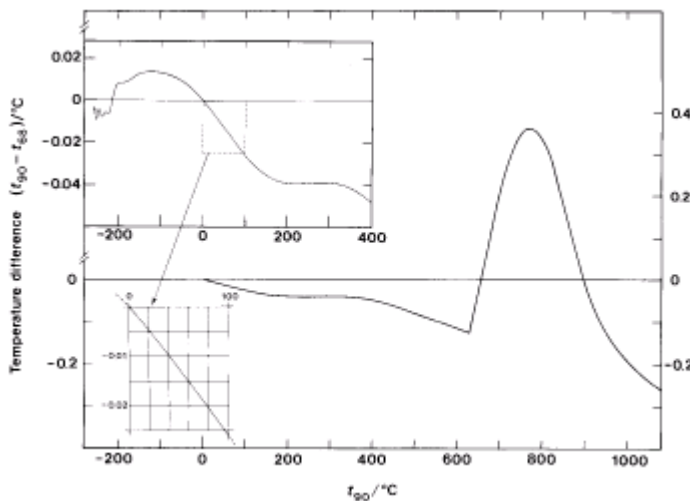


Figure 2.3. Difference between the T_{90} and the T_{68} .

ITS-90 ranges from 0.65 K to the highest attainable temperature measured by Planck's radiation law using monochromatic radiation. ITS-90 includes a number of intervals and subintervals from which T_{90} is defined. These are shown in Figure 2.4 below. Some of these intervals and subintervals are overlapped and where this overlapping takes place, different valid definitions of T_{90} exist which are essentially equivalent within the stated uncertainties (uncertainty components need to be included to allow for sub-range inconsistencies). Nearly all the sub-ranges, bar one, pivot around the water triple point.

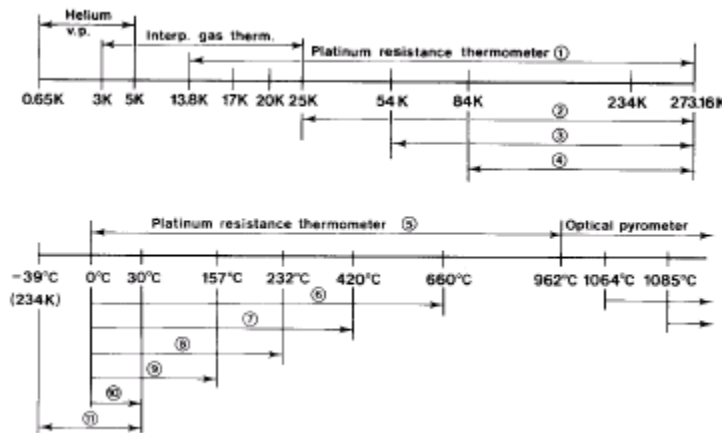


Figure 2.4. Scale of ITS-90.

It should be noted that the sub-range inconsistencies are very small (i.e. for high quality platinum resistance thermometers the magnitude of the sub-range inconsistency substantially never exceeds 0.5 mK within their range of normal use) and only measurements of very high precision can detect the numerical differences made at the same temperatures, but with the different sub-range definitions. In any case, these differences have no practical importance.

Standard devices used for ITS-90 scale realisation and range of applicability

The four main regions of the ITS-90 are [28]:

- Between 0.65 K and 5.0 K, T_{90} is defined in terms of the vapour-pressure temperature relations of ${}^3\text{He}$ and ${}^4\text{He}$.
- Between 3.0 K and the triple point of neon (24.5561 K) T_{90} is defined by means of a helium gas thermometer calibrated for three experimentally realizable temperatures having assigned numerical values (defined fixed points) and using specified interpolation procedures.
- Between the triple point of equilibrium hydrogen (13.8033 K) and the freezing point of silver ($961.78\text{ }^\circ\text{C}$) T_{90} is defined by means of platinum resistance thermometers calibrated at specified sets of defining fixed points and using specified interpolation procedures.
- Above the freezing point of silver ($961.78\text{ }^\circ\text{C}$), T_{90} is defined in terms of a defining fixed point and the Planck's radiation law.

Fixed points used in defined temperature scales

Fixed points of defined value are used in the ITS-90 to enable a scale very close to thermodynamic temperature values to be attained. Different sorts of fixed points are generally used, these are triple points, melting points and freezing points. However historically, in different international temperature scales, different change of phase points, or fixed points, have been used as temperature references. The historically important ones are listed below:

- Triple Points: Single value of pressure and temperature in which the three phases (solid, liquid and steam) of a pure substance coexist. The water triple point is used as the formal definition of the kelvin, and it, along with others (i.e. Hg, Ar) are used in the ITS-90 at low temperatures.

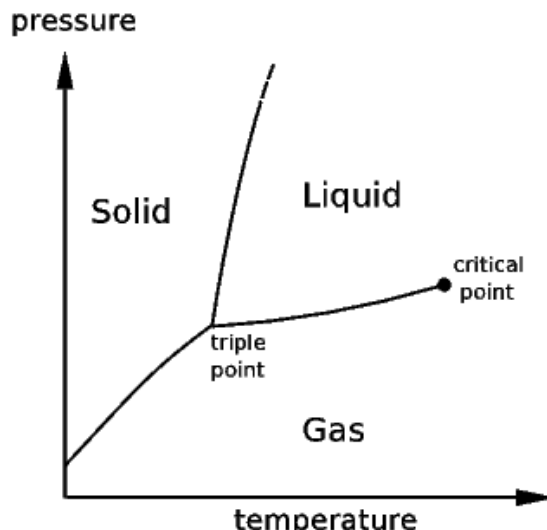


Figure 2.5. triple Point.

- Freezing points: Temperature where begins to form the solid from the liquid at 1 atm.

- Melting points: Temperature where the solid melts at 1 atm.

- Boiling points: The steam pressure of a pure substance is only function of the temperature. Usually it is considered the normal boiling point, that is the temperature where the steam pressure is 1 atm.

- Superconducting transition points (in the Provisional Scale of the 76, for very low temperatures < 10 K).

Given the difficulty in the realisation of the boiling point because of their great sensitivity to pressure variation, in ITS-90 all the boiling points of previous

scales have been eliminated, and have been replaced by melting point (gallium only), freezing points or triple points.

The adopted fixed points of the ITS-90 are:

Table 2.1. Table of fixed points adopted by ITS-90.

Number	Temperature		Substance ^a	State ^b
	T_{90}/K	$t_{90}/^\circ\text{C}$		
1	3 to 5	-270.15 to -268.15	He	V
2	13.8033	-259.3467	e-H ₂	T
3	~17	~-256.15	e-H ₂ (or He)	V (or G)
4	~20.3	~-252.85	e-H ₂ (or He)	V (or G)
5	24.5561	-248.5939	Ne	T
6	54.3584	-218.7916	O ₂	T
7	83.8058	-189.3442	Ar	T
8	234.3156	-38.8344	Hg	T
9	273.16	0.01	H ₂ O	T
10	302.9146	29.7646	Ga	□
11	429.7485	156.5985	In	F
12	505.078	231.928	Sn	F
13	692.677	419.527	Zn	F
14	933.473	660.323	Al	F
15	1234.93	961.78	Ag	F
16	1337.33	1064.18	Au	F
17	1357.77	1084.62	Cu	F

- a. All substances except ³He are of natural isotopic composition, e-H₂ is hydrogen at the equilibrium concentration of the ortho- and para- molecular forms.
- b. The symbols have the following meanings: V: vapour pressure point; T: triple point; G: gas thermometer point; □, F: melting point, freezing point.

2.4.3. Current thermometry developments in the ITS

In 2006, motivated by the need for a formal document to give definitive guidance for the practical realization of the kelvin, i.e., the measurement of temperature in kelvins, in accordance with the International System of Units, the Consultative Committee for Thermometry (CCT) created the *mise en pratique* for the definition of the kelvin (*MeP-K*) [29]. The International Committee for Weights and Measures (CIPM) foresaw that adoption of the proposed new definition of the kelvin, based on a fixed value for the Boltzmann constant, would require an *MeP-K* [30]. Subsequently, the CCT considered constructing a new

International Temperature Scale to replace the present ITS-90 and its low-temperature counterpart, the Provisional Low Temperature Scale from 0.9 mK to 1 K (PLTS-2000). However, the CCT decided not to do this because a new temperature scale would impose a large burden on industry, which has a large investment in hardware and process algorithms specific to the ITS-90. Instead, the CCT adopted the *MeP-K* to open a new and flexible path for updating and expanding the range of recognized thermometric methods without changing the status of the ITS-90. The *MeP-K* included direct realization of thermodynamic temperature, independent of the defined International Temperature Scale, ITS-90, where the techniques of primary thermometry had advanced sufficiently to confer benefit. This was thought to apply at very low and very high temperatures.

Very low temperatures (PLTS-2000)

The requirements of temperature measurement in the range well below 1 K differ from those at higher temperatures in nature as well as in degree. There are no longer any gases whose properties can be used in gas thermometry (for primary measurements or interpolation) or in vapour pressure thermometers (as used in the ITS-90). Thermal radiation is virtually extinct, and thermometry must rely mainly on the electrical, magnetic or nuclear properties of condensed matter, whose characteristic energies lie in the millikelvin range. Moreover, the rapid increase in thermal resistances on cooling means that measurements must be almost non-dissipative.

However, a thermometer using the melting pressure of ^3He , which was first proposed by Scribner and Adams [31], almost entirely meets the requirements. In 1996, the CCT called for a ^3He melting-pressure equation to be derived to serve as the basis for an extension of the ITS-90 down to a temperature of about 1 mK, analogous to the use of the vapour pressures of ^3He and ^4He in the ITS-90. ^3He is a well-defined substance, with sufficient availability, and the melting pressure, p_m , is sensitive to temperature over most of the range of interest.

The Provisional Low Temperature Scale of 2000, PLTS-2000, was adopted by the CIP[□] in October 2000 to provide an extension of the ITS-90, to

lower temperatures. It ranges from the Néel temperature of solid ^3He , $T_{2000} = 0.902 \text{ mK}$, up to 1 K, thus overlapping the ITS-90 between 0.65 K and 1 K. The definition and derivation of the PLTS-2000 has been published in [32].

Very high temperatures [33]

A task group of CCT-WG5 (working group in radiation thermometry) was established in May 2008 to examine the different methods of direct measurement of thermodynamic temperature above the silver point, and, in particular, to write the text for the *MeP-K* for this temperature range. Although the ITS-90 is experimentally simple to implement, other methods could convey significant advantages, either in terms of lower uncertainties or improved robustness/security of realization. The methods are: (a) absolute radiometry linked to the appropriate radiometric units and (b) high-temperature fixed points (HTFPs) as defining points or as radiometric reference standards for the realization/ dissemination of thermodynamic temperature.

Temperatures above the silver point were thought the prime candidate for recommending (or at least providing a regularized basis for) a primary realization of thermodynamic temperature as an alternative to the ITS-90. There were several reasons for this; the main three are:

- Absolute radiometry can already be implemented in several NIs, and at high temperatures, achieves uncertainties competitive with, or somewhat better than, ITS-90.

- The extrapolation of the ITS-90 from the defining fixed points to higher temperatures means that there are inherent limits to the scale realization uncertainty that can be achieved. The ITS-90 definition means that the uncertainty associated with scale realization increases (approximately) as T^2 from the reference fixed-point temperature.

- It is clear that the ITS-90 is not uniquely defined. Fixed-point blackbody cavities at the Ag, Au, or Cu freezing-point temperatures are all allowable reference sources for the basis of an ITS-90 realization. If the defined temperatures for these fixed points are not thermodynamically correct, the choice of fixed point would inevitably lead to different temperatures being realized.

Finally, an additional reason for considering alternatives to the ITS-90 above the silver point is that in practice the formal definition of the ITS-90 in this regime cannot be implemented, though this is certainly not an exception among the SI units. The ITS-90 formalism calls for the use of Planck's law in ratio form with strictly monochromatic blackbody radiation in vacuum. Neither of these conditions is achievable in practice: integral or mean effective wavelength forms of Planck's law are used to allow for the finite bandwidth of the radiation thermometer, and measurements of thermal radiation are usually made through a gas rather than a vacuum.

CHAPTER 3

Analysis of thermal modelling methods



Chapter 3. Analysis of Thermal Modelling Methods

3.1. Introduction

As has already been indicated, this study aims to solve a physical problem where heat transmission by conduction, convection and radiation are involved, using the equations that govern these phenomena through the use of numerical methods.

3.2. Characteristics of Computational Fluid Dynamics (CFD)

3.2.1. Introduction

Computational Fluid Dynamics (CFD) is a technique that allows one to find a numerical solution of the equations that govern the movement of the fluids in a space and temporary domain, as well as estimate values for other associated phenomena such as: heat transference, chemical reactions..., allowing to obtain a complete description of the fluid field.

The equations that govern the dynamics of Newtonian fluids, the equations of Navier-Stokes, were established more than a century ago, but a numerical solution was unthinkable with the calculation resources of that time. However it is known that if important simplifications are not made, analytical solutions for the Navier-Stokes equation do not exist. The area of experimentation in Fluids Mechanics has played a very important role in the validation of certain simplifying hypotheses of the equations that govern fluid transport, nevertheless, it's the cost of experimentation increases the cost of the design, and sometimes, to the point of inviability. It was therefore a step change advance when, with the continuous advance in the calculation speed of the computers and its memory capacity since 1950, allowed these problems to be tackled numerically. This originated the birth of CFD which has become a separate sub-disciple branch of Fluid Mechanics complementary to its analytical and experimental branch. The

improvement of calculation power in the numerical solution is what has really impelled the Computational Fluid Dynamics.

Nowadays CFD usually refers to the approach that allows a numerical solution to the equations of Navier-Stokes. The solution of these equations requires: the definition of certain boundary conditions in the limits of the physical domain of the problem, information referring to the properties of the fluid, like density, viscosity,..., and in addition, in non stationary problems, the definition of initial conditions, (eg pressure field, speed and initial temperature inside the computational volume). The equations are the same ones for any situation of fluid flow. The initial state is defined by the boundary conditions and the initial values.

Computational Fluid Dynamics as a science is comprised of many different disciplines such as fluid physics, applied mathematics and computer science. The fields of application of CFD are very varied. It is possible to find applications in Aerodynamics, (flow around cars, airplanes, boats, buildings), Environment (smoke, dispersion of polluting agents in the atmosphere), Air conditioning (heating, ventilation in closed sites) and Medicine (flow in veins, simulation of by-pass) and other fields. CFD uses computers as work tools to numerically solve the equations that govern the movement of fluids. In the existing software packages, the user must specify the conditions of the problem that is going to be solved, as well as providing to the computer the level of resolution required (the so called “gridding” of the problem) so that the program is able to find a correct solution of the problem.

The main tasks in obtaining a flow simulation can be grouped in three stages:

Pre-process: In this stage the geometric domain (the grid) is defined, the properties of the fluid that prevail and the initial and boundary conditions are specified. These conditions are those that, with the geometry, characterize the problem to be solved.

Solution: In this stage the equations to solve, the resolution algorithms and their parameters are specified -such as the step size of the iteration- and the solution to the equation’s system that govern the process is generated iteratively.

Post-process: In this stage, the obtained results are processed and stored to facilitate their later analysis. This is also the stage of visualization and analysis of the results in order to validate the behavior of the flow and to obtain conclusions

about their reliability or identification of possible errors, e.g. wrong grid size used.

3.2.2. Advantages and disadvantages of CFD

The main advantages that the use of CFD in the resolution of problems are:

- Substantial reduction of times and costs in new designs.
- Possibility of analyzing systems or conditions very difficult to simulate experimentally: hypersonic speeds, very high or low temperatures, relative movements, etc.
- Capability to study systems under dangerous conditions or beyond their operational limit conditions.
- To reach a solution that provides more complete and detailed information of the fields of speed, pressure, temperature..., in space and time, than is possible by experiment.

The disadvantages in the use of CFD are:

- It is an expensive technique, since machines of great calculation capacity are necessary, software has not an accessible price to the public, and qualified personnel is needed to use the program and analyze the results suitably.
- The limitation of the existing models for the turbulence, two-phase flow, combustion, etc.

Nevertheless despite these disadvantages CFD is an extremely powerful method, when used correctly, for solving and gaining insight into many very difficult physical problems. For e.g. the use of CFD in the predictions of flows has reached an apogee at the present time, thanks to the three-dimensional vision of the fluid-dynamic problems.

3.2.3. Methodology

In CFD software packages, the user must specify the conditions of the problem that is going to be solved, as well as provide to the code the resolution required (step size, grid size) so that it is able to find a correct solution of the problem. The steps in which this information is introduced into the software are the following ones:

1. Specification of the geometry of the problem. It is essential to introduce to the program the domain contours of the problem, i.e. the limits of the problem's geometry in which the program will solve the equations. This process is relatively simple when the problem can be reduced to two dimensions, because only the lines that limit the zone of the problem have to be defined. These lines can be very simple in the case of straight lines or circumferences. If the curves are of another type, they are simply introduced by loci. When the model is three-dimensional, the specification of geometry requires the specification of boundary surfaces to the problem.

2. Creation of the grid (or mesh) in which all the variables are going to be calculated. The grid can be structured or not. The not-structured grid can be made up of hexahedron or triangles, that can be deformed to fit the curved surfaces of the geometry. The structured grid is formed by squares or tetrahedrons, constructed from the division of the geometry contours. This last type of grid is simpler to create than the previous one and the calculation procedure converges better with structured meshes.

3. Imposition of the boundary conditions that fix the values of the variables required for the calculation to the limits of the domain. These conditions are imposed to the variables pressure, temperature, speed, or their gradients. Also it is necessary to impose conditions for the turbulence variables, according to the turbulence model that is being used.

4. Introduction of the initial conditions. In the case of a non-stationary problem it is necessary to define values of the variables for all the points of the domain, from which the program will begin to calculate the solutions of the successive temporal steps. In the case of a stationary problem, it is sufficient to introduce to the program initial values of the variables, from which it will start the iterative process.

5. Specification of the fluid variables, such as viscosity and density. These magnitudes can vary with the temperature, the pressure, etc. It is necessary to introduce in the program the mathematical model of variation of these parameters. Also several kinds of problem can be considered, according to whether one considers heat transference -like conduction, convection or radiation-

or not. In that case, it would be necessary to introduce to the program the thermal properties of the fluid.

6. Specification of the control parameters that affect the resolution of the problem, such as the step size, the convergence criteria and the limits of some of the fluid properties.

3.3. Working with FLUENT

As it was said, the CFD FLUENT software was chosen to perform the numerical analysis for the problems considered in this thesis. The good results obtained in previous studies [34], the robustness of its algorithms and familiarity with this software were the main reasons for its selection.

3.3.1. The heat transfer equation

FLUENT solves the energy equation in the following form:

$$\frac{\partial}{\partial t}(\rho E) + \nabla \cdot (\vec{v}(\rho E + p)) = \nabla \cdot \left(k_{\text{eff}} \nabla T - \sum_j h_j \vec{J}_j + (\bar{\tau}_{\text{eff}} \cdot \vec{v}) \right) + S_h \quad (3.1)$$

where:

ρ = density

E = energy

v = velocity

p = pressure

k_{eff} = effective thermal conductivity

T = temperature

h = enthalpy

J_j = diffusion flux of species j

$\bar{\tau}_{\text{eff}}$ = effective stress tensor

The species are all the constituent fluid materials of a mixture material. The first three terms on the right-hand side of equation 3.1 represent energy transfer due to conduction, species diffusion, and viscous dissipation,

respectively. S_h includes the heat of chemical reaction, and any other volumetric heat sources that might be contained within the problem.

In equation 3.1, the energy is defined as:

$$E = h - \frac{p}{\rho} + \frac{v^2}{2} \quad (3.2)$$

where enthalpy h is defined for ideal gases as

$$h = \sum_j Y_j h_j \quad (3.3)$$

and for incompressible flows as

$$h = \sum_j Y_j h_j + \frac{p}{\rho} \quad (3.4)$$

In equations 3.3 and 3.4, Y_j is the mass fraction of species j and

$$h_j = \int_{T_{\text{ref}}}^T c_{p,j} dT \quad (3.5)$$

where T_{ref} is 298.15 K or 25.0°C.

In solids, the energy transport equation used by FLUENT has the following form:

$$\frac{\partial}{\partial t} (\rho h) + \nabla \cdot (\vec{v} \rho h) = \nabla \cdot (k \nabla T) + S_h \quad (3.6)$$

The second term on the left-hand side of equation 3.6 represents convective energy transfer due to rotational or translational motion of the solids. The velocity field v is computed from the motion specified for the solid zone. The terms on the right-hand side of equation are the heat flux due to conduction and volumetric heat sources within the solid, respectively.

3.3.2. Radiative transfer equation

In order to introduce or calculate the values of the properties associated with the radiative heat transfer, the radiative transfer equation (RTE) should be included in the simulation when the radiant heat flux is large compared to the heat transfer rate due to convection or conduction. Typically this will occur at high

temperatures where the fourth-order dependence of the radiative heat flux on temperature implies that radiation will dominate.

The radiative transfer equation for an absorbing, emitting, and scattering medium at position \vec{r} in the direction \vec{s} is:

$$\frac{dI(\vec{r}, \vec{s})}{ds} + (a + \sigma_s)I(\vec{r}, \vec{s}) = an^2 \frac{\sigma T^4}{\pi} + \frac{\sigma_s}{4\pi} \int_0^{4\pi} I(\vec{r}, \vec{s}') \Phi(\vec{s} \cdot \vec{s}') d\Omega' \quad (3.7)$$

where \vec{r} = position vector

\vec{s} = direction vector

\vec{s}' = scattering direction vector

s = path length

a = absorption coefficient

n = refractive index

σ_s = scattering coefficient

σ = Stefan-Boltzmann constant ($5.672 \times 10^{-8} \text{ W.m}^{-2} \text{ K}^{-4}$)

I = radiation intensity, which depends on position r and direction s

T = local temperature

Φ = phase function

Ω' = solid angle

$(a + \sigma_s)s$ is the optical thickness or opacity of the medium. The refractive index n is important when considering radiation in semi-transparent media. Figure 3.1 illustrates the process of radiative heat transfer.

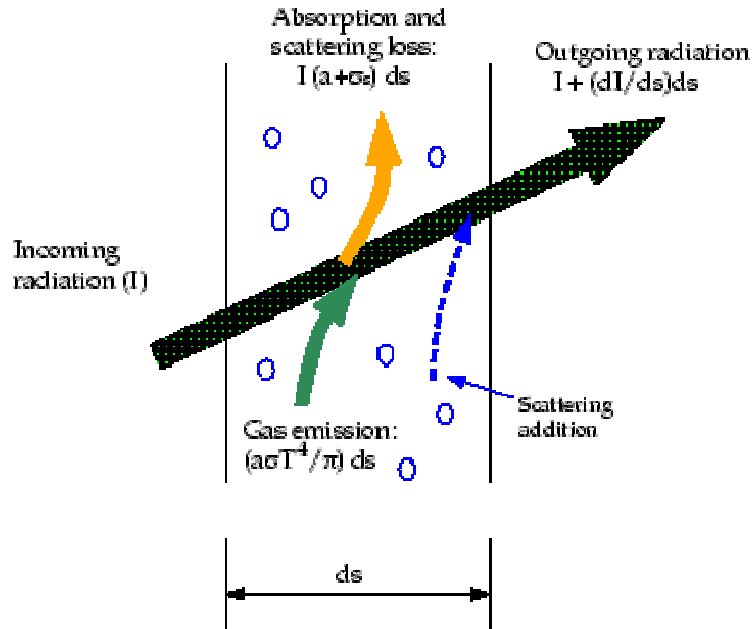


Figure 3.1. Radiative heat transfer.

FLUENT has five different possible heat transfer models which allow the inclusion of heat transport by radiation, with or without a participating medium. These five possibilities are:

- Discrete transfer radiation model (DTRM)
- P-1 radiation model
- Rosseland radiation model
- Surface-to-surface (S2S) radiation model
- Discrete ordinates (DO) radiation model

3.3.3. Description of the different types of radiation models for FLUENT 6.1

A brief introduction of the different types of radiation models is described below. Then an discussion explaining why a particular approach was chosen is given.

3.3.3.1. DTRM model (discrete to transfer radiation model) [35, 36]

The main hypothesis of this method is that the radiation that a surface in a certain solid angle emits can be approximated by a ray.

Advantages of the model:

- It is simple to model.
- The precision can be increased by increasing the number of rays.
- It is applicable for a wide range of optical thicknesses.

Disadvantages:

- The method assumes that all the surfaces are diffuse, this is the reason why the reflection of the incident radiation at the surface is isotropic respect the solid angle.
- The scattering effects are not considered.
- The method supposes gray radiation, i.e. it assumes that a surface's spectral emissivity and absorptivity do not depend on wavelength.
- To solve a problem a large number of rays is required – this approach is therefore computationally expensive.

3.3.3.2. P-1 model [37, 38]

The P-1 radiation model is the simplest case of the P-N model, that is based on the expansion of the radiation intensity, I , into an orthogonal series of spherical overtones.

Advantages:

- In this model, the radiation transfer equation RTE, is treated as a diffusion equation, which allows it to be solved with little demand on the CPU.
- It allows simulation of the effects of scattering.
- It is specially adapted to problems of high optical thickness that involve combustion and for complex geometries with curvilinear coordinates.

Disadvantages:

- Gray surfaces are supposed.
- Simulation of gray radiation only.
- Loss of exactitude, depending on the complexity of geometry, if the optical thickness is small.
- The model tends to overpredict radiation fluxes from localized heat sources or sinks.

3.3.3.3. Rosseland model [38]

This model is valid for high optical thickness geometries, $aL \gg 1$, where a is the absorption coefficient and L is an appropriate length scale for the domain, and in particular it is recommended for problems with an optical thickness greater than 3. It can be derived from of the P-1 model equations with some approximations.

Advantages:

- It does not solve additional equations to calculate the incident radiation.
- It is faster than the P-1 model and it requires less CPU memory.

Disadvantages:

- It can be only used for geometries of high optical thickness.

3.3.3.4. DO model (Discrete Ordinates) [39, 40, 41]

This method solves the radiation transfer equation for a discrete number of solid angles, in which a vector s of direction is associated to the global system of Cartesian coordinates (x, y, z). The refinement of the angular grid is controlled by the user, analogous to the choice of the number of rays in the DTRM model. Nevertheless, this model does not perform ray tracing as such, but it transforms the radiation transfer equation (RTE) to a radiation intensity transport equation in the spatial coordinates (x, y, z). The DO model can solve as many transport equations as directions s exist and by the same method can be used to solve the equations for flow and energy.

The implementation in FLUENT uses a conservative variant of the model of discrete ordinates called scheme of finite volumes, and its extension for unstructured meshes.

Advantages:

- It works for a wide range of optical thicknesses.
- It is able to simulate problems with and without participating environment.
- It simulates semitransparent environment.
- The computational costs are moderate for the typical angular grids.
- It implements gray and directional radiation.

Disadvantages:

- The necessary use of very fine angular grids causes a great use of the resources of the CPU.
- For the simulation of directional radiation, the absorptivity is assumed to be constant for each wavelength.

3.3.3.5. S2S model (surface to surface) [38]

This model can be used to calculate the interchange of radiation in an enclosure of gray surfaces and with diffuse radiation. The energy interchanged between two surfaces depends partly on its size, the separation distance and the direction. The parameters are calculated by a geometric function called the “form factor”. The main hypothesis of S2S model is that all the absorption, emission and dispersion can be ignored, therefore, it is only necessary to consider the radiation surface to surface.

Advantages:

- It is ideal to simulate cavities in which heat transference takes place by radiation without a participating environment, or at least one whose effect can be neglected.
- When iterating, this method is faster than the previous ones, although the calculation of the form factors matrix is computationally expensive.

Disadvantages:

- It assumes that all the surfaces are diffuse.
- It supposes gray radiation.
- The memory requirements increase quickly as the number of faces involved in the radiation increases.
- It cannot be used for problems that involve participating environments.
- It does not work with the sliding mesh model, which is used for simulating flows in multiple moving reference frames.
- It cannot be used if the model contains periodic or symmetry boundary conditions.

3.3.4. Choosing the radiation model

For certain problems, one radiation model may be more appropriate than another. When deciding which radiation model to use, the following should be considered:

- Optical thickness: The optical thickness ($a.L$) is a good indicator of which model to use in the problem. If $a.L \gg 1$, the best alternatives are the P-1 and Rosseland models. The P-1 model should typically be used for optical thicknesses > 1 . For optical thickness > 3 , the Rosseland model is more economic with CPU resources and more efficient. The DTRM and the DO model work across the range of optical thicknesses, but require greater computing power to implement. So the “thick-limit” models, P-1 and Rosseland, should be used if the problem allows it. For optically thin problems ($a.L < 1$), only the DTRM and the DO model are appropriate.
- Scattering and emissivity: The P-1, Rosseland, and DO models account for scattering, while the DTRM neglects it. Rosseland model is insensitive to wall emissivity because, since the diffusion approximation is not valid near walls, it needs to use a temperature slip boundary condition at the walls.
- Particulate effects: Only the P-1 and DO models account for exchange of radiation between gas and particulates.
- Semi-transparent media and specular boundaries: Only the DO model allows for specular reflection (e.g. for mirrors) and can calculate radiation transport in semi-transparent media such as glass.
- Non-gray radiation: Only the DO model allows computation of non-gray radiation using a gray band model, in which the number of bands with different wavelength intervals and their absorption coefficients can be specified.
- Localized heat sources: In problems with localized sources of heat, the P-1 model may overpredict the radiative flux. The DO model is probably the best suited for computing radiation for this case, although the DTRM, with a sufficiently large number of rays, is also acceptable.

- Enclosure radiative transfer with non-participating media: The surface-to-surface (S2S) model is suitable for this type of problem. The radiation models used with participating media may, in principle, be used to compute the surface-to-surface radiation, but they are not always effective.

P-1 and Rosseland models can be discarded for this application because both are used to model optically thick problems $\alpha L > 1$. The present study is essentially an optically thin problem, since the characteristic length is the blackbody cavity aperture ($L = 0.03 \text{ m}$) and the absorptivity of the participating media, i.e. the fluid, (usually argon) is almost zero. There are the other three models left, that, in principle would be valid to solve the problems to be tackled in this thesis.

These three models have been studied and it has been observed that DTRM model is not able to correctly calculate the temperature gradients, since it calculates a great drop, not observed in the experimental data. As to the S2S model, it does not allow the simplification of axysimetric symmetry so a 3D model has to be implemented. However this is very expensive on CPU resources and trials have shown that it does not give physically realistic satisfactory results. Finally, a DO model with several different angular grids has been studied, obtaining satisfactory results [34].

So, taking care of these considerations and the results of preliminary trials, also the great amount of information and additional studies available on the DO model [39, 42, 43, 44], it has been decided to implement models of the system under investigation here using the DO approach.

3.4. Summary

In this chapter the characteristics of computational fluid dynamics and in particular FLUENT software were explained. Although this software is mainly used to solve fluid systems, it also simulates solid regions and their interaction with the fluid field. Because of the characteristics of the furnaces used in high temperature measurements, which include fluid (the melted ingot and the argon inside the furnace) and solid parts (crucible, tube, heaters, radiation shields...) this software is in principle a good tool to model them. Also the familiarity with it and

the robustness of its algorithms were reasons to choose it.

As it was also said, numerical analysis is used in this study because experimental investigation of parameters inside the furnace (temperature profiles, heat losses...) is impossible in some cases and too costly in others.

The next chapter includes the validation of the approach of numerical modelling with FLUENT comparing it with a) other studies of radiative heat transfer problems done by the Division of Aerospace Engineering at the Korean Advanced Institute of Science and Technology, b) some experimental results of a three zone furnace used in the Spanish National Metrology Institute and c) another numerical software package called ANSYS.

CHAPTER 4

**Preliminary studies and
validation of the approach
of numerical modelling**



Chapter 4. Preliminary Studies and Validation of the Approach of Numerical Modelling

4.1. Introduction

Validation of the numerical model is one of the main tests that has to be performed. Numerical analysis has been used extensively to study heat transfer problems and research performed to understand what type of algorithms are better for specific problems. The study about the type of grid to be used and the grid size needed to obtain convergence is amply explained in a previous work [34]. In order to validate the radiation heat transfer model in high temperature furnaces constructed here, some previous studies performed by the Division of Aerospace Engineering at the Korean Advanced Institute of Science and Technology [45] are reproduced here by means of FLUENT and the results compared. The way they did their studies, focused in the accuracy obtained with different kinds of grid and the comparison with exact results of the same problems, make their findings to be a good model to test this approach.

Another validation approach was also performed where a 3D model of a three zone furnace for calibrating noble metal thermocouples and broad band radiation thermometers used in the Spanish National Metrology Institute (CEM) was constructed [46, 47]. This approach, in which heat transfer by conduction, convection and radiation is involved, is useful to better understand the behaviour of the complete system and how the different kinds of heat transport are solved. The performance of a 3D model also helped to build experience in construction of models because it implies a full understanding of FLUENT tools.

Finally, a comparison between FLUENT and another software package, ANSYS, is commented.

4.2. An equilateral triangular enclosure [43]

This case reproduces the findings of a study made by M. Y. Kim, S. W.

Baek and J. H. Park of the Korean Advanced Institute of Science and Technology. It is an equilateral triangle of 1 m side with an emissivity of the walls of $\epsilon \square 1$ and at 0 K. Inside there is a fluid at 1000 K with an absorption coefficient of 1 m^{-1} . The model presented in this study had 900 triangular cells and 496 nodes and it was solved by three different numerical approaches and two different angular grids.

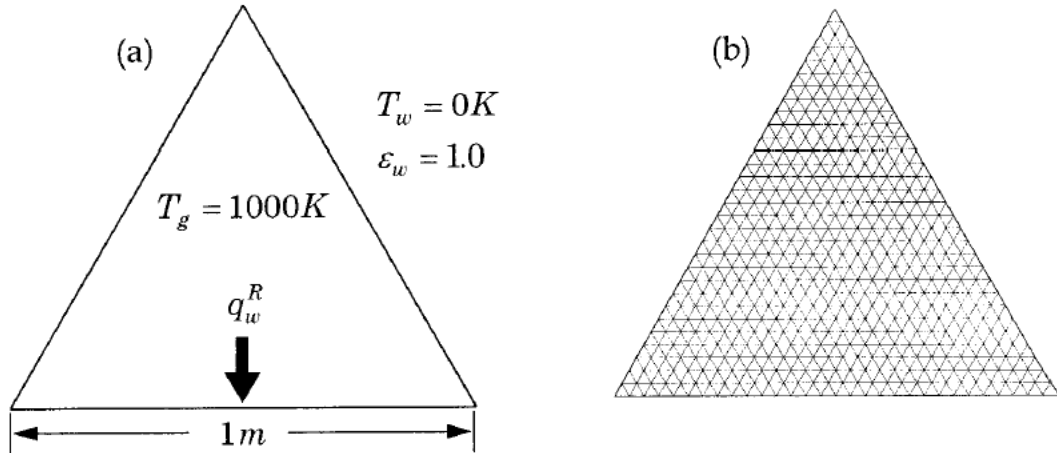


Figure 4.1. Geometry developed by [43].

The model made by FLUENT has 938 cells and 516 nodes:

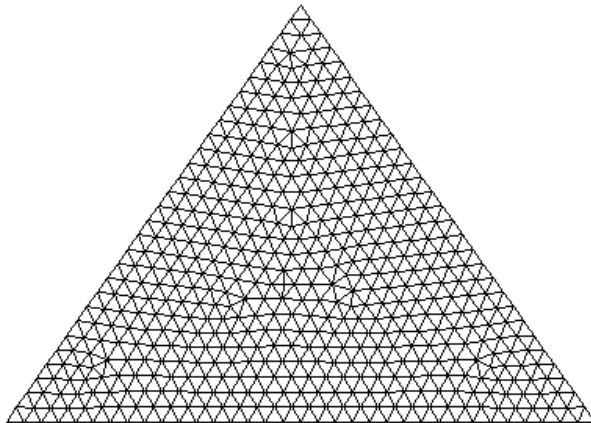


Figure 4.2. Geometry developed by means of FLUENT.

The checked variable is $q_w^R / \sigma \cdot T_g^4$, where q_w^R is the radiative heat flow in the bottom wall, σ the Stefan-Boltzmann constant and T_g the gas temperature. The two combinations of polar θ and azimuthal ϕ angles for the angular grids are $(\theta \square 4, \phi \square 8)$ and $(\theta \square 4, \phi \square 16)$ so that the results are:

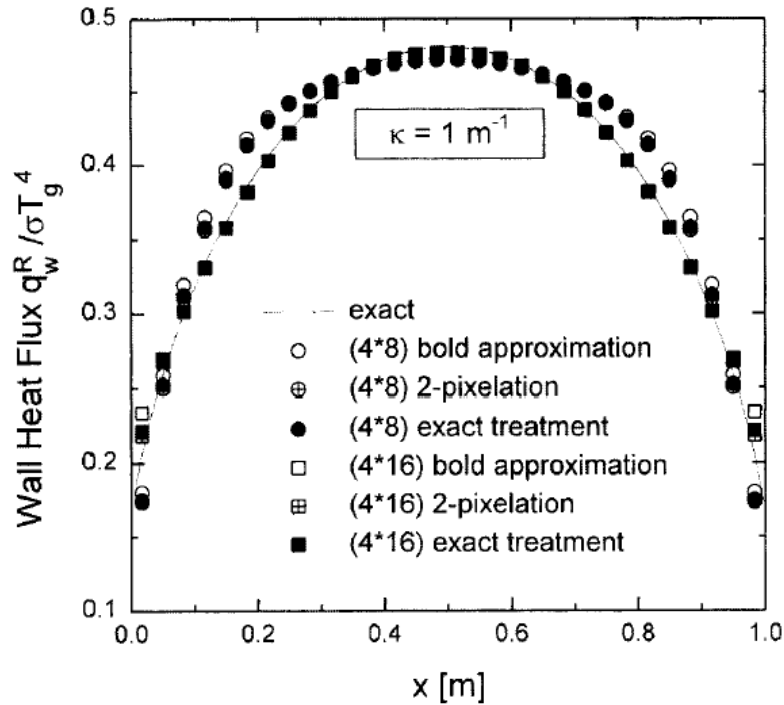


Figure 4.3. Data for the bottom wall heat flux as reported by [43].

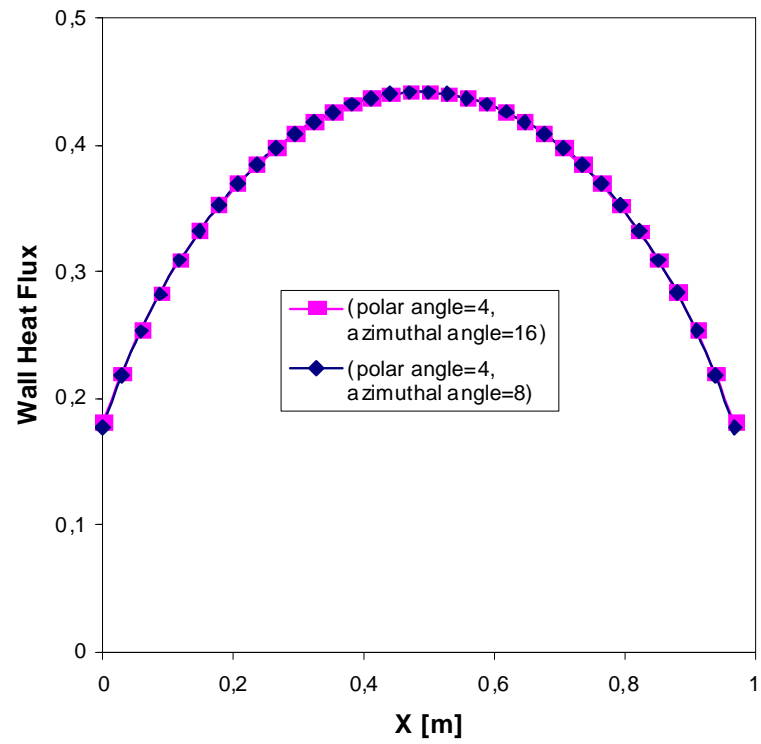


Figure 4.4. Data for the bottom wall heat flux by means of FLUENT.

Figures 4.3 and 4.4 show that the heat flow for both models was essentially the same, demonstrating that FLUENT can reproduce other researchers work in heat transfer. To confirm this other models were constructed and compared with the Korean's findings, this is reported below in Section 4.3.

4.3. An axisymmetric cylindrical enclosure with participating media [48]

Getting closer to the type of geometry involved in the crucibles of high temperature fixed points, a cylinder with an axisymmetric configuration is now modeled. The boundary conditions used by the Korean group were the following; dimensions are $r_c = 1$ m and $z_c = 2$ m; the walls are at 0 K with an emissivity of 1 ($\epsilon = 1$); the gas inside the cylinder is an absorbing-emitting medium at $T_g = 100$ K and three different absorption coefficients have been studied ($k_a = 0.1, 1, 5 \text{ m}^{-1}$).

Figures 4.5 and 4.6 shows the nondimensional wall heat flux ($q_w^R / (\sigma \cdot T_g^4)$) on the side wall for the three different absorption coefficients.

When the absorption coefficient is large, $k_a = 5.0$, the radiant energy arriving at the wall approaches the black body intensity due to heat blockage effect, i.e. the optically thick medium absorbs nearly all the radiation from neighbouring medium and the intensity impinging on the wall is influenced only by the emission of the hot gas near the enclosing wall. Near the corners, however, a sharp decrease in radiant heat flux is observed because of the neighbouring cold top and bottom walls.

When absorption coefficient is small, $k_a = 0.1$, the medium is optically thin, the emission of the medium is weak, and the radiant heat flux is significantly reduced. This is because of the far-reaching effect of the cold walls and negligible self-absorption (i.e. heat trapping) of the optically thin gas.

The good agreement between the findings of the Koran group and the FLUENT models with axisymmetrical distribution and an absorbing-emitting medium is clear. This gives increased confidence FLUENT can be used to construct appropriate and realistic models for radiant transfer problems.

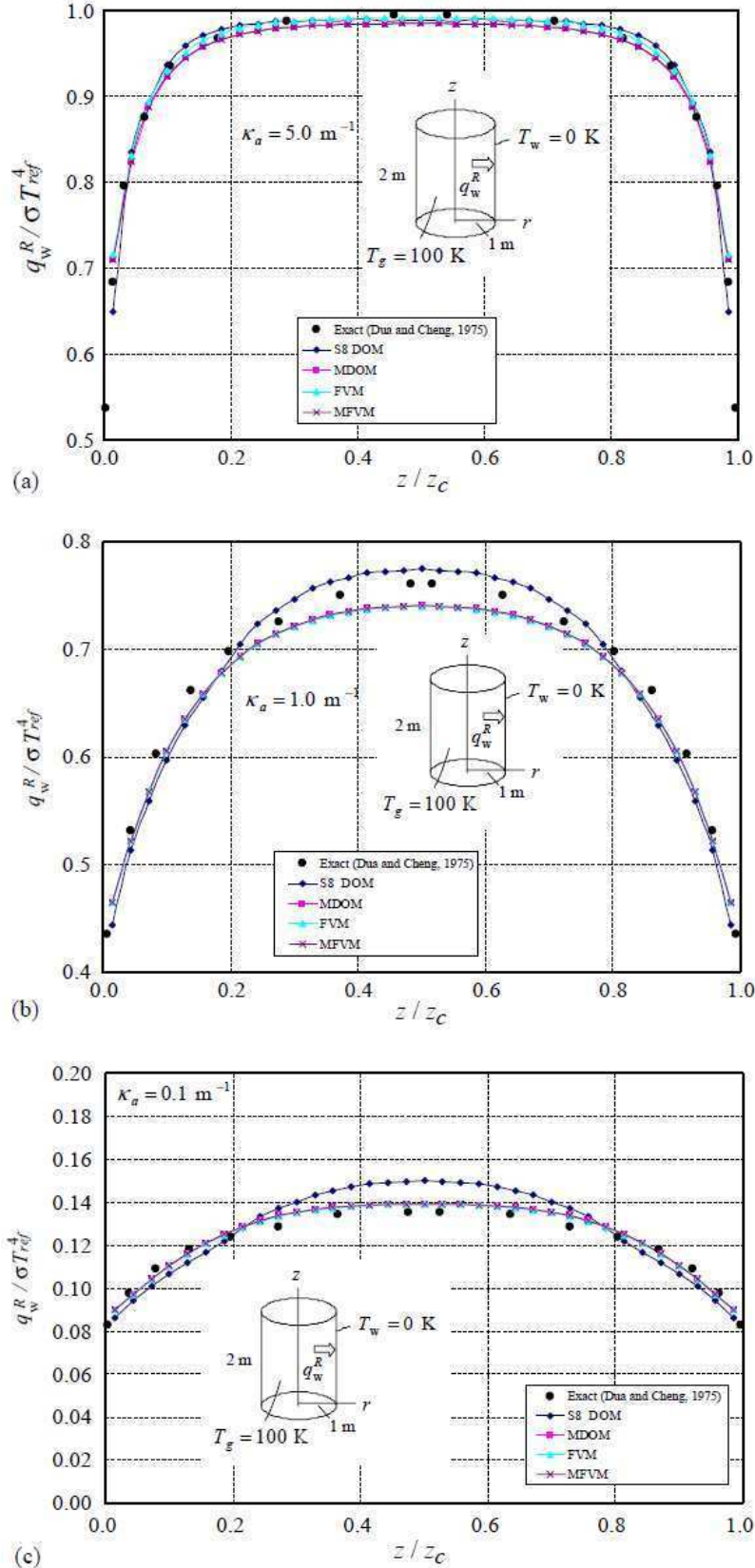


Figure 4.5. Comparison by means of [48] of nondimensional heat flux distribution for three optical thicknesses. (a) $k_a = 5.0 \text{ m}^{-1}$, (b) $k_a = 1.0 \text{ m}^{-1}$, (c) $k_a = 0.1 \text{ m}^{-1}$

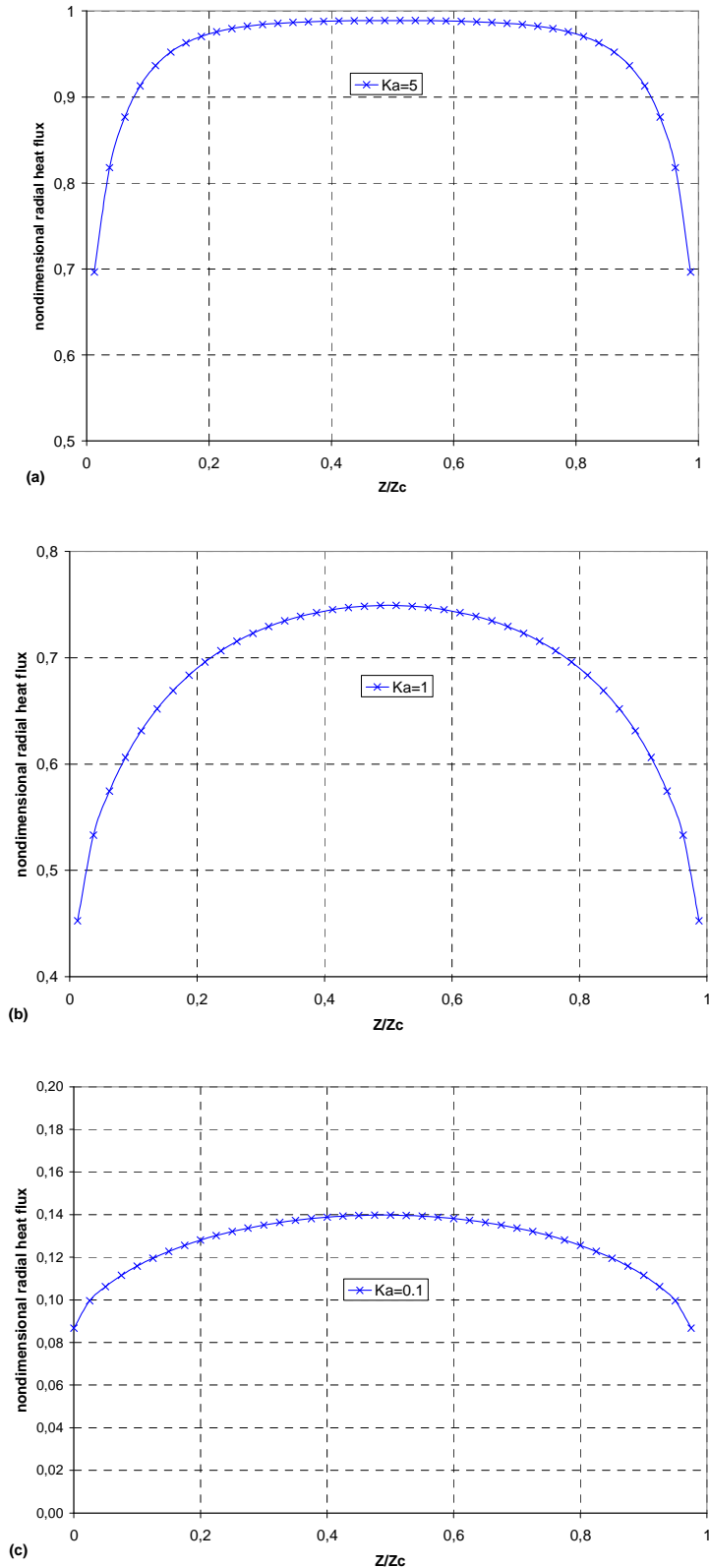


Figure 4.6. Comparison by means of FLUENT of nondimensional heat flux distribution for three optical thicknesses. (a) $k_a = 5.0 \text{ m}^{-1}$, (b) $k_a = 1.0 \text{ m}^{-1}$, (c) $k_a = 0.1 \text{ m}^{-1}$

4.4. A three zone high temperature furnace for thermocouples

The Spanish National Metrology Institute (CEM) has designed and constructed a three zone furnace intended for calibrating noble metal thermocouples and broad band radiation thermometers with reference to a standard monochromatic radiation thermometer up to 1600 °C. This three-zone furnace has been constructed with MoSi₂ heating elements with an interchangeable alumina tube containing a graphite blackbody [46].

A theoretical model was constructed in order to simulate the furnaces thermal behaviour. This is because the measurement of the gradients in the area where the measurements take place are time consuming.

4.4.1. Description of the high temperature furnace

A schematic diagram of the high temperature furnace is shown in figure 4.7. It has three heating zones: the central one, with three heating elements, and two end zones, with two heating elements. The heating elements are placed in the air surrounding the measuring tube.

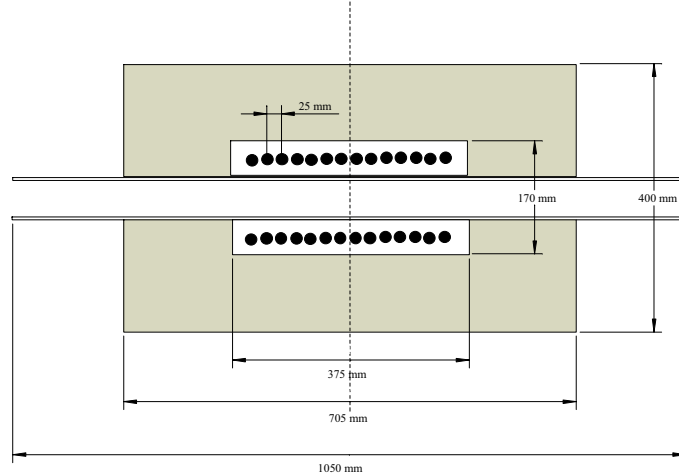


Figure 4.7. Plan view of the CEM horizontal high temperature furnace. The shadowed area is the insulation of the furnace.

The alumina "measuring" tube is interchangeable, and has different contents, depending on the type of thermometer to be calibrated: that is either a

thermocouple or a broad band radiation thermometer. Figure 4.8 shows the tube and contents constructed to calibrate thermocouples.

The two measuring tubes have four small diameter alumina tubes for inserting different type B thermocouples to measure the thermal homogeneity of the furnace. These small alumina tubes go along the whole measuring tube. These can be seen in Figure 4.8.

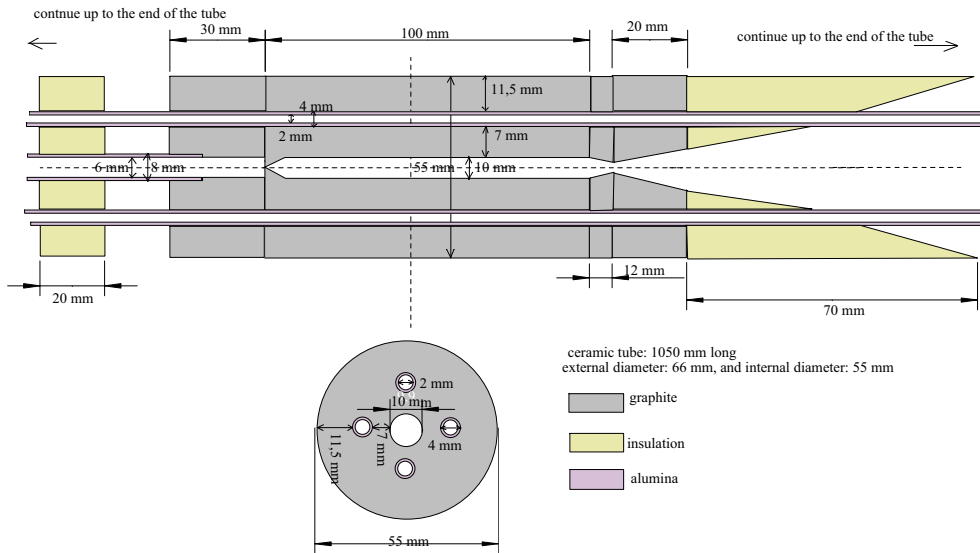


Figure 4.8. Measuring tube for calibrating thermocouples. The thermocouple insertion is in the left part of the measuring tube. The measurement junction of the thermocouple touches the rear part of the black body cavity, whose temperature is measured using a standard radiation thermometer from the right hand side.

4.4.2. Finite volume simulations [47]

A 3D model with a symmetry plane was constructed of the furnace. The material properties used in the model are in table 4.1.

Conduction, convection and radiation heat transfer were simulated with the following boundary conditions:

- Heating elements: They are fixed at constant temperature. Due to this condition, thermal properties of the heating elements don't affect the results and they are simulated as copper made.
- External walls: The external walls of the furnace include convection and radiation to the surrounding air which is at 300 K.

- Caps closing the ceramic tube: They are simulated with thermal properties similar to air and fixed at 300 K.

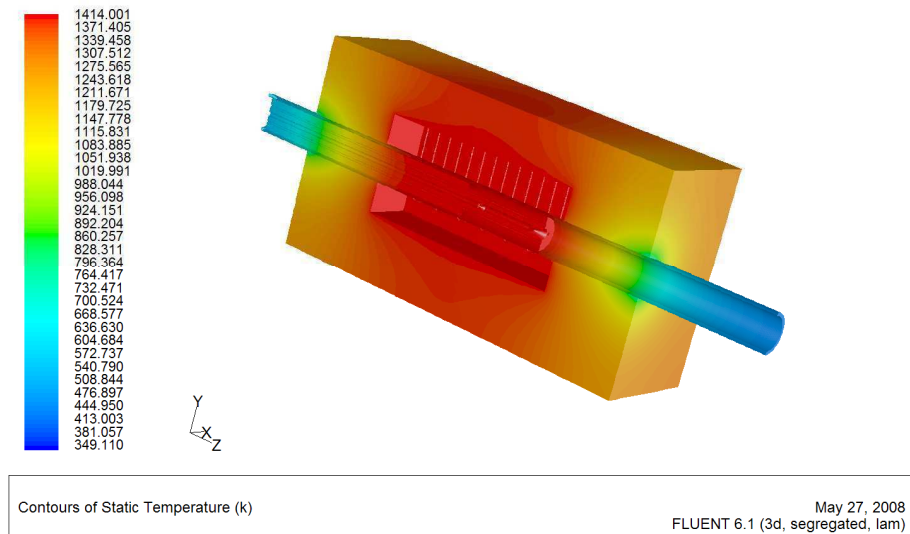
Table 4.1. Material properties.

	Density kg.m ⁻³	C_p J.kg ⁻¹ .K ⁻¹	Thermal conductivity W.m ⁻¹ .K ⁻¹	Viscosity Kg.m ⁻¹ .s ⁻¹	Molecular weight kg.kg ⁻¹ .mol ⁻¹
Graphite	1850	810	50	-	-
Alumina	3900	880	35	-	-
Copper	8978	381	387.6	-	-
Insulation	400	880	0.35	-	-
Air	1.225	p ₁	p ₂	1.79×10^{-5}	28.97

$$p_1 = 1.9327 \times 10^{-10}T^4 - 7.9999 \times 10^{-7}T^3 + 1.1407 \times 10^{-3}T^2 - 0.4499T + 1057.5$$

$$p_2 = 1.5207 \times 10^{-11}T^3 - 4.8574 \times 10^{-8}T^2 + 1.0184 \times 10^{-4}T - 3.9333 \times 10^{-4}$$

The thermal behaviour contours obtained for the heating cavity and the measuring tube are shown in figure 4.9.



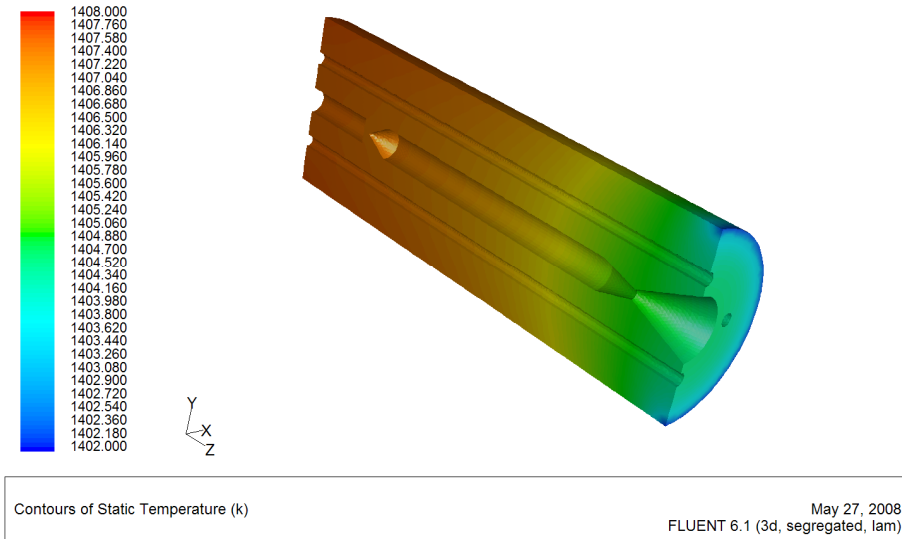


Figure 4.9. Temperature contours obtained with FLUENT for the high temperature furnace.

4.4.3. Results

The complexity of the 3D model, which includes the main parts of the furnace, has made necessary a parametric study of all the parameters of influence.

First, the material properties of the furnace have been tested in the range of use including the uncertainty in the values of the properties at nominal temperature, such as heat capacity and thermal conductivity of the furnace materials.

Then, the boundary conditions explained in the previous section were fixed after a study of the environment and the working conditions of the furnace.

Finally, each contribution to the model sensitivity, like the number of iterations and the grid size, have been determined and adjusted to make the model as real as possible.

Based on the thermal simulations performed it is possible to obtain a theoretical estimate of the temperature gradient at the thermocouple location. This theoretical gradient is compared with the experimental data for 1100 °C in figure 4.10 and for 1300 °C in figure 4.11.

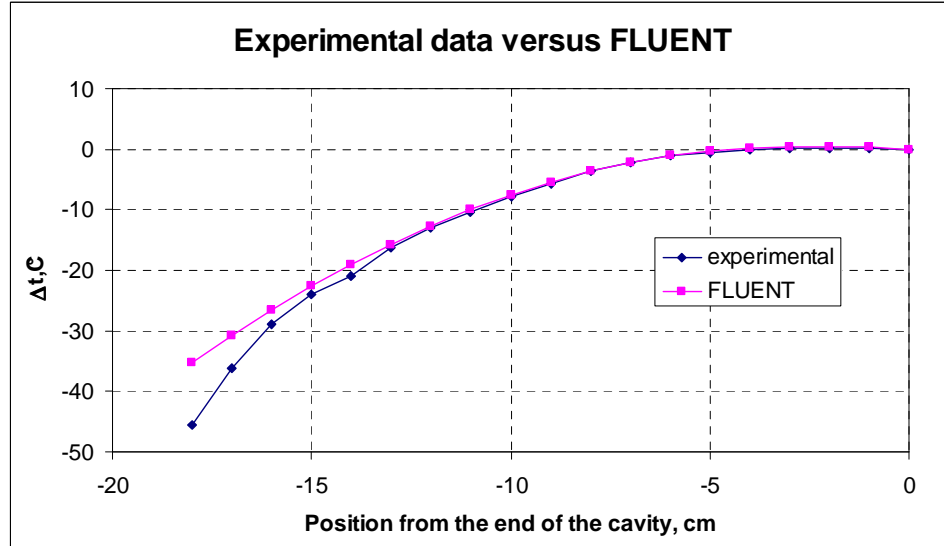


Figure 4.10. Comparison between the experimental data and the results obtained with FLUENT for 1100 °C.

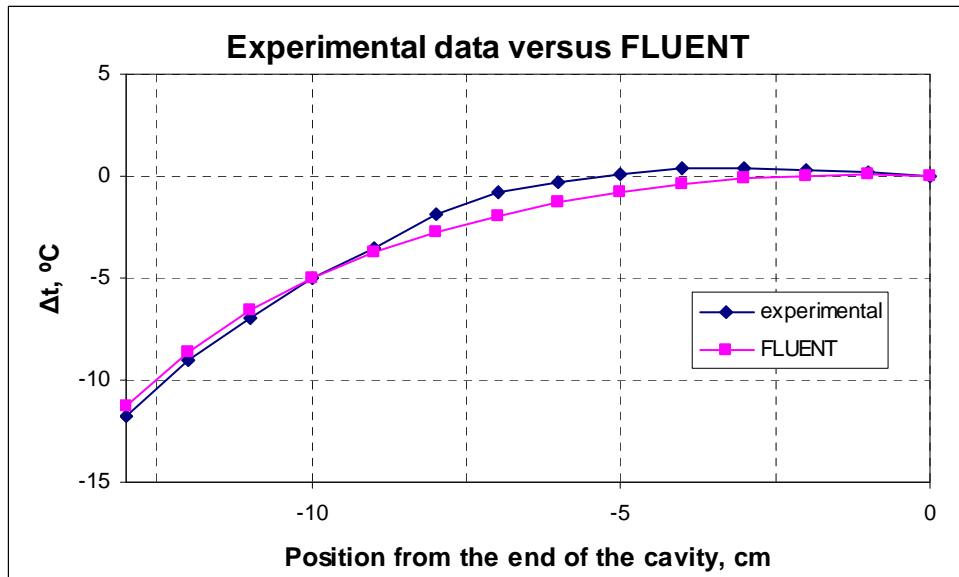


Figure 4.11. Comparison between the experimental data and the results obtained with FLUENT for 1300 °C.

The agreement between the simulations done and the data measured is reasonably good. Unfortunately there are too many parameters of influence to make the model a realistic way to estimate the temperature profile variations in the real furnace.

This study has been fruitful to better understand heat conduction, convection and radiation transport inside the furnace and has been a very useful vehicle

through which to gain experience of and validate FLUENT's heat transport equation models.

4.5. Comparison between FLUENT and ANSYS software packages for the numerical resolution of HTFP

In this study, FLUENT software is compared with previous results in the numerical analysis of crucibles and furnaces for high temperature fixed points done by means of ANSYS [26], a finite element software. In particular, the temperature drop across the back-wall of a crucible for the Re-C fixed point is calculated. This temperature difference has been evaluated for a joint crucible-furnace designed by the NMIJ (National Metrology Institute of Japan).

4.5.1. Description of the simulated system

The NMIJ furnace used in the simulations is the Nagano 'VR10-A19' model. A picture and a scheme of the furnace is shown in figure 4.12.

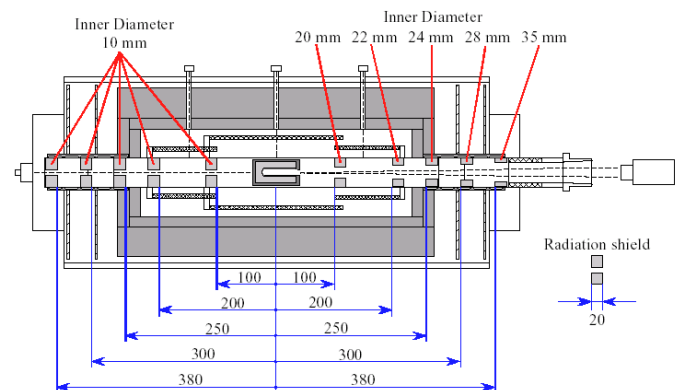
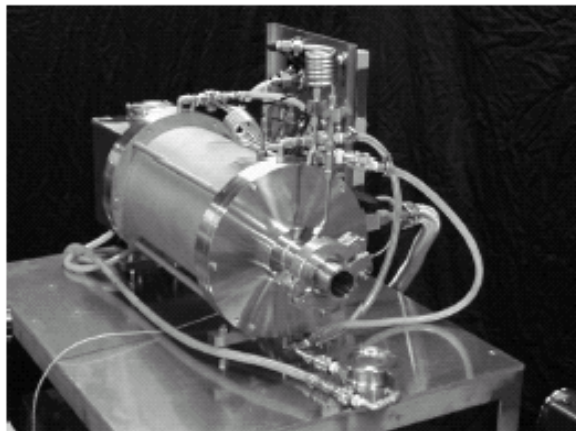


Figure 4.12. Nagano 'VR10-A19' furnace picture and scheme.

The part of the crucible in which the temperature profile is studied is the back-wall, i.e. the wall which is looking directly to the furnace aperture and where the radiation thermometer measures the temperature. In this wall a temperature drop from the melting temperature occurs mainly because of the radiation losses to

the outside environment. A scheme of the back-wall position of the crucible inside the furnace can be seen in figure 4.13.

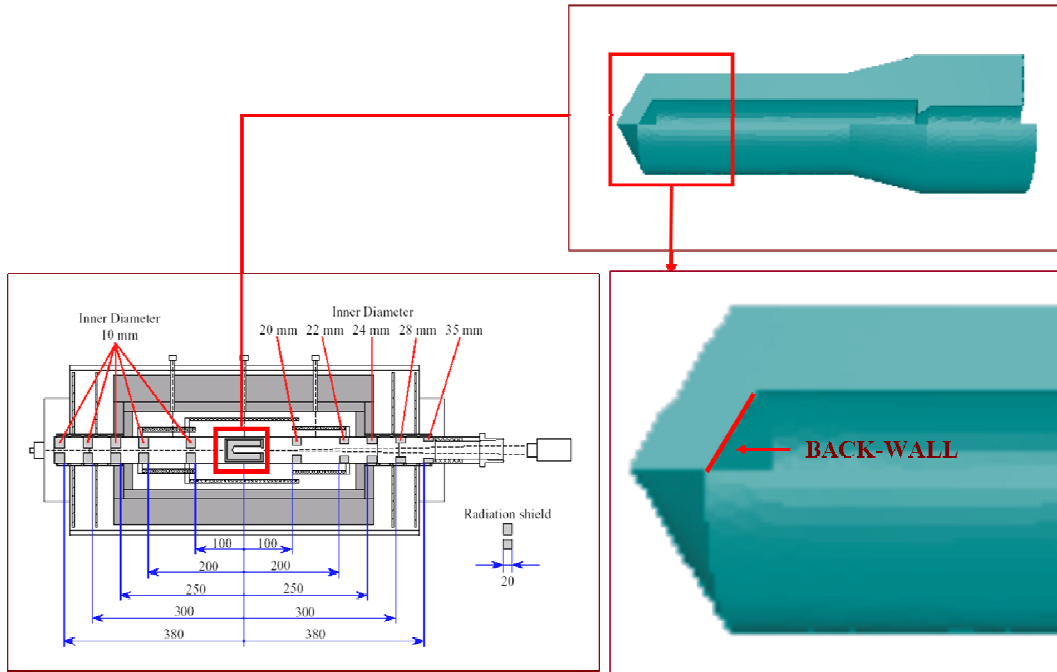


Figure 4.13. Scheme of the back-wall position of the crucible inside the furnace.

The crucible used is a 3S model from the NMIJ. The cavity of the crucible is 62 mm long, with a 3 mm internal diameter, the back-wall thickness is 2.6 mm and with a tilt angle of 30°.

4.5.2. Numerical models

Two different models were made and compared with the ones made by means of ANSYS. The first one is the bare crucible, without the furnace, and the second is with the crucible inside the furnace. The models are shown in figure 4.14.

The following simplifications have been made in the model:

- The model geometry is considered axisymmetric; this allowed us to construct a 2D model.

- The thermal resistance at contacting elements or screw parts is neglected because of its relatively small influence and the difficulty of estimating it.

- Heat transfer due to convection and conduction in the furnace atmosphere has been taken into account, but these turned out to be negligible.

- The model assumes steady-state conditions.

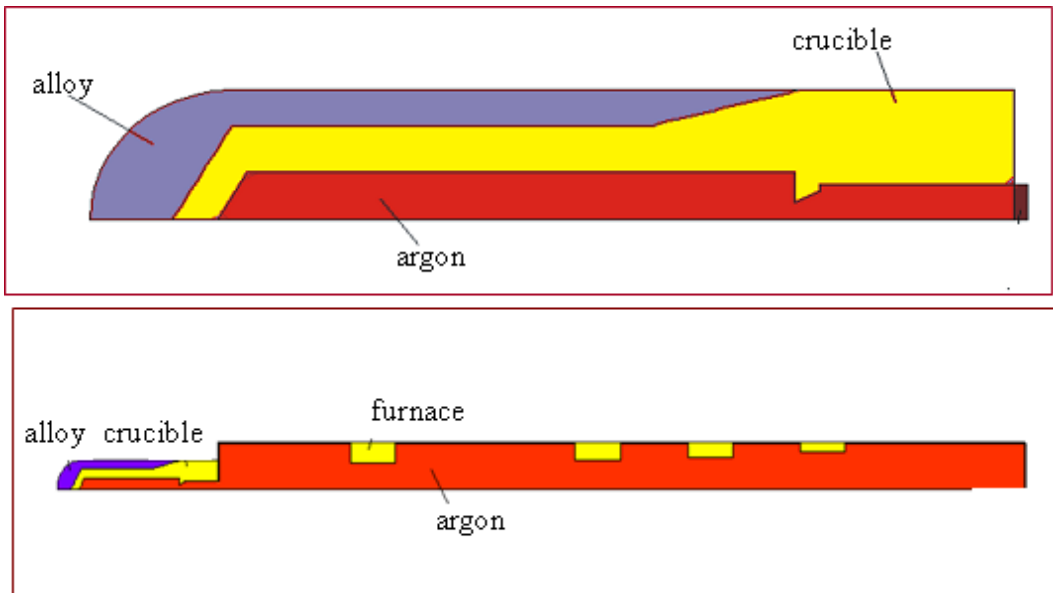


Figure 4.14. Simulated models: a) bare crucible, b) crucible inside the furnace.

4.5.3. Results

The results presented next are the temperature drops calculated by FLUENT and ANSYS in the back-wall of the crucible from the nominal temperature of Re-C (2748.15 K). Figures 4.17 and 4.19 represent the temperature profiles displayed by FLUENT and ANSYS. The x-axis (L) of figures 4.16 and 4.18 starts in the cone apex of the back-wall as can be seen in figure 4.15.

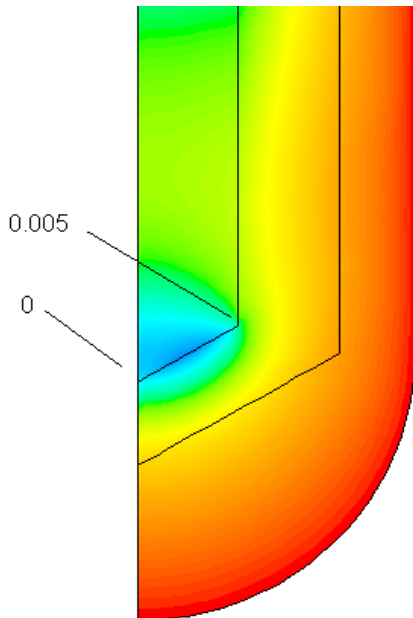


Figure 4.15. x-coordinates for the back-wall (in m)

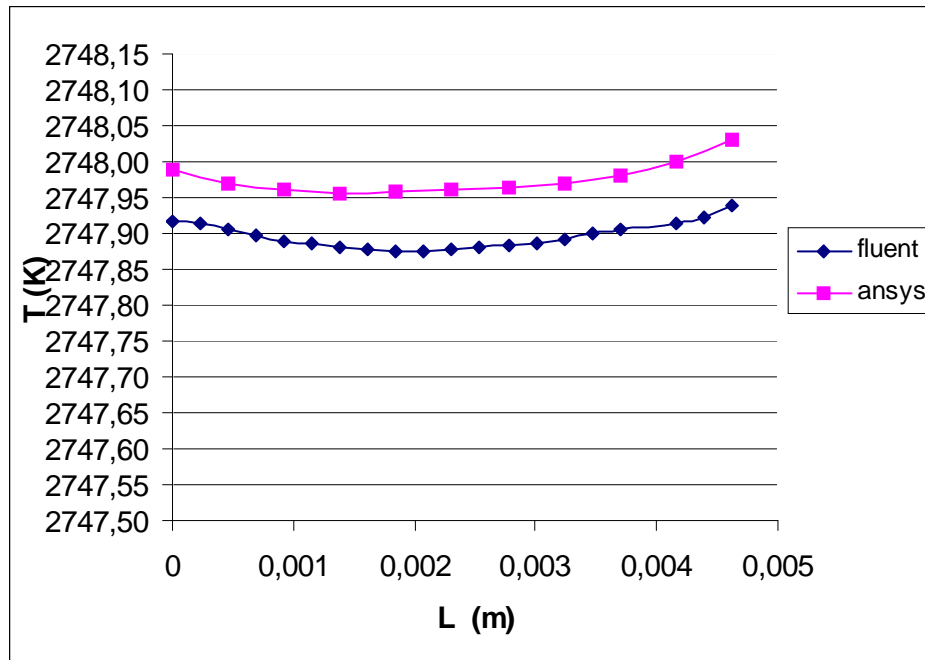


Figure 4.16. Temperature drop calculated by FLUENT and ANSYS in the back-wall for the bare crucible (case a).

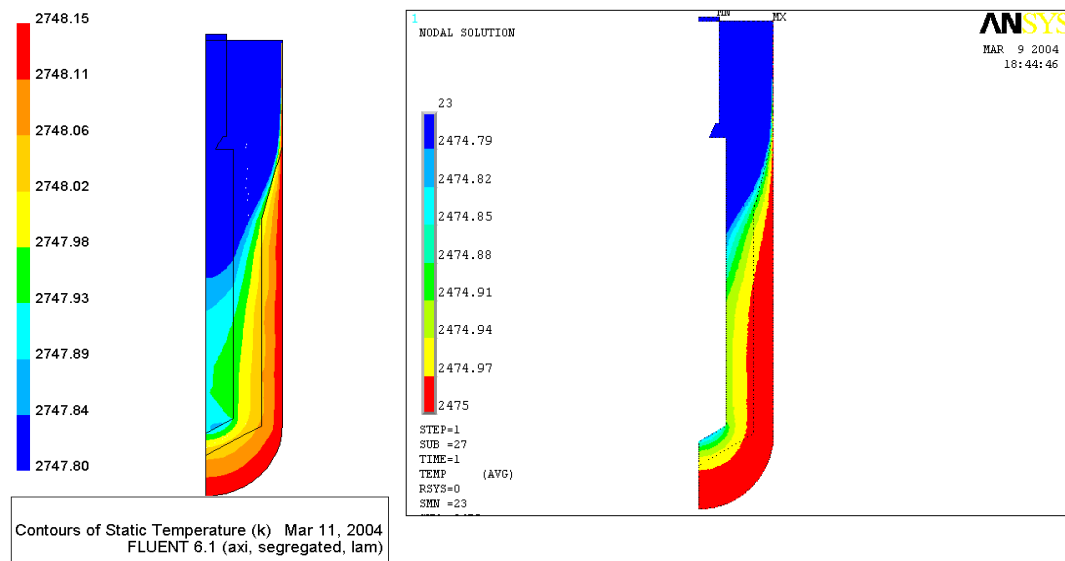


Figure 4.17. Temperature profile of the bare crucible (case a) calculated by FLUENT (in K) and ANSYS (in °C).

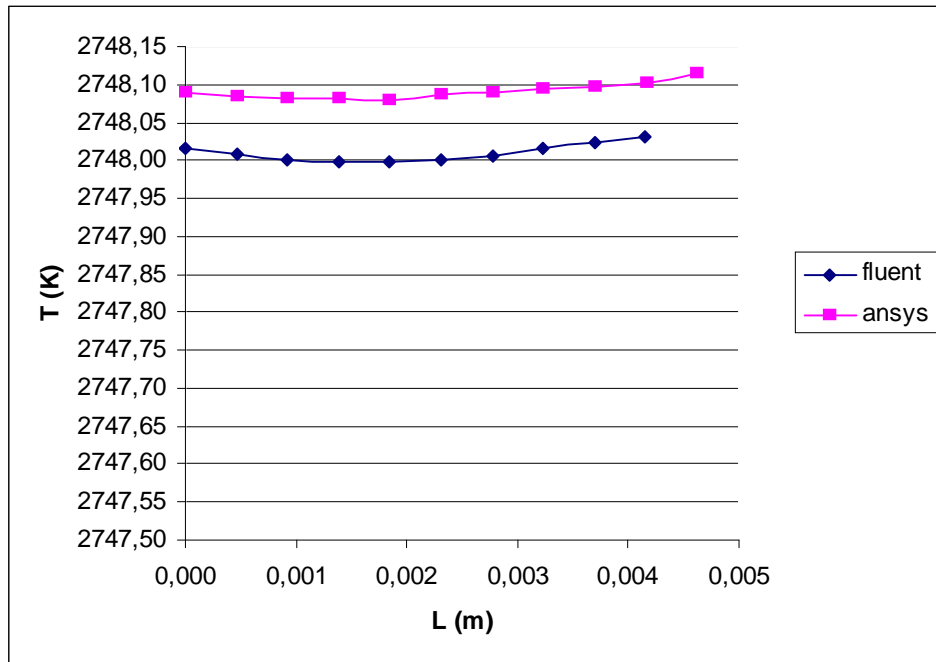


Figure 4.18. Temperature drop calculated by FLUENT and ANSYS in the back-wall for the crucible inside the furnace (case b).

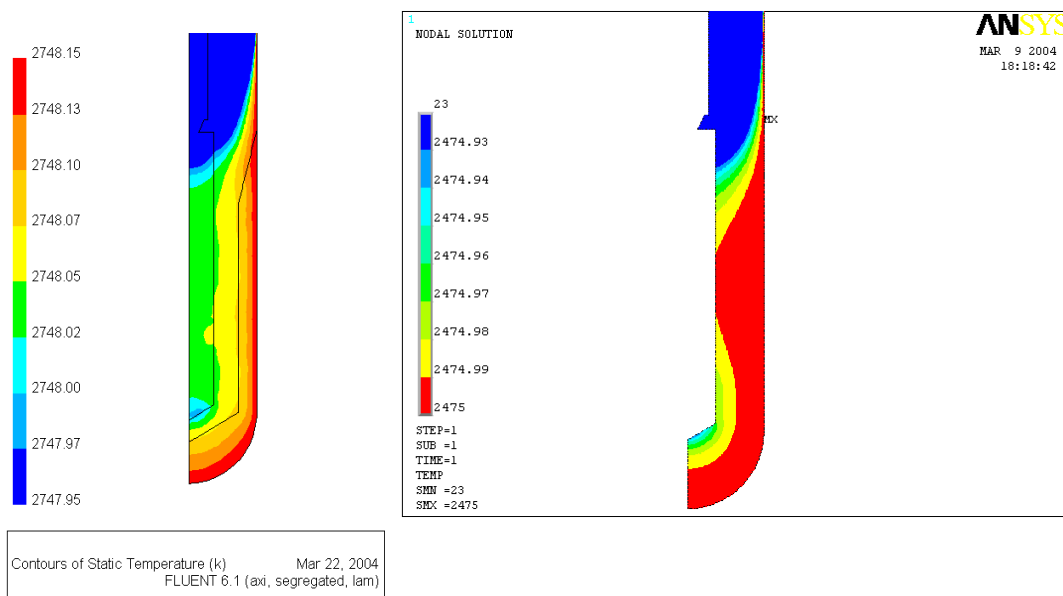


Figure 4.19. Temperature profile of the crucible inside the furnace (case b) calculated by FLUENT (in K) and ANSYS (in °C).

4.5.4. Conclusions

It has been demonstrated that both programs obtain similar results in the shape of the temperature drop and in its magnitude order although FLUENT

calculates a higher drop than the one estimated by ANSYS. It can be said that the comparison is satisfactory taking into account the structural differences between both software packages:

<u>FLUENT</u>	<u>ANSYS</u>
Uses finite-volume approach	Uses finite-element approach
Fluid inside the crucible is simulated (argon)	Vacuum inside the crucible is simulated
The algorithm for the radiation transfer equation is based on the solid angle	The algorithm for the radiation transfer equation is based on the form factors

4.□ Conclusions

The main reason of these preliminary studies was to validate and to test the accuracy of FLUENT software to solve heat transport problems which include a similar radiation transfer that the one involved in high temperature fixed points. These studies showed that FLUENT can be used to model the radiance transfer problems that will be encountered in this thesis.

The next chapters are focused in modelling and evaluating the uncertainty factors in the temperature drop associated with the HTFP, like the influence of imperfectly formed metal-ingots, the values of emissivity and thermal conductivity of graphite, the blackbody tube length and the back-wall thickness or the use of different furnaces, temperature profiles and measurement techniques.

CHAPTER 5

Uncertainty factors in the temperature drop I: temperature effects of imperfectly formed metal- ingots

Chapter 5. Uncertainty factors in the temperature drop I: Temperature Effects of Imperfectly Formed Metal-Ingots

5.1. Introduction

The CCT-WG5¹ has instigated a programme of research with the aim of establishing high temperature fixed points as routine temperature standards above 1100 °C by 2012 [49]. These high temperature fixed points (HTFPs) are based on ingots of metal–carbon eutectics, metal–carbide eutectics or peritectics cast in graphite crucibles [15]. However, the casting process is not straightforward and can result in imperfect filling of the crucible, in particular forming an ingot with holes or voids. Part of the CCT-WG5 research plan is to seek to understand the effects such imperfect filling might have on the resultant temperature. This is not possible to determine experimentally so a numerical thermal model of non-contact thermometry cells has been established to help understand this effect. Different models have been constructed simulating the presence of both voids or holes and “cracks” in the ingot. A crack in the ingot is potentially a major flaw allowing direct communication of the thermal radiation from the crucible wall to the blackbody tube.

These models were implemented using finite volume software and the areal average of the back-wall temperature calculated whilst the fixed point was raised from a fully frozen to a fully molten state. Furnace effects have been neglected, that is the crucible alone has been simulated. Two dimensional axisymmetric simulations have been performed for the following scenarios:

- Holes in the ingot adjacent to the crucible wall with the dimensions given in Table 5.1 were simulated. The position of the hole was varied along the crucible wall.

¹ CCT-WG5 is a Working Group of the Consultative Committee of Thermometry (CCT), one of the members of the Comité International des Poids et Mesures (CIPM). The terms of reference of CCT-WG5 are to study and advise the CCT on issues related to thermal radiation methods for temperature measurement and to develop and maintain an effective liaison with the Consultative Committee for Photometry and Radiometry (CCPR).

- Cracks of 1.5 mm and 3 mm width allowing direct line of sight of the hot outer crucible wall to the blackbody wall were modeled in turn. The position of the cracks was varied.

Table 5.1. Depth and width of simulated holes and width of simulated cracks in ingot.

	Depth /mm	Width /mm
Hole 1	2.5	3.0
Hole 2	2.5	1.5
Hole 3	1.0	1.5
Crack 1		1.5
Crack 2		3

This chapter describes the results of the simulations, in particular the effect of imperfectly formed ingots on the duration and quality of the melt profile.

5.2. Construction and implementation of thermal model

The thermal model was implemented using the software package FLUENT 6.1. To simulate these fixed points two dimensional axisymmetric models have been constructed. The fixed point modeled was of a typical NPL design [50]. These are constructed from high purity graphite and filled with an ingot of the metal-carbon mixture. In brief the outer crucible was 40 mm long and 24 mm of outer diameter. The crucible walls, including a thin sacrificial inner sleeve of graphite were 5 mm thick. The blackbody reentrant well was 7 mm outside diameter with a 3 mm blackbody internal diameter with a length of 27 mm and a 120° cone at the apex. The internal diameter of the crucible, where the ingot was cast, was 16 mm. The fixed-point modeled here was the Re-C point (2747 K) but the results are applicable in general. A photograph of one of these fixed-points is shown in Figure 5.1 in [51].

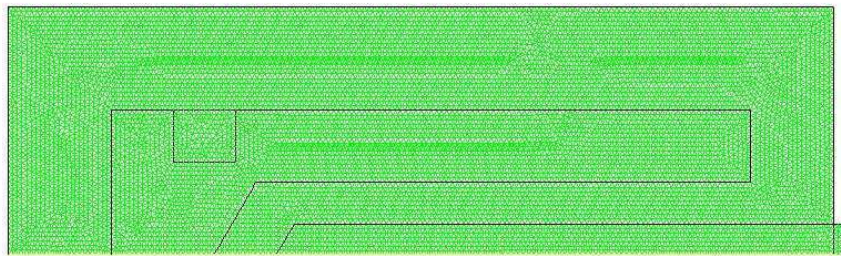
The important thermophysical properties were: graphite emissivity 0.86, Re-C emissivity 0.35, thermal conductivity of graphite $36.5 \text{ W.m}^{-1}\text{.K}^{-1}$, the thermal conductivity of Re-C around the melting point $55 \text{ W.m}^{-1}\text{.K}^{-1}$. For the purposes of the model Re-C is assumed to have the same thermal properties as pure Re.

The boundary conditions were set with a uniform temperature of the outside wall of

the crucible i.e. it did not experience any temperature gradients. The outside world at the fixed point aperture was simulated with a baffle at room temperature looking directly to the back-wall of the crucible.

The numerical experimentation was performed as follows. The initial condition was that the crucible was held 7 K below the melting point. A temperature step function above the melting point was then implemented by raising the outside graphite wall to 20 K above the melting point. The areal average of the temperature of the back-wall was then calculated during the simulated melting process.

The holes and cracks described in the introduction were implemented and modeled in turn. A typical numerical grid, showing a simulated hole, is given in Figure 5.1.



Grid	Sep 22, 2008 FLUENT 6.1 (2d, segregated, lam)
------	--

Figure 5.1. A typical numerical grid for a NPL HTFP.

5.3. Simulation results

5.3.1. Results with the holes

The holes given in table 5.1 were modeled at four different locations around the ingot. The holes were always assumed to be on the outside wall of the ingot facing the

outside graphite wall, as shown in Figure 5.2. These were designated (x, y) (see the key to Figure 5.3), where x designates the location of the hole and y identifies its dimension.

Four different positions were modeled, position 1 was at the rear wall of the crucible and positions 2, 3 and 4 were along the side walls of the cavity, with position 4 being the furthest from the radiating back-wall.

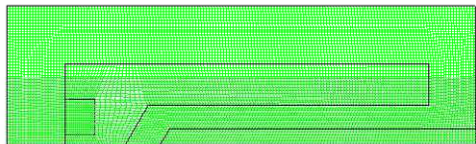
1) Position x=1. The centre of the hole 1 (2.5 mm x 3 mm) was 2.5 mm above the axis of the crucible and the centers of holes 2 (2.5 mm x 1.5 mm) and 3 (1 mm x 1.5 mm) were 1.75 mm above the axis.

2) Position x=2. The centre of the hole 1 was 9.5 mm from the external wall of the rear of the crucible (the left vertical side in figure 5.2) and the centers of holes 2 and 3 were 8.75 mm from the rear.

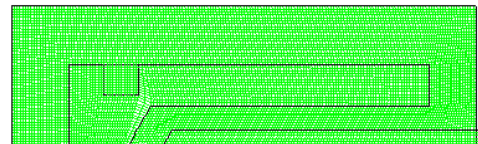
3) Position x=3. The centre of the hole was 19.5 mm from the external wall of the rear of the crucible and the centers of holes 2 and 3 were 18.75 mm from the rear.

4) Position x=4. The centre of the hole was 29.5 mm from the external wall of the rear of the crucible and the centers of holes 2 and 3 were 28.75 mm from the rear.

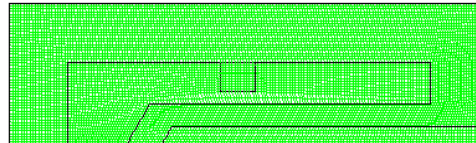
(position 1)



(position 2)



(position 3)



(position 4)

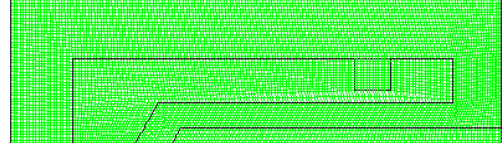


Figure 5.2. The four different positions of the holes around the ingot.

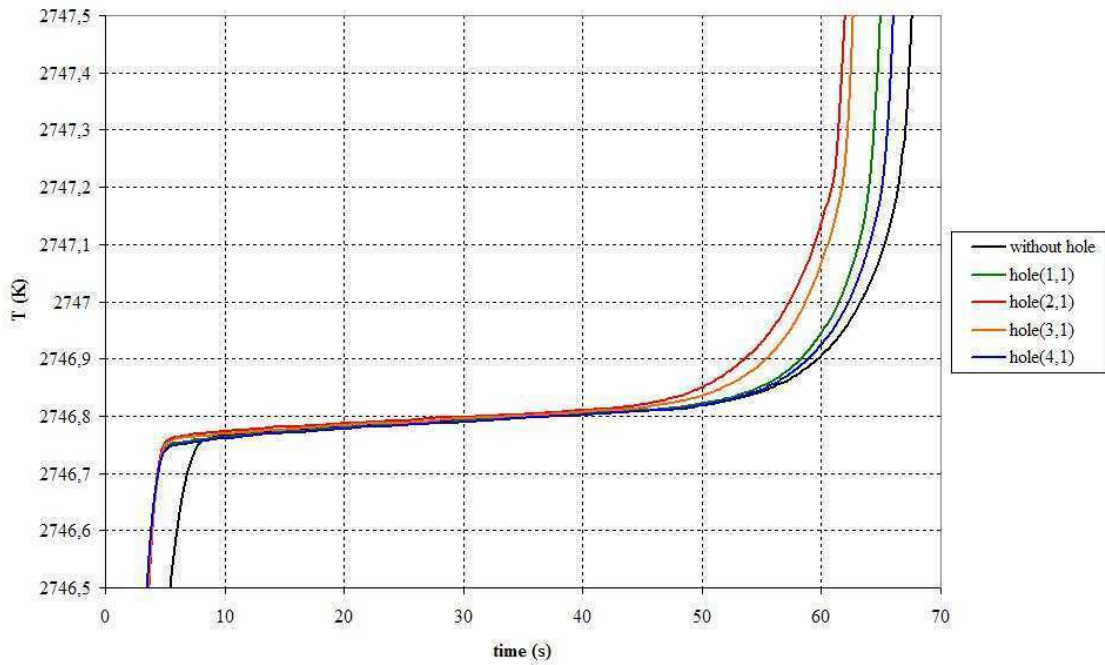


Figure 5.3. Results of thermal model for the hole 1 ($2.5\text{ mm} \times 3\text{ mm}$) in the different locations of figure 5.2. The no-hole model is plotted for reference. The key is hole(x =position indicated in figure 5.2, y =dimension of the hole given in table 5.1).

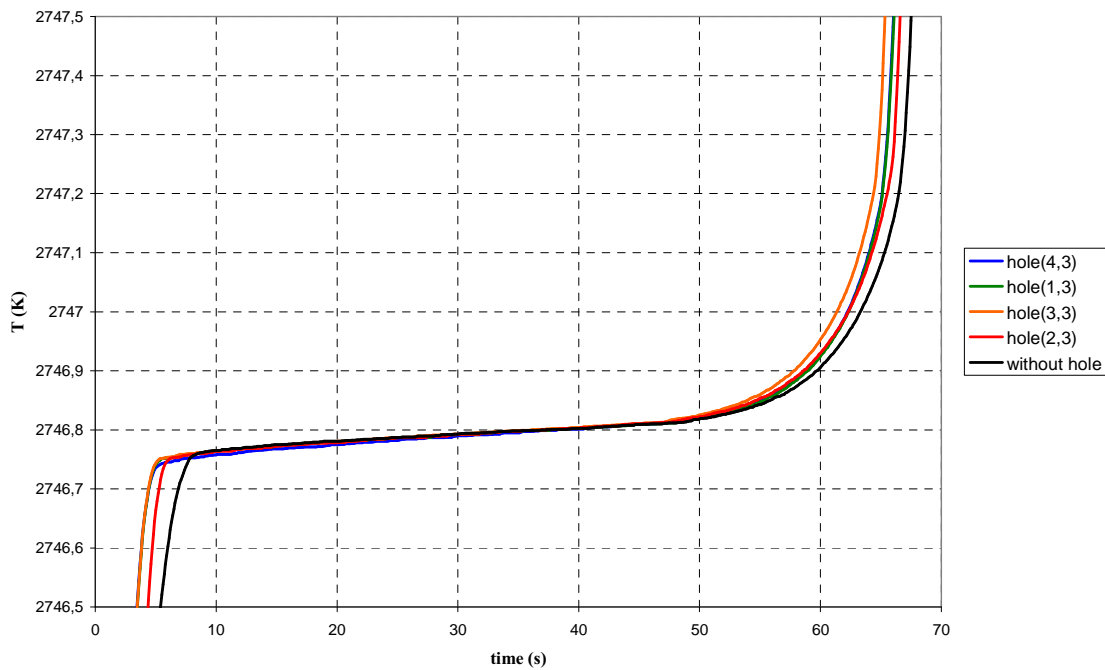


Figure 5.4. Results of thermal model for the hole 3 ($1\text{ mm} \times 1.5\text{ mm}$) in the different locations of figure 5.2. The key is hole(x =position indicated in figure 5.2, y =dimension of the hole given in table 5.1).

The results of the thermal modeling for the holes of differing dimensions and hole position are shown in Figures 5.3 and 5.4. Here the areal average of the back-wall temperature is plotted with time. Note the time units are arbitrary and a function of the thermal conductivity and density of the system.

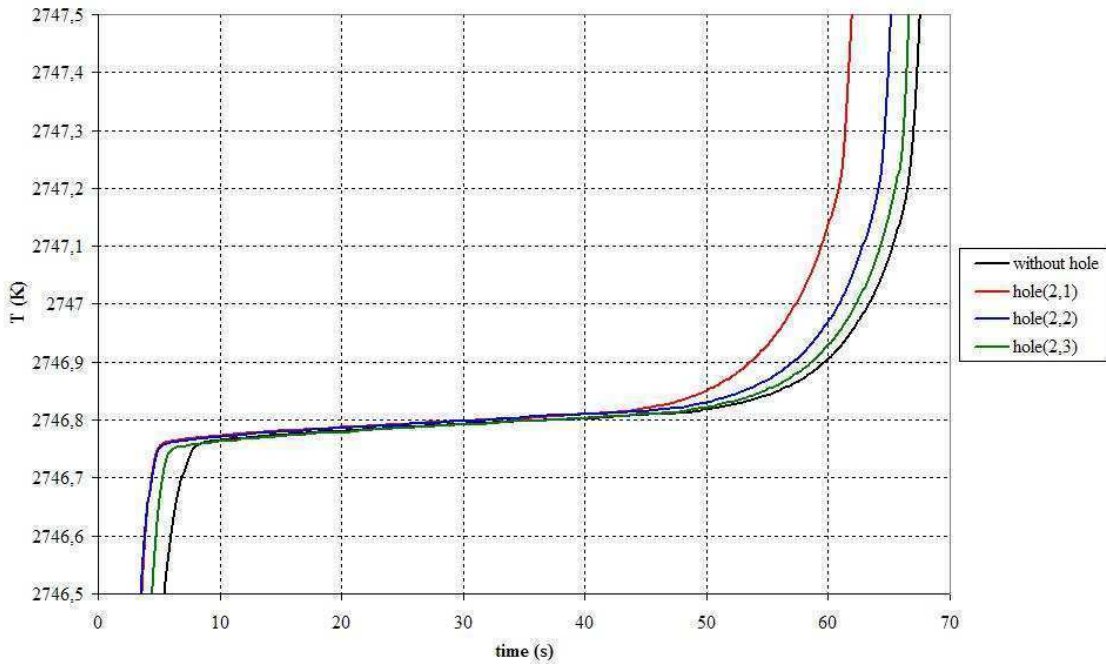


Figure 5.5. Results of thermal model for the three different size holes of table 5.1 in the same location that is position 2 (as shown in Figure 5.1 and Figure 5.2). The key is hole(x =position indicated in figure 5.2, y =dimension of the hole given in table 5.1)

The model shows that the fixed-point is very tolerant to the presence of holes, even quite large holes, in the surface of the ingot. The position of the hole makes very little difference to neither the resultant radiance temperature nor the duration of the melt.

Figure 5.5 shows the effect on the radiance temperature of the three different size holes given in table 5.1 in the location showed in figure 5.1 and figure 5.2 (position 2). Again it is clear that the dimension of the hole does not have a significant effect on the overall melting curve of the fixed point, though the duration is slightly shorter for larger holes.

5.3.2. Results with the cracks

The two cracks of width 1.5 mm (crack 1) and 3 mm (crack 2) were modeled at

three different locations around the fixed point. These were all on the crucible wall perpendicular to the blackbody tube. Position 1 is closest to the back wall, position 3 is relatively close to the front face of the crucible, as it can be seen in figure 5.6.

1) Position $x=1$. The centre of the crack 1 was 18.75 mm from the external wall of the rear of the crucible (the left vertical side in figure 5.6) and the centre of crack 2 was 19.5 mm from the rear.

2) Position $x=2$. The centre of the crack 1 was 24.75 mm from the external wall of the rear of the crucible and the centre of crack 2 was 25.5 mm from the rear.

3) Position $x=3$. The centre of the crack 1 was 30.75 mm from the external wall of the rear of the crucible and the centre of crack 2 was 31.5 mm from the rear.

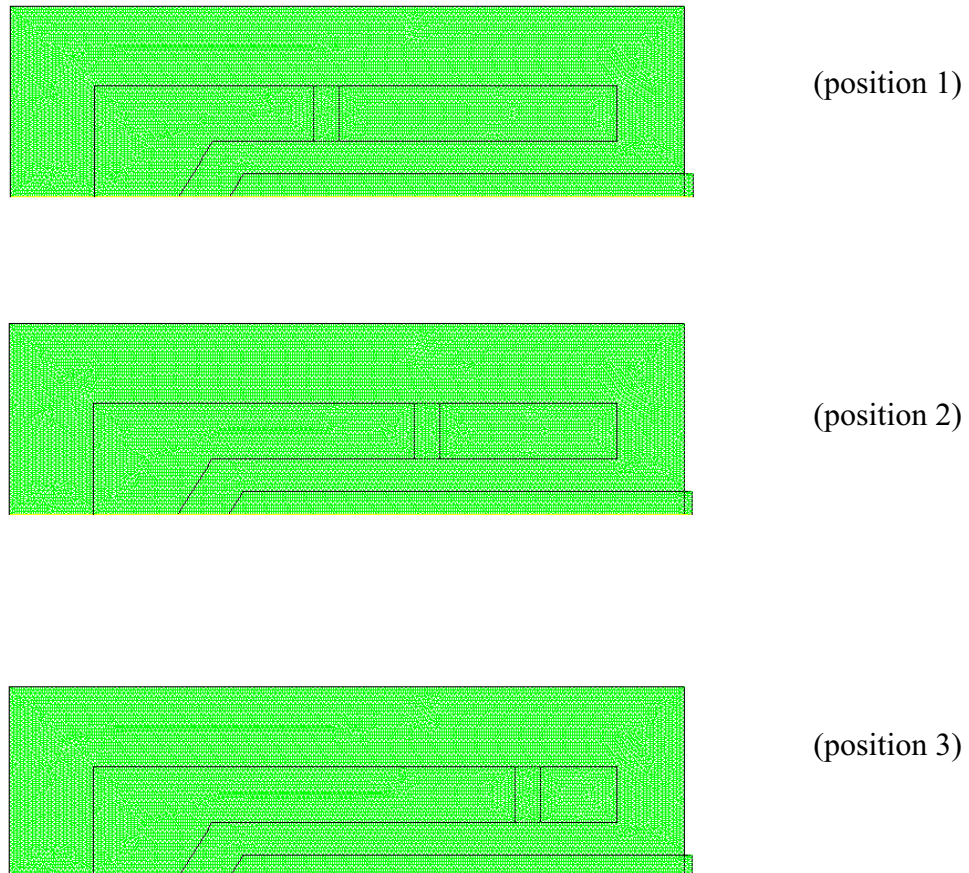


Figure 5.6. The three different positions of the cracks inside the ingot.

The cracks in principle allow for direct line of sight from the outer crucible wall to the blackbody. Figure 5.7 shows the effect on the radiance temperature of cracks of the two different dimensions in the three different locations.

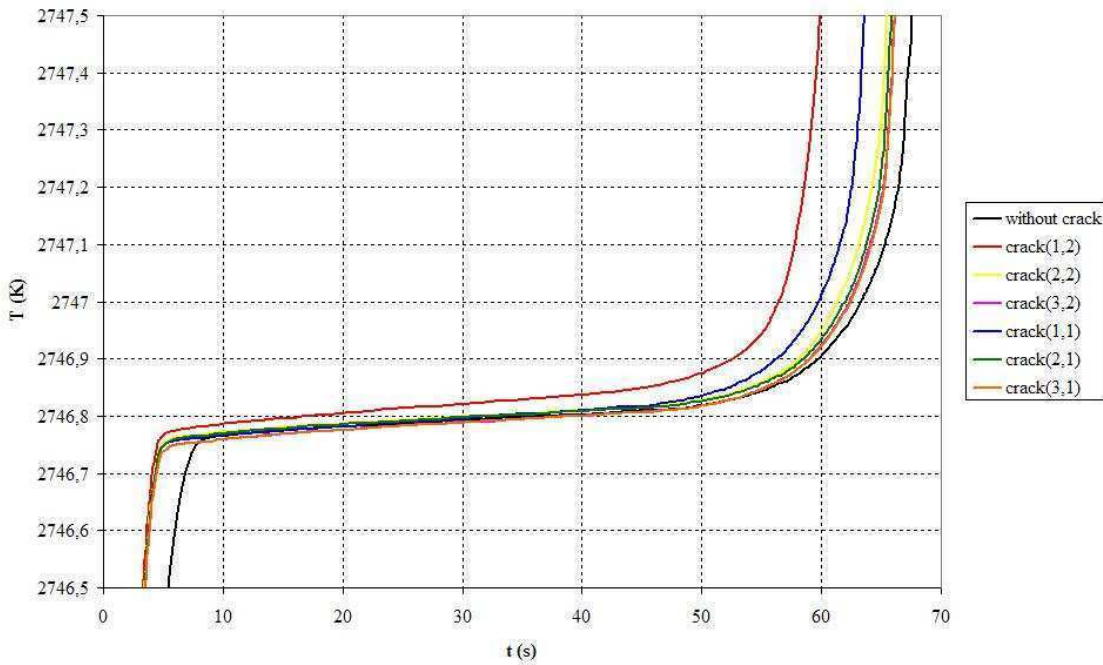


Figure 5.7. Results of thermal model for the two different size cracks of table 5.1 in the three different locations of figure 5.6. The no-crack model is plotted for reference. The key is crack(x =position indicated in figure 5.6, y =dimension of the crack given in table 5.1).

In this case the large crack close to the back-wall significantly affected the radiance temperature, increasing it by about 0.1 °C and shortening the melting point duration. The smaller crack in the same location ($x=1$) had a smaller but also noticeable effect. Interestingly however, cracks further away from the back wall only had a marginal effect on the areal average back-wall temperature.

5.4. Discussion

These results of these models were initially rather surprising. It was anticipated that transfer by radiation was such an efficient heat transfer mechanism compared to conduction that it would dominate over the latter. In fact this is clearly not the case. This was borne out when the thermal model was examined in detail. When the dynamic model of the melt of a hole was examined closely conduction was clearly seen as much more effective at transferring heat than radiation – so much so that the melt front in the solid actually “caught up” the melt front induced by radiative transfer.

This can be understood through a simple one-dimensional analytic calculation of

heat flux between two parallel surfaces comparing conductive and radiative heat flux. The ratio of radiative heat-flux to conductive heat flux is given by equation 5.1.

$$\frac{q_r}{q_c} = \frac{4\sigma T^3 x}{k(\varepsilon_1^{-1} + \varepsilon_2^{-1} - 1)} \quad (5.1)$$

Where q_r/q_c is the ratio of radiative to conductive heat fluxes, σ is the Stefan Boltzmann constant, T is the thermodynamic temperature, x is the separation between the parallel surfaces, k is the thermal conductivity of the material, ε_1 is the emissivity of the hotter material and ε_2 is the emissivity of the cooler material.

If the typical values at the Re-C point (2747 K) given at the beginning of Section 5.2 are used for the material properties of Re and graphite then for a small hole of 2.5 mm width, compared to conduction across a 2.5 mm slab of Re, the ratio of heat fluxes is 0.071 showing that conduction strongly dominates. For illustrative purposes if the hole became 25 mm then the ratio becomes 0.71 with radiative heat flux becoming almost as effective as conductive heat flux.

It is therefore clear that a small number of even quite large hole like flaws on the surface ingot can be tolerated, even when close to the back-wall of the blackbody. This is a direct consequence of conductive heat transfer being so much more efficient than radiative heat transfer on the small scales present in the ingot. By the time the melt front has penetrated well into the ingot the effect of the hole has effectively been smoothed out.

Even the presence of small cracks in the ingot if located well away from the back-wall of the cavity have little effect, provided the temperature gradient along the crucible wall is small. However caution needs to be exercised here because cracks in the ingot near the region of the back wall can have a significant effect on the resultant radiance temperature. There is an interesting implication from these results. As it appears that the radiance temperature of the fixed point is not significantly affected by small cracks when a reasonable distance from the back-wall of the radiating cavity, it might well be possible to reduce the ingot size (the exact amount to be calculated through modelling) without adversely affecting the overall temperature performance of the fixed point. This conclusion is of course contingent on having a reasonably uniform furnace. But it seems that it may be possible to construct HTFPs with reduced material at the front of the fixed-point without significantly impairing its radiometric performance (though of

course the duration of the melt would be somewhat reduced, but this is of little significance for radiation thermometry). This is important, particularly when constructing ingots from expensive materials such as platinum.

5.5. Conclusions

The conclusions to be drawn from this chapter are:

- That even at high temperatures, for the dimensions of the structures under consideration in this chapter, conductive heat transfer is still more effective than radiative transport.
- Minor imperfections in fixed-point ingots such as holes on the ingot surface can be neglected.
- Cracks in the ingot when near the back-wall of the cavity have a significant impact on the radiance temperature but are of less importance when away from the back-wall.
- It seems possible, that the length of the ingot in a good furnace could be significantly reduced in size covering only the rear portion of the blackbody tube. This influences the duration of the plateau but not particularly the achieved temperature.

CHAPTER 6

Uncertainty factors in the temperature drop II: emissivity, thermal conductivity and Nagano- M furnace temperature profile

Chapter 6. Uncertainty factors in the temperature drop II: Emissivity, Thermal Conductivity and Effect of Nagano- M Furnace Temperature Profile

6.1. Introduction

At or below the copper point ($T = 1357.77$ K) the correction for the temperature drop ΔT across the back-wall of the cavity has been found to be smaller than the uncertainty in the fixed-point realization itself [29]. Since radiative heat exchange increases with T^4 , the situation might be different for high-temperature fixed points such as the metal-carbon or metal carbide-carbon eutectic fixed points [15]. In this chapter the uncertainty $u(\Delta T)$ in the temperature drop ΔT is evaluated for the high-temperature eutectic fixed points Co-C, Pt-C and Re-C with eutectic temperatures T_E of 1597 K, 2011 K and 2747 K, respectively, for a variety of cavity-furnace geometries.

It should be mentioned that these fixed points are presently objects of an extensive study within the international ‘High-temperature fixed-point project’, coordinated by Working Group 5 of the CCT, and this research is part of that endeavour [52].

The systems to be modeled are described in section 6.2. Model structure and quantities to be calculated are surveyed in section 6.3. Results are presented in section 6.4 and discussed in section 6.5. The main conclusions are presented in section 6.6.

This study is to be considered as an extension to [53] and [54]. Survey of earlier studies on this subject can be seen in [53]. Modelling of the various systems to be considered below is done by FLUENT a software package utilizing finite-volume analysis, usually applied to the study of liquids and gases. Validation of this software for this type of analysis has been demonstrated in Chapter 4 of this thesis. The work on the temperature drop presented in [53] and [54] was based upon finite-element analysis implemented in the ANSYS package. Results obtained with FLUENT and ANSYS, applied to some typical cases within the sphere of the present study, showed that they can be considered equivalent within the resolution of the calculations.

6.2. Systems to be modelled

The system serving in the main as the experimental environment to the calculations to be surveyed in section 6.3 is shown in figure 6.1. It is the Nagano 'VR10-A23', designed by NMIJ, within which the fixed-point cell is placed for observation by a radiation thermometer mounted in front of the furnace. A picture of the cell, type 6ST, designed by NMIJ, is shown in figure 6.2C; its geometry is specified in table 6.1.

Furnace-temperature profiles, carried by eight radiation shields placed ahead of the cell are measured at the Co-C, Pt-C and Re-C eutectic fixed points; these are shown by the continuous curves in figure 6.3, denominated as RP (real profile) in the legend. The radiation shields are 1 mm thick C/C composite plates, placed 10 mm apart, with holes increasing in diameter, from the blackbody aperture, in 1 mm increments. The measurements have been carried out with an LP-5 thermometer with 1 mm target size at a measurement distance of 760 mm. The average width viewable for each shield is only 0.5 mm, therefore the readings represent the radiance averaged over three consecutive shields.

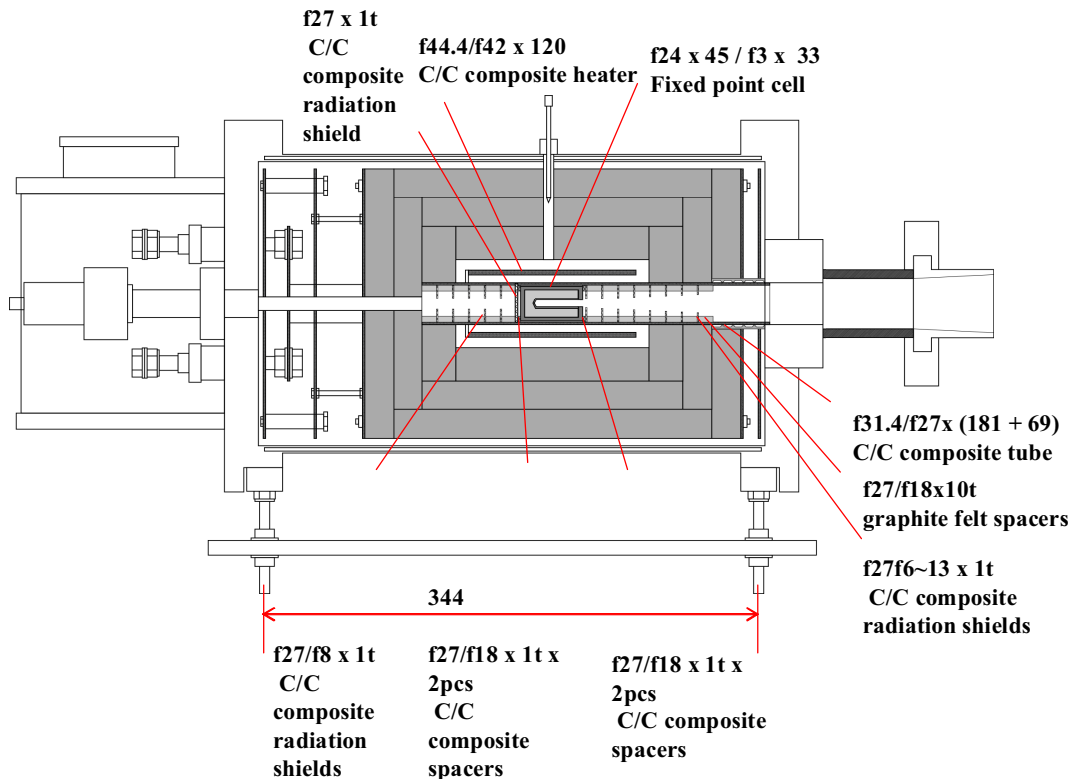


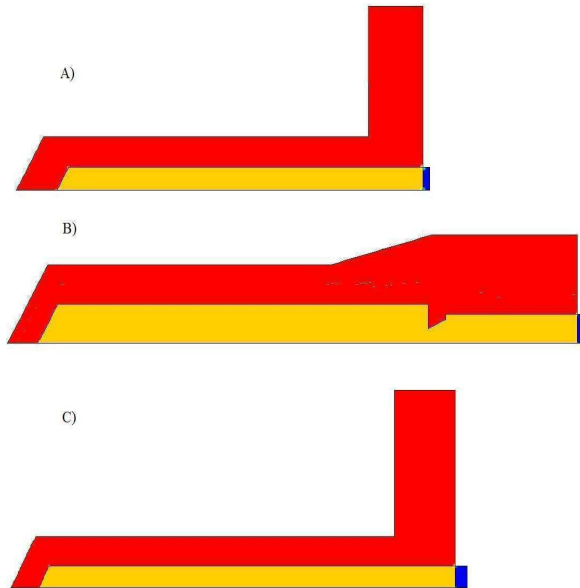
Figure 6.1: Nagano VR10-A23 furnace with crucible. Dimensions in mm.

Table 6.1. Cell parameters for the cells Mk-4, 3S, 6ST.

cell/ dimensions ¹⁾	cavity diameters ²⁾	backwall thickness	cavity length	tilt angle
Mk-4	3 / 3	2.6	27	30°
3S	8 / 3	2.6	62	30°
6ST	3 / 3	2	34	30°

¹⁾ Dimensions in mm, ²⁾ $D(\text{cyl})/ D(\text{aperture})$

In order to evaluate the influence of the furnace-temperature profile (FTP) on ΔT and its uncertainty $u(\Delta T)$, calculations for the 6ST cell have been extended to include additional FTP's as well. These are denominated as NF, RP, CP and HP, specified as follows: NF: cell without furnace, RP: real profile, as measured in Nagano VR10-A23 and CP: isothermal profile set to the eutectic temperature T_E of the fixed point in question. As to the profile HP, shown in figure 6.3: it has been derived from measurements done in another furnace -a three-zone furnace, the Nagano 'VR10-A19'- which is larger than the Nagano 'VR10-A23' by shrinking the x dimension of

**Figure 6.2.** The cells in study: Mk-4 (A), 3S (B), 6ST (C).

the temperature profile at the Re-C eutectic fixed point [53]. It is represented by the upper discontinuous curve (denominated as HP in the legend) in figure 6.3. The two lower discontinuous curves are obtained by shifting the upper one parallel to the T -

axis such that their maximum is located at the fixed-point temperature of eutectic Pt-C and Co-C, respectively.

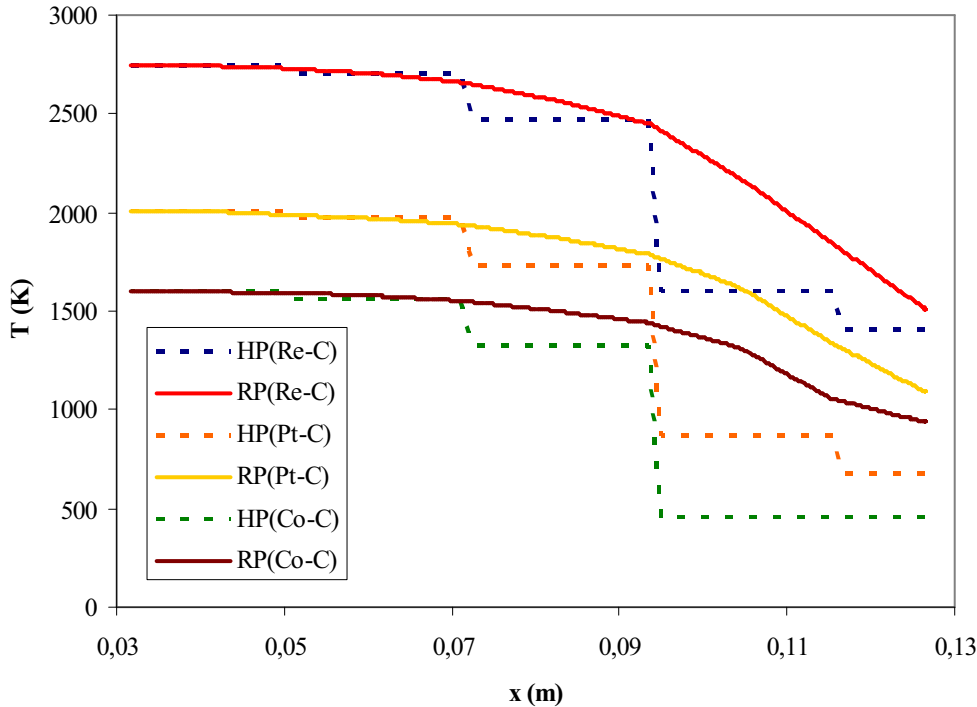


Figure 6.3. Furnace-temperature profiles: continuous curves: real profiles (RP), as measured for Nagano VR10-A23 at the fixed-point temperatures of the eutectics Co-C, Pt-C, Re-C. Discontinuous curves: based upon measurements for Nagano VR10-A19, cf. the text. x measures the distance to the centre of the furnace.

Finally: To gain an understanding of the influence of the cell geometry, calculations have been performed for three cells of different geometry, denominated as 6ST, 3S, Mk-4; like 6ST, 3S is designed by NMIJ, Mk-4 was designed by NPL. The comparison is done for the ‘worst case’ i.e. with no furnace. Pictures of the cells are given in figure 6.2, cell geometries are specified in table 6.1.

As in [53, 54] the results to be reported in section 6.4 are compared with the results obtained from the simple eq. (1), suggested earlier by Fischer and Jung [55]:

$$\Delta T = \cos\theta \cdot (r/L)^2 \cdot d \cdot (\varepsilon_g/K_g) \cdot \sigma \cdot T^4, \quad (6.1)$$

where θ is the tilt angle of the cavity bottom, r the cavity-aperture radius, L the cavity length, d the thickness of the cavity bottom, ε_g the wall emissivity of graphite, K_g the thermal conductivity of graphite, σ the Stefan-Boltzmann constant and T the

cavity's temperature in K. In the derivation of this equation radiant heat exchange within the cell and between cell and the front end of the furnace has been neglected.

6.3. Calculations

6.3.1. Model structure and material properties

As in [53] several assumptions were necessary in order to simplify the problem of calculating the parameters in question; without these simplifications either the modelling would have taken too much computer time or couldn't even have been performed.

1-The model geometry is considered axisymmetric; this allowed us to construct a 2D model.

2-The thermal resistance at contacting elements or screw parts is neglected because of its relatively small influence and the difficulty of estimating it [56,57].

3-Heat transfer due to convection and conduction in the furnace atmosphere has been taken into account, but these turned out to be negligible.

4-The model assumes steady-state conditions.

The thermal conductivity of graphite as a function of temperature over the range of interest is taken from [58]. From this the values 53.6, 45.6, 36.5 in $\text{Wm}^{-1}\text{K}^{-1}$ at the fixed-point temperatures of the eutectics Co-C(1597 K), Pt-C (2011 K), Re-C (2747 K), respectively, are derived. The emissivity of graphite, quoted nominally as 0.86, is from [55].

6.3.2. Quantities to be calculated

Quantities, calculated and discussed in section 6.4 and 6.5, respectively, given here in the order presented below, are:

Temperature drop: ΔT

It should be noted that ΔT is calculated with the temperature all over the outside of the cavity wall, or all over the inside of the ingot, set to the eutectic temperature T_E . This simulates the end of the melting process in an idealized fashion and obviates the need of implementing the ingot in the modelling.

The temperature drop is defined as $\Delta T = T_E - T_{\text{cav}}$, where T_{cav} is taken as the areal

average of the cavity bottom temperature.

Sensitivity coefficients: $(\partial \Delta T / \partial K_g)_{\varepsilon_g}$ and $(\partial \Delta T / \partial \varepsilon_g)_{K_g}$

These coefficients are denoted occasionally in the text as *SCK* (Sensitivity Coefficient for thermal conductivity of graphite K_g) and *SCE* (Sensitivity Coefficient for the wall Emissivity of graphite ε_g), respectively. They are useful for estimating the influence of these graphite properties on the temperature drop.

As demonstrated in figures 6.4.a and 6.4.b for the cell 6ST, the parameters *SCK* or *SCE* are obtained by calculating ΔT over a suitable range of values of the independent variable K_g or ε_g , respectively, and taking the slope of the thus obtained graph ΔT versus K_g or ΔT versus ε_g at the respective nominal values.

It should be mentioned here that according to eq. (6.1) we would have, in good approximation:

$$(\partial \Delta T / \partial K_g)_{\varepsilon_g} = -\Delta T / K_g \quad (6.2a)$$

$$(\partial \Delta T / \partial \varepsilon_g)_{K_g} = \Delta T / \varepsilon_g \quad (6.2b)$$

Standard uncertainty in the parameters K_g and ε_g : $u(K_g)$ and $u(\varepsilon_g)$

These are the uncertainties $u(K_g)$ in K_g and $u(\varepsilon_g)$ in ε_g , which are somewhat arbitrarily assigned the values 2 units and 0.15 unit, respectively, according to the range of use for these parameters in the modelling.

Partial uncertainties:

- $u(\Delta T; K_g)$: Uncertainty in ΔT due to the uncertainty $u(K_g)$ in K_g . It is defined as,

$$u(\Delta T; K_g) = (\partial \Delta T / \partial K_g)_{\varepsilon_g} \cdot u(K_g) \quad (6.3)$$

- $u(\Delta T; \varepsilon_g)$: Uncertainty in ΔT due to the uncertainty $u(\varepsilon_g)$ in ε_g . It is defined as,

$$u(\Delta T; \varepsilon_g) = (\partial \Delta T / \partial \varepsilon_g)_{K_g} \cdot u(\varepsilon_g) \quad (6.4)$$

FTP: furnace temperature profile, HP: high profile, RP: real profile, CP: constant profile, NF: no furnace, SCK: sensitivity coefficient for thermal conductivity of graphite K_g , and SCE: sensitivity coefficient for the wall emissivity of graphite ε_g .

- $u(\Delta T; K_g, \varepsilon_g)$: Uncertainty in ΔT due to the combined uncertainties $u(K_g)$ in K_g and $u(\varepsilon_g)$ in ε_g . It is defined as,

$$u(\Delta T; K_g, \varepsilon_g) = \{u(\Delta T; K_g)^2 + u(\Delta T; \varepsilon_g)^2\}^{1/2} \quad (6.5)$$

Uncertainty due to the furnace temperature profile (FTP):

- $u(\Delta T; \text{FTP})$: Uncertainty in ΔT due to the uncertainty in the furnace temperature profile (FTP). It represents the estimated uncertainty in ΔT associated with the uncertainty $u(\text{FTP})$ in the furnace-temperature profile (FTP) which for the time being is estimated to be,

$$u(\Delta T; \text{FTP}) = [\Delta T(\text{HP}) - \Delta T(\text{CP})]/2 \quad (6.6)$$

The rationale to this can be appreciated from an inspection of figure 6.5.a, from which it is seen that the ΔT associated with the RP is bracketed in-between the values obtained for HP and CP. It is clear that the CP is an upper profile bound and the HP can be considered as a lower bound as it is below the RP values.

Overall standard uncertainty in ΔT : $u(\Delta T)$

With the previous quantities defined, the overall standard uncertainty in temperature drop $u(\Delta T)$ can be expressed by,

$$u(\Delta T) = \{u(\Delta T; K_g, \varepsilon_g)^2 + u(\Delta T; \text{FTP})^2\}^{1/2} \quad (6.7)$$

6.4. Results

Table 6.2, upper section, shows ΔT calculated at the fixed-point temperatures of Re-C, Pt-C and Co-C for the furnace-temperature profiles (FTP's) NF, HP, RP, CP. The results obtained when applying eq. (6.1) are shown in the last column. The calculations are done for a wall emissivity ε_g of 0.86 and for thermal conductivities K_g associated with the fixed-point temperatures in question [55, 58].

Results for the profiles NF, HP, RP, CP obtained at the fixed points in question are shown in the histograms presented in figures 6.5.a. and 6.5.b. Figure 6.6 shows

ΔT , calculated for the profile CP, as a function of the (nominal) eutectic temperature T_E of the eutectics Co-C, Pd-C, Pt-C, Ir-C, and Re-C. The full line represents the fit $\Delta T = 1.50 \cdot 10^{-15} \cdot T_E^4$.

Table 6.2, mid and lower section, show the sensitivity coefficients $(\partial \Delta T / \partial K_g)_{eg}$ and $(\partial \Delta T / \partial \varepsilon_g)_{Kg}$, respectively, at the three fixed points, again as a function of the temperature profile, for the cell 6ST.

The data under Eq. (6.2a) and Eq. (6.2b) are obtained when applying the equations: $\partial \Delta T / \partial K_g = -\Delta T / K_g$ and $\partial \Delta T / \partial \varepsilon_g = \Delta T / \varepsilon_g$, respectively, but with ΔT calculated for the CP furnace-temperature profile, shown in figure 6.6.

Table 6.2. ΔT , $(\partial \Delta T / \partial K_g)_{eg}$, $(\partial \Delta T / \partial \varepsilon_g)_{Kg}$ for different furnace-temperature profiles¹⁾; cell: 6ST

$\Delta T / \text{mK}$		Furnace Temperature Profile			
System	NF	HP	RP	CP	Eq. (6.1)
Re-C	107	94	92	89	256
Pt-C	29	27	25	24	59
Co-C	12	12	12	12	20
$(\partial \Delta T / \partial K_g)_{eg}$ mK / unit²⁾					
System	NF	HP	RP	CP	Eq. (6.2a)
Re-C	-2,35	-2.27	-1.95	-2.13	-2.44
Pt-C	-0.800	-0.650	-0.705	-0.550	-0.526
Co-C	-0.339	-0.212	-0.212	-0.212	-0.224
$(\partial \Delta T / \partial \varepsilon_g)_{Kg}$ mK / unit					
System	NF	HP	RP	CP	Eq. (6.2b)
Re-C	55.0	60.0	60.0	55.0	103
Pt-C	15.0	15.0	10.0	15.0	27.9
Co-C	5.0	5.0	5.0	5.0	14.0

¹⁾ Calculations with $K_g = 36.5, 45.6, 53.6 \text{ Wm}^{-1}\text{K}^{-1}$ for Re-C, Pt-C, Co-C, respectively, and $\varepsilon_g = 0.86$.

²⁾ Unit = $\text{Wm}^{-1}\text{K}^{-1}$.

FTP: furnace temperature profile, HP: high profile, RP: real profile, CP: constant profile, NF: no furnace, SCK: sensitivity coefficient for thermal conductivity of graphite K_g , and SCE: sensitivity coefficient for the wall emissivity of graphite ε_g .

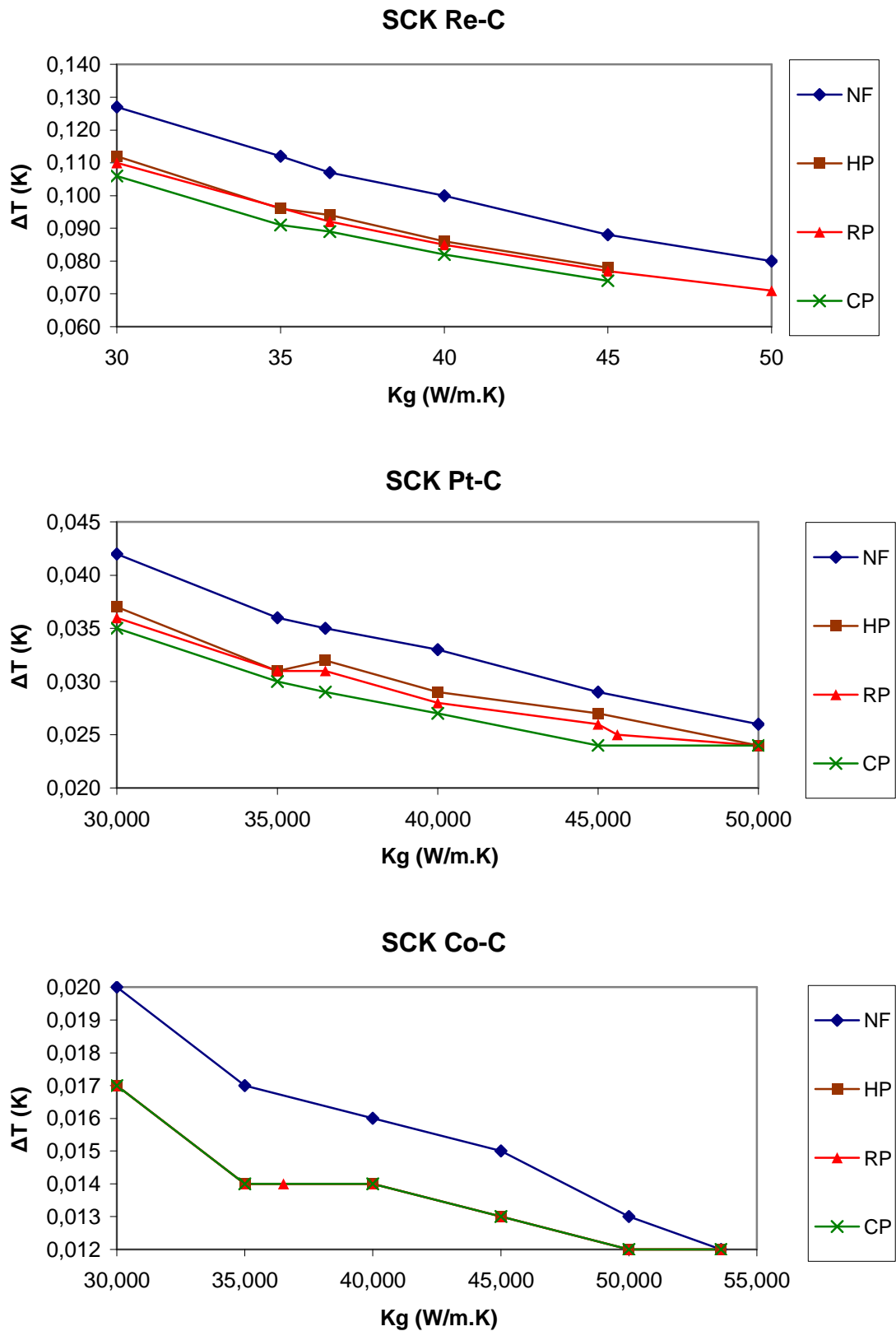


Figure 6.4a. Determining $(\partial \Delta T / \partial K_g) \varepsilon_g$, SCK. ΔT versus K_g for the cell 6ST

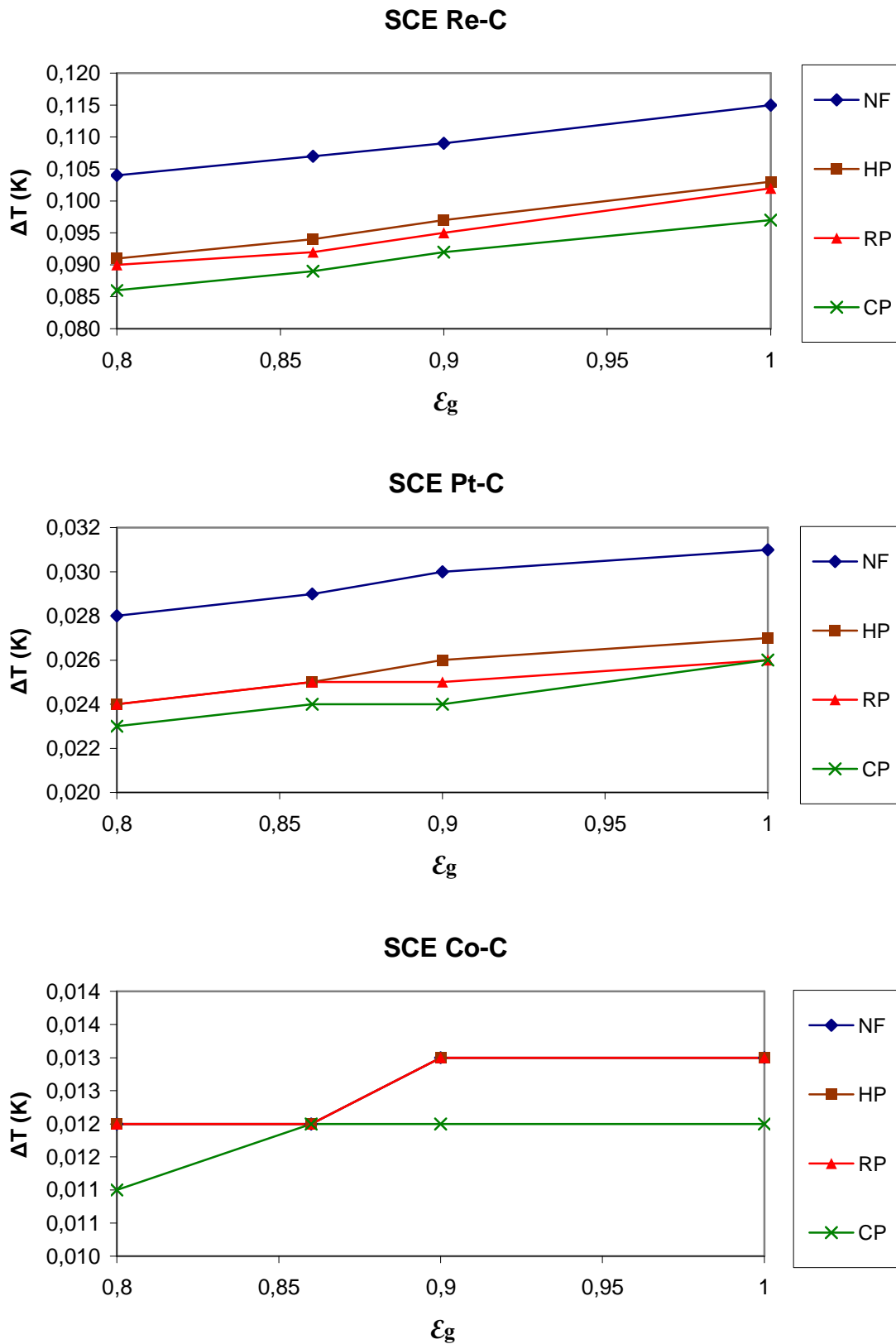


Figure 6.4b. Determining $(\partial \Delta T / \partial \varepsilon_g)_{Kg}$, SCE. ΔT versus ε_g for the cell 6ST.

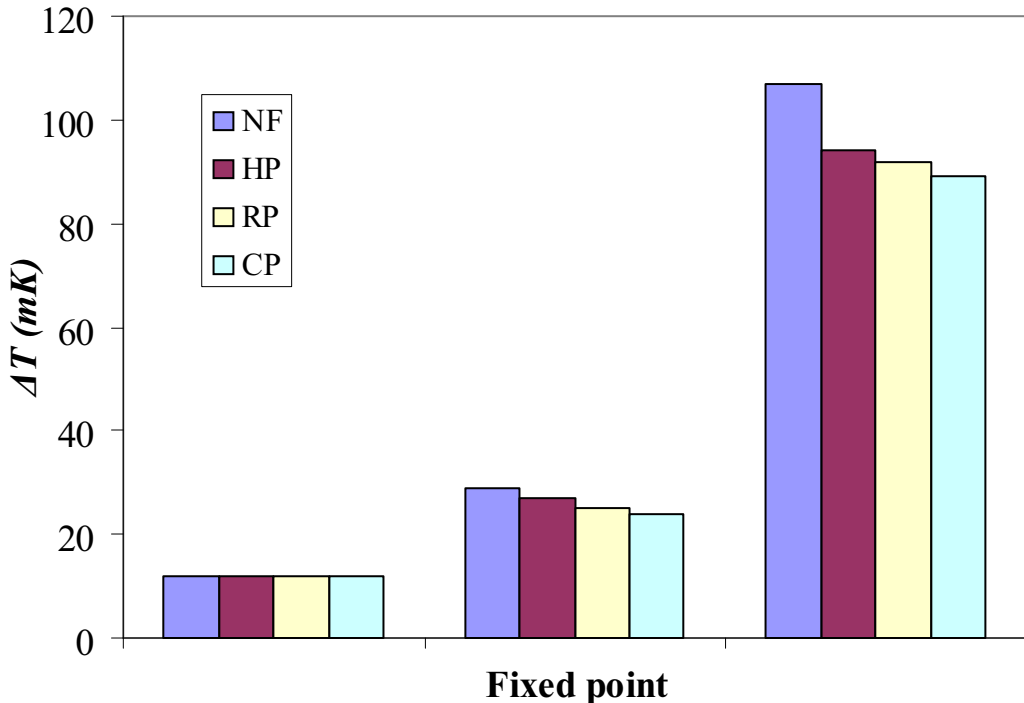


Figure 6.5.a. ΔT versus fixed point: Co-C, Pt-C, Re-C for the furnace-temperature profiles: NF, HP, RP, CP. Cell: 6ST.

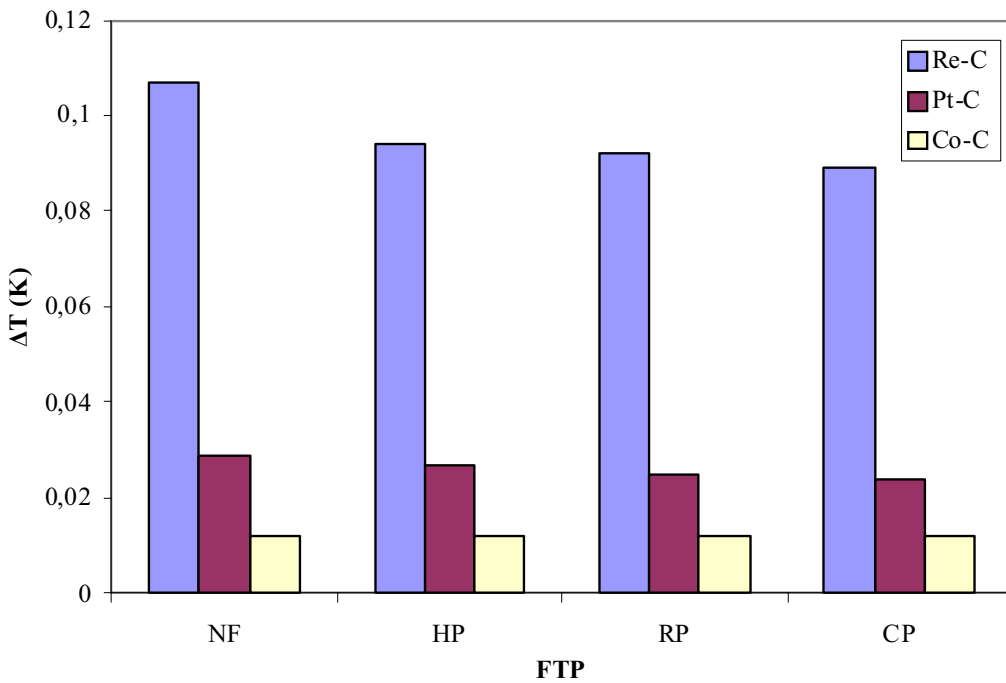


Figure 6.5.b. ΔT versus FTP: NF, HP, RP, CP for the fixed points: Co-C, Pt-C, Re-C. Cell: 6ST.

In table 6.3 is compared ΔT and the sensitivity coefficients $(\partial \Delta T / \partial K_g) \epsilon_g$ and

$(\partial \Delta T / \partial \varepsilon_g)_{Kg}$, respectively, calculated for the cells 3S, 6ST and Mk-4 at the three fixed points for the ‘profile’ NF.

Table 6.3. ΔT , $(\partial \Delta T / \partial K_g) \varepsilon_g$, $(\partial \Delta T / \partial \varepsilon_g)_{Kg}$ for different cells¹⁾; furnace-temperature profile: NF

ΔT / mK	Cell		
System	3S	6ST	Mk-4
Re-C	144	107	169
Pt-C	35	29	40.5
Co-C	21	12	14
$(\partial \Delta T / \partial K_g) \varepsilon_g$ mK / unit ²⁾			
System	3S	6ST	Mk-4
Re-C	-3.10	-2.35	-4.10
Pt-C	-1.00	-0.800	-1.21
Co-C	-0.424	-0.339	-0.364
$(\partial \Delta T / \partial \varepsilon_g)_{Kg}$ mK / unit			
System	3S	6ST	Mk-4
Re-C	65.0	55.0	85.6
Pt-C	25.0	15.0	28.5
Co-C	5.0	5.0	8.7

¹⁾ Calculations with $K_g = 36.5, 45.6, 53.6 \text{ Wm}^{-1}\text{K}^{-1}$ for Re-C, Pt-C, Co-C, respectively, and $\varepsilon_g = 0.86$. ²⁾ Unit = $\text{Wm}^{-1}\text{K}^{-1}$.

Finally tables 6.4a and 6.4b summarise the uncertainty estimates leading to the estimated standard uncertainty $u(\Delta T)$ in ΔT ; all uncertainties are meant to represent standard uncertainties. Table 6.4a gives the uncertainty estimates $u(\Delta T; K_g)$ and $u(\Delta T; \varepsilon_g)$ and their combined values $u(\Delta T; K_g, \varepsilon_g)$ associated with the uncertainties $u(K_g)$ in K_g and $u(\varepsilon_g)$ in ε_g .

FTP: furnace temperature profile, HP: high profile, RP: real profile, CP: constant profile, NF: no furnace, SCK: sensitivity coefficient for thermal conductivity of graphite K_g , and SCE: sensitivity coefficient for the wall emissivity of graphite ε_g .

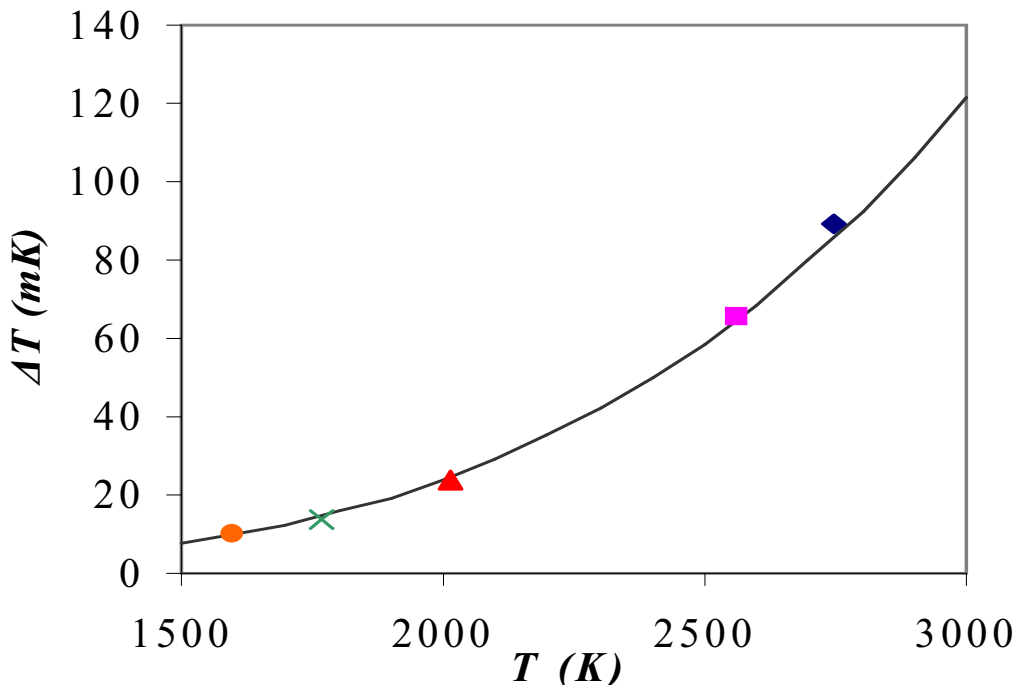
Table 6.4a. Uncertainty components in ΔT for cell 6ST; furnace-temperature profile: RP

T_E	$(\partial \Delta T / \partial K_g) \epsilon_g$	$u(\Delta T; K_g)$	$(\partial \Delta T / \partial \epsilon_g)_{K_g}$	$u(\Delta T; \epsilon_g)$	$u(\Delta T; K_g, \epsilon_g)$
K	mK / unit ¹⁾	mK	mK / unit	mK	mK
2747	1.95	3.90	60.0	9.0	9.81
2011	0.705	1.41	10.0	1.50	2.06
1597	0.212	0.424	5.0	0.75	0.86

¹⁾Absolute values, unit = $\text{Wm}^{-1}\text{K}^{-1}$

Table 6.4b. Overall uncertainty $u(\Delta T)$ in ΔT for cell 6ST; furnace-temperature profile: RP

T_E	ΔT	$u(\Delta T; K_g, \epsilon_g)$	$u(\Delta T; \text{FTP})$	$u(\Delta T)$	$u(\Delta T)/\Delta T$
K	mK	mK	mK	mK	
2747	92	9.81	2.50	10.1	0.11
2011	25	2.06	1.50	2.6	0.10
1597	12	0.86	0.00	0.9	0.07

**Figure 6.6.** ΔT versus eutectic temperature T_E calculated for the fixed-points Co-C (1597 K), Pd-C (1765 K), Pt-C (2011 K), Ir-C (2564 K) and Re-C (2747 K). Cell: 6ST. Furnace-temperature profile: CP. The full line represents $\Delta T = 1.50 \cdot 10^{-15} \cdot T_E^4$.

6.5. Discussion

Sensitivity coefficients, cell: 6ST

The results ΔT illustrated in figure 6.5.a show a significant increase with fixed point from Co-C towards Re-C and a more gradual decrease with FTP from NF towards CP. For Co-C, the results show no dispersion within the resolution of the calculations due to its lower nominal temperature, this is because the sensitivity coefficients associated to this point have less effect than those calculated for Pt-C and Re-C. Figure 6.6 for FTP-CP shows that for a given FTP ΔT would increase as T_E^4 in agreement with eq. (6.1); it reflects the increase of the total radiant flux emitted by a blackbody radiator radiating at a temperature T with T^4 according to the Stefan-Boltzmann law.

The results for $(\partial \Delta T / \partial K_g) \varepsilon_g$, SCK and $(\partial \Delta T / \partial \varepsilon_g)_{K_g}$, SCE compiled for HP, RP and CP in table 6.2, mid and lower section, respectively, show that the sensitivity coefficients in question are essentially *immune* to variations of the FTP. (For SCE this observation can be extended to include NF as well). This is an important observation for it means that the associated uncertainties can be calculated on the basis of results obtained for CP, i.e. for this the actual FTP (for a given cell-furnace geometry) is not needed.

The results from Eq. (6.2a) and Eq. (6.2b), last column, which describe the approximation to the sensitivity coefficients calculated as $-\Delta T/K_g$ and $\Delta T/\varepsilon_g$, cf. section 6.3.2, are in reasonably good agreement with the direct calculations for the FTP's in question for SCK, but less so for SCE, where they still might serve the purpose of serving as an upper bound. In principle the results under eq. (6.2a) and (6.2b) can be obtained from one calculation of ΔT for a given T_E for profile CP. The larger difference for SCE (results differ by a factor of about two) can be understood qualitatively by noting that ΔT is still less sensitive to changes in ε_g than predicted by the equations, even when adapted for ΔT . The effects of the interaction of the cavity's back-wall with the cylindrical cavity wall as well as with the front end of the furnace are neglected in eq.(6.1), which assumes free radiation to the outside world and is the basis to eq. (6.2a) and (6.2b). So empirically is found that $(\partial \Delta T / \partial K_g) \varepsilon_g \approx -\Delta T/K_g$,

FTP: furnace temperature profile, HP: high profile, RP: real profile, CP: constant profile, NF: no furnace, SCK: sensitivity coefficient for thermal conductivity of graphite K_g , and SCE: sensitivity coefficient for the wall emissivity of graphite ε_g .

$(\partial \Delta T / \partial \epsilon_g)_{Kg} \approx 0.5 \cdot \Delta T / \epsilon_g$ for the cell 6ST in combination with the CP and -as it turns out- with any of the other furnace-temperature profiles considered.

Comparing cells, FTP: NF

Table 6.3 shows ΔT , $(\partial \Delta T / \partial K_g) \epsilon_g$, SCK and $(\partial \Delta T / \partial \epsilon_g)_{Kg}$, SCE respectively, calculated for the cells 3S, 6ST and Mk-4 for the profile NF. Differences between the values of these parameters for the ‘worst case’ NF are of interest since they give insight into the influence of the cell geometry.

As may be appreciated from an inspection of the table the differences for the cells 3S and 6ST are not drastic, the values for 3S being systematically larger (in the absolute sense) with the exception of SCE for Co-C. As regards 3S versus 6ST this may have to do in part with the larger back-wall thickness d for 3S: 2.6 mm versus 2 mm for 6ST, involving a larger ΔT and thus larger values of SCK and SCE . The values obtained for Mk-4, calculated by L. Wright [59], on the basis of the software program Abaqus, are still significantly larger than for 3S, although in this case again $d = 2.6$ mm. This may be understood from the differences in cavity geometry: whereas Mk-4 (a) (like the cavity of 6ST) consists of a cylindro-cone of 3 mm diameter over a length of 27 mm, the cavity of 3S (b) consists of a cylindro-cone 8 mm in diameter over a length of 62 mm, but diaphragmed by a 3 mm aperture. This means that the cavity (b) may be supposed to be better than (a) approximating more closely to ideal-blackbody conditions, involving a smaller temperature drop and thus smaller values for SCK and SCE in case (b).

Uncertainties. Cell: 6ST, FTP: RP

Finally the comment to tables 6.4a and 6.4b reviewing the uncertainty values. This is to be considered a first qualitative approach, especially as regards the derivation of the component $u(\Delta T; \text{FTP})$. From the present provisional analysis it appears that the uncertainty $u(\Delta T)$ amounts to about 10 % of ΔT . It probably represents an upper bound to $u(\Delta T)$.

6.6. Conclusions

-For a given fixed-point cell, radiating at a temperature T , and a given furnace-temperature profile (FTP) the temperature drop ΔT across the backwall of the fixed-point cavity varies with T^4 over the temperature range considered. For the specific case studied in this chapter ΔT varies from about 5 mK at the copper point ($T=1357.77$ K) to 90 mK at the Re-C eutectic temperature ($T_E = 2747$ K). For the case in question at 3500 K we would have $\Delta T = 220$ mK.

-The sensitivity coefficients $(\partial \Delta T / \partial K_g) \varepsilon_g$ and $(\partial \Delta T / \partial \varepsilon_g)_{Kg}$ are essentially *immune* to the FTP. This is an important observation for it means that the associated uncertainties can be calculated on the basis of results obtained for the constant-temperature profile CP i.e. for this estimate the actual FTP (for a given cell-furnace geometry) is not needed.

-Empirically it is found that $(\partial \Delta T / \partial K_g) \varepsilon_g \approx -\Delta T / K_g$, $(\partial \Delta T / \partial \varepsilon_g)_{Kg} \approx 0.5 \cdot \Delta T / \varepsilon_g$ over the temperature range in question for the cell 6ST in combination with any of the furnace-temperature profiles considered.

-A first estimate of the uncertainty $u(\Delta T)$ for a given cell-furnace geometry, 6ST/RP, yields $u(\Delta T) \approx 0.1 \cdot \Delta T$ over the temperature range considered.

-For more precise statements regarding $u(\Delta T)$ the uncertainties in the thermal conductivity $u(K_g)$ of graphite, in the wall emissivity $u(\varepsilon_g)$ and in the furnace-temperature profile $u(\Delta T; \text{FTP})$ still have to be definitively assessed.

-For a given cell geometry ΔT and $u(\Delta T)$ can be minimized by minimizing the thickness d of the backwall of the cavity and the aperture of a diaphragm positioned in front of the cavity to allowable minima.

-When replacing the real furnace-temperature profile RP by its isothermal counterpart CP for the cell 6ST the errors introduced in ΔT would amount to only 3 mK, 1 mK and zero at the eutectic temperatures of Re-C, Pt-C, Co-C, respectively, corresponding with relative errors of 3%, 4% and (virtually) zero in ΔT (92, 25 and 12 mK, respectively) at these temperatures. From this point of view the profile CP would be good enough for generating ΔT as well.

- The uncertainties calculated in ΔT for these eutectics are very small compared to the measured uncertainty for realistic variation in the parameters K_g and ε_g .

FTP: furnace temperature profile, HP: high profile, RP: real profile, CP: constant profile, NF: no furnace, SCK: sensitivity coefficient for thermal conductivity of graphite K_g , and SCE: sensitivity coefficient for the wall emissivity of graphite ε_g .

CHAPTER 7

Uncertainty factors in the temperature drop III: blackbody tube length, backwall thickness and Thermogage furnace temperature profile

Chapter 7. Uncertainty factors in the temperature drop III: Blackbody Tube Length, Back-wall Thickness and Thermogage Furnace Temperature Profile

7.1. Introduction

The temperature drop, and the associated uncertainty, for the following high temperature fixed points (HTFPs), Co-C (1324 °C), Pd-C (1492 °C), Pt-C (1738 °C), Re-C (2474 °C) and WC-C (2749 °C) is estimated, when realized in a Thermogage furnace. The following conditions are modeled:

- Ideal conditions: HTFP in an isothermal furnace at the HTFP temperature.
- Intermediate conditions: HTFP in a furnace that has a sine temperature profile from the centre of the furnace to its aperture.
- Extreme conditions: Furnace has a linear gradient from the centre of the furnace to its aperture.
- Reference conditions: The bare HTFP crucible i.e. not in a furnace. This forms the upper bound of the temperature drop value.

In addition the influence of the thickness of the graphite back-wall on the value of the temperature drop is estimated for the five HTFPs in the reference and ideal conditions. This parameter is often indeterminate due to erosion of the back-wall during filling. The calculations of this effect here enable boundaries to be placed on the effect of back-wall thickness variation on temperature drop.

Due to some variations in the length of the crucibles used by the National Institutes of Metrology, three different cell sizes (30, 40 and 50 mm long) have also been modeled for the five HTFPs in the reference and ideal conditions.

In this chapter how these calculations were performed is described and a summary of the calculations is given. Finally a discussion of the implications of these results for the use of HTFPs as temperature references is given.

7.2. Description of the model

The studies described here are all performed for a Thermogage 24 kW furnace (Fig. 7.1). It has a 24 mm internal diameter graphite tube of 290 mm long and is held between water-cooled copper electrodes and electrically heated by direct current. A detailed description of such a furnace is found in [60].

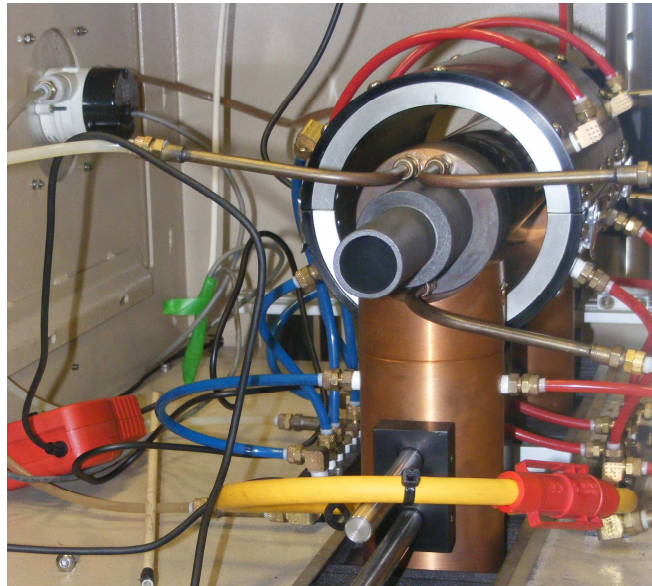


Figure 7.1. Thermogage picture.

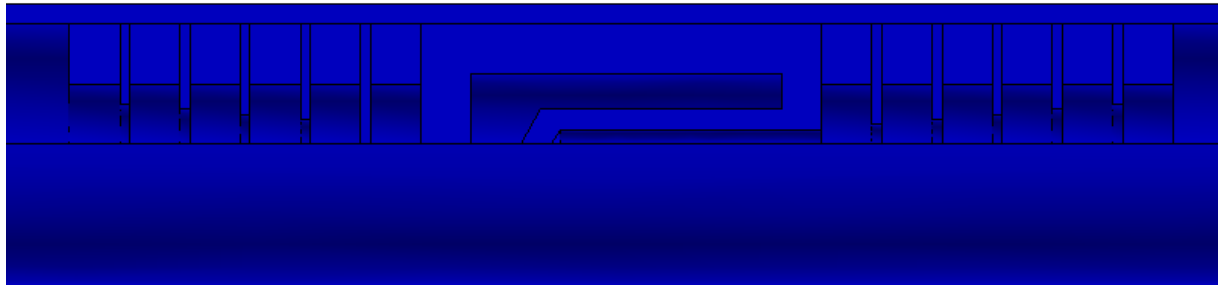


Figure 7.2. Thermogage model, side view.

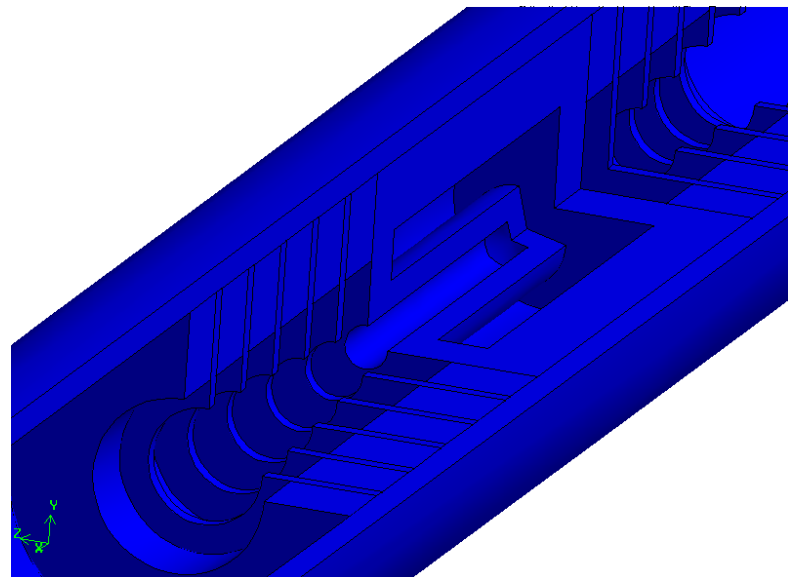


Figure 7.3. Thermogage model, isometric view.

A 2D axisymmetrical model of the tube was constructed (Fig. 7.2 and 7.3) with the following characteristics:

- Geometrical dimensions:

For investigating the effect of the furnace the following configuration was modeled.

- A mark 4 NPL HTFP cell [61] was modeled. The graphite blackbody internal length was 27 mm, the aperture diameter was 3 mm and the back-wall thickness was 2.6 mm, with a 120° back-wall cone. The model was constructed with the HTFP crucible at the middle of the furnace tube, with six graphite foam and five radiation baffle insulation rings at both sides on the crucible. All together this configuration was 110 mm long so the tube continues 90 mm in each direction after the insulation.

In addition for investigating the effect of the variation in back-wall thickness due to erosion and in crucible length the following was modeled.

- The same mark 4 HTFP cell but with five different back-wall thicknesses: 0.1, 1, 2, 2.6 and 4 mm. Two cases were modeled one with the uniform furnace conditions the other a bare mark-4 NPL crucible, without furnace.

To investigate the effect of the length of the blackbody tube lengths, for a given aperture of 3 mm the following configuration was modeled.

- The mark 4 HTFP cell with 2.6 mm back-wall thickness with three different internal lengths: 17, 27 and 37 mm, which corresponds to the external crucible lengths of 30, 40 and 50 mm. They were modeled without furnace and with the uniform furnace conditions.
- Material properties:

Table 7.1 gives the main material properties used in the modeling, the quantities are heat capacity C_p ($\text{J} \cdot \text{kg}^{-1} \cdot \text{K}^{-1}$), thermal conductivity K ($\text{Wm}^{-1} \cdot \text{K}^{-1}$), density d ($\text{kg} \cdot \text{m}^{-3}$), emissivity and melting temperature (K). Thermal conductivity value for graphite decreases with the temperature from $53.6 \text{ Wm}^{-1} \cdot \text{K}^{-1}$ at 1597 K to $32.4 \text{ Wm}^{-1} \cdot \text{K}^{-1}$ at 3022 K [58].

Table 7.1. Thermal properties of furnace materials.

	Cp (J.kg⁻¹.K⁻¹)	K (W.m⁻¹.K⁻¹)	d (kg.m⁻³)	emissivity	melting temperature (K)
Co-C	456	45	7200		1597
Pd-C	244	50	12023		1765
Pt-C	133	50	21450		2011
Re-C	214.5	55	21030		2747
WC-C	200	50	15800		3022
graphite	690	32.4, 36.5, 45.6, 51.1, 53.6	2250	0.86	
foams	370	0.35	50	0.86	
argon	520.64	0.0158	1.6228		

- Model boundary conditions:

Five different HTFP were modeled, each of them in 4 different thermal conditions:

- 1) Reference conditions: The bare crucible with the metal ingot at the nominal temperature of the fixed point and without furnace. The outer wall of the crucible is assumed to be uniform in temperature.
- 2) Extreme conditions: Furnace has a linear gradient from the centre of the furnace to its aperture.
- 3) Intermediate conditions: HTFP in furnace that has a sine temperature profile from the centre of the furnace to its aperture.
- 4) Ideal conditions: HTFP in a uniform furnace at the HTFP temperature.

The furnace temperature profile (FTP) for conditions 2 to 4 can be seen in Fig. 7.4, 7.5 and 7.6.

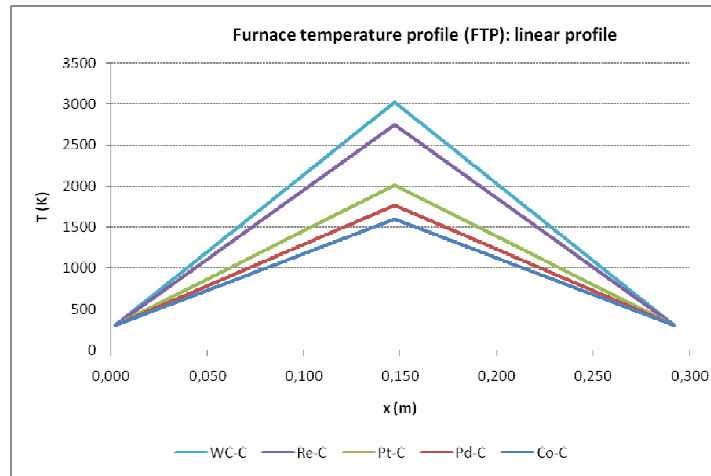


Figure 7.4. Extreme condition: linear furnace temperature profile (LP).

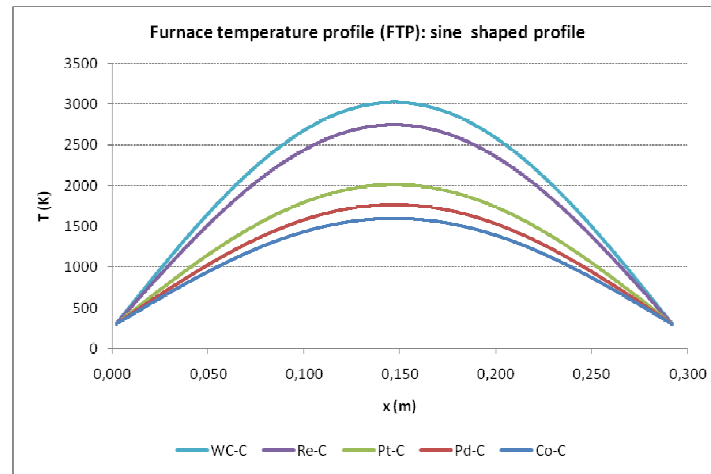


Figure 7.5. Intermediate conditions: Sine shaped furnace temperature profile (sin P).

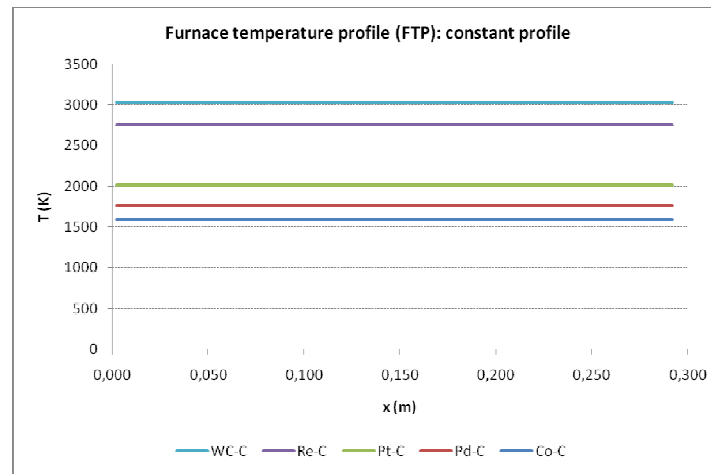


Figure 7.6. Ideal conditions: constant furnace temperature profile (CP).

7.3. Simulation results

7.3.1. Temperature drop

The temperature drop across the back-wall of the cells has been calculated as the difference between the nominal temperature of each HTFP and the areal temperature average for the back-wall. The back-wall thickness of the blackbody cavity for these conditions was taken to be 2.6 mm.

In Table 7.2 the temperature drop for the five fixed points in the four thermal conditions studied are shown.

Table 7.2. Temperature drop (K) for studied fixed points.

Fixed point	bare crucible	linear profile (LP)	Sine profile (sin P)	constant profile (CP)
Co-C	0.022	0.020	0.018	0.017
Pd-C	0.031	0.029	0.027	0.024
Pt-C	0.053	0.047	0.042	0.037
Re-C	0.207	0.173	0.154	0.132
WC-C	0.338	0.273	0.244	0.205

Figure 7.7 displays the temperature drop values given in Table 7.2, i.e. the temperature drop with the furnace conditions and nominal temperature are plotted.

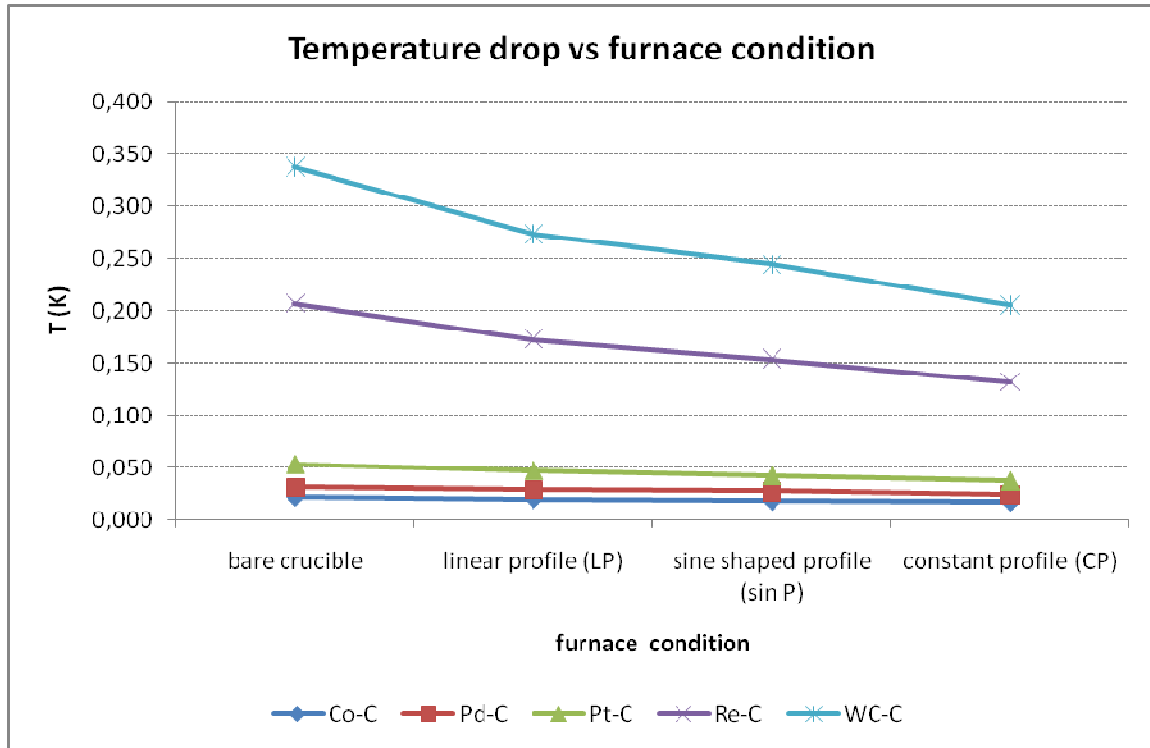


Figure 7.7. Temperature drop variation with the furnace conditions.

7.3.2. Effect of back-wall thickness

In Tables 7.3 and 7.4 the temperature drop for the five fixed points for reference and ideal conditions with five different back-wall thicknesses are given.

Table 7.3. Temperature drop (K) at reference conditions (no furnace) for different back-wall thicknesses.

Fixed point \ backwall thickness (mm)	0.1	1	2	2.6	4
Co-C	0.004	0.015	0.021	0.022	0.041
Pd-C	0.005	0.021	0.030	0.031	0.054
Pt-C	0.01	0.036	0.049	0.053	0.078
Re-C	0.039	0.154	0.199	0.207	0.279
WC-C	0.064	0.253	0.322	0.338	0.455

Table 7.4. Temperature drop (K) at ideal conditions (uniform furnace) for different back-wall thicknesses.

Fixed point \ backwall thickness (mm)	0.1	1	2	2.6	4
Co-C	0.003	0.010	0.016	0.017	0.034
Pd-C	0.004	0.014	0.022	0.024	0.041
Pt-C	0.007	0.023	0.034	0.037	0.056
Re-C	0.026	0.092	0.125	0.132	0.175
WC-C	0.042	0.148	0.198	0.205	0.264

In Fig. 7.8 and 7.9 the curves for the temperature drop variation with back-wall thickness are given.

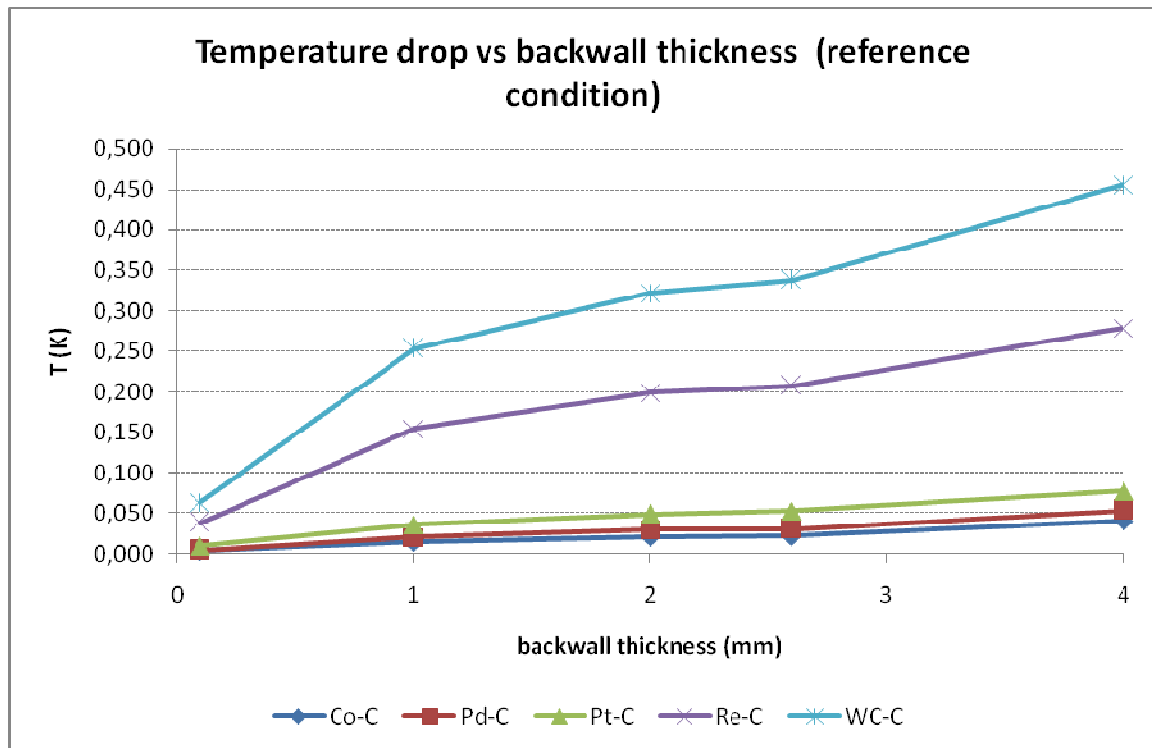


Figure 7.8. Temperature drop variation with back-wall thickness for bare crucible (reference condition).

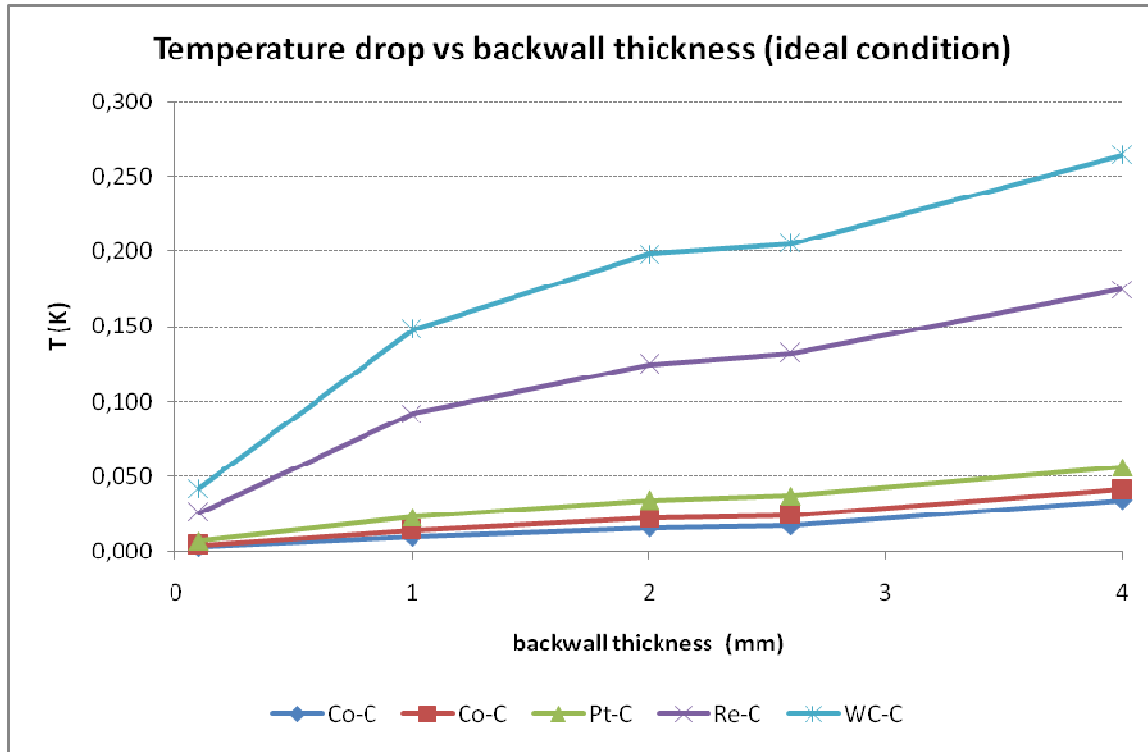


Figure 7.9. Temperature drop variation with the back-wall thickness for ideal conditions (uniform furnace).

7.3.3. Effect of the crucible length

In Tables 7.5 and 7.6 the temperature drop for the five fixed points for reference and ideal conditions with three different crucible lengths are given.

Table 7.5. Temperature drop (K) at reference conditions (no furnace) for different crucible lengths.

Fixed point \ crucible length (mm)	30	40	50
Co-C	0.051	0.022	0.013
Pd-C	0.078	0.031	0.019
Pt-C	0.140	0.053	0.030
Re-C	0.635	0.207	0.102
WC-C	1.085	0.338	0.162

Table 7.6. Temperature drop (K) at ideal conditions (uniform furnace) for different crucible lengths.

Fixed point \ crucible length (mm)	30	40	50
Co-C	0.022	0.017	0.016
Pd-C	0.031	0.024	0.023
Pt-C	0.052	0.037	0.030
Re-C	0.197	0.132	0.092
WC-C	0.322	0.205	0.140

In Fig. 7.10 and 7.11 the curves for the temperature drop variation with crucible length are given.

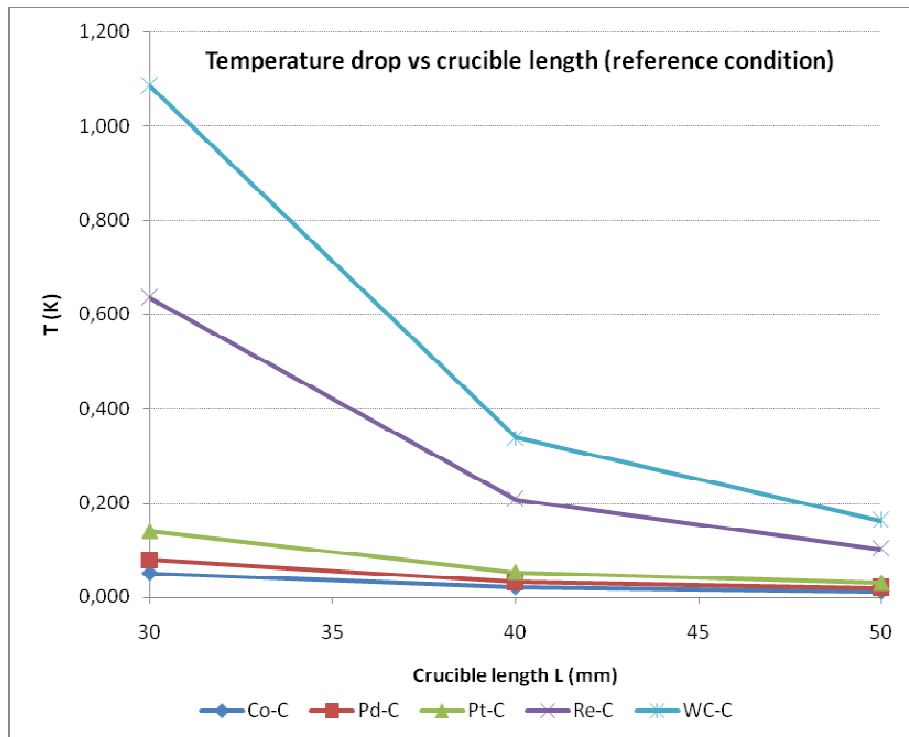


Figure 7.10. Temperature drop variation with crucible length for bare crucible (reference condition).

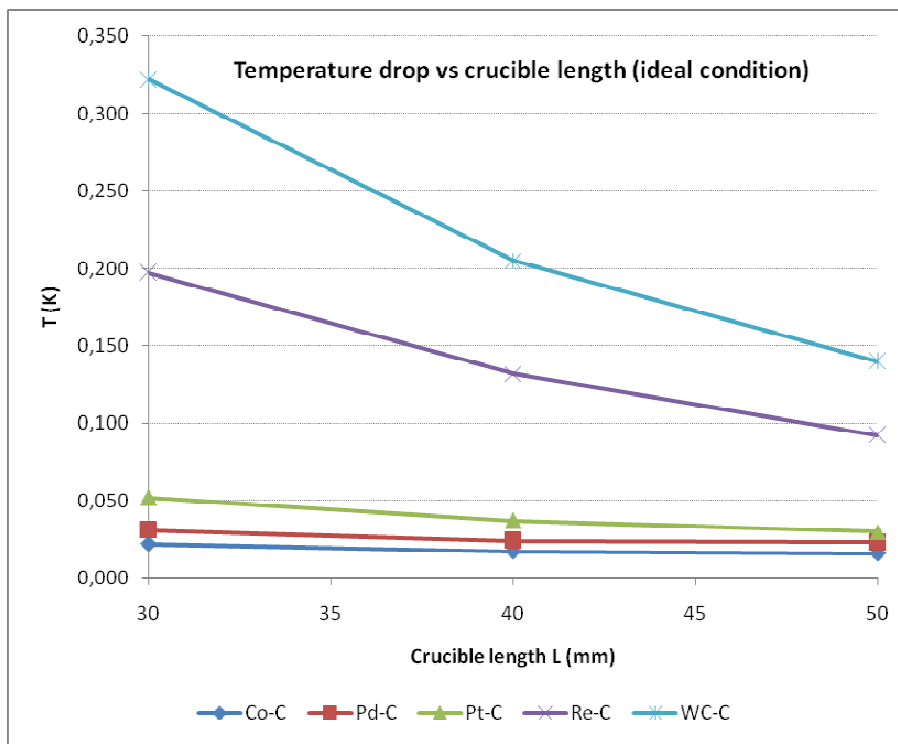


Figure 7.11. Temperature drop variation with crucible length for ideal conditions (uniform furnace).

7.4. Discussion

7.4.1. Furnace conditions

The radiation heat loss increases as the fourth power of the nominal temperature, the upper bound of which is given by theory (equation 7.1) [55]. This form can be used to represent all the data given in Fig. 7.12. This is fitted by the simple power law aT^4 .

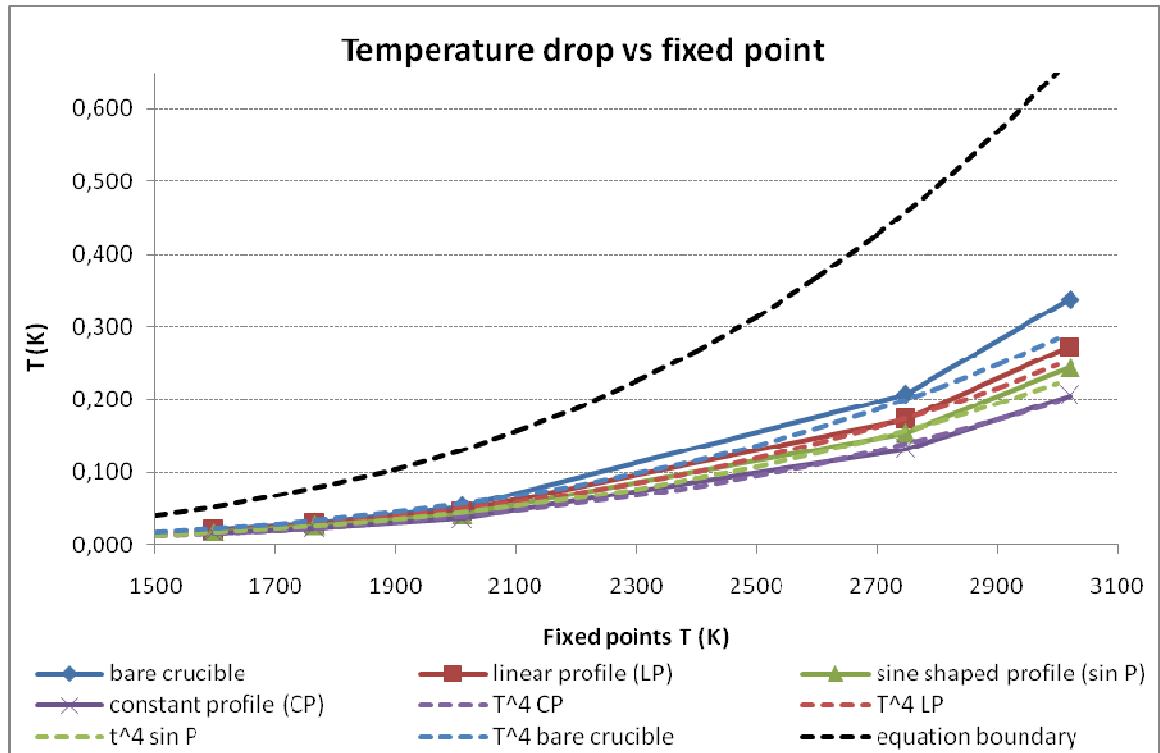
$$\Delta T = \cos \theta \cdot \varepsilon \cdot \sigma \cdot \frac{d}{K} \cdot \left(\frac{r}{L} \right)^2 \cdot T^4 \quad (7.1)$$

The fitted coefficient a of the exponential for the theoretical free radiating cavity and for the four conditions is given in table 7.7:

Table 7.7. Coefficient a of the exponential expression.

Coefficient	Eq.7.1	Bare crucible	Linear profile	Sine profile	Constant profile
a	8.026e-15	3.5e-15	3.05e-15	2.749e-15	2.431e-15

In Fig 7.12, the temperature drop variation with nominal temperature is plotted with the fitted exponential curves (dotted lines) and with the upper boundary given by (eq. 7.1). It is clear that the simple power law aT^4 is a good representation of the modeled data. It is also clear that even a bare crucible does not follow the simple theoretical expression; this is because radiance from the side walls of the cavity make up some of the radiance loss from the back-wall [59]. The various different furnace conditions mitigate to a different extent the effect of radiance loss, this can be characterized by the ratio c , given in Table 7.8 which is the ratio a (*furnace various conditions*) / a (*ideal equation*).

**Figure 7.12.** Temperature drop variation with the nominal temperature and the corresponding exponential curves.

A simple use of equation 7.1 overestimates the correction that needs to be applied for radiance loss by at least a factor of 2 compared to the bare crucible and by larger amounts depending upon furnace conditions. This equation has been used in the past to estimate the temperature drop in uncertainty calculations [62] and this contribution needs to be revised to lower more realistic values to take into account furnace effects.

Table 7.8. Ratio factor for the exponential expression.

Ratio factor	(Eq. 7.1)	Bare crucible	Linear profile	Sine profile	Constant profile
c	1	0.44	0.38	0.34	0.3

Through use of these calculations estimates of the correction for the temperature drop for this design HTFP blackbody can be made. The difference between a constant and linear furnace profile is less than 0.1 indicating that a temperature correction could be made to HTFPs realized in thermogage furnaces with that order of type B contribution to the uncertainty.

7.4.2. Back-wall thickness

The simple theory (equation 7.1) that presupposes a freely radiation back-wall, predicts that the temperature drop should increase linearly with the back-wall thickness d , but as can be shown in Fig 7.8 and 7.9, the back-wall thickness influence is greater than this for the first 2 mm. This is probably due to gridding problems which appear when the back-wall becomes thinner (0.1 and 1 mm) and the number of nodes and also the accuracy of the model decrease.

The standard uncertainty associated to back-wall thickness $u(\Delta T; d)$ can be expressed as:

$$u(\Delta T; d) = (\delta T / \delta d) \cdot u(d) \quad (7.2)$$

The sensitivity coefficient $\delta T / \delta d$ can be approximated to:

$$\delta T / \delta d = \Delta T / d \quad (7.3)$$

And the standard back-wall thickness variation for different crucible configurations $u(d)$ can be estimated as $u(d) \approx 0.5 \text{ mm}$.

With these approximations the standard uncertainty $u(\Delta T; d)$ expressed in K for the ideal conditions is shown in Table 7.9. Similar studies for the variation in the wall emissivity and the thermal conductivity of the graphite cell are given in [61].

Table 7.9. Standard uncertainty $u(\Delta T; d)$ expressed in K for the ideal conditions.

	Co-C	Pd-C	Pt-C	Re-C	WC-C
$\Delta T / \delta d (\text{K/mm})$	0.013	0.017	0.028	0.102	0.162
$u(\Delta T; d) (\text{K})$	0.006	0.008	0.014	0.051	0.081
$u(\Delta T; d) / \Delta T$	0.399	0.386	0.407	0.409	0.416

7.4.3. Crucible length

The simple theory (equation 7.1) predicts that the radiation heat loss decreases as the second power of the internal length of the radiation cavity. As can be seen in Fig. 7.10 and 7.11 this behavior is well represented by the model and the simple equation gives again an upper boundary.

The standard uncertainty associated to the crucible length $u(\Delta T; L)$ can be expressed as:

$$u(\Delta T; L) = (\delta T / \delta L) \cdot u(L) \quad (7.4)$$

The sensitivity coefficient $\delta T / \delta L$ can be approximated to:

$$\delta T / \delta L = \Delta T / L \quad (7.5)$$

And the standard crucible length variation for different crucible configurations $u(L)$ can be estimated as $u(L) \approx 10 \text{ mm}$.

With these approximations the standard uncertainty $u(\Delta T; L)$ expressed in K for the ideal conditions is shown in Table 7.10.

Table 7.10. Standard uncertainty $u(\Delta T; L)$ expressed in K for the ideal conditions.

	Co-C	Pd-C	Pt-C	Re-C	WC-C
$\Delta T / \delta L (\text{K/m})$	0.788	1.111	1.747	6.324	10.106
$u(\Delta T; L) (\text{K})$	0.008	0.011	0.017	0.063	0.101
$u(\Delta T; L) / \Delta T$	0.436	0.435	0.463	0.495	0.510

This influence is especially important for Re-C and WC-C which reduce their losses by a half from 30 mm to 50 mm crucible long for the ideal conditions. However it should be noted that the uncertainty here is a large over estimate as the length of the blackbody crucible is likely to be known to within a millimeter. This would reduce the uncertainties by a very significant factor (>10) rendering the variation due to blackbody tube length negligible.

7.4.4. Graphic data presentation

As a graphic resume of these different influences in the heat losses, curves of the temperature drop with nominal temperature for different furnace conditions (Fig 7.13), for different back-wall thicknesses (Fig 7.14 and 7.15) and for different crucible lengths (Fig 7.16 and 7.17) are plotted.

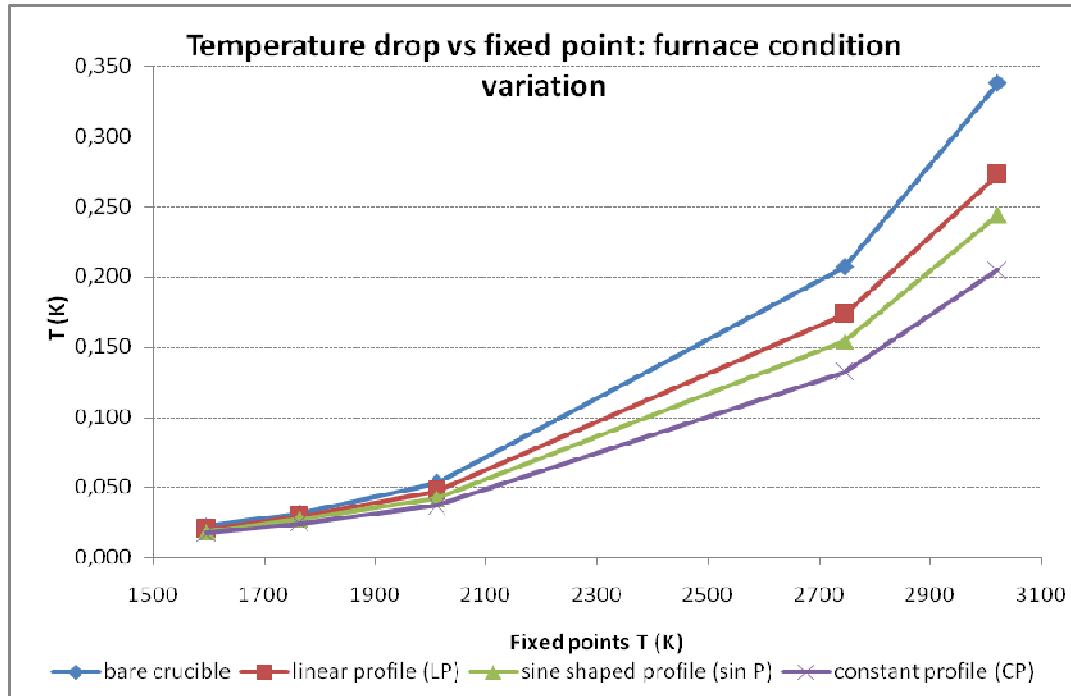


Figure 7.13. Temperature drop variation with the nominal temperature for different furnace conditions.

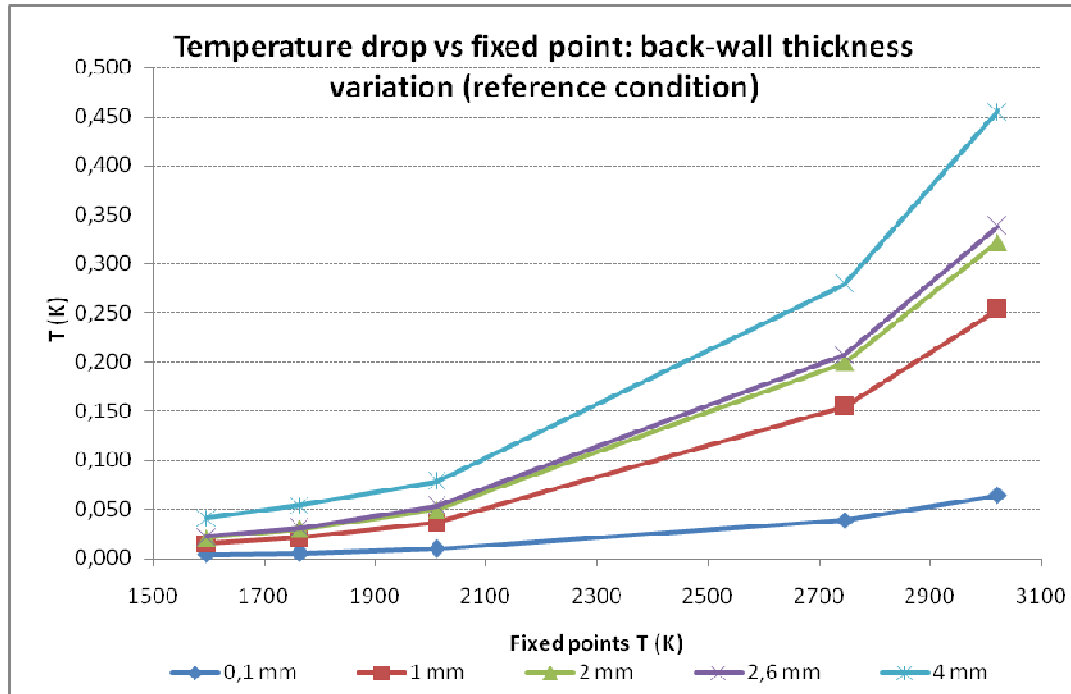


Figure 7.14. Temperature drop variation with the nominal temperature for different back-wall thicknesses at reference conditions.

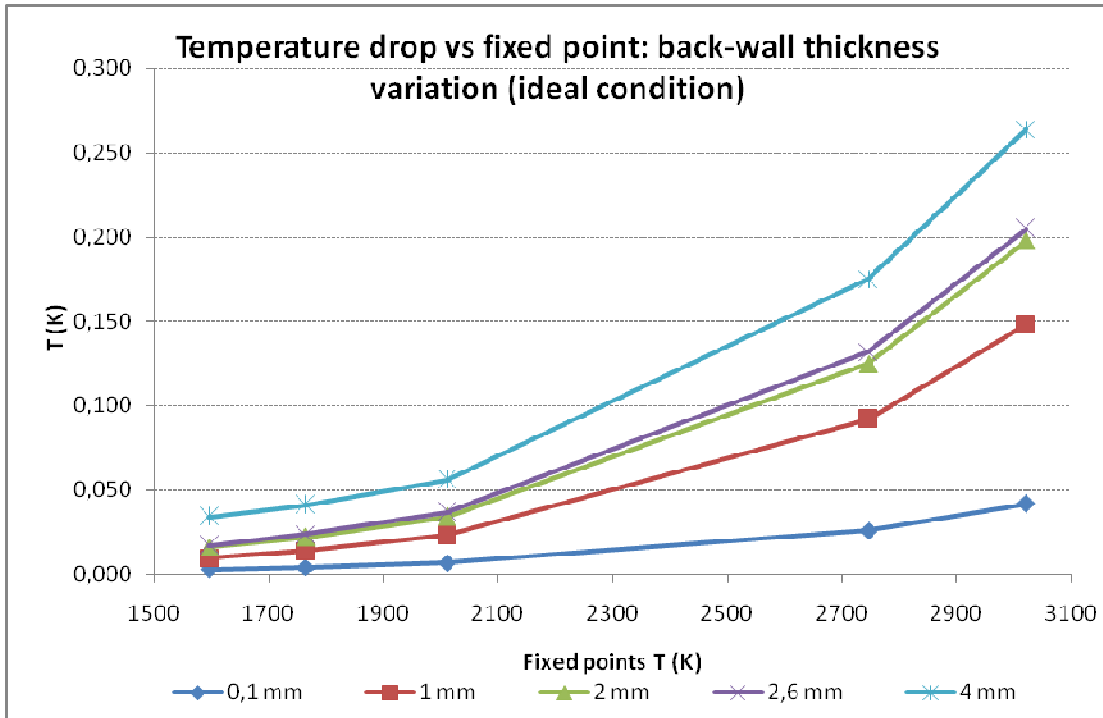


Figure 7.15. Temperature drop variation with the nominal temperature for different back-wall thicknesses at ideal conditions.

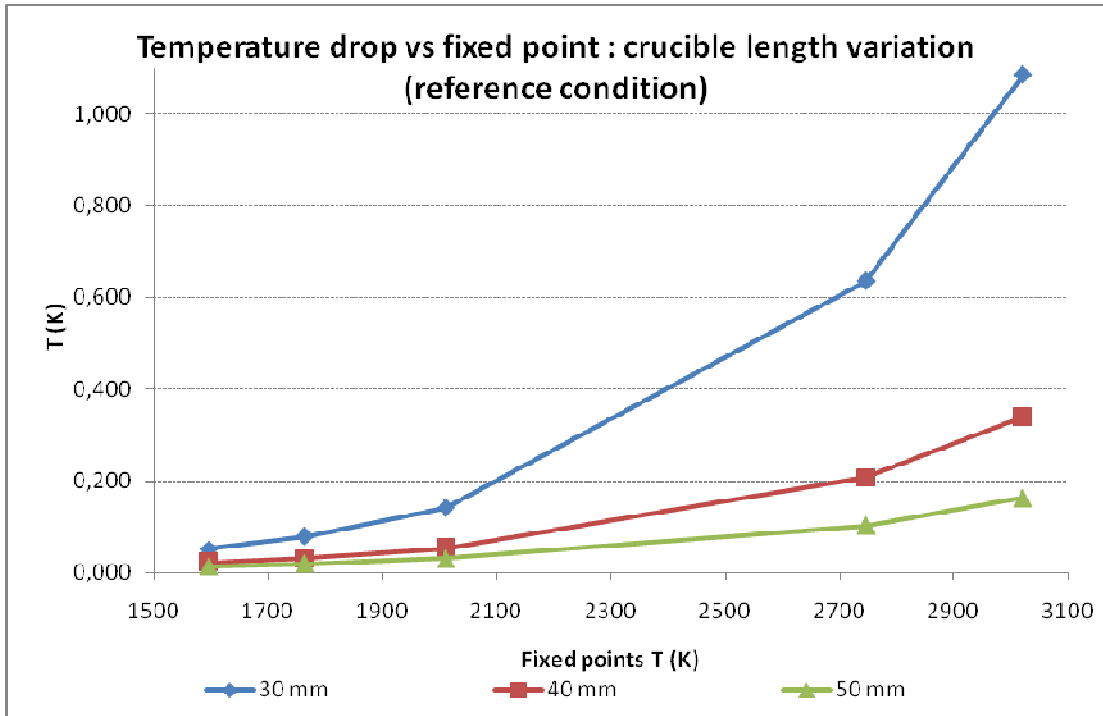


Figure 7.16. Temperature drop variation with the nominal temperature for different crucible length at reference conditions.

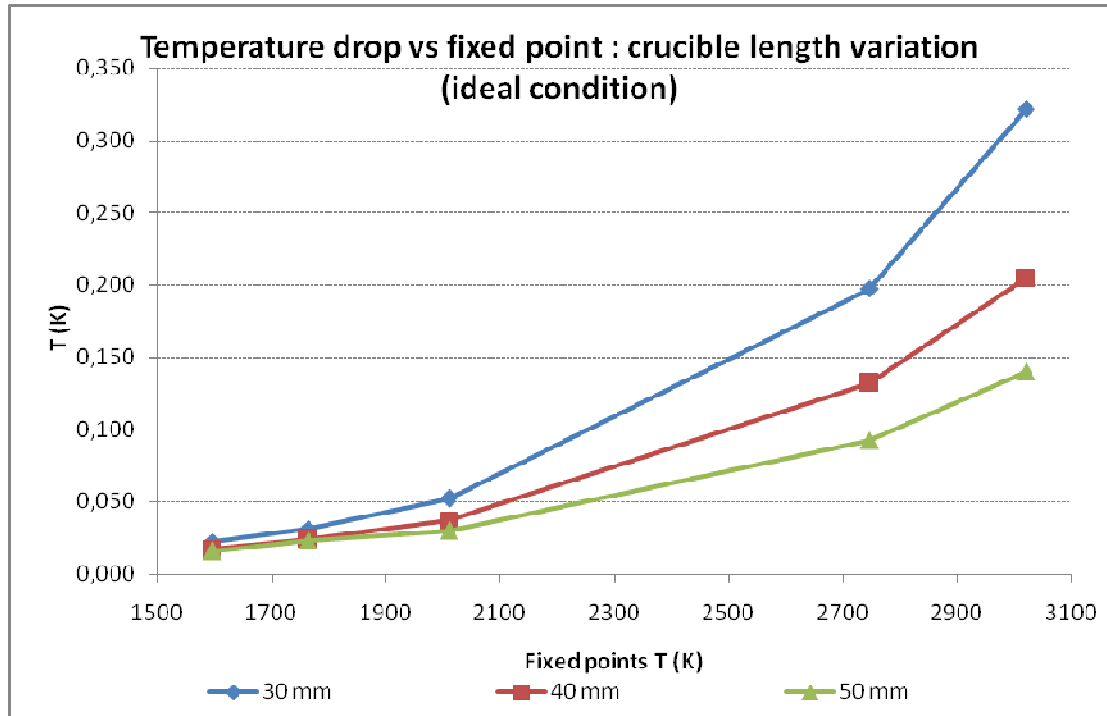


Figure 7.17. Temperature drop variation with the nominal temperature for different crucible length at ideal conditions.

7.5. Conclusions

Temperature drop: Influence of furnace temperature profile:

It is clear that the furnace temperature profile has an influence on the temperature drop of the back-wall which nominally increases as the fourth power of the nominal temperature of the HTFP. This influence can be compared with the theoretical equation for the temperature drop of a freely radiating back-wall which gives the upper bound of radiance loss. Using the model results given here a reasonable correction can be made and uncertainty estimated for the temperature drop for a HTFP blackbody of similar design to those considered here. If a different furnace is used then to ensure all possibilities are covered the range of values should be widened from the bare furnace to the uniform furnace. The average value could be used as the

correction, with the difference used as the estimate of the type B standard uncertainty, i.e. the calculated difference divided by $2\sqrt{3}$.

Temperature drop: Influence of back-wall thickness:

The uncertainty associated with uncertainty in the back-wall thickness, which could vary significantly due to erosion, can be expressed to a first approximation as $u(\Delta T; d) \approx 0.4\Delta T$. Alternatively one could estimate a loss of say 1 mm of graphite from the back wall during the filling process and use Fig. 7.14 and Fig. 7.15 to estimate the likely change in temperature drop due to this erosion and estimate the uncertainty accordingly.

Temperature drop: Influence of blackbody tube length:

The blackbody tube length has a strong influence in the temperature drop of the higher temperature fixed points even for the constant furnace profile. Use of longer crucibles for these fixed points would be the easiest way to reduce the heat losses to acceptable values. Of course this would have to be within the bounds of the length of the uniform zone of the furnace. If the uncertainty in blackbody tube length is not known then an upper bound estimate of the uncertainty associated with the variation in blackbody tube length is given approximately by $u(\Delta T; L) \approx 0.47\Delta T$. Alternatively if the tube length is well constrained, as is often the case, the values given in Fig. 7.16 and Fig. 7.17 could be used to estimate by interpolation the variation in temperature drop due to uncertainty in blackbody tube length.

CHAPTER 8

**Thermal modelling of the
eutectic fixed points Co-C,
Pt-C and Re-C as input for
the determination of the
cavity effective emissivity**

Chapter 8. Thermal Modelling of the Eutectic Fixed Points Co-C, Pt-C and Re-C as Input for the Determination of the Effective Cavity Emissivity¹

8.1. Introduction

In previous chapters this thesis has focused on the following aspects of uncertainty in the realisation of HTFPs: imperfectly formed metal-ingots [64], the values of emissivity and thermal conductivity of graphite, the blackbody tube length and the back-wall thickness or the use of different furnaces and temperature profiles [65].

Here in this chapter the thermal modelling is used as input for the determination of the blackbody cavity spectral effective emissivities for Co-C, Pt-C and Re-C at two different wavelengths. These spectral effective emissivities are influenced by the reflective properties of the graphite from which the cavity is constructed, the temperature distribution within the blackbody and also the radiation-shield structure in front of the cavity.

The determination of these effective emissivities takes 7 steps in total, involving reflectance measurements on representative graphite samples (steps 1 to 3), angle dependent emittance measurements, furnace-temperature profile measurements, calculations of temperature distributions by thermal modelling, and, finally, based upon this information, calculation of the cavity-emissivity dependencies.

Section 8.2 elaborates on the thermal modelling. Modelling of the various systems considered is performed using FLUENT (this software is described in chapter 3).

Section 8.3 shows the results obtained thus far and these are discussed in Section 8.4.

¹ The direct contribution of the work reported in this thesis is given in section 8.2. The rest of the chapter is research done by NIM, NIST and NMJ/AIST [63]. However the work is included here in order to show the modelling studies carried out in the thesis in the perspective of the global research in HTFP. Also the modelling described here played a key role in data interpretation and application. The complete data and further explanations can be found in annex III.

8.2. Thermal modelling of the temperature distributions within the cavity

Thermal modelling is used to estimate the temperature distribution inside the blackbody cavity, which include the temperature profile inside the furnace walls, along the fixed point blackbody tube and in the back-wall of the crucible.

Several assumptions were necessary in order to simplify the problem of calculating these temperature distributions: 1) the model geometry is considered axisymmetric□this allows a 2D model to be constructed□2) the thermal resistance at contacting elements or screw parts is neglected because of its relatively small influence and the difficulty of estimating it□3) heat transfer due to convection and conduction by the furnace gas has been taken into account, but these turned out to be negligible□and 4) the model assumes steady-state conditions.

A 3D cross-sectional view of the cavity structure is shown in figure 8.1. The paired numbers represent the locations in mm along, and perpendicular to, the primary (X) axis, respectively.

- FTP: start point (31.5;13.5), end point (126.5;9)
- X axis inside furnace: start point (2.3;0), end point (126.5;0)
- Cavity aperture: start point (36.5;0), end point (36.5;1.5)
- Backwall: start point (2.3;0), end point (3.17;1.5)
- Sidewall: start point (3.17;1.5), end point (36.5;1.5)
- Internal furnace wall: start point (36.5;1.5), end point (126.5;9)

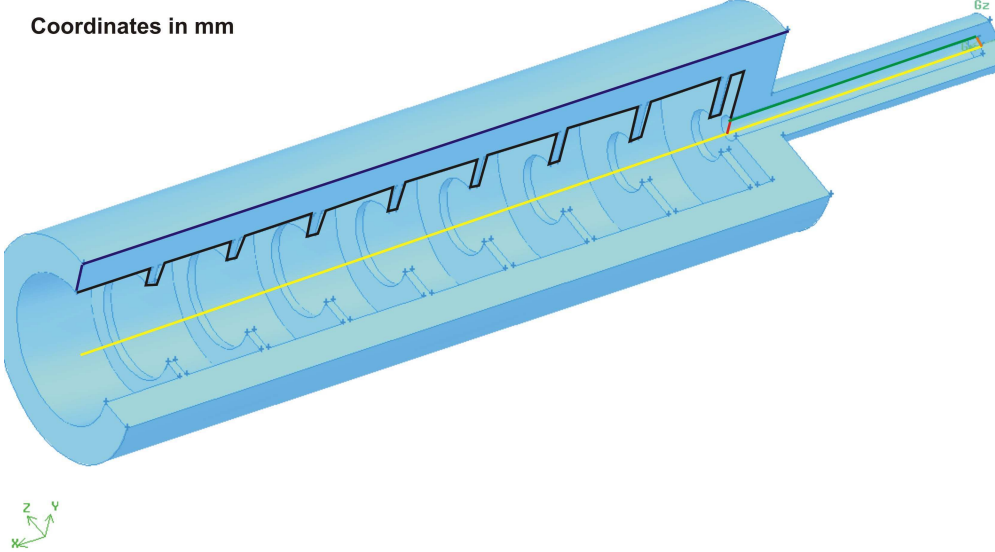


Figure 8.1. 3D cross-sectional view of the cavity structure including the eight furnace baffles at the front of the blackbody tube. These are used to present a uniform temperature field to the smaller fixed point crucible section at the far right.

The thermal conductivity of graphite as a function of temperature over the range of interest is taken from reference [58]. From this the values 53.6, 45.6, 36.5 in $\text{Wm}^{-1}\text{K}^{-1}$ at the fixed point temperatures of the eutectics Co-C(1597 K), Pt-C (2011 K), Re-C (2747 K), respectively, are derived. The emissivity of graphite, quoted nominally as 0.86, is taken from reference [55].

Furnace-temperature profiles, carried by the eight radiation shields placed ahead of the cell are measured by NMIIJ using radiation thermometry at the Co-C, Pt-C and Re-C eutectic fixed points. These measurements have been reported earlier in chapter 6 as real profile (RP). The cell and furnace modeled are the same described in chapter 6, a type 6ST cell inside the Nagano VR10-A23 furnace model, both designed by NMIIJ. The temperature between the measured points is then interpolated and the profile is introduced as a contour condition of the model on the external wall of the blackbody tube facilitating the modelling of the cavity temperature distributions. Then, the temperature distribution inside the furnace and the temperature profiles of the inner walls of the crucible (figure 8.2) are calculated. The model simulates the end of the melting process in an idealized fashion, i.e. the temperature all over the outside of the cavity wall which is in contact with the metal is set to the eutectic temperature, and obviates the need of implementing the ingot in the modelling.

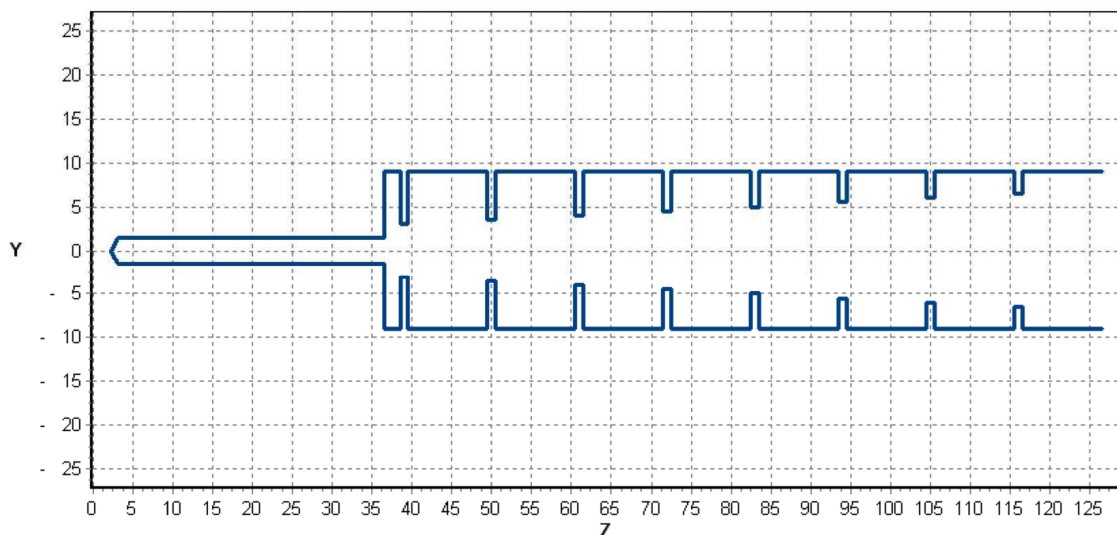


Figure 8.2. Inner walls of the crucible and furnace (coordinates in mm).

The resulting temperature profiles of the inner walls are shown in figure 8.3 (a) and (b) in both absolute and relative terms, respectively. A graphic distribution of temperature inside the furnace for Re-C is shown in figure 8.4. These results are used for the radiance calculations in the next section.

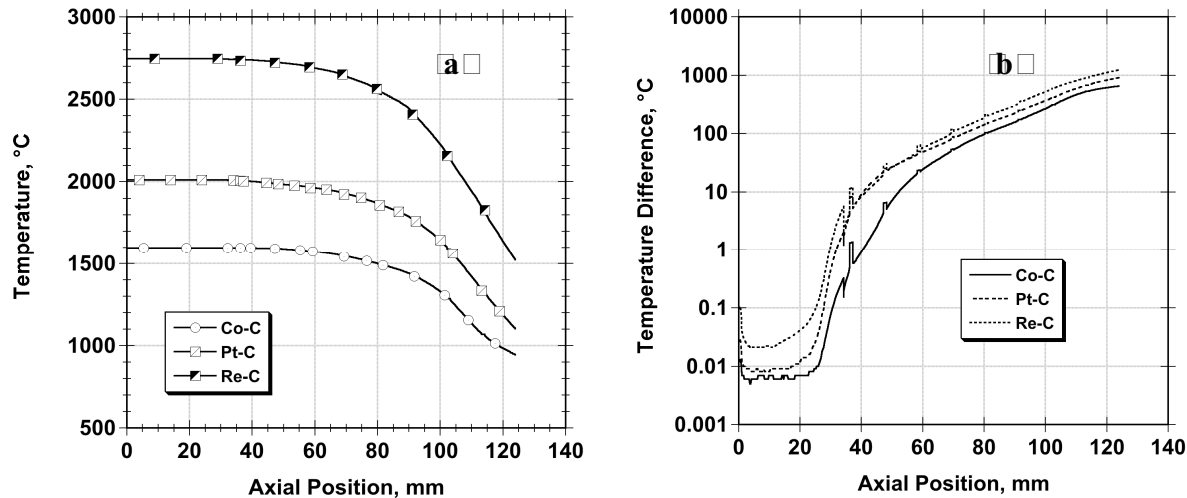


Figure 8.3. (a) Calculated temperature profiles along the fixed-point crucible and furnace (shown in figure 8.1) for the three carbon eutectics. (b) The same profiles shown in terms of the temperature difference relative to the crucible apex temperature.

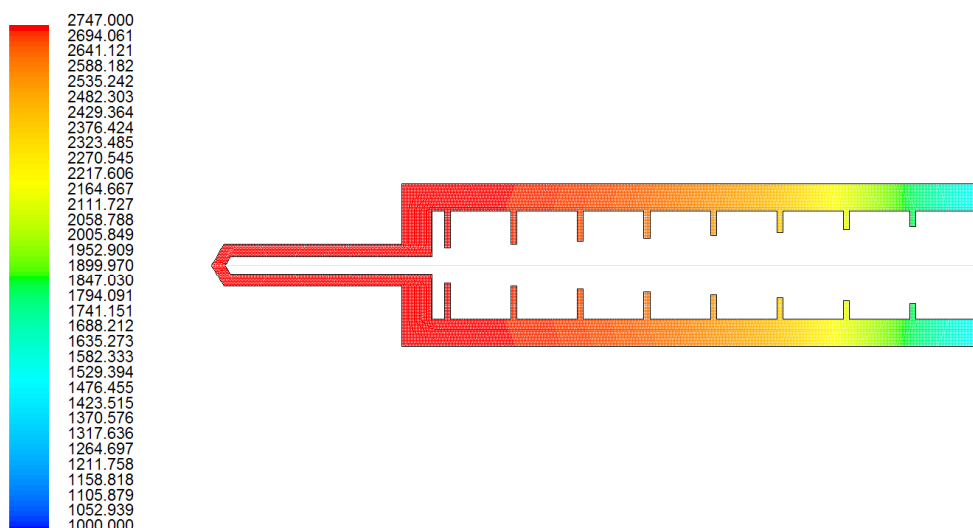


Figure 8.4. Distribution of temperature inside the furnace for Re-C eutectic point.

8.3. Attained results of effective emissivity and radiance temperature from the thermal modelling

A multipurpose custom-developed Monte Carlo ray-trace program has been employed by Hanssen et al. [63] to determine various radiance parameters on the cavity structure shown in figure 8.1, with the temperature distribution calculated in section 8.2 as input. It assumes and incorporates the effects of ambient radiation as an isotropic perfectly black background having temperature T_{bg} (assumed to be 300 K). It can take spectral (wavelength dependent) cavity surface reflectance or surface emittance as input and can produce spectrally dependent cavity emissivity, radiance and radiance temperature as output.

A detailed explanation of the Monte Carlo method used and the measurement of the graphite optical properties can be found in [63], as part of the research done by NIM, NIST and NMIJ/AIST in collaboration with Valladolid University and included in annex III of this thesis.

Since the actual emittance of the graphite surface in the crucibles and furnaces during operation are not well known at this point in the study a range of values for the emissivity were applied to the modeled system to understand the influence of this parameter.

The graphite emissivity values were 0.7, 0.8 and 1.0 (to show the ideal blackbody case for comparison). The results are for these three emissivity values for two different wavelengths, 405 nm and 650 nm, and for the isothermal graphite case. In figures 8.5 (a), (c) and (e), the calculated radiance temperatures of the Co-C, Pt-C and Re-C crucibles are shown. The radiance temperature for emissivity value of 1 doesn't change with the wavelength but for 0.7 and 0.8 emissivity values the radiance temperature decreases with the wavelength. Also the radiance temperature is lower as the value of emissivity decrease. The calculated effective emissivities corresponding to Co-C, Pt-C and Re-C crucibles respectively, are shown in figures 8.5 (b), (d) and (f), including data for both isothermal cavities as well as for ones with temperature distributions calculated by thermal modelling and shown in figure 8.3.

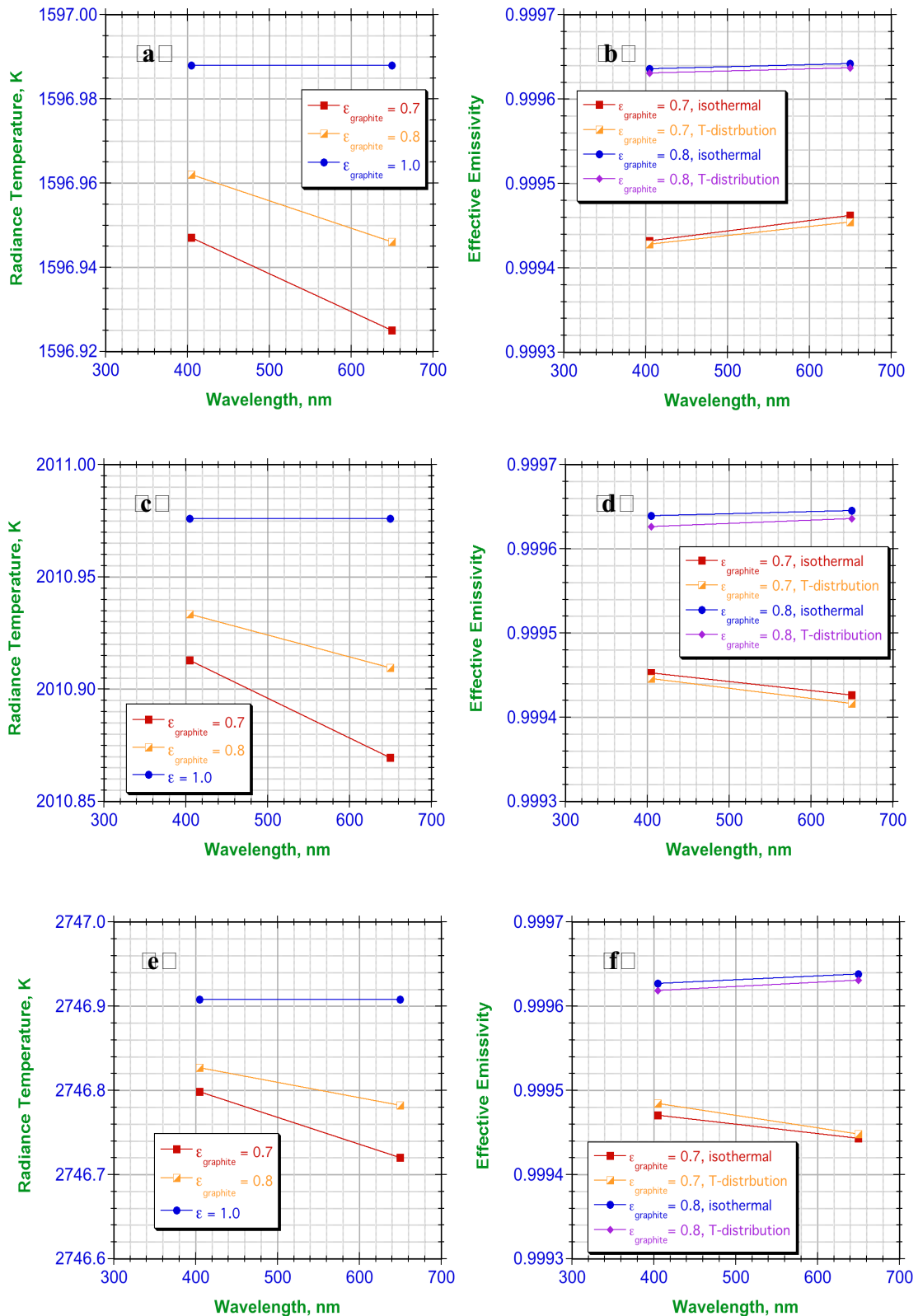


Figure 8.5. Radiance temperature (a, c, e) and effective emissivity (b, d, f) dependence on graphite emissivity and wavelength of the graphite fixed point cavities near the melting points of Co-C (a, b), Pt-C (c, d) and Re-C (e, f).

As can be seen in figures 8.5 (b), (d) and (f), there is almost no effect of the calculated non-isothermal temperature distributions on the cavity emissivities. Conversely, the results show that the furnace design yields a sufficient approximation to isothermality, provided the graphite reflectance is Lambertian, i.e., the surface exitance of graphite is isotropic. Effective emissivity has also a very slight variation with the wavelength for the three fixed points and it seems that the influence of the wavelength is higher for the lower values of graphite emissivity.

8.4. Summary and conclusions

This work, which is currently in progress, seeks to establish effective emissivity values, with minimal uncertainties, for fixed-point blackbody cavities using the eutectics Co-C, Pt-C and Re-C. The temperature distribution within one cavity design optimized for and presently employed in the operation of existing eutectic blackbodies [61] has been studied by measurement and modelling.

The temperature distributions, have, in turn, been used as input data to examine the potential variability of the cavity effective emissivity due to the temperature distributions and the graphite reflectance characteristics. Simulating the graphite with Lambertian reflectance, the modelling results indicate that a realistic non-uniform cavity temperature results only in a small change in the cavity effective emissivity.

CHAPTER 9

Investigation of influence parameters for a contact thermometry HTFP cell



Chapter 9. Investigation of Influence Parameters for a Contact Thermometry HTFP Cell

9.1. Introduction

The technique used for the measurement of high temperature fixed points has an influence in the melting plateau shape and to some extent on the nominal temperature measured [66]. With regards to modelling an uncertainty in the values of some of the thermo-physical properties of the eutectic material has also an influence in the estimated temperature drop and melting duration.

In previous chapters the emphasis has been on investigating HTFP cells for radiation thermometry applications, here the study will be for HTFPs for contact thermometry. In particular a Co-C cell [67] is modeled and the differences between the temperature measured by a thermocouple and that by a radiation thermometer are studied. A parametric study for density, viscosity, latent heat and melting range values for Co-C, again with the emphasis on contact thermometry applications, is also made.

9.2. Description of the model

The HTFP investigated in this study is that of the Laboratoire National D'Essais (LNE) and it is one used for contact and radiation thermometry. The geometry can be seen in figure 9.1.

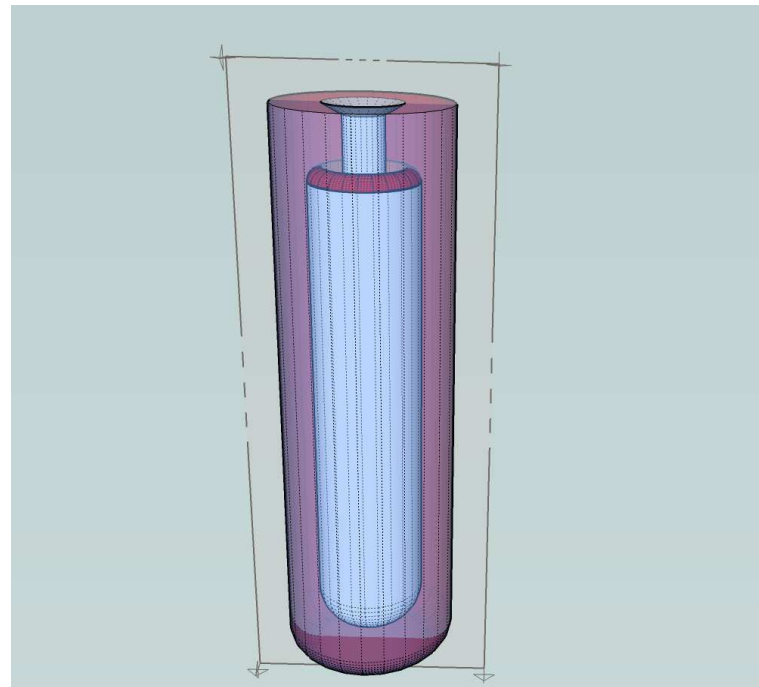


Figure 9.1. Schematic diagram of the LNE cell

The cell is 125 mm in height, with 36 mm and 8 mm external and internal (thermometer well) diameters.

The material properties used in the simulation are given in table 9.1.

Table 9.1. Material properties.

Materials	Properties			
	Thermal conductivity (W.m ⁻¹ .K ⁻¹)	Density (Kg.m ⁻³)	Specific heat (J.Kg ⁻¹ K ⁻¹)	Emissivity
Cobalt molecular weight (59) Enthalpy 16.19 kJ/mol	45 (solid and liquid)	7200 (1324°C)	456 at 25°C	/
Alumina	6.08	3900	1300	0.4
Platinum	92	21090	170	0.19
Graphite SGL	36	1870	2012	0.86

The thermal conditions imposed in the simulation are:

- Crucible outer wall temperature set at 16°C above the melting temperature.
- Melting temperature of Co-C: 1324 °C.
- Temperature distribution along the thermocouple sheath is so that the temperature of the sheath becomes equal to the temperature of the furnace at 100 mm away from the tip of the thermocouple. This situation corresponds approximately to experimental observations.

To determine the upper boundary of the effect the simulation is performed with no furnace in place.

9.3. Simulation results

In order to study the differences in the melting behaviour using contact and non contact thermometry, the same melting process has been simulated in two conditions:

- 1) With a thermocouple inside the cell. For purposes of the model the simulated temperature is that at the tip of the thermocouple, which is situated 5 mm away of the radiation back-wall.
- 2) With a radiation thermometer focused on the back-wall of the cell. The areal average of the back-wall temperature is taken to represent the temperature measured by the radiation thermometer.

The two conditions are simulated with axisymmetrical 2D models as can be seen in figures 9.2 and 9.3.

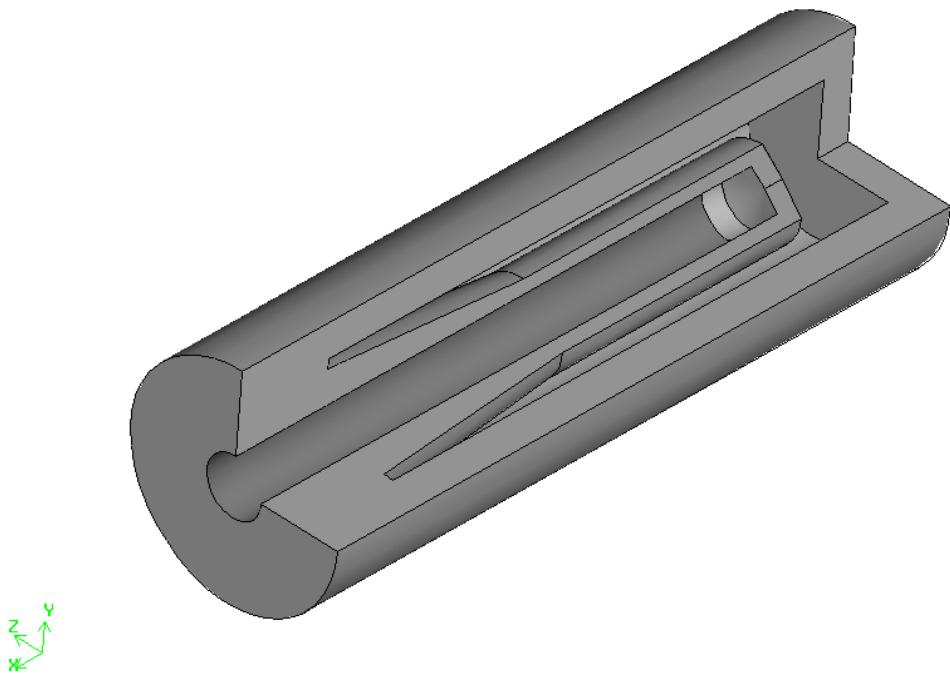


Figure 9.2. Co-C cell model for radiation thermometry simulation.

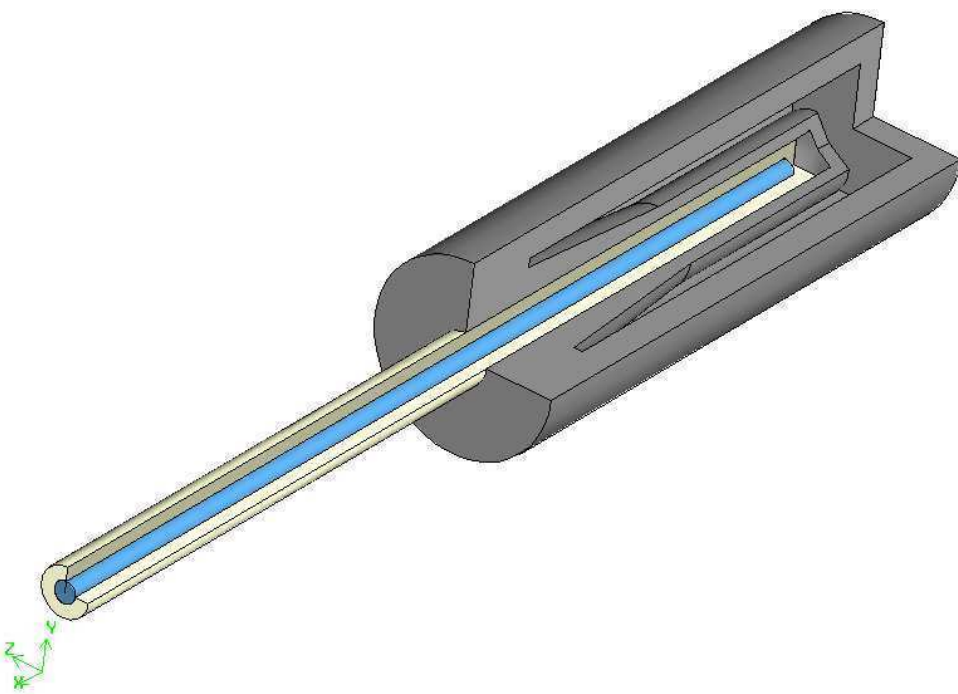


Figure 9.3. Co-C cell model for thermocouple thermometry simulation.

The melting process has to be modelled incorporating time dependency. The preliminary investigation that needs to be performed is a parametric study of the influence variables in the time duration process, these relate to the thermal properties of Co-C density, viscosity, latent heat and melting range.

Parametric study of the influence variables:

According to the difficulties of obtaining accurate data for all these variables at high temperatures, a range of values are taken (table 9.2).

Table 9.2. Range of properties values.

Property	range	Unit
Density	7200-8000	Kg.m ⁻³
Viscosity	0.005-100	Kg.m ^{-1.s⁻¹}
latent heat	674.267-2697.070	KJ.Kg ⁻¹
Melting frame	0.1-1	K

The results show that the melting time is influenced by density, latent heat and melting range but viscosity has no representative influence.

a) Co-C density: Density has a significant influence on the duration of the melting plateau, as can be seen in figure 9.4. This dependence is meant to be linear as an increase in the alloy density at constant volume (the same crucible is used in all the simulations) results in a direct increase in the alloy mass. While Q, the amount of energy absorbed during the change of phase, can be expressed as,

$$Q=m \cdot L \quad (9.1)$$

Where m is the mass of the melted ingot and L is the latent heat of the alloy. If the latent heat is constant, the amount of energy needed to melt the ingot will increase in the same way as mass does and so the time spent in the process.

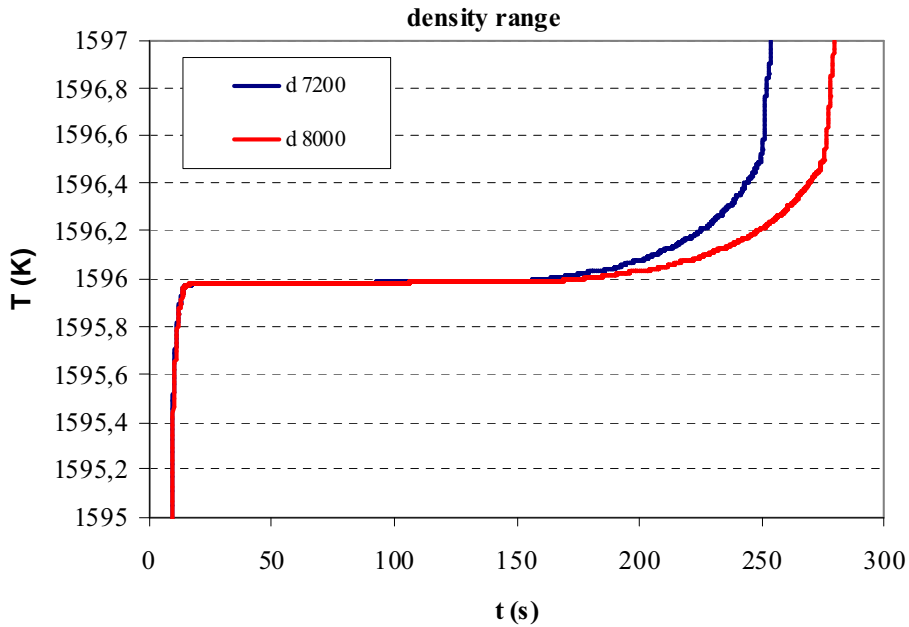


Figure 9.4. Co-C melting plateau for density value variation. Density units Kg.m^{-3}

b) Co-C latent heat: The model results indicate a linear dependence with the value of latent heat. The physical explanation for this dependence is related to the same equation 9.1. In this case, mass doesn't change so if the latent heat increases, the amount of energy needed to melt the ingot will increase in the relation and so the time. Figure 9.5 shows this influence.

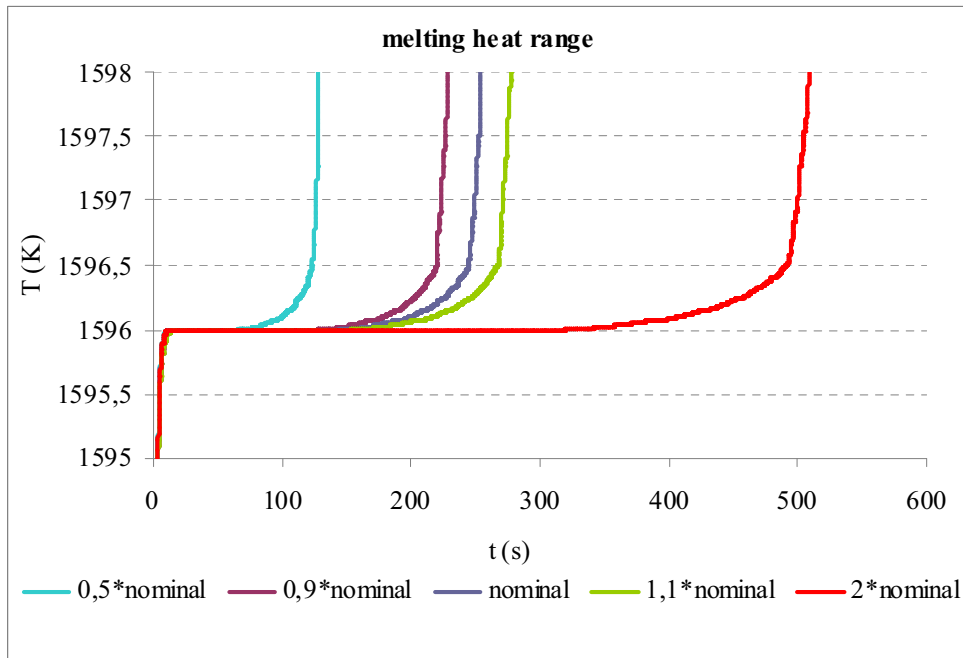


Figure 9.5. Co-C melting plateau duration for latent heat value variation. The nominal value for the latent heat is $1348.535 \text{ KJ.Kg}^{-1}$

c) Co-C melting temperature range: This is more a theoretical result rather than a real one because the melting temperature range is an input of the model which configures immediately the shape of the melting plateau. This is the reason of the differences in figure 9.6 and it would not be expected to see such a range of values in practice.

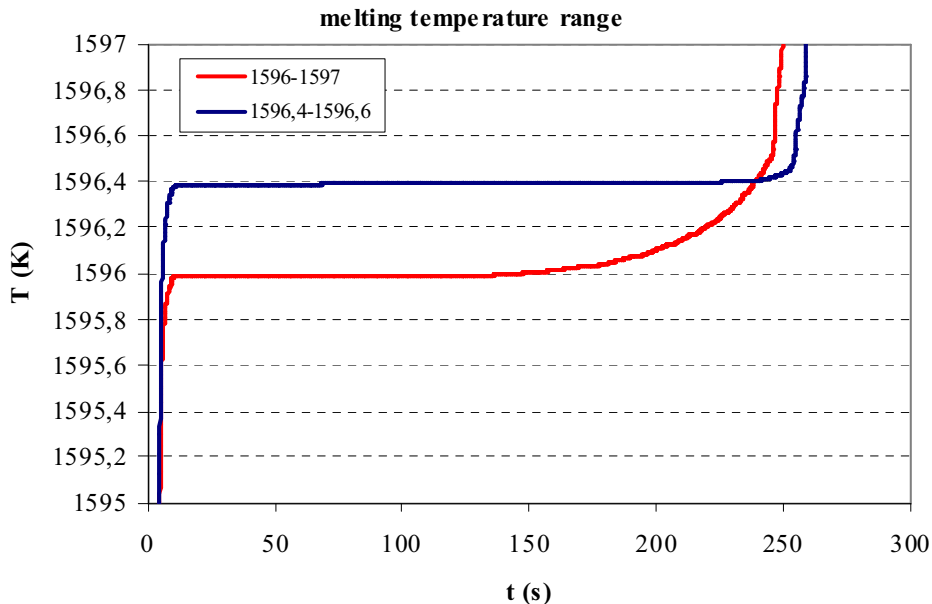


Figure 9.6. Co-C melting plateau for melting temperature range variation.

Comparison between the two measurement methods, thermocouple and radiation thermometer:

Both measurement techniques have specific physical characteristics which affect in different way the temperature measured during the melting plateau.

The radiation thermometers generally used in National Measurement Institutes have very sharply defined focus. They generally focus on the front aperture of the cavity with a spot size of 1 mm from approximately 1 m distance. When a simple geometric calculation is done what the radiation thermometer actually samples is a part of the back-wall only.

Thermocouples work in a very different way. The thermo-voltage is generated by the temperature gradient along the thermocouple so the measurement is affected by a higher region inside the crucible.

Not only the different measurement region affects the nominal temperature measured, also the way that heat flux inside the crucible and environment occurs.

With the radiation thermometer, the radiation heat transfer is directly influenced by the environment because the back-wall is seeing the outside. In the other case, the thermocouple is blocking the radiation to go outside the furnace and the thermocouple sheath is affected by both radiation inside the furnace and conduction from the crucible walls in contact with the thermocouple.

These are the main reasons why it is expected to see that the thermocouple measurement is different from the radiation thermometer one. The question is if the heat loss by radiance (temperature drop) exceeds the heat loss by conduction (up the thermocouple sheath) in which case the radiation thermometer would measure lower temperatures than the thermocouple method. This effect is supposed to increase with the nominal temperature as radiation losses increase with the fourth power of temperature but conduction has a linear behaviour.

The main result obtained in the simulated comparison between the two measurement methods is that the difference in the melting point temperature is only about 25 mK. In addition when the area-weighted average of the radiation heat flux at the back-wall is calculated by simulation, the flux corresponding to the radiation thermometer is more than two times higher than the back-wall flux in case of the thermocouple. So if the process is measured with the radiation thermometer, the melting seems to start earlier, more sharply and the nominal melting temperature seems to be a few mK below of the case measured with the thermocouple as can be seen in figure 9.7.

There are still few experimental comparisons between both methods so all these observations should be checked with new real measurements in order to confirm the results.

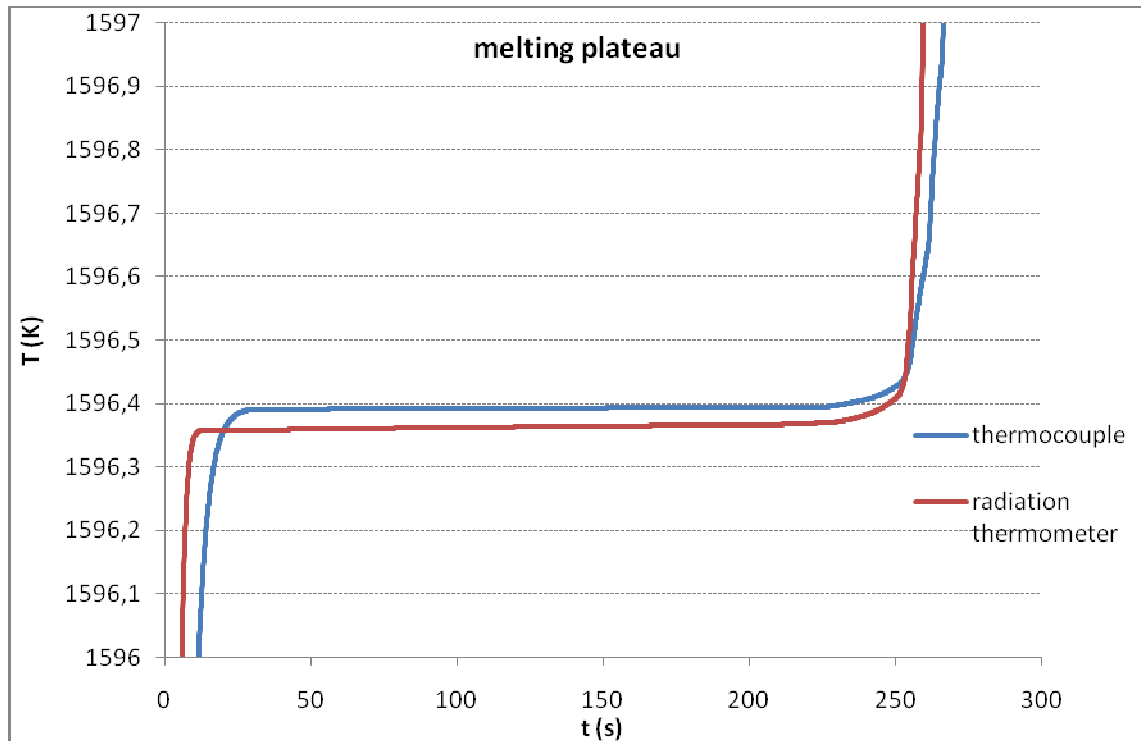


Fig 9.7. Co-C melting plateau for different measurement technique

9.4. Conclusions

Precise knowledge of the thermal properties of the HTFP at the nominal melting temperature are critical to simulate a realistic melting transient process. In the absence of such data a parametric study of all the available possible ranges of data need to be explored.

The modelling shows that the measurement technique does have a small influence in the measured temperature of the HTFP. It seems that radiation heat losses are slightly more significant than those due to the conduction through the thermocouple. This is a very small amount at the Co-C point but may be greater at higher temperatures and further studies should be performed particularly at the Pd-C point where precise thermocouples (Pt/Pd types) are being calibrated using the Pd-C point with low uncertainties [68]. This effect is small enough to be neglected at the Co-C point, or at worst taken as a minor contribution to the

uncertainty budget – particularly where the HTFP temperature has been derived by radiance means but is being used for contact thermometry calibrations.

This study was performed with the most extreme boundary conditions which is the bare crucible without any furnace. It is recommended to extend the study to different nominal temperatures (e.g. Pd-C) and to study the influence of a furnace environment. Note that the presence of a furnace will be thought to reduce the observed effect even more to potentially negligible levels.

CHAPTER 10

Final conclusions



Chapter 10. Final Conclusions

10.1. Conclusions

The numerical approach undertaken through using the FLUENT software has been successfully demonstrated through the work reported in this thesis as an essential tool for understanding the behaviour of HTFPs.

The following issues were successfully investigated through FLUENT simulations:

- 1) The effect of imperfectly formed metal-ingots on the measured temperature by a radiation thermometry. The conclusions of that study were that minor imperfections such as holes on the ingot surface or cracks away from the blackbody back-wall can be neglected but cracks near the back-wall of the cavity can have a significant impact on the radiance temperature. It seems possible that if required the length of the ingot in a good furnace could be significantly reduced in size, covering only the rear portion of the blackbody tube.
- 2) The influence of the back-wall thickness and the blackbody tube length was quantified. As anticipated a higher temperature drop, ΔT , was calculated for shorter blackbody tubes and thicker back-walls.
- 3) The uncertainty in the temperature drop due to uncertain values of the emissivity and thermal conductivity of the graphite was quantified at the nominal temperature of the fixed point. The uncertainties calculated in the temperature drop value, ΔT , for these eutectics are very small - 5mK at the copper point to 90 mK at Re-C. This was evaluated for realistic variation in the values of the parameters K_g and ε_g .
- 4) Measurement of the temperature profile inside the furnace allowed the use of thermal modelling to study the effect of furnace environment and the effective emissivity of the cavity on the resultant measured temperature. The conclusion was that for most physically realistic furnaces, no matter what the real gradient, isothermally conditions inside the furnace can be assumed without much loss of accuracy.

5) Finally, the modelling showed that the measurement technique has a small influence in the measured temperature of the HTFP. With radiation heat losses being slightly more significant than those due to the conduction through measurement with a thermocouple.

10.2. Future research lines on this field

The next research lines could be:

- To reach a unique uncertainty value for the heat losses associated to the furnace temperature profile, the material properties and the heat exchange with the environment.
- To optimize the cell geometry in order to maximise the stability of the melt and to minimise the amount of fixed point material required.
- To recalculate effective cavity emissivities base on new graphite data.
- To extend the study of the influence of the measurement technique to different nominal temperatures (e.g. Pd-C) including the influence of a furnace environment.
- To study the transient model effects of the melting and how the melting process influences the measured melting point.

ANNEX I

Bibliography

Annex I. Bibliography

- [1] Quinn T.J., "News from the BIPM", *Metrologia*, **34**, 1997, pp.187-194.
- [2] Bedford R.E., Bonnier G., Maas H. and Pavese F., "Recommended values of temperature on the International Temperature Scale of 1990 for a selected set of secondary reference points", *Metrologia*, **33**, 1996, pp. 133-154.
- [3] Kim Y.-G., Gam K.S. and Kang K.H., "Fabrication of a nickel freezing-point cell and preliminary study of its behaviour", *Metrologia*, **37**, 2000, pp. 243-245.
- [4] Quinn T.J. and Chandler T.R.D., "A new determination of the freezing point of platinum", *Metrologia*, **7**, 1971, pp. 132-133.
- [5] Jones T.P. and Tapping J., "The freezing point of platinum", *Metrologia*, **12**, 1976, pp. 19-26.
- [6] Jones T.P., "The freezing point of palladium in argon", *Metrologia*, **25**, 1988, pp. 191-192.
- [7] Kim Y.-G., Gam K.S. and Kang K.H., "Realization of the palladium freezing point for thermocouple calibrations", *Metrologia*, **36**, 1999, pp. 465-472.
- [8] Machin G., McEvoy H.C. and Boyes S.J., "A realisation of the Pd point at NPL", *Proceedings of Tempmeko 1996*, Torino, 1996, pp.301-303.
- [9] Jones T.P. and Hall K.G., "The melting point of palladium and its dependence on oxygen", *Metrologia*, **15**, 1979, pp. 161-163.
- [10] Sakate H., Sakuma F. and Ono A., "Observation of Al₂O₃ melting and freezing plateaus using a cavity-type tungsten crucible", *Metrologia*, **32**, 1995, pp. 129-131.
- [11] Yamada Y., Sakate H., Sakuma F. and Ono A., "Radiometric observation of melting and freezing plateaus for a series of metal-carbon eutectic points in the range 1330 °C to 1950 °C", *Metrologia*, **36**, 1999, pp. 207-209.
- [12] Yamada Y., Sakate H., Sakuma F. and Ono A., "A possibility of practical high temperature fixed points above the copper point", *Proceedings of Tempmeko 1999*, Delft, 1999, pp.535-540.

- [13] Yamada Y., Sasajima N., Sakuma F. and Ono A., “Realizing fixed points above the copper point up to 2500 °C using metal-carbon eutectics”, *Proceedings of Tempmeko 2001*, Berlin, 2001, pp.19-26.
- [14] Sasajima N., Yamada Y. and Sakuma F., “Investigation of fixed points exceeding 2500 °C using metal carbide-carbon eutectics”, *Temperature: Its Measurement and Control in Science and Industry*, 7, edited by Ripple D.C., AIP Conference Proceedings, 2003, pp. 291-296.
- [15] Woolliams E., Machin G., Lowe D., Winkler R., “Metal(carbide)-carbon eutectics for thermometry and radiometry. A review of the first seven years”, *Metrologia*, 43, 2006, R11-R25.
- [16] Sadli M., Machin G., Lowe D., Hartmann J. and Morice R., “Realisation and comparison of metal-carbon eutectic points for radiation thermometry applications and W-Re thermocouple calibration”, *Proceedings of Tempmeko 2001*, Berlin, 2001, pp.507-512.
- [17] Machin G., Beynon G., Edler F., Fourrez S., Hartmann J., Lowe D., Morice R., Sadli M. and Villamanan M., “HIMERT: a pan-European project for the development of metal carbon eutectics as temperature standards”, *Temperature: Its Measurement and Control in Science and Industry*, 7, edited by Ripple D.C., AIP Conference Proceedings, 2003, pp. 285-290.
- [18] Sapritsky V., Ogarev S., Khlevnov B., Samoylov M. and Khromchenko V., “Development of metal-carbon high-temperature fixed-point blackbodies for precision photometry and radiometry”, *Metrologia*, 40, 2003, pp. S128-S131.
- [19] Yamada Y., Duan Y., Ballico M., Park S.N., Sakuma F. and Ono A. “Measurement of Rh-C, Pt-C and Ru-C eutectic points by four national metrology institutes”, *Metrologia*, 38, 2001, pp. 203-211.
- [20] Machin G., Yamada Y., Lowe D., Sasajima N., Anhalt K., Hartmann J., Goebel R., McEvoy M. C. and Bloembergen P., “A comparison of high temperature fixed-points of Pt-C and Re-C constructed by BIPM, NMIIJ and NPL”, *Proceedings of Tempmeko 2004*, Cavtat-Dubrovnik, 2004.
- [21] Machin G., Yamada Y., Lowe D., Sasajima N., Sakuma F., and Fan Kai, “A comparison of metal-carbon eutectic blackbody cavities of rhenium, iridium, platinum and palladium between NPL and NMIIJ”, *Proceedings of Tempmeko 2001*, Berlin, 2001, pp. 851-856.

- [22] Hartmann J., Anhalt K., Sperfeld P., Hollandt J., Sakharov M., Khlevnovy B.,
Pikalev Yu., Ogarev S. and Sapritsky V., “Thermodynamic temperature
measurements of the melting curves of Re-C, TiC-C and ZrC-C eutectics”,
Proceedings of Tempmeko 2004, Cavtat-Dubrovnik, 2004.
- [23] Goebel R., Yamada Y. and Stock M., “Thermodynamic temperature
measurements of metal-carbon eutectic fixed points”, *Proceedings of
Tempmeko 2004*, Cavtat-Dubrovnik, 2004.
- [24] Machin G., Gibson C.E., Lowe D., Allen D.W., Yoon H.W. “A comparison
of ITS-90 and detector based scales between NPL and NIST using metal-
carbon eutectics” *Proceedings of Tempmeko 2004*, Cavtat-Dubrovnik, 2004.
- [25] Sadli M., Fischer J., Yamada Y., Sapritsky V., Lowe D. and Machin G.,
“Review of metal-carbon eutectic temperatures: proposal for new ITS-90
secondary points”, *Proceedings of Tempmeko 2004*, Cavtat-Dubrovnik, 2004.
- [26] Jimeno Largo P., “novel high temperature metal-carbon eutectic fixed points:
influence of impurities and of the temperature distribution at the radiant
cavity”. *Doctoral Thesis*. April 2005. Valladolid University.
- [27] Preston-Thomas H., “International Temperature Scale of 1990 (ITS-90)”,
Metrologia, **27(1)**, 1990, pp. 3-10.
- [28] Bureau International des Poids et Mesures, “Supplementary information for
the International Temperature Scale of 1990”. 1997.
- [29] “Mise en pratique for the definition of the kelvin”.
http://www.bipm.org/utils/en/pdf/MeP_K.pdf
- [30] CIPM Recommendation 1 (CI-2005).
<http://www.bipm.org/cc/CIPM/Allowed/94/CIPM-Recom1CI-2005-EN.pdf>
- [31] Scribner R A and Adams E D 1970 *Rev. Sci. Instrum.* **41** pp. 287-288.
- [32] Rusby R L, Durieux M, Reesink A L, Hudson R P, Schuster G, Kühne M,
Fogle W E, Soulen R J, and Adams E D 2002, *Journal of Low Temperature
Physics* **126** 633-642.
- [33] Machin G., Bloembergen P., Anhalt K., Hartmann J., Sadli M., Saunders P.,
Woolliams E., Yamada Y., Yoon H., “Practical Implementation of the *Mise en
Pratique* for the Definition of the Kelvin Above the Silver Point”. *Int J
Thermophys* **31**, 2010, pp. 1779–1788.

- [34]. P. Castro. "modelado mediante el código fluent de la distribución de temperatura en el conjunto crisol-horno para puntos fijos eutécticos carbono-metálicos a muy alta temperatura". *Master Thesis*. Valladolid University. April 2004.
- [35]. M. G. Carvalho, T. Farias, and P. Fontes. "Predicting Radiative Heat Transfer in Absorbing, Emitting, and Scattering Media Using the Discrete Transfer Method". In W.A. Fiveland et al., editor, *Fundamentals of Radiation Heat Transfer*, volume 160, pages 17-26. ASME HTD, 1991.
- [36]. N. G. Shah. "A New Method of Computation of Radian Heat Transfer in Combustion Chambers". *PhD thesis*, Imperial College of Science and Technology, London, England, 1979.
- [37]. P. Cheng. "Two-Dimensional Radiating Gas Flow by a Moment Method". *AIAA Journal*, 2:1662-1664, 1964.
- [38]. R. Siegel and J. R. Howell. *Thermal Radiation Heat Transfer*. Hemisphere Publishing Corporation, Washington D.C., 1992.
- [39]. E. H. Chui and G. D. Raithby. "Computation of Radian Heat Transfer on a Non-Orthogonal Mesh Using the Finite-Volume Method". *Numerical Heat Transfer, Part B*, 23:269-288, 1993.
- [40]. G. D. Raithby and E. H. Chui. "A Finite-Volume Method for Predicting a Radian Heat Transfer in Enclosures with Participating Media". *J. Heat Transfer*, 112:415-423, 1990.
- [41]. J. Y. Murthy and S. R. Mathur. "A Finite Volume Method For Radiative Heat Transfer Using Unstructured Meshes". AIAA-98-0860, January 1998.
- [42]. J. C. Chai, S. V. Patankar. "Finite-Volume Method For Radiation Heat Transfer". *Advances in Numerical Heat Transfer*, pp 109-138 Vol 2, 2000.
- [43]. M. Y. Kim, S. W. Baek, J. H. Park. "Unstructured Finite-Volume Method For Radiative Heat Transfer in a Complex Two-Dimensional Geometry With Obstacles". *Numerical Heat Transfer, Part B*, Vol 39, pp 617-635 , 2001.
- [44]. G. D. Raithby. "Evaluation of Discretization Errors in Finite-Volume Radiant Heat Transfer Predictions". *Numerical Heat Transfer, Part B*, Vol 36, pp 241-264, 1999.

- [45]. M. Y. Kim, S. W. Baek, J. H. Park. "Evaluation of the Finite-Volume Solutions of Radiative Heat Transfer in a Complex Two-dimensional Enclosure with Unstructured Polygonal Meshes". *Numerical Heat Transfer, Part B*, Vol 54, pp 116-137 , 2008.
- [46]. C. García, M. J. Martín, D. del Campo, J. P. Pérez and V. Chimenti, "CEM facilities for high temperature calibration". *Proceedings of HTFP'2006 International Workshop*, Paris (2006).
- [47]. P. Castro, M. A. Villamañan, M. J. Martin, D. del Campo, "Modelling a High Temperature Furnace Using Finite Volume Software", *Proceedings of Conference on Advanced Mathematical and Computational Tools in Metrology and Testing*, Paris 2008.
- [48]. M. Y. Kim, S. W. Baek, J. H. Park. "Modelling of Radiative Heat Transfer in an Axisymmetric Cylindrical Enclosure with Participating Medium" *Journal of Quantitative Spectroscopy & Radiative Transfer*, 90, pp 377-388 , 2005.
- [49]. Machin, G., Bloembergen, P., Hartmann, J., Sadli, M., Yamada Y., "A concerted international project to establish high temperature fixed-points for primary thermometry", *Int. J. Thermophys.*, 28, 1976-1982, 2007
- [50]. Lowe, D., Machin, G., "Development of metal-carbon eutectic blackbody cavities to 2500 °C at NPL", In: *Tempmeko 01, The 8th International Symposium on Temperature and Thermal Measurements in Industry and Science*, Berlin, Germany, Eds. B Fellmuth, J. Seidel, G. Scholz, Published: VDE VERLAG GMBH, 519-524, 2002
- [51]. Machin, G., "Realising the benefits of improvements in high temperature metrology", *Acta Metrologica Sinica*, 29, p. 10-17, 2008.
- [52]. M. Sadli, B. Khlevnov, T. Wang, Y. Yamada, G. Machin, "International study of the long-term stability of metal-carbon eutectic cells". *Proceedings of International Symposium on Temperature, Humidity, Moisture and Thermal Measurements in Industry and Science*, Slovenia, 2010.
- [53]. P. Jimeno-Largo, Y. Yamada, P. Bloembergen, M.A. Villamanan, G. Machin. "Numerical analysis of the temperature drop across the cavity bottom of high-temperature fixed points for radiation thermometry". In *Proceedings of TEMPMEKO 2004*. Edited by D.Zvizdić, L.G. Bermanec, T. Veliki, T.Stašić. Zagreb: FSB/LPM, 2004, 335-340.

- [54]. P.Bloembergen, B.B. Khlevnovy, P. Jimeno-Largo, Y.Yamada. “Spectral and total effective emissivity of a high-temperature fixed-point radiator considered in relation to the temperature drop across its backwall”. *Int. J. Thermophysics*, 2008.
- [55]. J. Fischer, H.J. Jung, “Determination of the thermodynamic temperatures of the freezing points of silver and gold by near-infrared pyrometry”. *Metrologia*.1989, **26**, 245-252.
- [56]. C.K. Ma. “Calculation of the distribution of emissivity and temperature for a baffled cylindrical cavity at the freezing points of Ag, Au and Cu”. In *Proceedings of TEMPBEIJING 1997*. Edited by B. Zhang et al. Beijing: Standard press of China, 1997, 72-77.
- [57]. T.J. Horn and A.N. Abdelmessih. “Experimental and numerical characterization of a steady-state cylindrical blackbody cavity at 1100 degrees Celsius”. TM-2000-209022, National Aeronautics and Space Administration Dryden Flight Research Centre, 2000.
- [58]. Y.S. Touloukian, R.W. Powell, C.Y. Ho and P.G. Klemens. “Thermal conductivity: Nonmetallic Solids, Thermophysical properties of Matter”. The TPRC Data Series, 2, New York, Plenum Press, 1978.
- [59]. Machin, G., Wright, L., Lowe, D., Pearce J.V., “Optimising the implementation of high temperature fixed-points through the use of thermal modelling”, *Int. J. Thermophys.*, 29, 26-270, 2008.
- [60]. C.E. Brookley, W.E. Llewellyn, “Determination of blackbody radiance at temperatures above 2300 °C”, proceedings of *Temperature, Its Measurement and Control in Science and Industry*, vol. 6, edited by J. Schooley, AIP, pp. 1195-1200, 1992.
- [61]. P. Castro, P .Bloembergen, Y. Yamada, M. A. Villamañan and G. Machin, “On the Uncertainty in the Temperature Drop across the Backwall of High-Temperature Fixed Points”. *Acta Metrologica Sinica*. Vol. 29. pp 253-260. 2008. Proceedings of International Conference on Temperature and Thermal Measurements, Beijing, 2008.
- [62]. Fischer, J., Sadli, M., Ballico, M., Battuello, M., Park, S. N., Saunders, P., Yuan Zundong, Johnson, B. C., van der Ham, E., Sakuma, F., Machin, G., Fox, N., Wang Li, Ugur, S., Matveyev M., “Uncertainty budgets for the realisation of ITS-90 by radiation thermometry”, In Proceedings of

- Temperature its Measurement and Control in Science and Industry*, Vol. 7, ed. Ripple D., AIP Conference Proceedings, Chicago, 2003, pp 631-638
- [63]. P. Bloembergen, L. M. Hanssen, S. N. Mekhontsev, P. Castro, Y. Yamada, “A determination study of the cavity emissivity of the eutectic fixed points Co-C, Pt-C and Re-C”. *Proceedings of International Symposium on Temperature, Humidity, Moisture and Thermal Measurements in Industry and Science*, Slovenia, 2010. Submitted for publication in International Journal of Thermophysics.
- [64]. G. Machin , P. Castro , A. Levick , M. Á. Villamañan, “Quantifying the Temperature Effects of Imperfectly Formed Metal-Ingots in High Temperature Fixed Point Crucibles”. *Proceedings of International Conference on Temperature and Thermal Measurements, Beijing, 2008. Measurement* 44 (2011), pp. 738–742.
- [65]. P. Castro, G. Machin, M. A. Villamañan, D. Lowe, “Calculation of the Temperature Drop for High Temperature Fixed Points for Different Furnace Conditions”. *Proceedings of International Symposium on Temperature, Humidity, Moisture and Thermal Measurements in Industry and Science*, Slovenia, 2010. Submitted for publication in International Journal of Thermophysics.
- [66]. S. G. R. Salim, E. R. Woolliams, M. Dury, D. H. Lowe, J. V. Pearce, G. Machin, N. P. Fox, T. Sun and K.T. V. Grattan. “Furnace uniformity effects on Re–C fixed-point melting plateaux”. *Metrologia*, vol. **46**, 2009, pp. 33–42.
- [67]. M. Sadli, O. Pehlivan, F. Bourson, A. Diril, K. Ozcan. “Collaboration Between UME and LNE-INM on Co–C Eutectic Fixed-Point Construction and Characterization”. *Int. J. Thermophys.*, 30, 36–46, 2009.
- [68]. Pearce J. V., Ogura H., Izuchi, M., Machin G., “Evaluation of the Pd–C eutectic fixed point and the Pt/Pd thermocouple”, *Metrologia*, **46**, p.473-479, 2009.

ANNEX II

Glossary of key metrological terms



Annex II. Glossary of key metrological terms¹

1. Quantities and units

1.1 Quantity

Property of a phenomenon, body, or substance, where the property has a magnitude that can be expressed as a number and a reference.

1.2 Kind of quantity

Aspect common to mutually comparable **quantities**.

1.3 System of quantities

Set of quantities together with a set of non-contradictory equations relating those quantities.

1.4 Base quantity

Quantity in a conventionally chosen subset of a given system of quantities, where no subset quantity can be expressed in terms of the others.

1.5 Derived quantity

Quantity, in a system of quantities, defined in terms of the base quantities of that system.

1.6 International System of Quantities (ISQ)

System of quantities based on the seven base quantities: length, mass, time, electric current, thermodynamic temperature, amount of substance, and luminous intensity.

1.7 Quantity dimension

¹ From International vocabulary of metrology (VIM) — Basic and general concepts and associated terms. BIPM 2008.

Expression of the dependence of a quantity on the base quantities of a system of quantities as a product of powers of factors corresponding to the base quantities, omitting any numerical factor.

1.8 Quantity of dimension one

Quantity for which all the exponents of the factors corresponding to the base quantities in its quantity dimension are zero.

1.9 Measurement unit

Real scalar quantity, defined and adopted by convention, with which any other quantity of the same kind can be compared to express the ratio of the two quantities as a number.

1.10 Base unit

Measurement unit that is adopted by convention for a base quantity.

1.11 Derived unit

Measurement unit for a derived quantity.

1.12 Coherent derived unit

Derived unit that, for a given system of quantities and for a chosen set of base units, is a product of powers of base units with no other proportionality factor than one.

1.13 System of units

Set of base units and derived units, together with their multiples and submultiples, defined in accordance with given rules, for a given system of quantities.

1.14 Coherent system of units

System of units, based on a given system of quantities, in which the measurement unit for each derived quantity is a coherent derived unit.

1.15 Off-system measurement unit

Measurement unit that does not belong to a given system of units.

1.16 International System of Units (SI)

System of units, based on the International System of Quantities, their names and symbols, including a series of prefixes and their names and symbols, together with rules for their use, adopted by the General Conference on Weights and Measures (CGPM).

1.17 Multiple of a unit

measurement obtained by multiplying a given measurement unit by an integer greater than one.

1.18 Submultiple of a unit

Measurement unit obtained by dividing a given measurement unit by an integer greater than one.

1.19 Quantity value

Value of a quantity value number and reference together expressing magnitude of a quantity.

1.20 numerical quantity value

Number in the expression of a quantity value, other than any number serving as the reference.

1.21 Quantity calculus

Set of mathematical rules and operations applied to quantities other than ordinal quantities.

1.22 Quantity equation

Mathematical relation between quantities in a given system of quantities, independent of measurement units.

1.23 Unit equation

Mathematical relation between base units, coherent derived units or other measurement units.

1.24 Conversion factor between units

Ratio of two measurement units for quantities of the same kind.

1.25 numerical value equation

Mathematical relation between numerical quantity values, based on a given quantity equation and specified measurement units.

1.26 Ordinal quantity

Quantity, defined by a conventional measurement procedure, for which a total ordering relation can be established, according to magnitude, with other quantities of the same kind, but for which no algebraic operations among those quantities exist.

1.27 Quantity-value scale

Ordered set of quantity values of quantities of a given kind of quantity used in ranking, according to magnitude, quantities of that kind.

1.28 Ordinal quantity-value scale

Quantity-value scale for ordinal quantities.

1.29 Conventional reference scale

Quantity-value scale defined by formal agreement.

1.30 Nominal property

Property of a phenomenon, body, or substance, where the property has no magnitude.

2. Measurement

2.1 Measurement

Process of experimentally obtaining one or more quantity values that can reasonably be attributed to a quantity.

2.2 Metrology

Science of measurement and its application.

2.3 Measurand

Quantity intended to be measured.

2.4 Measurement principle

Phenomenon serving as a basis of a measurement.

2.5 Measurement method

Generic description of a logical organization of operations used in a measurement.

2.6 Measurement procedure

Detailed description of a measurement according to one or more measurement principles and to a given measurement method, based on a measurement model and including any calculation to obtain a measurement result.

2.7 Reference measurement procedure

Measurement procedure accepted as providing measurement results fit for their intended use in assessing measurement trueness of measured quantity values obtained from other measurement procedures for quantities of the same kind, in calibration, or in characterizing reference materials.

2.8 Primary reference measurement procedure

Reference measurement procedure used to obtain a measurement result without relation to a measurement standard for a quantity of the same kind.

2.9 Measurement result

Set of quantity values being attributed to a measurand together with any other available relevant information.

2.10 Measured quantity value

Quantity value representing a measurement result.

2.11 True quantity value

Quantity value consistent with the definition of a quantity.

2.12 Conventional quantity value

Quantity value attributed by agreement to a quantity for a given purpose.

2.13 Measurement accuracy

Closeness of agreement between a measured quantity value and a true quantity value of a measurand.

2.14 Measurement trueness

Closeness of agreement between the average of an infinite number of replicate measured quantity values and a reference quantity value.

2.15 Measurement precision

Closeness of agreement between indications or measured quantity values obtained by replicate measurements on the same or similar objects under specified conditions.

2.16 Measurement error

Measured quantity value minus a reference quantity value.

2.17 Systematic measurement error

Component of measurement error that in replicate measurements remains constant or varies in a predictable manner.

2.18 Measurement bias

Estimate of a systematic measurement error.

2.19 Random measurement error

Component of measurement error that in replicate measurements varies in an unpredictable manner.

2.20 Repeatability condition of measurement

Condition of measurement, out of a set of conditions that includes the same measurement procedure, same operators, same measuring system, same operating conditions and same location, and replicate measurements on the same or similar objects over a short period of time.

2.21 Measurement repeatability

measurement precision under a set of repeatability conditions of measurement.

2.22 Intermediate precision condition of measurement

Condition of measurement, out of a set of conditions that includes the same measurement procedure, same location, and replicate measurements on the same or similar objects over an extended period of time, but may include other conditions involving changes.

2.23 Intermediate measurement precision

Measurement precision under a set of intermediate precision conditions of measurement

2.24 Reproducibility condition of measurement

Condition of measurement, out of a set of conditions that includes different locations, operators, measuring systems, and replicate measurements on the same or similar objects.

2.25 Measurement reproducibility

Measurement precision under reproducibility conditions of measurement.

2.26 Measurement uncertainty

Non-negative parameter characterizing the dispersion of the quantity values being attributed to a measurand, based on the information used.

2.27 Definitional uncertainty

Component of measurement uncertainty resulting from the finite amount of detail in the definition of a measurand.

2.28 Type A evaluation of measurement uncertainty

Evaluation of a component of measurement uncertainty by a statistical analysis of measured quantity values obtained under defined measurement conditions.

2.29 Type B evaluation of measurement uncertainty

Evaluation of a component of measurement uncertainty determined by means other than a Type A evaluation of measurement uncertainty.

2.30 Standard measurement uncertainty

Measurement uncertainty expressed as a standard deviation.

2.31 Combined standard measurement uncertainty

Standard measurement uncertainty that is obtained using the individual standard measurement uncertainties associated with the input quantities in a measurement model

2.32 Relative standard measurement uncertainty

standard measurement uncertainty divided by the absolute value of the measured quantity value.

2.33 Uncertainty budget

Statement of a measurement uncertainty, of the components of that measurement uncertainty, and of their calculation and combination.

2.34 Target measurement uncertainty

Measurement uncertainty specified as an upper limit and decided on the basis of the intended use of measurement results.

2.35 Expanded measurement uncertainty

Product of a combined standard measurement uncertainty and a factor larger than the number one.

2.36 Coverage interval

Interval containing the set of true quantity values of a measurand with a stated probability, based on the information available.

2.37 Coverage probability

Probability that the set of true quantity values of a measurand is contained within a specified coverage interval

2.38 Coverage factor

Number larger than one by which a combined standard measurement uncertainty is multiplied to obtain an expanded measurement uncertainty.

2.39 Calibration

Operation that, under specified conditions, in a first step, establishes a relation between the quantity values with measurement uncertainties provided by measurement standards and corresponding indications with associated measurement uncertainties and, in a second step, uses this information to establish a relation for obtaining a measurement result from an indication.

2.40 Calibration hierarchy

Sequence of calibrations from a reference to the final measuring system, where the outcome of each calibration depends on the outcome of the previous calibration.

2.41 Metrological traceability

Property of a measurement result whereby the result can be related to a reference through a documented unbroken chain of calibrations, each contributing to the measurement uncertainty.

2.42 metrological traceability chain

Sequence of measurement standards and calibrations that is used to relate a measurement result to a reference.

2.43 Metrological traceability to a measurement unit

Metrological traceability where the reference is the definition of a measurement unit through its practical realization.

2.44 Verification

Provision of objective evidence that a given item fulfils specified requirements.

2.45 Validation

Verification, where the specified requirements are adequate for an intended use.

2.46 Metrological comparability of measurement results

Comparability of measurement results, for quantities of a given kind, that are metrologically traceable to the same reference.

2.47 metrological compatibility of measurement results

Property of a set of measurement results for a specified measurand, such that the absolute value of the difference of any pair of measured quantity values from two different measurement results is smaller than some chosen multiple of the standard measurement uncertainty of that difference.

2.48 Measurement model

Mathematical relation among all quantities known to be involved in a measurement.

2.49 Measurement function

Function of quantities, the value of which, when calculated using known quantity values for the input quantities in a measurement model, is a measured quantity value of the output quantity in the measurement model.

2.50 Input quantity in a measurement model

Quantity that must be measured, or a quantity, the value of which can be otherwise obtained, in order to calculate a measured quantity value of a measurand.

2.51 Output quantity in a measurement model

Quantity, the measured value of which is calculated using the values of input quantities in a measurement model.

2.52 Influence quantity

Quantity that, in a direct measurement, does not affect the quantity that is actually measured, but affects the relation between the indication and the measurement result.

2.53 Correction

Compensation for an estimated systematic effect.

3. Devices for measurement

3.1 Measuring instrument

Device used for making measurements, alone or in conjunction with one or more supplementary devices.

3.2 Measuring system

Set of one or more measuring instruments and often other devices, including any reagent and supply, assembled and adapted to give information used to generate measured quantity values within specified intervals for quantities of specified kinds.

3.3 Indicating measuring instrument

Measuring instrument providing an output signal carrying information about the value of the quantity being measured.

3.4 Displaying measuring instrument

Indicating measuring instrument where the output signal is presented in visual form.

3.5 Scale of a displaying measuring instrument

Part of a displaying measuring instrument, consisting of an ordered set of marks together with any associated quantity values.

3.6 Material measure

Measuring instrument reproducing or supplying, in a permanent manner during its use, quantities of one or more given kinds, each with an assigned quantity value.

3.7 Measuring transducer

Device, used in measurement, that provides an output quantity having a specified relation to the input quantity.

3.8 Sensor

Element of a measuring system that is directly affected by a phenomenon, body, or substance carrying a quantity to be measured.

3.9 Detector

Device or substance that indicates the presence of a phenomenon, body, or substance when a threshold value of an associated quantity is exceeded.

3.10 Measuring chain

Series of elements of a measuring system constituting a single path of the signal from a sensor to an output element.

3.11 Adjustment of a measuring system

Set of operations carried out on a measuring system so that it provides prescribed indications corresponding to given values of a quantity to be measured.

3.12 Zero adjustment of a measuring system

Adjustment of a measuring system so that it provides a null indication corresponding to a zero value of a quantity to be measured.

4. Properties of measuring devices

4.1 Indication

Quantity value provided by a measuring instrument or a measuring system.

4 .2 Blank indication

Indication obtained from a phenomenon, body, or substance similar to the one under investigation, but for which a quantity of interest is supposed not to be present, or is not contributing to the indication.

4.3 Indication interval

Set of quantity values bounded by extreme possible indications.

4.4 Nominal indication interval

Set of quantity values, bounded by rounded or approximate extreme indications, obtainable with a particular setting of the controls of a measuring instrument or measuring system and used to designate that setting.

4.5 Range of a nominal indication interval

Absolute value of the difference between the extreme quantity values of a nominal indication interval.

4.6 Nominal quantity value

Rounded or approximate value of a characterizing quantity of a measuring instrument or measuring system that provides guidance for its appropriate use.

4.7 Measuring interval

Set of values of quantities of the same kind that can be measured by a given measuring instrument or measuring system with specified instrumental uncertainty, under defined conditions.

4.8 Steady-state operating condition

Operating condition of a measuring instrument or measuring system in which the relation established by calibration remains valid even for a measurand varying with time.

4.9 Rated operating condition

Operating condition that must be fulfilled during measurement in order that a measuring instrument or measuring system perform as designed.

4.10 Limiting operating condition

Extreme operating condition that a measuring instrument or measuring system is required to withstand without damage, and without degradation of specified metrological properties, when it is subsequently operated under its rated operating conditions.

4.11 Reference operating condition

Operating condition prescribed for evaluating the performance of a measuring instrument or measuring system or for comparison of measurement results.

4.12 Sensitivity of a measuring system

Quotient of the change in an indication of a measuring system and the corresponding change in a value of a quantity being measured.

4.13 Selectivity of a measuring system

Property of a measuring system, used with a specified measurement procedure, whereby it provides measured quantity values for one or more measurands such that the values of each measurand are independent of other measurands or other quantities in the phenomenon, body, or substance being investigated.

4.14 Resolution

Smallest change in a quantity being measured that causes a perceptible change in the corresponding indication.

4.15 Resolution of a displaying device

Smallest difference between displayed indications that can be meaningfully distinguished.

4.16 Discrimination threshold

Largest change in a value of a quantity being measured that causes no detectable change in the corresponding indication.

4.17 Dead band

Maximum interval through which a value of a quantity being measured can be changed in both directions without producing a detectable change in the corresponding indication.

4.18 Detection limit

Measured quantity value, obtained by a given measurement procedure, for which the probability of falsely claiming the absence of a component in a material is β , given a probability α of falsely claiming its presence.

4.19 Stability of a measuring instrument

Property of a measuring instrument, whereby its metrological properties remain constant in time.

4.20 Instrumental bias

Average of replicate indications minus a reference quantity value.

4.21 Instrumental drift

Continuous or incremental change over time in indication, due to changes in metrological properties of a measuring instrument.

4.22 Variation due to an influence quantity

Difference in indication for a given measured quantity value, or in quantity values supplied by a material measure, when an influence quantity assumes successively two different quantity values.

4.23 Step response time

duration between the instant when an input quantity value of a measuring instrument or measuring system is subjected to an abrupt change between two specified constant quantity values and the instant when a corresponding indication settles within specified limits around its final steady value.

4.24 Instrumental measurement uncertainty

Component of measurement uncertainty arising from a measuring instrument or measuring system in use.

4.25 Accuracy class

class of measuring instruments or measuring systems that meet stated metrological requirements that are intended to keep measurement errors or instrumental uncertainties within specified limits under specified operating conditions.

4.26 Maximum permissible measurement error

Extreme value of measurement error, with respect to a known reference quantity value, permitted by specifications or regulations for a given measurement, measuring instrument, or measuring system.

4.27 Datum measurement error

Measurement error of a measuring instrument or measuring system at a specified measured quantity value.

4.28 Zero error

Datum measurement error where the specified measured quantity value is zero.

4.29 Null measurement uncertainty

Measurement uncertainty where the specified measured quantity value is zero

4.30 Calibration diagram

Graphical expression of the relation between indication and corresponding measurement result.

4.31 Calibration curve

Expression of the relation between indication and corresponding measured quantity value.

5. Measurement standards

5.1 Measurement standard

Realization of the definition of a given quantity, with stated quantity value and associated measurement uncertainty, used as a reference.

5.2 International measurement standard

Measurement standard recognized by signatories to an international agreement and intended to serve Worldwide.

5.3 National measurement standard

Measurement standard recognized by national authority to serve in a state or economy as the basis for assigning quantity values to other measurement standards for the kind of quantity concerned.

5.4 Primary measurement standard

Measurement standard established using a primary reference measurement procedure, or created as an artifact, chosen by convention.

5.5 Secondary measurement standard

Measurement standard established through calibration with respect to a primary measurement standard for a quantity of the same kind.

5.6 Reference measurement standard

Measurement standard designated for the calibration of other measurement standards for quantities of a given kind in a given organization or at a given location.

5.7 Working measurement standard

Measurement standard that is used routinely to calibrate or verify measuring instruments or measuring Systems.

5.8 Travelling measurement standard

Measurement standard, sometimes of special construction, intended for transport between different locations.

5.9 Transfer measurement device

Device used as an intermediary to compare measurement standards.

5.10 Intrinsic measurement standard

Measurement standard based on an inherent and reproducible property of a phenomenon or substance.

5.11 Conservation of a measurement standard

Set of operations necessary to preserve the metrological properties of a measurement standard within stated limits.

5.12 Calibrator

Measurement standard used in calibration

5.13 Reference material

Material, sufficiently homogeneous and stable with reference to specified properties, which has been established to be fit for its intended use in measurement or in examination of nominal properties.

5.14 Certified reference material (CRM)

Reference material, accompanied by documentation issued by an authoritative body and providing one or more specified property values with associated uncertainties and traceabilities, using valid procedures.

5.15 Commutability of a reference material

Property of a reference material, demonstrated by the closeness of agreement between the relation among the measurement results for a stated quantity in this material, obtained according to two given measurement procedures, and the relation obtained among the measurement results for other specified materials.

5.16 Reference data

Data related to a property of a phenomenon, body, or substance, or to a system of components of known composition or structure, obtained from an identified source, critically evaluated, and verified for accuracy.

5.17 Standard reference data

Reference data issued by a recognized authority.

5.18 Reference quantity value

Quantity value used as a basis for comparison with values of quantities of the same kind.

ANNEX III

**Published papers and
contributions to
International Conferences
from this work**

Annex III. Published Papers and Contributions to International Conferences from this Work

HTFP 2006 International Workshop, 6-7 June 2006, LNE, Paris, France.

- P. Castro, P. Jimeno-Largo, M.A. Villamañán, M.C. Martín and R.M. Villamañán, “Comparison Between Analytical and Numerical Solutions of the Temperature Drop Across the Cavity Wall of High-Temperature Fixed Points for Radiation Thermometry”, *Proceedings of the HTFP 2006 International Workshop*, LNE, Paris.
- P. Castro, P. Jimeno-Largo, M.A. Villamañán, J.J. Segovia and C.R. Chamorro, “Numerical Study of the Temperature Drop in Set Crucible-furnace for Eutectic Fixed Points Used in Radiation Thermometry”, *Proceedings of the HTFP 2006 International Workshop*, LNE. Paris.

Conference on Advanced Mathematical and Computational Tools in Metrology and Testing, 23-25 June 2008, Paris, France.

- P. Castro, M. A. Villamañan, M. J. Martin, D. del Campo, “Modelling a High Temperature Furnace Using Finite Volume Software”, *Proceedings of Conference on Advanced Mathematical and Computational Tools in Metrology and Testing*, Paris 2008.

International Conference on Temperature and Thermal Measurements, 20-23 October 2008, Beijing, China.

- P. Castro, P .Bloembergen, Y. Yamada, M. A. Villamañan, G. Machin, “On the Uncertainty in the Temperature Drop across the Backwall of High-Temperature Fixed Points”. *Proceedings of International Conference on Temperature and*

Thermal Measurements, Beijing, 2008. *Acta Metrologica Sinica*. Vol. 29. pp 253-260. 2008.

- G. Machin , P. Castro , A. Levick , M. Á. Villamañan, “Quantifying the Temperature Effects of Imperfectly Formed Metal-Ingots in High Temperature Fixed Point Crucibles”. *Proceedings of International Conference on Temperature and Thermal Measurements, Beijing, 2008. Measurement* 44 (2011), pp. 738–742.

International Symposium on Temperature, Humidity, Moisture and Thermal Measurements in Industry and Science TEMPMEKO & ISHM 2010, 1-4 June 2010, Portorož, Slovenia.

- P. Castro, G. Machin, M. A. Villamañan, D. Lowe, “Calculation of the Temperature Drop for High Temperature Fixed Points for Different Furnace Conditions”. *Proceedings of International Symposium on Temperature, Humidity, Moisture and Thermal Measurements in Industry and Science*, Slovenia, 2010. Submitted for publication in International Journal of Thermophysics.
- P. Bloembergen, L. Hanssen, S. Mekhontsev, V. Khormchenko, B. Wilthan, Jinan Zeng, P. Castro, Y. Yamada, “Determination Study of the Cavity Emissivity of the Eutectic Fixed Points Co-C, Pt-C and Re-C”. *Proceedings of International Symposium on Temperature, Humidity, Moisture and Thermal Measurements in Industry and Science*, Slovenia, 2010. Submitted for publication in International Journal of Thermophysics.



Contents lists available at ScienceDirect



Measurement

journal homepage: www.elsevier.com/locate/measurement

Temperature effects of imperfectly formed metal-ingots in high temperature fixed point crucibles

Graham Machin ^{a,1}, Pablo Castro ^{b,*2}, Andrew Levick ^{a,1}, Miguel Ángel Villamañán ^{b,2}^a National Physical Laboratory, Hampton Rd., Teddington, Middlesex, TW11 0LW, UK^b Engineering School, Paseo del Cauce s/n, Valladolid University, 47071 Valladolid, Spain

ARTICLE INFO

Article history:

Received 27 June 2010

Received in revised form 2 December 2010

Accepted 7 January 2011

Available online 13 January 2011

Keywords:

Thermal modeling

High temperature fixed points

Eutectics

ABSTRACT

This paper investigates, through thermal modeling the effect on the radiance temperature of imperfectly filled thermometric fixed points. A two dimensional axisymmetric thermal model was established and the effect on the radiance temperature of various ingot imperfections such as voids and cracks in different places and of different dimensions in the ingot structure was calculated. It was found that the radiance temperature of the fixed point is quite tolerant to even relatively large flaws in the ingot structure. Only when flaws of significant dimensions near the radiating back wall were introduced was the overall radiance temperature significantly affected.

© 2011 Elsevier Ltd. All rights reserved.

1. Introduction

The CCT-WG5 (Consultative Committee of Thermometry – working group on radiation thermometry) has instigated a programme of research with the aim of establishing high temperature fixed points as routine temperature standards above 1100 °C by 2012 [1]. These high temperature fixed points (HTFPs) are based on ingots of metal–carbon eutectics, metal–carbide eutectics or peritectics cast in graphite crucibles [2]. However, the casting process is not straightforward and can result in imperfect filling of the crucible, in particular forming an ingot with holes or voids. Part of the CCT-WG5 research plan is to seek to understand the effects such imperfect filling might have on the resultant temperature. This is not possible to determine experimentally so a numerical thermal model of non-contact thermometry cells has been established to help understand this effect. Different models have been

constructed simulating the presence of both voids or holes and “cracks” in the ingot. A crack in the ingot is potentially a major flaw allowing direct communication of the thermal radiation from the crucible wall to the blackbody tube.

These models were implemented using finite volume software and the areal average of the back wall temperature calculated whilst the fixed point was raised from a fully frozen to a fully molten state. Furnace effects have been neglected, that is the crucible alone has been simulated. Two dimensional axisymmetric simulations have been performed for the following scenarios:

- Holes in the ingot adjacent to the crucible wall with the dimensions 1.5 mm and 3 mm width and 1 mm and 2.5 mm depth were simulated. The position of the hole was varied along the crucible wall.
- Cracks of 1.5 mm and 3 mm width allowing direct line of sight of the hot outer crucible wall to the blackbody wall were modeled in turn. The position of the cracks was varied.

This paper describes the results of the simulations, in particular the effect of imperfectly formed ingots on the duration and quality of the melt profile.

^{*} Corresponding author. Tel.: +34 983 423 364; fax: +34 983 423 363.E-mail address: pablocastroal@yahoo.es (P. Castro).¹ Tel.: +44 20 8943 6742.² Tel.: +34 983 423 364; fax: +34 983 423 363.

2. Construction and implementation of thermal model

The thermal model was implemented using the software package FLUENT 6.1. FLUENT is a general purpose computational fluid dynamics (CFD) package based on the finite volume method. The subject of study is divided into a finite set of control volumes and the general equations for mass, momentum and energy conservation are simplified into algebraic equations and then solved to give individual values in each volume.

To simulate these fixed points two dimensional axisymmetric models have been constructed. The fixed-point modeled was of a typical NPL design [3]. These are constructed from high purity graphite and filled with an ingot of the metal–carbon mixture. In brief the outer crucible was 40 mm long and 24 mm of outer diameter. The crucible walls, including a thin sacrificial inner sleeve of graphite were 5 mm thick. The blackbody reentrant well was 7 mm outside diameter with a 3 mm blackbody internal diameter with a length of 27 mm and a 120° cone at the apex. The internal diameter of the crucible, where the ingot was cast, was 16 mm. The fixed-point modeled here was the Re–C point (2747 K) but the results are applicable in general. A photograph of one of these fixed-points is shown in Fig. 1 in [4].

The important thermophysical properties were; graphite emissivity 0.86, Re–C emissivity 0.35, thermal conductivity of graphite $36.5 \text{ W m}^{-1} \text{ K}^{-1}$, the thermal conductivity of Re around the melting point $55 \text{ W m}^{-1} \text{ K}^{-1}$. The uncertainty of graphite emissivity and thermal conductivity values is studied in references [5] and [6].

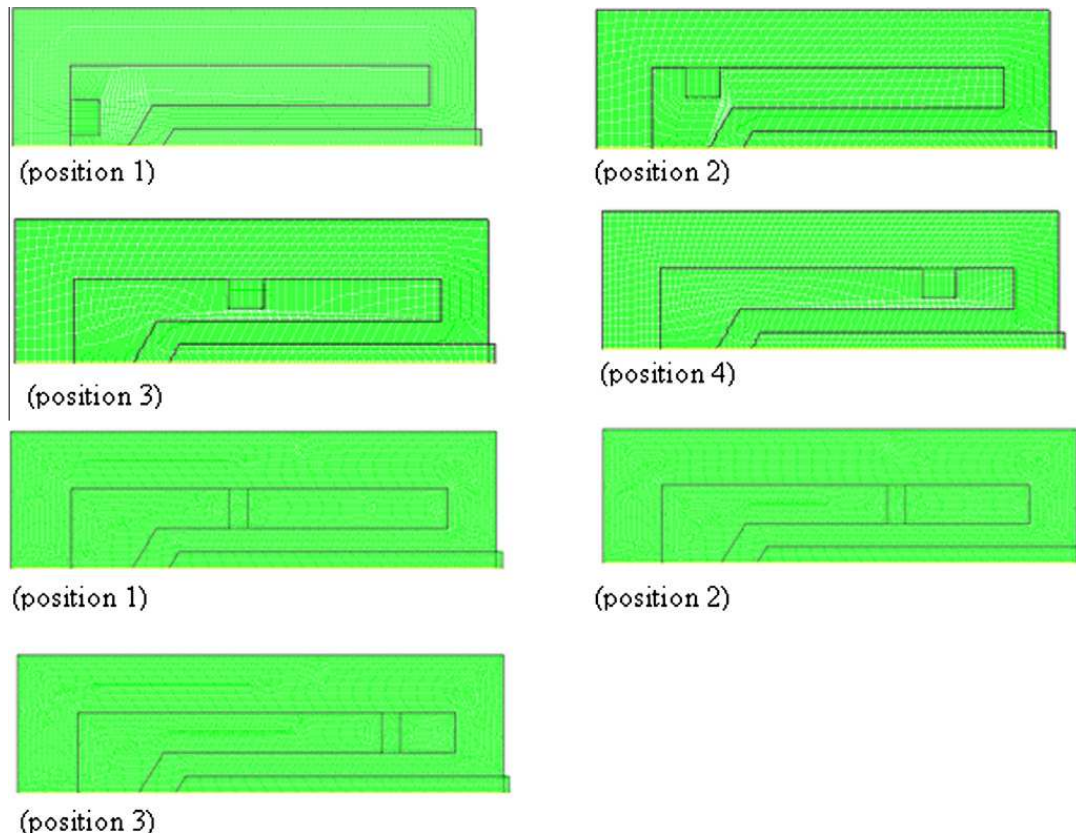


Fig. 1. The different positions of the holes and cracks inside the ingot.

For the purposes of the model Re–C is assumed to have the same thermal properties as pure Re.

The boundary conditions were set with a uniform temperature of the outside wall of the crucible i.e. it did not experience any temperature gradients. The outside world at the fixed point aperture was simulated with a baffle at room temperature looking directly to the back wall of the crucible.

The numerical experimentation was performed as follows. The initial condition was that the crucible was held 7 K below the melting point. A temperature step function above the melting point was then implemented by raising the outside graphite wall to 20 K above the melting point. The areal average of the temperature of the back wall was then calculated during the simulated melting process.

The holes and cracks described in the introduction were implemented and modeled in turn. A typical numerical grid, showing the different positions of the holes and cracks inside the ingot, is given in Fig. 1.

3. Results

3.1. Results with the holes

The holes given in Table 1 were modeled at four different locations around the ingot. The holes were always assumed to be on the outside wall of the ingot facing the outside graphite wall, as shown in Fig. 1. These were designated (x, y) (see Fig. 2), where x designates the location of the hole and y identifies its dimension.

Table 1

Depth and width of simulated holes and width of simulated cracks in ingot.

	Depth/mm	Width/mm
Hole 1	2.5	3.0
Hole 2	2.5	1.5
Hole 3	1.0	1.5
Crack 1		1.5
Crack 2		3

Four different positions were modeled position $x = 1$ was at the rear wall of the crucible, nearest to the back wall of the radiating cavity (see Fig. 1), and positions 2, 3 and 4 were along the side walls of the cavity, with position 4 being the furthest from the radiating back wall. The results of the thermal modeling for the hole $2.5 \text{ mm} \times 3 \text{ mm}$ in different locations are shown in Fig. 2. Here the areal average of temperature is plotted with time. Note the time units are arbitrary and a function of the thermal conductivity and density of the system.

The model shows that the fixed-point is very tolerant to the presence of holes, even quite large holes, in the surface of the ingot. The position of the hole makes very little difference to neither the resultant radiance temperature nor the duration of the melt.

Fig. 3 shows the effect on the radiance temperature of holes of differing dimensions in the same location. Again it is clear that the dimension of the hole does not have a significant effect on the overall melting curve of the fixed point, though the duration is slightly shorter for larger holes.

3.2. Results with the cracks

The two cracks of width 1.5 mm (crack 1) and 3 mm (crack 2) were modeled at three different locations around the fixed point. These were all on the crucible wall perpendicular to the blackbody tube. Position 1 is closest to the

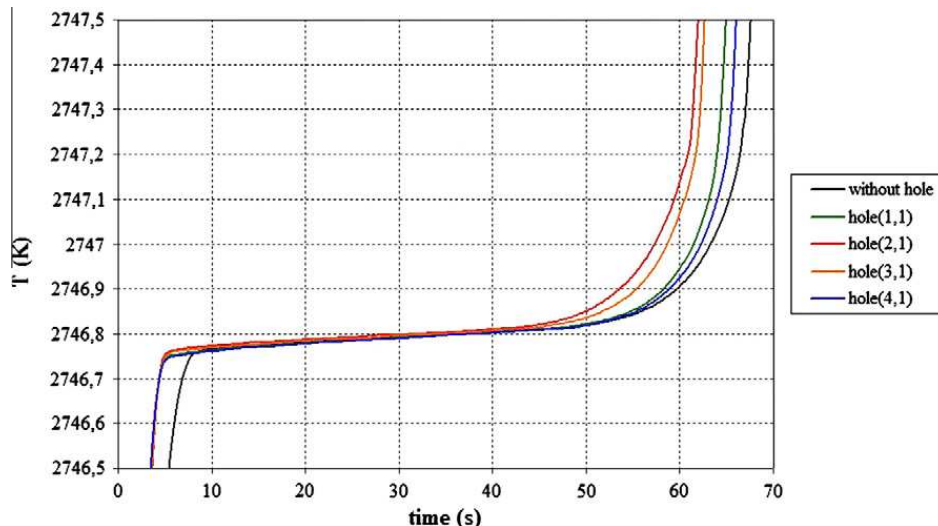


Fig. 2. Results of thermal model for the hole $2.5 \text{ mm} \times 3 \text{ mm}$ in different locations. The no-hole model is plotted for reference.

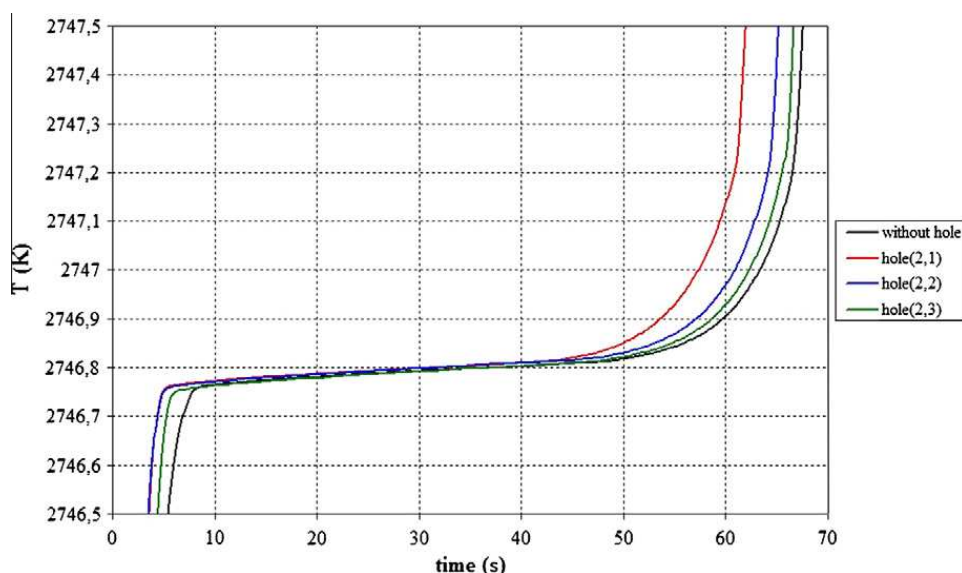


Fig. 3. Results of thermal model for the three different size holes in the same location that is position 2 (as shown in Fig. 1). The no-hole model is plotted for reference.

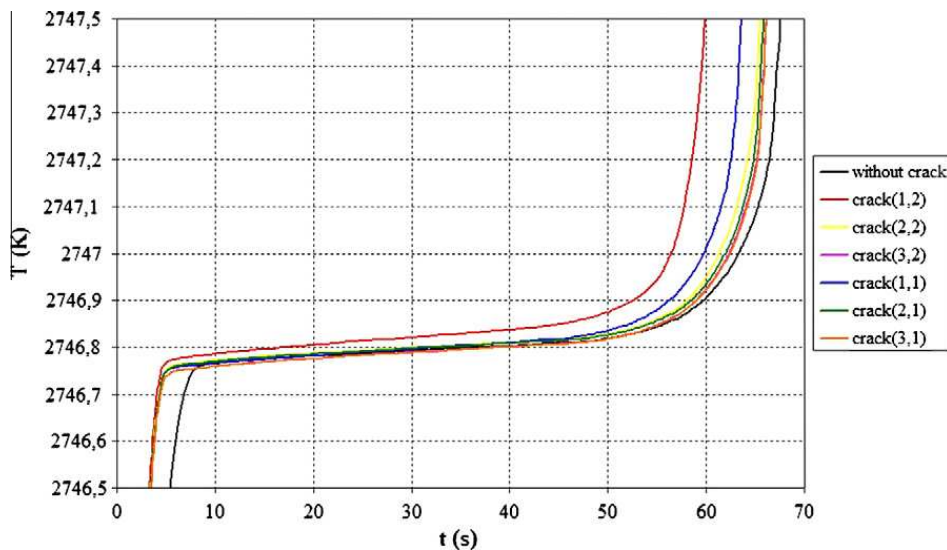


Fig. 4. Results of thermal model for the two different cracks in three different locations. The no-crack model is plotted for reference.

back wall, position 3 is relatively close to the front face of the crucible (see Fig. 1). The cracks in principle allow for direct line of sight from the outer crucible wall to the blackbody. Fig. 4 shows the effect on the radiance temperature of cracks of the two different dimensions in the three different locations.

In this case the large crack close to the back wall significantly affected the radiance temperature, increasing it by about 0.1 °C and shortening the melting point duration. The smaller crack in the same location ($x = 1$) had a smaller but noticeable effect. Interestingly however, cracks further away from the back wall only had a marginal effect on the areal average temperature.

4. Discussion

These results were initially rather surprising. The authors anticipated that transfer by radiation was such an efficient heat transfer mechanism compared to conduction that it would dominate over the latter. In fact this is clearly not the case. This was borne out when the thermal model was examined in detail. When the dynamic model of the melt was examined closely conduction was clearly seen as much more effective at transferring heat than radiation – so much so that the melt front in the solid actually “caught up” the melt front induced by radiative transfer.

This can be understood through a simple one-dimensional analytic calculation of heat flux between two parallel surfaces comparing conductive and radiative heat flux. The ratio of radiative heat flux to conductive heat flux is given by

$$\frac{q_r}{q_c} = \frac{4\sigma T^3 x}{k(\varepsilon_1^{-1} + \varepsilon_2^{-1} - 1)} \quad (1)$$

Where q_r/q_c is the ratio of radiative to conductive heat fluxes, σ is the Stefan Boltzmann constant, T is the

thermodynamic temperature, x is the separation between the parallel surfaces, k is the thermal conductivity of the material, ε_1 is the emissivity of the hotter material and ε_2 is the emissivity of the cooler material.

If the typical values at the Re–C point (2747 K) given at the beginning of Section 2 are used for the material properties of Re and graphite then for a small hole of 2.5 mm width, compared to conduction across a 2.5 mm slab of Re, the ratio of heat fluxes is 0.071 showing that conduction strongly dominates. For illustrative purposes if the hole became 25 mm then the ratio becomes 0.71 with radiative heat flux becoming almost as effective as conductive heat flux.

It is therefore clear that a small number of even quite large hole like flaws on the surface ingot can be tolerated, even when close to the back wall of the blackbody. This is a direct consequence of conductive heat transfer being so much more efficient than radiative heat transfer *on the small scales* present in the ingot. By the time the melt front has penetrated well into the ingot the effect of the hole has effectively been smoothed out.

Even the presence of small cracks in the ingot if located well away from the back wall of the cavity have little effect, provided the temperature gradient along the crucible wall is small. However caution needs to be exercised here because cracks in the ingot near the region of the back wall can have a significant effect on the resultant radiance temperature. There is an interesting implication from these results. As it appears that the radiance temperature of the fixed point is not significantly affected by small cracks when a reasonable distance from the back wall of the radiating cavity, it might well be possible to reduce the ingot size (the exact amount to be calculated through modeling) without adversely affecting the overall temperature performance of the fixed point. This conclusion is of course contingent on having a reasonably uniform furnace. But it seems that it may be possible to construct HTFPs with reduced material at the front of the fixed-point without

significantly impairing its radiometric performance (though of course the duration of the melt would be somewhat reduced, but this is of little significance for radiation thermometry). This is important, particularly when constructing ingots from expensive materials such as platinum.

5. Conclusions

The conclusions to be drawn from this work are:

- That even at high temperatures, for the dimensions of the structures under consideration in this paper, conductive heat transfer is still more effective than radiative transport.
- Minor imperfections in fixed-point ingots such as holes on the ingot surface can be neglected.
- Cracks in the ingot when near the back wall of the cavity have a significant impact on the radiance temperature but are of less importance when away from the back wall.
- It seems possible, though further study should be undertaken to confirm this finding, that the length of the ingot in a good furnace could be significantly reduced in size – covering only the rear portion of the blackbody tube. This influences the duration of the plateau but not particularly the achieved temperature.

Acknowledgements

G. Machin gratefully acknowledges the UK government's Department of Innovation, Universities and Skills for supporting this work through the NMS programme for Materials and Thermal Metrology (2007–2010).

References

- [1] G. Machin, P. Bloembergen, J. Hartmann, M. Sadli, Y. Yamada, A concerted international project to establish high temperature fixed-points for primary thermometry, *Int. J. Thermophys.* 28 (2007) 1976–1982.
- [2] E. Woolliams, G. Machin, D. Lowe, R. Winkler, Metal (carbide)-carbon eutectics for thermometry and radiometry: a review of the first seven years, *Metrologia* 43 (2006) R11–R25.
- [3] D. Lowe, G. Machin, Development of metal–carbon eutectic blackbody cavities to 2500 °C at NPL, in: B. Fellmuth, J. Seidel, G. Scholz (Eds.), Tempmeko 01, The 8th International Symposium on Temperature and Thermal Measurements in Industry and Science, Berlin, Germany, Published: VDE VERLAG GMBH, 2002, pp. 519–524.
- [4] G. Machin, Realising the benefits of improvements in high temperature metrology, *Acta Metrologica Sinica* 29 (2008) 10–17.
- [5] P. Castro, P. Bloembergen, Y. Yamada, M.A. Villamanan, G. Machin, On the uncertainty in the temperature drop across the backwall of high-temperature fixed points, *Acta Metrologica Sinica* 29 (2008) 253–260.
- [6] P. Jimeno Largo, P. Bloembergen, Y. Yamada, G. Machin, M.A. Villamanan, 2005. Numerical analysis of the temperature drop across the cavity wall of high temperature fixed points for radiation thermometry, in: Davor Zvizdic (Ed.), Tempmeko 04, The 9th International Symposium on Temperature and Thermal Measurements in Industry and Science, Zagreb, Croatia, Published: LPM/FSB, pp. 335–340.

On the Uncertainty in the Temperature Drop across the Backwall of High-Temperature Fixed Points

P.Castro¹, P.Bloembergen², Y.Yamada³, M.A. Villamanan¹, G. Machin⁴

¹University of Valladolid, Spain, ²Formerly at NMIJ, AIST, Japan, ³NMIJ, AIST, Japan, ⁴NPL, UK.

Abstract: In this paper we evaluate ΔT , the temperature drop across the cavity's backwall, and its standard uncertainty $u(\Delta T)$ for the high-temperature eutectic fixed points Co-C, Pt-C and Re-C with eutectic temperatures T_E of 1597 K, 2011 K and 2747 K, respectively; the evaluation involves a variety of cavity-furnace geometries. For the derivation of $u(\Delta T)$ the partial uncertainties in ΔT associated with the uncertainties in the thermal conductivity K_g of graphite, in the cavity-wall emissivity ε_g and in the furnace-temperature profile ahead of the cavity are evaluated and quantified. ΔT is shown to vary with T_E^4 for a given cell-furnace configuration, with typical values of 12 mK, 25 mK and 92 mK at the Co-C, Pt-C and Re-C fixed-point temperatures, respectively. For the uncertainty in the temperature drop we find globally $u(\Delta T) \approx 0.1 \cdot \Delta T$.

Key words: Temperature drop; Fixed points; High-Temperature; Sensitivity coefficients; Uncertainty

CLC number:

Document code:

Article ID:

1. Introduction

At or below the copper point ($T = 1357.77$ K) the correction for the temperature drop ΔT across the backwall of the cavity has been found to be smaller than the uncertainty in the fixed-point realization itself. Since radiative heat exchange increases with T^4 , the situation might be different for high-temperature fixed points such as the metal-carbon or metal carbide-carbon eutectic fixed points[1]. In this paper we evaluate the uncertainty $u(\Delta T)$ in the temperature drop ΔT affecting the high-temperature eutectic fixed points Co-C, Pt-C and Re-C with eutectic temperatures T_E of 1597 K, 2011 K and 2747 K, respectively, for a variety of cavity-furnace geometries.

It should be mentioned that these fixed points are presently objects of an extensive study within the international 'High-temperature fixed-point project', coordinated by Working Group 5 of the CCT[2].

The systems to be modeled are described in section

2. Model structure and quantities to be calculated are surveyed in section 3. Results are presented in section 4 and discussed in section 5. The main conclusions are presented in section 6.

This study is to be considered a follow up to [3] and [4]. For a survey of earlier studies on this subject we refer to [3]. Modeling of the various systems to be considered below is done by FLUENT a software package utilizing *finite-volume* analysis, usually applied in the study of liquids and gases. The work on the temperature drop presented in [3] and [4] was based upon *finite-element* analysis implemented in the ANSYS package. Results obtained with FLUENT and ANSYS, applied to some typical cases within the sphere of the present study, showed that they can be considered equivalent within the resolution of the calculations.

2. Systems to be modeled

The system serving in the main as the experimental

Received:

Corresponding e-mail address: pablocastroal@yahoo.es

environment to the calculations to be surveyed in section 3 is shown in figure 1.

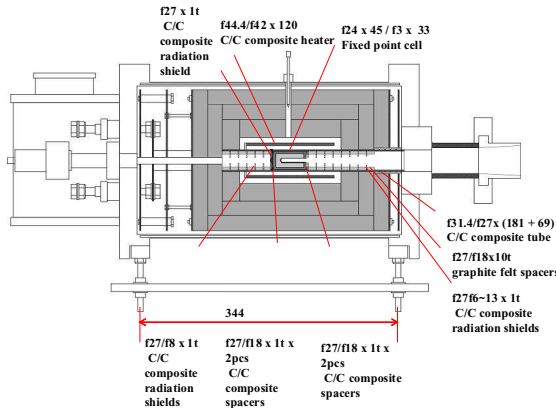


Figure 1: Nagano VR10-A23 furnace with crucible.

Dimensions in mm.

It is the Nagano ‘VR10-A23’, designed by NMIJ, within which the fixed-point cell is placed for observation by a radiation thermometer mounted in front of the furnace. A picture of the cell, type 6ST, designed by NMIJ, is shown in figure 2C; its geometry is specified in table 1.

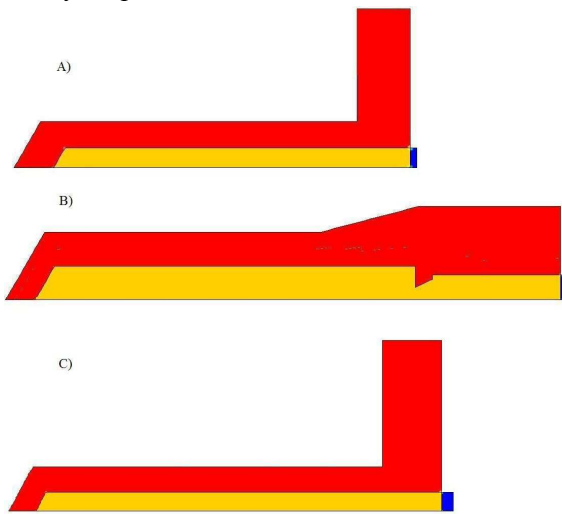


Figure 2: The cells in study: Mk-4 (A), 3S (B), 6ST (C).

Furnace-temperature profiles, carried by eight radiation fields placed ahead of the cell are measured at the Co-C, Pt-C and Re-C eutectic fixed points; these are shown by the continuous curves in figure 3, denominated as RP (real profile) in the legend. The radiation shields are 1 mm thick C/C composite plates, placed 10 mm apart, with holes increasing in diameter

in 1 mm increment. The measurements have been carried out with an LP-5 thermometer with 1 mm target size at a measurement distance of 760 mm. The average width viewable for each shield is only 0.5 mm, therefore the readings represent the radiance averaged over three consecutive shields.

Table 1. Cell parameters for the cells Mk-4, 3S, 6ST.

cell/dimensions ¹⁾	cavity diameters ²⁾	backwall thickness	cavity length	tilt angle
Mk-4	3 / 3	2.6	27	30°
3S	8 / 3	2.6	62	30°
6ST	3 / 3	2	34	30°

¹⁾ Dimensions in mm, ²⁾ $D(\text{cyl})/D(\text{aperture})$

In order to evaluate the influence of the furnace-temperature profile (FTP) on ΔT and its uncertainty $u(\Delta T)$, calculations for the 6ST cell have been extended to include additional FTP’s as well, to be denominated as NF, HP, RP and CP, specified as follows: NF: cell without furnace, RP: real profile, as measured in Nagano VR10-23, CP: isothermal profile set to the eutectic temperature T_E of the fixed point in question. As to the profile HP, shown in figure 3: it has been derived from measurements done in another furnace, a three-zone furnace, Nagano ‘VR10-A19’, by shrinking the x dimension at the Re-C eutectic fixed point [3]. It is represented by the upper discontinuous curve (denominated as HP in the legend) in figure 3. The two lower discontinuous curves are obtained by shifting the upper one parallel to the T -axis such that their maximum is located at the fixed-point temperature of eutectic Pt-C and Co-C, respectively.

Finally: To get an impression of the influence of the cell geometry, calculations have been performed for three cells of different geometry, denominated as 6ST, 3S, Mk-4; like 6ST, 3S is designed by NMIJ, Mk-4 was designed by NPL. The comparison is done for the ‘worst case’ i.e. the NF profile only. Pictures of the cells are given in figure 2, cell geometries are specified in table 1.

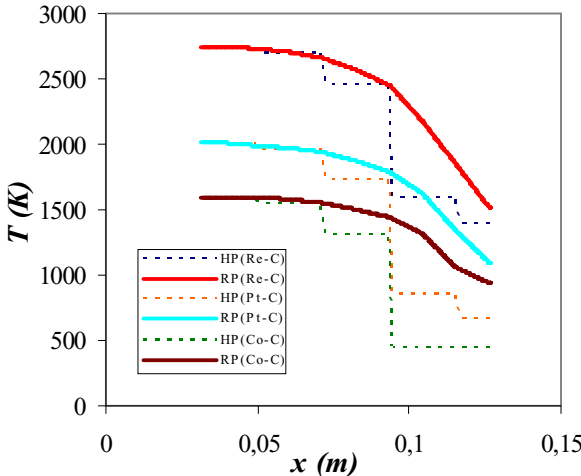


Figure 3: Furnace-temperature profiles: continuous curves : real profiles (RP), as measured for Nagano VR10-A23 at the fixed-point temperatures of the eutectics Co-C, Pt-C, Re-C. Discontinuous curves: based upon measurements for Nagano VR10-A19, cf. the text. x measures the distance to the centre of the furnace.

As in [3,4] the results to be reported in section 4 are compared with the results obtained from the simple eq.(1), suggested earlier by Fischer and Jung [5]:

$$\Delta T = \cos\vartheta \cdot (r/L)^2 \cdot d \cdot (\varepsilon_g/K_g) \cdot \sigma \cdot T^4, \quad (1)$$

where ϑ is the tilt angle of the cavity bottom, r the cavity-aperture radius, L the cavity length, d the thickness of the cavity bottom, ε_g the emissivity of graphite, K_g the thermal conductivity of graphite, σ the Stefan-Boltzmann constant and T the cavity's temperature in K. In the derivation of this equation radiant heat exchange within the cell and between cell and the front end of the furnace has been neglected.

3. Calculations

3.1. Model structure and material properties

As in [3] several assumptions were necessary in order to simplify the problem of calculating the parameters in question; without these simplifications either the modeling would have taken too much computer time or couldn't even have been carried out at all.

1-The model geometry is considered axisymmetric; this allowed us to construct a 2D model.

2-The thermal resistance at contacting elements or screw parts is neglected because of its relatively small influence and the difficulty of estimating it [6,7].

3-Heat transfer due to convection and conduction in the furnace atmosphere has been taken into account, but these turned out to be negligible.

4-The model assumes steady-state conditions.

The thermal conductivity of graphite as a function of temperature over the range of interest, is taken from [8]. From this the values 53.6, 45.6, 36.5 in $\text{Wm}^{-1}\text{K}^{-1}$ at the fixed-point temperatures of the eutectics Co-C(1597 K), Pt-C (2011 K), Re-C (2747 K), respectively, are derived. The emissivity of graphite, quoted nominally as 0.86, is from [5].

3.2. Quantities to be calculated

Quantities, calculated and discussed in section 4 and 5, respectively, given here in the order presented below, are:

(1) Temperature drop: ΔT

It should be noted that ΔT is calculated with the temperature all over the outside of the cavity wall, or all over the inside of the ingot, set to the eutectic temperature T_E . This simulates the end of the melting process in an idealized fashion and obviates the need of implementing the ingot in the modeling.

The temperature drop is defined as $\Delta T = T_E - T_{\text{cav}}$, where T_{cav} is taken as the areal average of the bottom temperature over the field of view of the radiation thermometer.

(2) Sensitivity coefficients: $(\partial \Delta T / \partial K_g)_{\varepsilon_g}$ and $(\partial \Delta T / \partial \varepsilon_g)_{K_g}$

These coefficients are denoted occasionally in the text as SCK and SCE , respectively.

As demonstrated in figures 4a and 4b for the case: cell: 6ST, fixed-point: Re-C, FTP: RP, the parameters SCK or SCE are obtained by calculating ΔT over a suitable range of values of the independent variable K_g or ε_g , respectively, and taking the slope of the thus obtained graph ΔT versus K_g or ΔT versus ε_g at the respective nominal values.

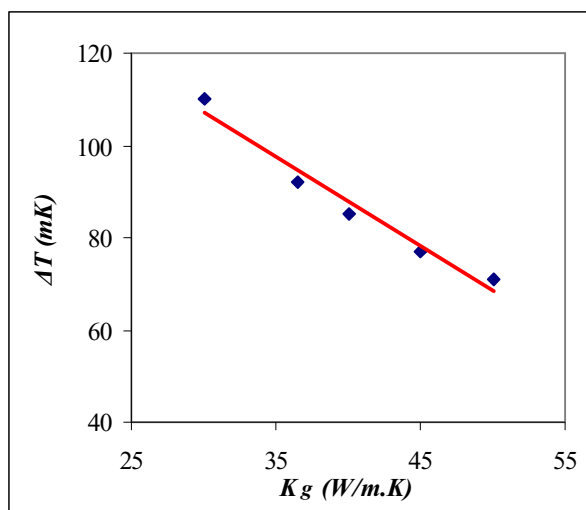


Figure 4a: Determining $(\partial \Delta T / \partial K_g)_{eg}$, SCK, cf. the text.

It should be mentioned here that according to eq. (1) we would have, in good approximation :

$$(\partial \Delta T / \partial K_g)_{eg} = -\Delta T / K_g \quad (2a)$$

$$(\partial \Delta T / \partial \varepsilon_g)_{Kg} = \Delta T / \varepsilon_g \quad (2b)$$

(3) Standard uncertainty in the parameters K_g and ε_g : $u(K_g)$ and $u(\varepsilon_g)$

(4) Partial uncertainties :

$u(\Delta T; K_g)$:

Uncertainty in ΔT due to the uncertainty $u(K_g)$ in K_g

$u(\Delta T; \varepsilon_g)$:

Uncertainty in ΔT due to the uncertainty $u(\varepsilon_g)$ in ε_g

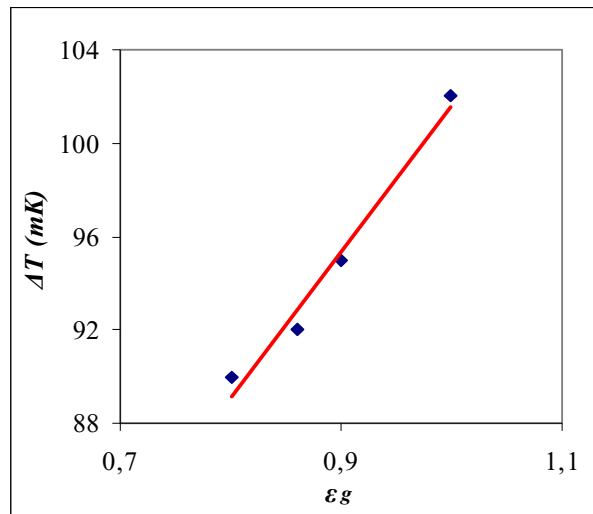


Figure 4b: Determining $(\partial \Delta T / \partial \varepsilon_g)_{Kg}$, SCE, cf. the text.

$u(\Delta T; K_g, \varepsilon_g)$:

Uncertainty in ΔT due to the combined uncertainties $u(K_g)$ in K_g and $u(\varepsilon_g)$ in ε_g

$u(\Delta T; \text{FTP})$:

Uncertainty in ΔT due to the uncertainty in the FTP

(5) Overall standard uncertainty in ΔT : $u(\Delta T)$

4. Results

Cell: 6ST

Table 2, upper section, shows ΔT calculated at the fixed-point temperatures of Re-C, Pt-C and Co-C for the furnace-temperature profiles (FTP's) NF, HP, RP, CP. The results obtained when applying eq.(1) are

Table 2. ΔT , $(\partial \Delta T / \partial K_g)_{eg}$, $(\partial \Delta T / \partial \varepsilon_g)_{Kg}$ for different furnace-temperature profiles¹⁾; cell: 6ST

ΔT / mK		Furnace Temperature Profile				
System	NF	HP	RP	CP	Eq. (1)	
Re-C	107	94	92	89	256	
Pt-C	29	27	25	24	59	
Co-C	12	12	12	12	20	
$(\partial \Delta T / \partial K_g)_{eg}$ mK / unit ²⁾						
System	NF	HP	RP	CP	Eq. (2a)	
Re-C	-2,35	-2,27	-1,95	-2,13	-2,44	
Pt-C	-0,800	-0,650	-0,705	-0,550	-0,526	
Co-C	-0,339	-0,212	-0,212	-0,212	-0,224	
$(\partial \Delta T / \partial \varepsilon_g)_{Kg}$ mK / unit						
System	NF	HP	RP	CP	Eq. (2b)	
Re-C	55,0	60,0	60,0	55,0	103	
Pt-C	15,0	15,0	10,0	15,0	27,9	
Co-C	5,0	5,0	5,0	5,0	14,0	

¹⁾ Calculations with $K_g = 36,5, 45,6, 53,6 \text{ Wm}^{-1}\text{K}^{-1}$ for Re-C, Pt-C, Co-C, respectively, and $\varepsilon_g = 0,86$.

²⁾ Unit = $\text{Wm}^{-1}\text{K}^{-1}$.

shown in the last column. The calculations are done for a wall emissivity ε_g of 0.86 and for thermal conductivities K_g associated with the fixed-point temperatures in question[5, 8].

Results for the profiles NF, HP, RP, CP obtained at the fixed points in question are shown in the histogram presented in figure 5. Figure 6 shows ΔT , calculated for the profile CP, as a function of the (nominal) eutectic temperature T_E of the eutectics Co-C, Pd-C, Pt-C, Ir-C, and Re-C. The full line represents the fit $\Delta T = 1.50 \cdot 10^{-15} \cdot T_E^4$.

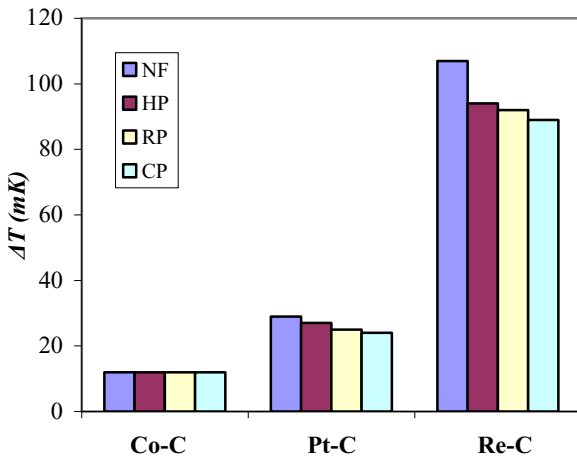


Figure 5: ΔT versus fixed point: Co-C, Pt-C, Re-C for the furnace-temperature profiles: NF, HP, RP, CP. Cell: 6ST.

Table 2, mid and lower section, show the sensitivity coefficients $(\partial \Delta T / \partial K_g)_{eg}$ and $(\partial \Delta T / \partial \varepsilon_g)_{kg}$, respectively, at the three fixed points, again as a function of the temperature profile, for the cell 6ST.

The data under Eq. (2a) and Eq. (2b) are obtained when applying the equations: $\partial \Delta T / \partial K_g = -\Delta T / K_g$ and $\partial \Delta T / \partial \varepsilon_g = \Delta T / \varepsilon_g$, respectively, but with ΔT calculated for the CP furnace-temperature profile, shown in figure 6.

Comparing cells, FTP: NF

In table 3 we compare ΔT and the sensitivity coefficients $(\partial \Delta T / \partial K_g)_{eg}$ and $(\partial \Delta T / \partial \varepsilon_g)_{kg}$, respectively, calculated for the cells 3S, 6ST and Mk-4 at the three fixed points for the ‘profile’ NF.

Uncertainties. Cell: 6ST, FTP: RP

Finally tables 4a and 4b review the uncertainty estimates leading to the estimated standard uncertainty $u(\Delta T)$ in ΔT ; all uncertainties are meant to

represent standard uncertainties. Table 4a gives the uncertainty estimates $u(\Delta T; K_g)$ and $u(\Delta T; \varepsilon_g)$ and their combined values $u(\Delta T; K_g, \varepsilon_g)$ associated with the uncertainties $u(K_g)$ in K_g and $u(\varepsilon_g)$ in ε_g , which we deliberately estimate as two units and 0.1 unit, respectively. With this we have $u(\Delta T; K_g) = (\partial \Delta T / \partial K_g) \cdot u(K_g)$ and $u(\Delta T; \varepsilon_g) = (\partial \Delta T / \partial \varepsilon_g) \cdot u(\varepsilon_g)$. Finally: $u(\Delta T; K_g, \varepsilon_g) = \{ u(\Delta T; K_g)^2 + u(\Delta T; \varepsilon_g)^2 \}^{1/2}$.

$u(\Delta T ; \text{FTP})$ in table 4b represents the estimated uncertainty in ΔT associated with the uncertainty $u(\text{FTP})$ in the furnace-temperature profile (FTP) which for the time being is taken roughly as $u(\text{FTP}) = [\Delta T(\text{HP}) - \Delta T(\text{CP})]/2$. The rationale to this can be appreciated from an inspection of figure 5, from which we see that the ΔT associated with the RP is bracketed in-between the values obtained for HP and CP. $u(\Delta T)$ is given by $u(\Delta T) = \{ u(\Delta T; K_g, \varepsilon_g)^2 + u(\Delta T; \text{FTP})^2 \}^{1/2}$.

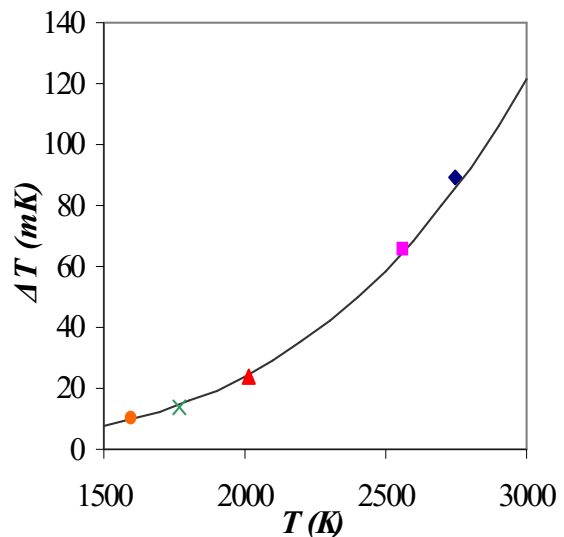


Figure 6: ΔT versus eutectic temperature T_E calculated for the fixed-point temperatures of the eutectics Co-C, Pd-C, Pt-C, Ir-C and Re-C. Cell: 6ST. Furnace-temperature profile: CP. The full line represents $\Delta T = 1.50 \cdot 10^{-15} \cdot T_E^4$.

5. Discussion

Cell: 6ST

The results ΔT illustrated in figure 5 show a significant increase with fixed point from Co-C towards Re-C and a more gradual decrease with FTP from NF towards CP. For Co-C the results show no dispersion within the resolution of the calculations. Figure 6 for FTP-CP shows that for a given FTP ΔT

would increase as T_E^4 in agreement with eq. (1); it reflects the increase of the total radiant flux emitted by a blackbody radiator radiating at a temperature T with T^4 according to the law of Stefan-Boltzmann.

The results for $(\partial \Delta T / \partial K_g)_{eg}$, SCK and $(\partial \Delta T / \partial \varepsilon_g)_{Kg}$, SCE compiled for HP, RP and CP in table 2, mid and lower section, respectively, show that the sensitivity coefficients in question are essentially *immune* to variations of the FTP. (For SCE this observation can be extended to include NF as well). This is an important observation for it means that the associated uncertainties can be calculated on the basis of results obtained for CP i.e. for this the actual FTP (for a given cell-furnace geometry) is not needed.

The results under Eq. (2a) and Eq. (2b), last column, calculated as $-\Delta T/K_g$ and $\Delta T/\varepsilon_g$, cf. section 4, are in reasonably good agreement with the direct calculations for the FTPs in question for SCK , but less so for SCE , where they still might serve the purpose of serving as an upper bound. In principle the results under Eqs (2a), (2b) can be obtained from one calculation of ΔT for a given T_E for profile CP, cf. figure 6. The larger difference for SCE (results differ by a factor of about two) can be understood qualitatively by noting that through the interaction of the cavity's backwall with the cylindrical cavity wall as well as with the front end of the furnace, neglected in eq.(1), the basis to eqs (2a) and (2b), ΔT is still less sensitive to changes in ε_g than predicted by the latter equation, even when adapted for ΔT . So empirically we find $(\partial \Delta T / \partial K_g)_{eg} \approx -\Delta T/K_g$, $(\partial \Delta T / \partial \varepsilon_g)_{Kg} \approx 0.5 \cdot \Delta T/\varepsilon_g$ for the cell 6ST in combination with the CP and -as it turns out- with any of the other furnace-temperature profiles considered.

Table 4a. Uncertainty components in ΔT for cell 6ST; furnace-temperature profile: RP

T_E	$(\partial \Delta T / \partial K_g)_{eg}$	$u(\Delta T; K_g)$	$(\partial \Delta T / \partial \varepsilon_g)_{Kg}$	$u(\Delta T; \varepsilon_g)$	$u(\Delta T; K_g, \varepsilon_g)$
K	mK / unit ¹⁾	mK	mK / unit	mK	mK
2747	1.95	3.90	60.0	6.0	7.16
2011	0.705	1.41	10.0	1.0	1.73
1597	0.212	0.424	5.0	0.5	0.65

¹⁾Absolute values, unit = $\text{Wm}^{-1}\text{K}^{-1}$

Comparing cells, FTP: NF

Table 3 shows ΔT , $(\partial \Delta T / \partial K_g)_{eg}$, SCK and $(\partial \Delta T / \partial \varepsilon_g)_{Kg}$, SCE respectively, calculated for the cells 3S, 6ST and Mk-4 for the profile NF. Differences between the values of these parameters for the ‘worst case’ NF are of interest since they give an impression of the influence of the cell geometry.

Table 3. ΔT , $(\partial \Delta T / \partial K_g)_{eg}$, $(\partial \Delta T / \partial \varepsilon_g)_{Kg}$ for different cells¹⁾; furnace-temperature profile: NF

ΔT / mK	Cell		
System	3S	6ST	Mk-4
Re-C	144	107	169
Pt-C	35	29	40.5
Co-C	21	12	14
$(\partial \Delta T / \partial K_g)_{eg}$ mK / unit ²⁾			
System	3S	6ST	Mk-4
Re-C	-3.10	-2.35	-4.10
Pt-C	-1.00	-0.800	-1.21
Co-C	-0.424	-0.339	-0.364
$(\partial \Delta T / \partial \varepsilon_g)_{Kg}$ mK / unit			
System	3S	6ST	Mk-4
Re-C	65.0	55.0	85.6
Pt-C	25.0	15.0	28.5
Co-C	5.0	5.0	8.7

¹⁾ Calculations with $K_g = 36.5, 45.6, 53.6 \text{ Wm}^{-1}\text{K}^{-1}$ for Re-C, Pt-C, Co-C, respectively, and $\varepsilon_g = 0.86$. ²⁾ Unit = $\text{Wm}^{-1}\text{K}^{-1}$.

Table 4b. Overall uncertainty $u(\Delta T)$ in ΔT for cell 6ST; furnace-temperature profile: RP

T_E	ΔT	$u(\Delta T; K_g, \varepsilon_g)$	$u(\Delta T; \text{FTP})$	$u(\Delta T)$	$u(\Delta T)/\Delta T$
K	mK	mK	mK	mK	
2747	92	7.16	2.50	7.6	0.08
2011	25	1.73	1.50	2.3	0.09
1597	12	0.65	0.00	0.6	0.05

As may be appreciated from an inspection of the table the differences for the cells 3S and 6ST are not drastic, the values for 3S being systematically larger (in the absolute sense) with the exception of *SCE* for Co-C. As regards 3S versus 6ST this may have to do in part with the larger backwall thickness d for 3S: 2.6 mm versus 2 mm for 6ST, involving a larger ΔT and thus larger values of *SCK* and *SCE*, cf. the discussion in the preceding paragraph. The values obtained for Mk-4, calculated by L. Wright [9], on the basis of the software program Abaqus, are still significantly larger than for 3S, although in this case again $d = 2.6$ mm. This may be understood from the differences in cavity geometry: whereas Mk-4 (a) (like the cavity of 6ST) consists of a cylindro-cone of 3 mm diameter over a length of 27 mm, the cavity of 3S (b) consists of a cylindro-cone 8 mm in diameter over a length of 62 mm, but diaphragmed by a 3 mm aperture. This means that the cavity (b) may be supposed to better than (a) approximate ideal-blackbody conditions, involving a smaller temperature drop and thus smaller values for *SCK* and *SCE* in case (b).

Uncertainties. Cell: 6ST, FTP: RP

Finally the comment to tables 4a and 4b reviewing the uncertainty estimates, calculated as explained in section 4, last two paragraphs. This is to be considered a first qualitative approach, especially as regards the derivation of the component $u(\Delta T; \text{FTP})$; it will be further refined in on-going investigations. Also the estimates given for $u(K_g)$ and $u(\varepsilon_g)$, section 4, will have to be reconsidered taking into account the differences between the values of these parameters, reported in the literature. From the present provisional analysis it appears that the uncertainty $u(\Delta T)$ amounts to about 10 % of ΔT . It probably represents an upper bound to $u(\Delta T)$.

6. Conclusions

-For a given fixed-point cell, radiating at a temperature T , and a given furnace-temperature profile (FTP) the temperature drop ΔT across the backwall of the fixed-point cavity varies with T^4 over the temperature range considered. For a specific case studied in this paper ΔT would vary from about 5 mK at the copper point ($T=1357.77$ K) to 90 mK at the Re-C eutectic temperature ($T_E = 2747$ K). For the case in question at 3500 K we would have $\Delta T = 220$ mK.

-The sensitivity coefficients $(\partial \Delta T / \partial K_g)_{eg}$ and $(\partial \Delta T / \partial \varepsilon_g)_{Kg}$ are essentially *immune* to the FTP. This is an important observation for it means that the associated uncertainties can be calculated on the basis of results obtained for the constant-temperature profile CP i.e. for this the actual FTP (for a given cell-furnace geometry) is not needed.

-Empirically we find $(\partial \Delta T / \partial K_g)_{eg} \approx -\Delta T / K_g$, $(\partial \Delta T / \partial \varepsilon_g)_{Kg} \approx 0.5 \cdot \Delta T / \varepsilon_g$ over the temperature range in question for the cell 6ST in combination with any of the furnace-temperature profiles considered.

-A first estimate of the uncertainty $u(\Delta T)$ for a given cell-furnace geometry, 6ST/RP, yields $u(\Delta T) \approx 0.1 \cdot \Delta T$ over the temperature range considered.

-For more precise statements regarding $u(\Delta T)$ the uncertainties in the thermal conductivity $u(K_g)$ of graphite, in the wall emissivity $u(\varepsilon_g)$ and in the furnace-temperature profile $u(\Delta T; \text{FTP})$ have to be definitively assessed.

-For a given cell geometry ΔT and $u(\Delta T)$ can be minimized by minimizing the thickness d of the backwall of the cavity and the aperture of a diaphragm

positioned in front of the cavity to allowable minima.

-When replacing the real furnace-temperature profile RP by its isothermal counterpart CP for the cell 6ST the errors introduced in ΔT would amount to only 3 mK, 1 mK and zero at the eutectic temperatures of Re-C, Pt-C, Co-C, respectively, corresponding with relative errors of 3%, 4% and (virtually) zero in ΔT (92, 25 and 12 mK, respectively) at these temperatures. From this point of view the profile CP would be good enough for generating ΔT as well.

-In our analysis uncertainties associated with the uncertainty in cell dimensions-influenced by temperature- and the uncertainty in the dimensions of the structure of radiation shields ahead of the cell have been disregarded. It has yet to be demonstrated that these can indeed be neglected.

ACKNOWLEDGEMENTS. The contributions of Naohiko Sasajima of NMIJ to some of the drawings presented in this paper are acknowledged.

REFERENCES

1. E.R.Wooliams, G. Machin, D. Lowe, R. Winkler, *Metrologia*. 2006, 43, R11.
2. G. Machin, This conference.
3. P. Jimeno-Largo, Y. Yamada, P. Bloembergen, M.A. Villamanan, G. Machin. Numerical analysis of the temperature drop across the cavity bottom of high-temperature fixed points for radiation thermometry. In *Proceedings of TEMPMEKO 2004*. Edited by D.Zvizdić, L.G. Bermanec, T. Veliki, T.Stasić. Zagreb: FSB/LPM, 2004, 335-340.
4. P.Bloembergen, B.B. Khlevnov, P. Jimeno-Largo, Y.Yamada. Spectral and total effective emissivity of a high-temperature fixed-point radiator considered in relation to the temperature drop across its backwall. *Int. J. Thermophysics*, 2008.
5. J. Fischer, H.J. Jung, Determination of the thermodynamic temperatures of the freezing points of silver and gold by near-infrared pyrometry. *Metrologia*.1989, 26, 245-252.
6. C.K. Ma. Calculation of the distribution of emissivity and temperature for a baffled cylindrical cavity at the freezing points of Ag, Au and Cu. In *Proceedings of TEMPBEIJING 1997*. Edited by B. Zhang et al. Beijing: Standard press of China, 1997, 72-77.
7. T.J. Horn and A.N. Abdelmessih. Experimental and numerical characterization of a steady-state cylindrical blackbody cavity at 1100 degrees Celsius. TM-2000-209022, National Aeronautics and Space Administration Dryden Flight Research Centre, 2000.
8. Y.S. Touloukian, R.W. Powell, C.Y. Ho and P.G. Klemens. Thermal conductivity: Nonmetallic Solids, Thermophysical properties of Matter. The TPRC Data Series, 2, New York, Plenum Press, 1978.
9. L. Wright, private communication.

Calculation of the Temperature Drop for High Temperature Fixed Points for Different Furnace Conditions

(to be published in International Journal of Thermophysics)

P. Castro¹ · G. Machin² · M. A. Villamañan¹ · D. Lowe²

¹ School of Engineering, Universidad de Valladolid, E-47071, Valladolid, Spain

² Engineering Measurement Division, National Physical Laboratory (NPL), Teddington, Middlesex, UK

E-mail: pablocastroal@yahoo.es

Abstract High temperature fixed points (HTFPs) based on eutectic and peritectic reactions of metals and carbon are likely to become, in the near term, reference standards at high temperatures. Typically these HTFPs, for radiation thermometry applications, are generally formed of a graphite crucible, with a reentrant well, an included 120° cone and a nominal aperture of 3 mm. It is important to quantify the temperature-drop at the back-wall of the cavity, and to understand the influence of the crucible configuration and furnace conditions on this drop.

In order to study these influences three different situations have been modeled by means of the finite volume method for numerical analysis. The first one is to study the influence of the furnace temperature profile by simulating four different furnace conditions. The other two situations study some variations in crucible configuration: the thickness of the graphite back-wall and the length of the blackbody tube.

Keywords Crucible · Fixed point · Back-wall · Blackbody tube · Furnace temperature profile

1. Introduction

We estimate the temperature drop for the following HTFPs, Co-C (1324 °C), Pd-C (1492 °C), Pt-C (1430 °C), Re-C (2424 °C) and WC-C (2449 °C), when realized in a Thermogage furnace. The following conditions are modeled:

- Ideal conditions: HTFP in uniform furnace at the HTFP temperature.
- Intermediate conditions: HTFP in furnace that has a sine temperature profile from the centre of the furnace to its aperture.
- Extreme conditions: Furnace has a linear gradient from the centre of the furnace to its aperture.
- Reference conditions: The bare HTFP crucible i.e. not in a furnace. This forms the upper bound of the temperature drop value.

In addition the influence of the thickness of the graphite back-wall on the value of the temperature drop is estimated for the five HTFPs in the reference and ideal conditions. This parameter is often indeterminate due to erosion of the back-wall during filling. The calculations of this effect here enable boundaries to be placed on the effect of back-wall thickness variation on temperature drop.

Due to some variations in the length of the crucibles used by the National Institutes of Metrology, three different blackbody tube lengths (1□, 2□ and 3□ mm long) have been also modeled for the five HTFPs in the reference and ideal conditions.

In this paper we describe how these calculations were performed and a summary given of the calculations. Finally a discussion of the implications of these results for the use of HTFPs as temperature references is given.

2. Description of the model

The studies described here are all performed for in a Thermogage 24 kW furnace (Fig. 1). It has a 24 mm internal diameter graphite tube of 290 mm long and is held between water-cooled copper electrodes and electrically heated by direct current. A detailed description of such a furnace is found in [1].

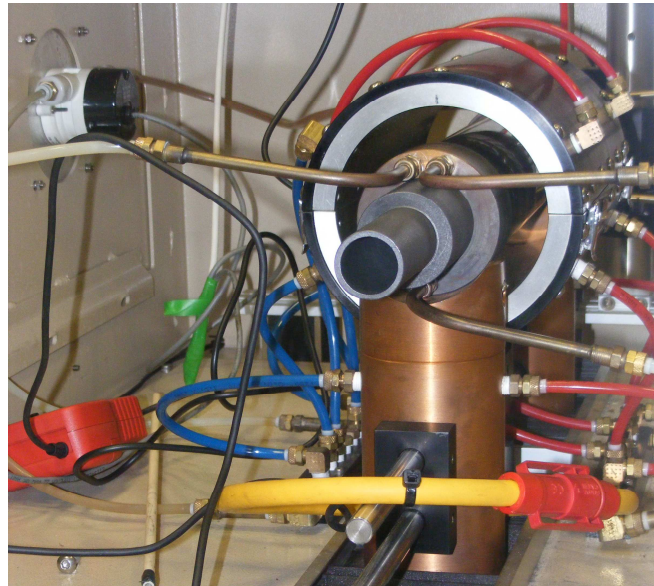


Fig. 1. Thermogage picture

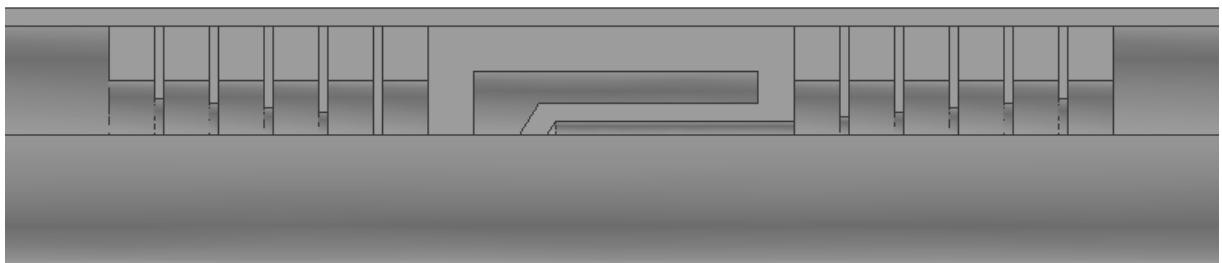


Fig. 2. Thermogage model, side view

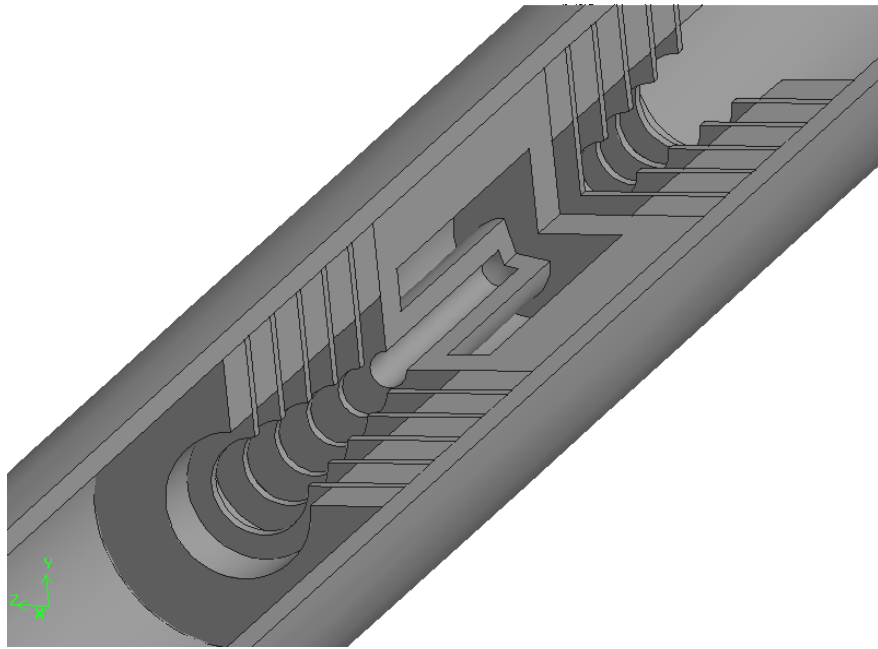


Fig. 3. Thermogage model, isometric view

A 2D axisymmetrical model of the tube was constructed (Fig. 2 and 3) with the following characteristics:

- Geometrical dimensions:

For investigating the effect of the furnace the following configuration was investigated.

- A mark 4 model NPL HTFP cell [2] was modeled. The graphite blackbody tube length was 20 mm, the aperture diameter was 3 mm and the back-wall thickness was 2.6 mm, with a 120° back-wall cone. The model was constructed with the HTFP crucible at the middle of the furnace tube, with six graphite foam and five radiation baffle insulation rings at both sides on the crucible. All together this configuration was 110 mm long so the tube continues 90 mm in each direction after the insulation.

In addition for investigating the effect of the variation in back-wall thickness due to erosion and in blackbody tube length the following was modeled.

- The same mark 4 HTFP cell but with five different back-wall thicknesses: 0.1, 1, 2, 2.6 and 4 mm. Two cases were modeled one with the uniform furnace conditions the other a bare mark-4 NPL crucible, without furnace.
- The mark 4 HTFP cell with 2.6 mm back-wall thickness with three different blackbody tube lengths: 10, 20 and 30 mm, which corresponds to the external crucible lengths of 30, 40 and 50 mm. They were modeled without furnace and with the uniform furnace conditions.

- Material properties:

Table 1 gives the main material properties used in the modeling, the quantities are heat capacity C_p (J/kg.K), thermal conductivity K (W/m.K), density ρ (kg.m⁻³), emissivity and melting temperature (K). Thermal conductivity value for graphite increases with the temperature from 32.4 W/m.K at 159 K to 53.6 W/m.K at 3022 K.

Table 1. Thermal properties of furnace materials

	Cp (J/kg.K)	K (W/m.K)	ρ (kg.m ⁻³)	emissivity	melting T (K)
Co-C	456	45	1200		1590
Pd-C	244	50	12023		1665
Pt-C	133	50	21450		2011
Re-C	214.5	55	21030		2440
WC-C	200	50	15000		3022
graphite	690	32.4, 36.5, 45.6, 51.1, 53.6	2250	0.06	
alumina	100	35	3900	0.35	
foams	30	0.35	50	0.06	
argon	520.64	0.0150	1.6220		

- Model boundary conditions:

Five different HTFP are simulated, each of them in 4 different thermal conditions:

- 1) Reference conditions. The bare crucible with the metal ingot at the nominal temperature of the fixed point and without furnace. The outer wall of the crucible is assumed to be uniform in temperature.
- 2) Extreme conditions: Furnace has a linear gradient from the centre of the furnace to its aperture.
- 3) Intermediate conditions: HTFP in furnace that has a sine temperature profile from the centre of the furnace to its aperture.
- 4) Ideal conditions: HTFP in uniform furnace at the HTFP temperature, i.e. the temperature along the graphite tube is constant at nominal temperature.

The furnace temperature profile (FTP) for conditions 2 to 4 can be seen in Fig. 4, 5 and 6.

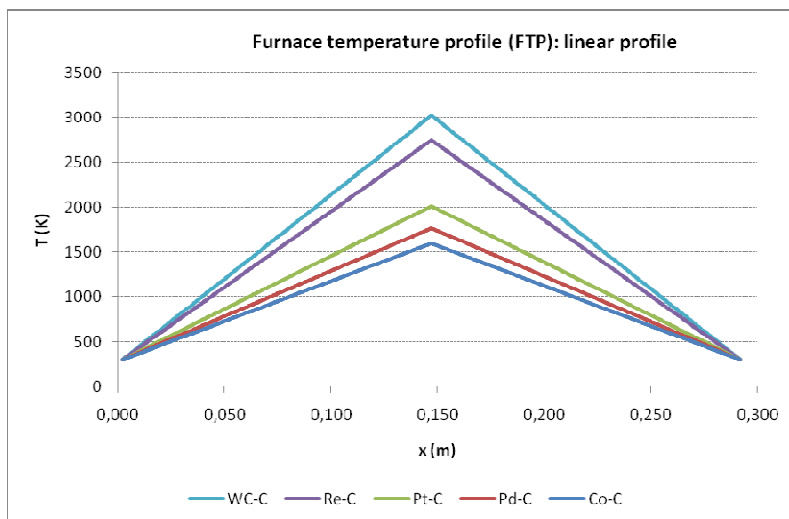


Fig. 4. Extreme condition: linear furnace temperature profile (LP)

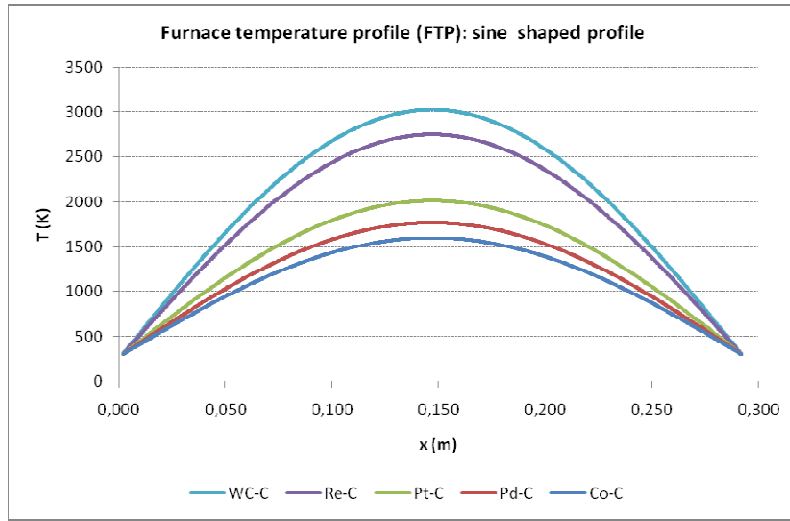


Fig. 5. Intermediate conditions: Sine shaped furnace temperature profile (sin P)

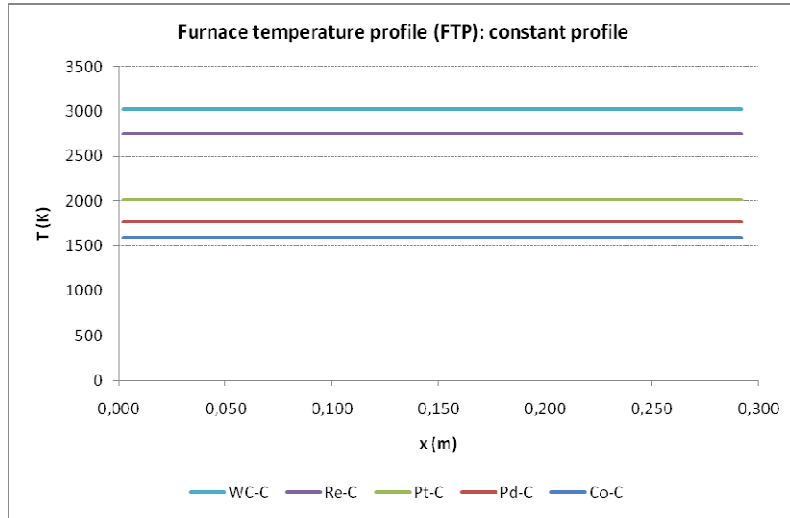


Fig. 6. Ideal conditions: constant furnace temperature profile (CP)

3. Simulation results

3.1 Temperature drop

The temperature drop across the back-wall of the cells has been calculated as the difference between the nominal temperature of each HTFP and the areal temperature average for the back-wall. The results are shown in Tables 2 and 3. The back-wall thickness of the blackbody cavity for these conditions was 2.6 mm.

In Table 2 the temperature drop for the five fixed points in the four thermal conditions studied are shown.

Table 2. Temperature drop (K) for studied fixed points

Fixed point	bare crucible	linear profile (LP)	sine shaped profile (sin P)	constant profile (CP)
Co-C	0.022	0.020	0.01□	0.01□
Pd-C	0.031	0.029	0.02□	0.024
Pt-C	0.053	0.04□	0.042	0.03□
Re-C	0.20□	0.1□□	0.154	0.132
WC-C	0.33□	0.2□□	0.244	0.205

Fig. 7 displays the temperature drop values given in Table 2, i.e. the temperature drop with the furnace conditions and nominal temperature are plotted.

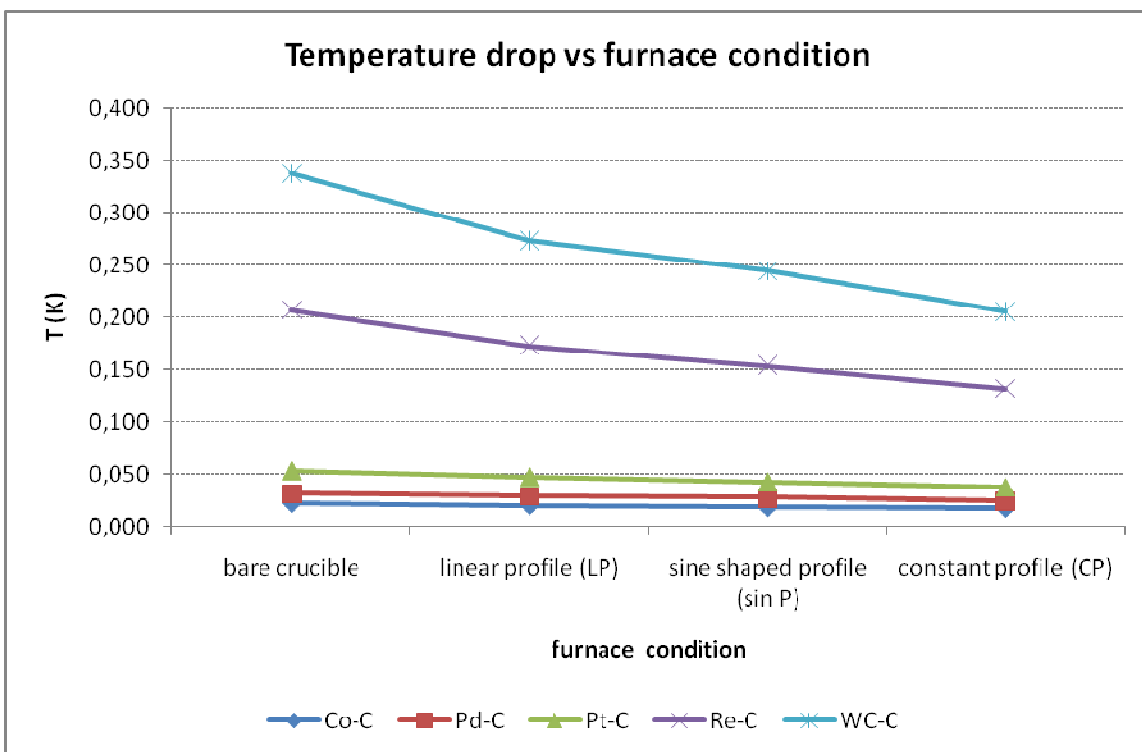


Fig. 7. Temperature drop variation with the furnace conditions

3.2 Effect of back-wall thickness

In Tables 3 and 4 the temperature drop for the five fixed points for reference and ideal conditions with five different back-wall thicknesses are given.

Table 3. Temperature drop (K) at reference conditions (no furnace) for different back-wall thicknesses

Fixed point \ backwall thickness (mm)	0.1	1	2	2.6	4
Co-C	0.004	0.015	0.021	0.022	0.041
Pd-C	0.005	0.021	0.030	0.031	0.054
Pt-C	0.01	0.036	0.049	0.053	0.062
Re-C	0.039	0.154	0.199	0.202	0.209
WC-C	0.064	0.253	0.322	0.332	0.455

Table 4. Temperature drop (K) at ideal conditions (uniform furnace) for different back-wall thicknesses

Fixed point \ backwall thickness (mm)	0.1	1	2	2.6	4
Co-C	0.003	0.010	0.016	0.012	0.034
Pd-C	0.004	0.014	0.022	0.024	0.041
Pt-C	0.005	0.023	0.034	0.032	0.056
Re-C	0.026	0.092	0.125	0.132	0.155
WC-C	0.042	0.142	0.192	0.205	0.264

In Fig. 8 and 9 the curves for the temperature drop variation with back-wall thickness are given.

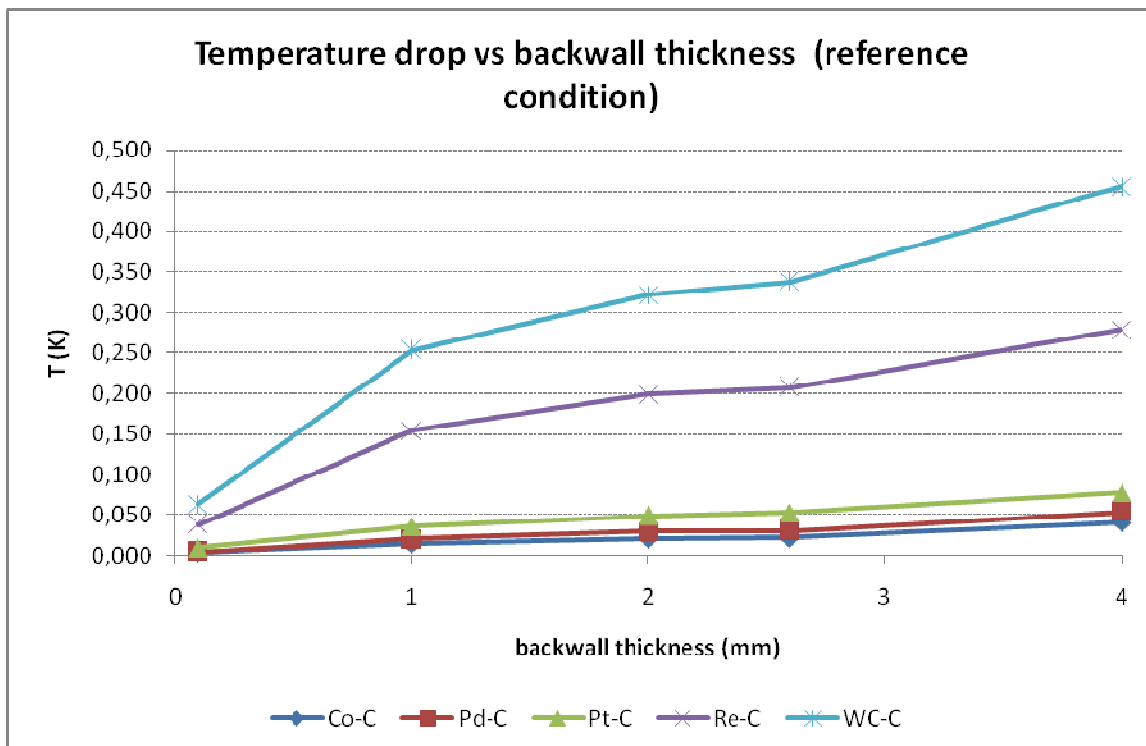


Fig 8. Temperature drop variation with back-wall thickness for bare crucible (reference condition)

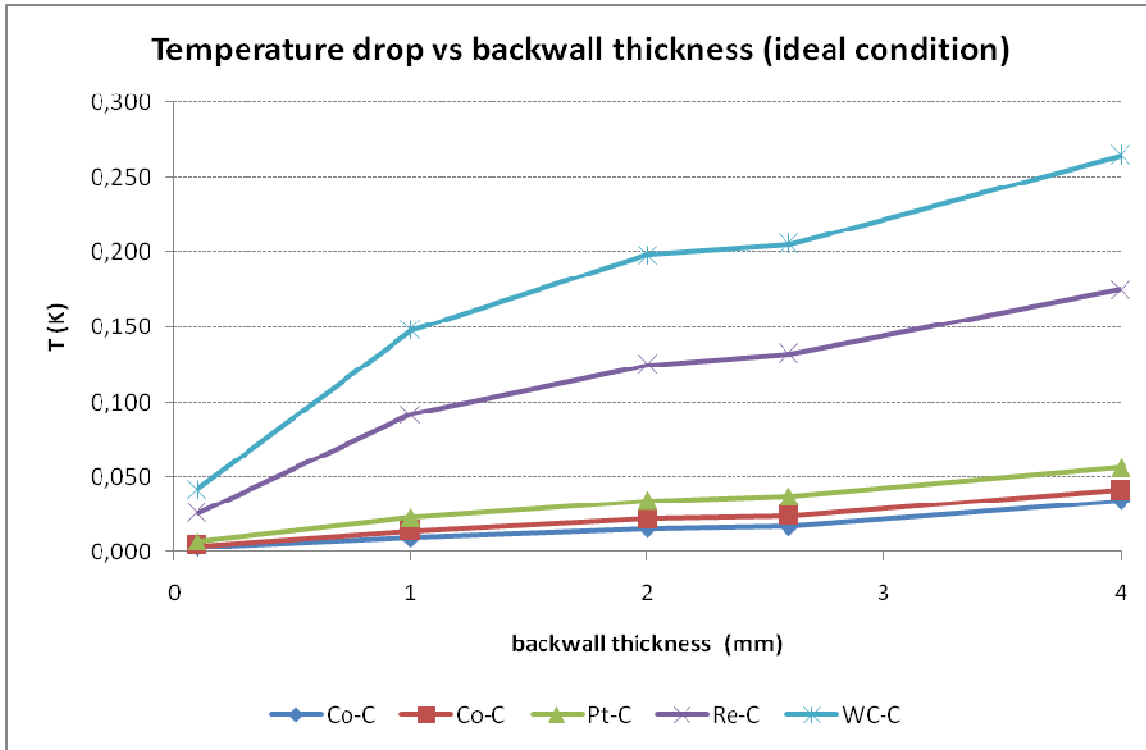


Fig 9. Temperature drop variation with the back-wall thickness for ideal conditions (uniform furnace)

3.3 Effect of the blackbody tube length

In Tables 5 and 6 the temperature drop for the five fixed points for reference and ideal conditions with three different blackbody tube lengths are given.

Table 5. Temperature drop (K) at reference conditions (no furnace) for different blackbody tube lengths

Fixed point \ blackbody tube length (mm)	17	27	37
Co-C	0.051	0.022	0.013
Pd-C	0.022	0.031	0.019
Pt-C	0.140	0.053	0.030
Re-C	0.635	0.200	0.102
WC-C	1.055	0.330	0.162

Table 6. Temperature drop (K) at ideal conditions (uniform furnace) for different blackbody tube lengths

Fixed point \ blackbody tube length (mm)	17	27	37
Co-C	0.022	0.010	0.016
Pd-C	0.031	0.024	0.023
Pt-C	0.052	0.030	0.030
Re-C	0.190	0.132	0.092
WC-C	0.322	0.205	0.140

In Fig. 10 and 11 the curves for the temperature drop variation with blackbody tube length are given.

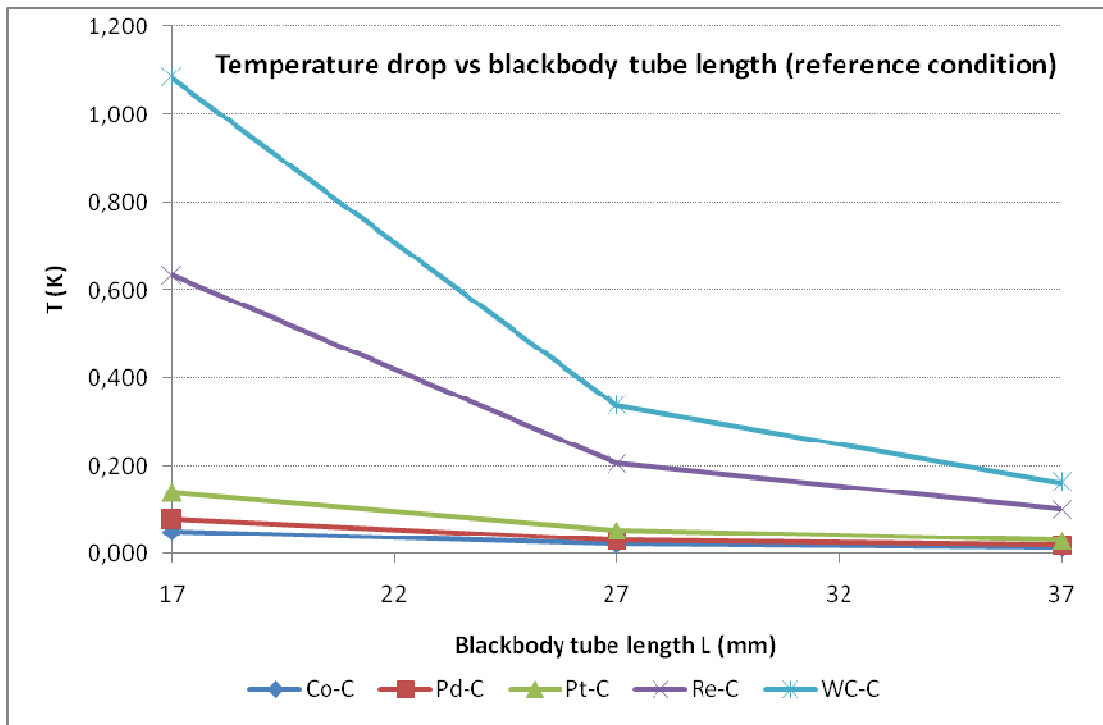


Fig 10. Temperature drop variation with blackbody tube length for bare crucible (reference condition)

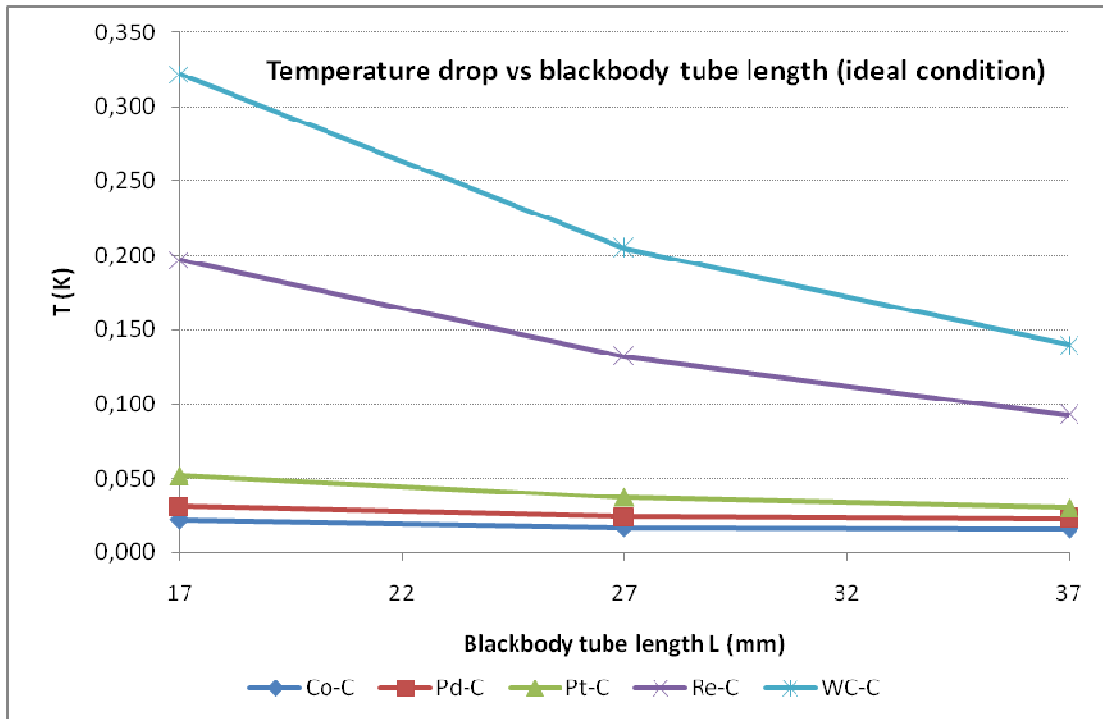


Fig 11. Temperature drop variation with blackbody tube length for ideal conditions (uniform furnace)

4. Discussion

4.1 Furnace conditions:

The radiation heat loss increases as the fourth power of the nominal temperature, the upper bound of which is given by theory (1) [3]. This form can be used to represent all the data given in Fig. 12. This is fitted by the simple power law aT^4 .

$$\Delta T = \cos \theta \cdot \varepsilon \cdot \sigma \cdot \frac{d}{K} \cdot \left(\frac{r}{L} \right)^2 \cdot T^4 \quad (1)$$

Where:

θ is the tilt angle

ε is the emissivity of graphite

σ is the Stefan-Boltzmann constant

T is the temperature in Kelvin

d is the thickness of the back-wall

K is the thermal conductivity of graphite

r is the aperture radius

L is the blackbody tube length

The fitted coefficient a of the exponential for the theoretical free radiating cavity and for the four conditions is:

Table 5. Coefficient a of the exponential expression

Coefficient	Eq.1	Bare crucible	Linear profile	Sine profile	Constant profile
a	0.026e-15	3.5e-15	3.05e-15	2.049e-15	2.431e-15

In Fig 12, the temperature drop variation with nominal temperature is plotted with the fitted exponential curves (dotted lines) and with the upper boundary given by (1). It is clear that the simple power law aT^4 is a good representation of the modeled data. It is also clear that even a bare crucible does not follow the simple theoretical expression; this is because radiance from the side walls of the cavity make up some of the radiance loss from the back-wall [4]. The various different furnace conditions mitigate to different extent the effect of radiance loss, this can be characterized by the ratio c , given in Table 6 which is the ratio a (*furnace various conditions*)/ a (ideal equation).

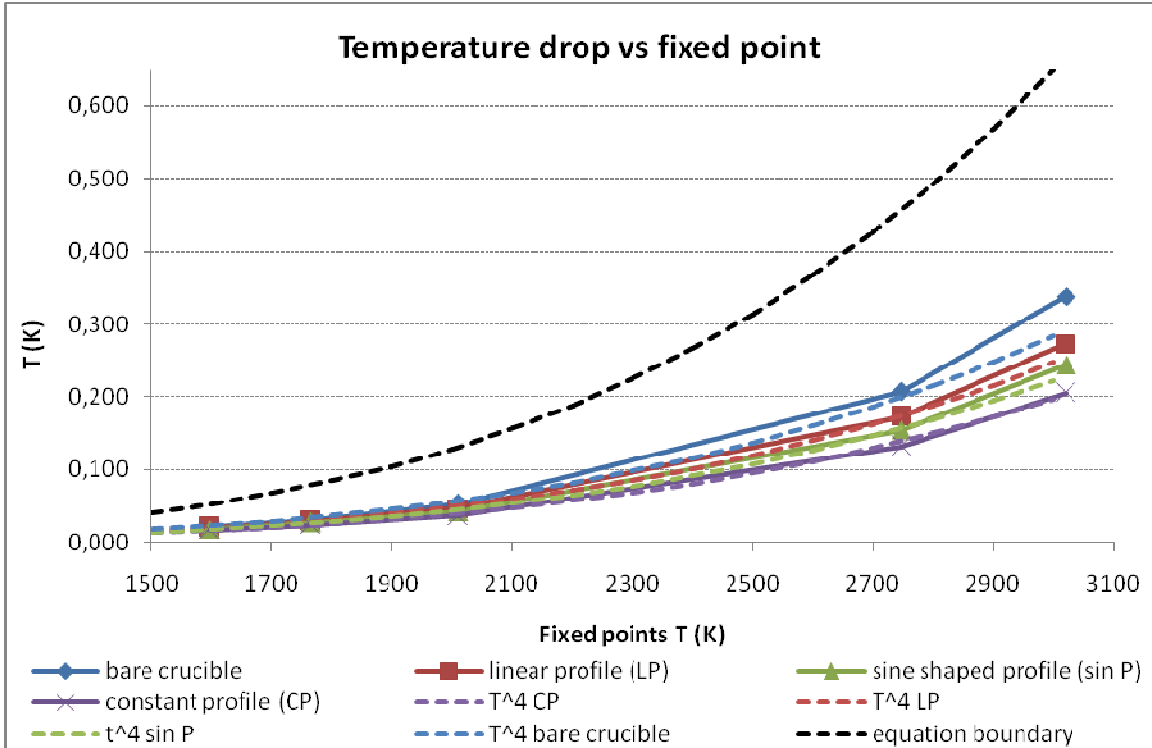


Fig 12. Temperature drop variation with the nominal temperature and the corresponding exponential curves

A simple use of (1) overestimates the correction that needs to be applied for radiance loss by a factor of 2 compared to the bare crucible and by larger amounts depending upon furnace conditions. This equation has been used to estimate the temperature drop in uncertainty calculations [5] and this contribution may need to be revised to lower values to take into account furnace effects.

Table 6. Ratio factor for the exponential expression

Ratio factor	(1)	Bare crucible	Linear profile	Sine profile	Constant profile
c	1	0.44	0.34	0.34	0.3

Through use of these calculations estimates of the correction for the temperature drop for this design HTFP blackbody can be made. The difference between a constant and linear furnace profile is less than 0.1 indicating that a reasonable temperature correction could be made with that order of type B contribution to the uncertainty.

4.2 Back-wall thickness:

The simple theory (1) that presupposes a freely radiation back-wall, predicts that the temperature drop should increase linearly with the back-wall thickness d , but as can be shown in Fig 8 and 9, the back-wall thickness influence is greater than this for the first 2 mm. The possible reason for that is the difficulty to obtain accuracy solving the numerical equations when the geometry gets thinner. This is the case for 0.1 mm and probably for 1 mm back-wall thickness.

The standard uncertainty associated to back-wall thickness $u(\Delta T; d)$ can be expressed as:

$$u(\Delta T; d) = (\delta T / \delta d) \cdot u(d) \quad (2)$$

Where $\delta T / \delta d$ is the sensitivity coefficient and $u(d)$ is the standard back-wall thickness variation.

The sensitivity coefficient $\delta T / \delta d$ can be approximated to:

$$\delta T / \delta d = \Delta T / d \quad (3)$$

And the standard back-wall thickness variation for different crucible configurations $u(d)$ can be estimated as $u(d) \approx 0.5 \text{ mm}$.

With these approximations the standard uncertainty $u(\Delta T; d)$ expressed in K for the ideal conditions is shown in Table 7. Similar studies for emissivity and thermal conductivity of the graphite cell can be seen in [2].

Table 7. Standard uncertainty $u(\Delta T; d)$ expressed in K for the ideal conditions

	Co-C	Pd-C	Pt-C	Re-C	WC-C
$\Delta T/d \text{ (K/mm)}$	0.013	0.012	0.022	0.102	0.162
$u(\Delta T; d) \text{ (K)}$	0.006	0.002	0.014	0.051	0.081
$u(\Delta T; d) / \Delta T$	0.399	0.326	0.402	0.409	0.416

4.3 Blackbody tube length:

The simple theory (1) predicts that the radiation heat loss decreases as the second power of the blackbody tube length. Fig. 10 and 11 show this second power decrease with blackbody tube length accentuated for the higher fixed points Re-C and WC-C. The simple equation gives again an upper boundary.

The standard uncertainty associated to the blackbody tube length $u(\Delta T; L)$ can be expressed as:

$$u(\Delta T; L) = (\delta T / \delta L) \cdot u(L) \quad (4)$$

Where $\delta T / \delta L$ is the sensitivity coefficient and $u(L)$ is the standard blackbody tube length variation.

The sensitivity coefficient $\delta T / \delta L$ can be approximated to:

$$\delta T / \delta L = \Delta T / L \quad (5)$$

And the standard blackbody tube length variation for different crucible configurations $u(L)$ can be estimated as $u(L) \approx 10 \text{ mm}$.

With these approximations the standard uncertainty $u(\Delta T; L)$ expressed in K for the ideal conditions is shown in Table □

Table 8. Standard uncertainty $u(\Delta T; L)$ expressed in K for the ideal conditions

	Co-C	Pd-C	Pt-C	Re-C	WC-C
$\Delta T/L (K/m)$	0.□□□	1.111	1.□4□	6.324	10.106
$u(\Delta T; L) (K)$	0.00□	0.011	0.01□	0.063	0.101
$u(\Delta T; L)/\Delta T$	0.436	0.435	0.463	0.495	0.510

This influence is especially important for Re-C and WC-C which reduce their losses in a half from 30 mm to 50 mm crucible long for the ideal conditions.

4.4 Graphic data presentation

As a graphic resume of these different influences in the heat losses, curves of the temperature drop with nominal temperature for different furnace conditions (Fig 13), for different back-wall thicknesses (Fig 14 and 15) and for different blackbody tube lengths (Fig 16 and 1□) are plotted.

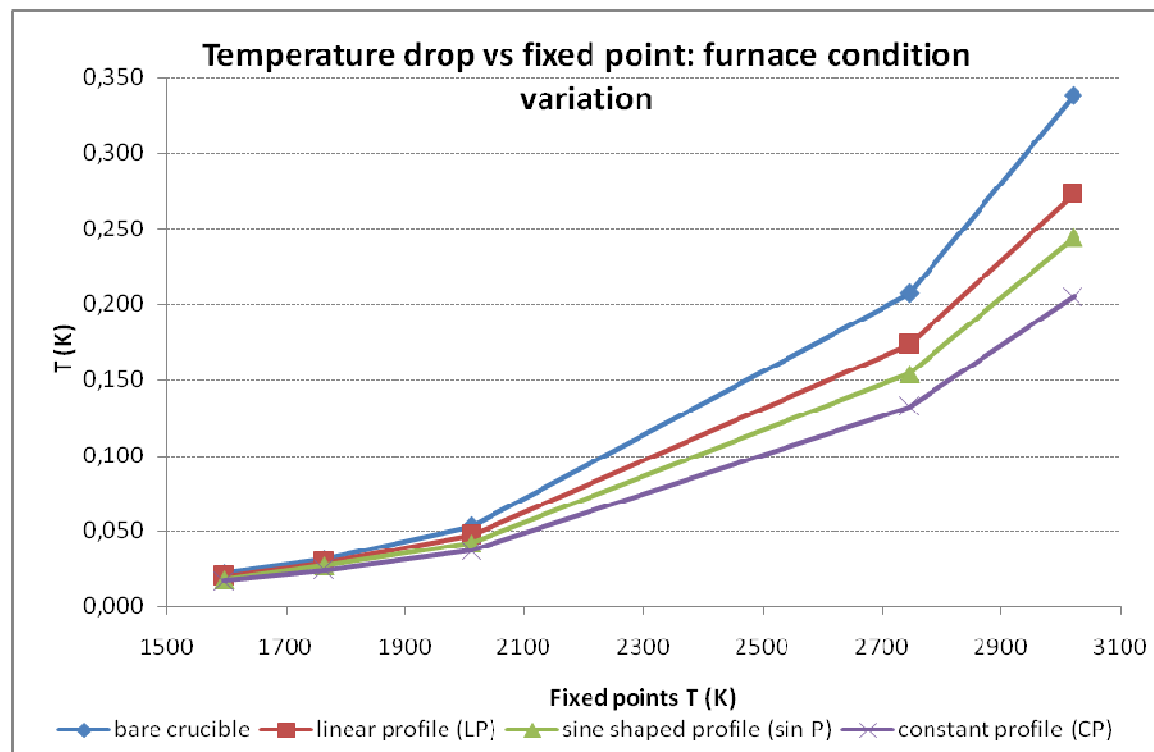


Fig 13. Temperature drop variation with the nominal temperature for different furnace conditions

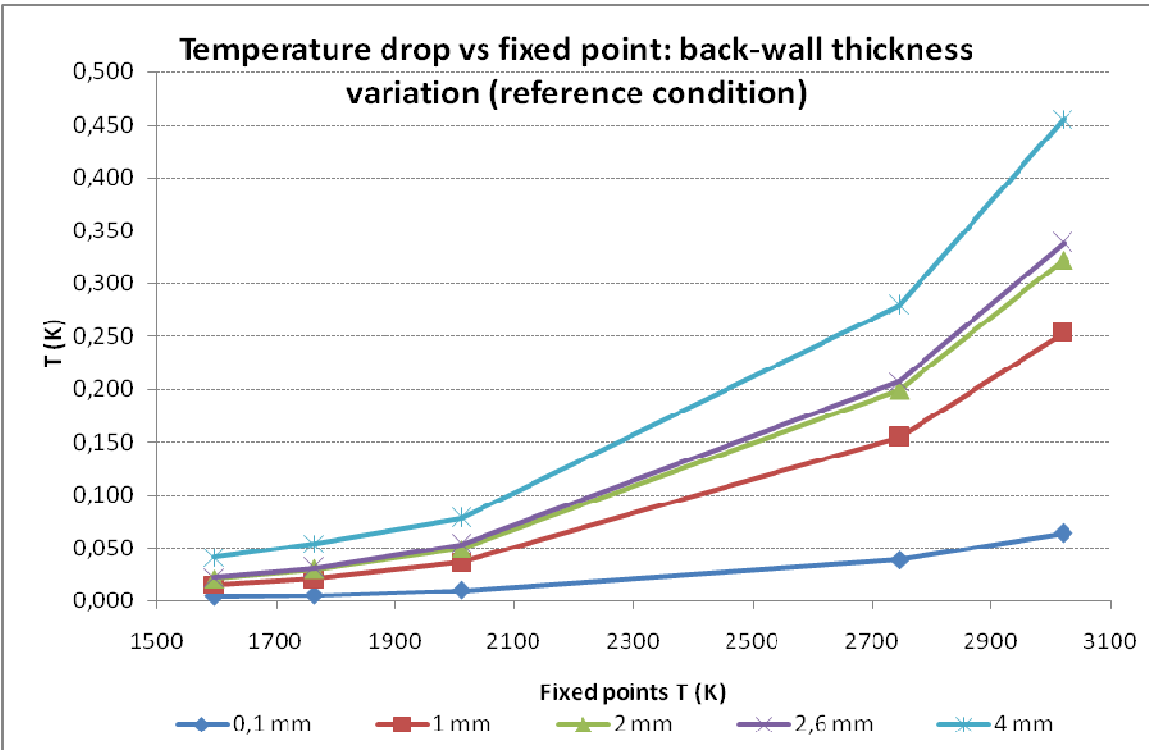


Fig 14. Temperature drop variation with the nominal temperature for different back-wall thicknesses at reference conditions

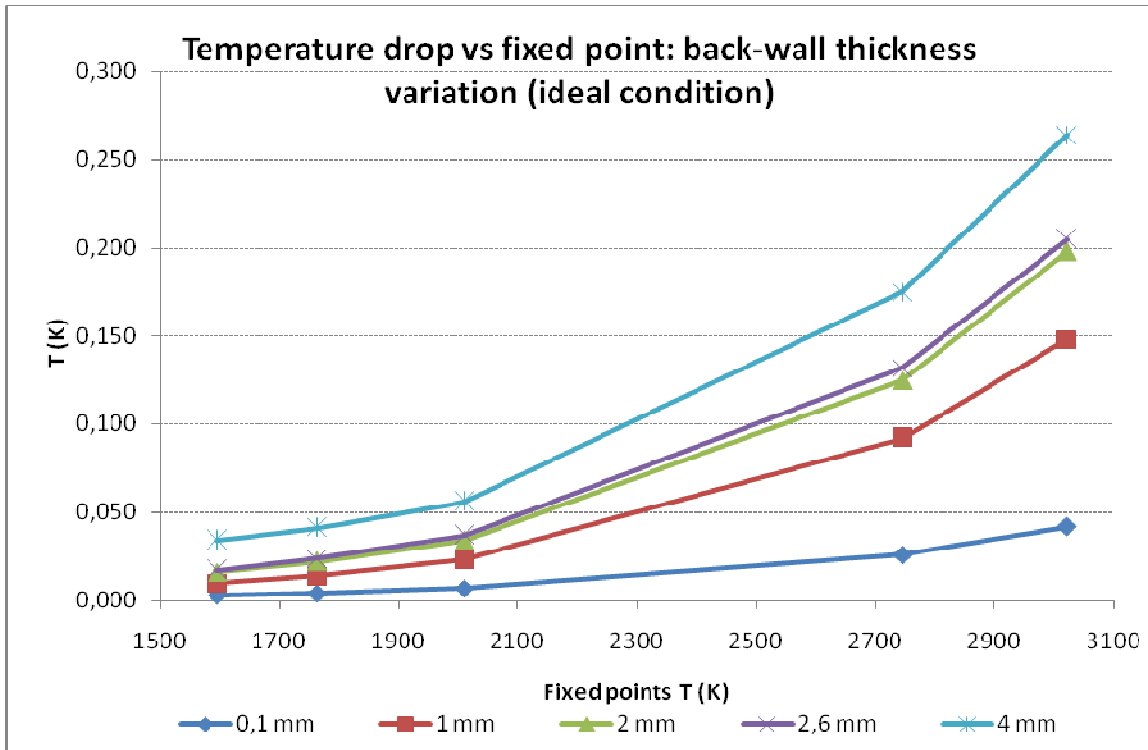


Fig 15. Temperature drop variation with the nominal temperature for different back-wall thicknesses at ideal conditions

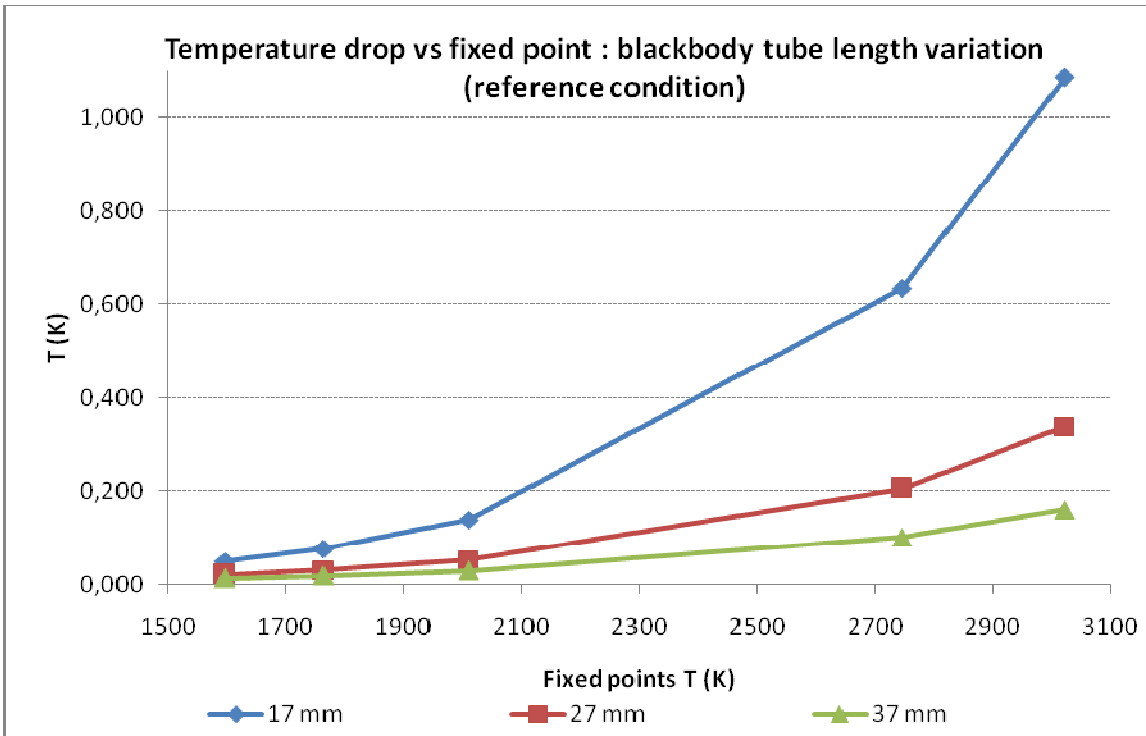


Fig 16. Temperature drop variation with the nominal temperature for different blackbody tube lengths at reference conditions

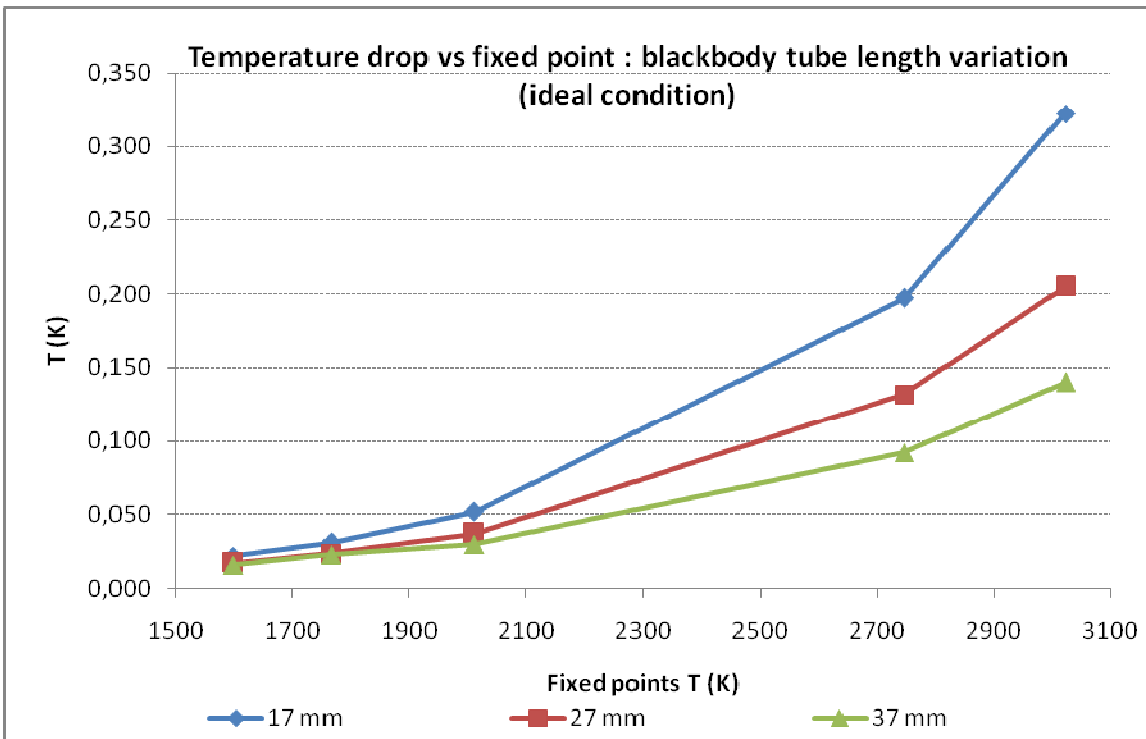


Fig 17. Temperature drop variation with the nominal temperature for different blackbody tube lengths at ideal conditions

5. Conclusions

The furnace temperature profile has an influence in the temperature drop of the back-call which increases as the fourth power of the nominal temperature of the HTFP. This influence can be compared with the theoretical equation for the temperature drop of a freely radiating back-wall which gives the upper bound of radiance loss. A reasonable correction can be made and uncertainty estimated from the results given here for a HTFP blackbody of similar design. If a different furnace is used then the range of values should be widened from the bare furnace to the uniform furnace, the average value could be used as the correction, with the difference used as the estimate of the type B uncertainty, i.e. the calculated difference divided by $2\sqrt{3}$.

The uncertainty associated to the back-wall thickness, which could vary significantly due to erosion, can be calculated and in a first approximation can be expressed as $u(\Delta T; d) \approx 0.4 \cdot \Delta T$.

The blackbody tube length has a strong influence in the temperature drop of the upper fixed points even for the constant furnace profile. Using longer crucibles for these fixed points could be a good way to reduce the heat losses to accepted values. The uncertainty associated to the blackbody tube length can be expressed as $u(\Delta T; L) \approx 0.47 \cdot \Delta T$.

References

1. C.E. Brookley, W.E. Llewellyn, "Determination of blackbody radiance at temperatures above 2300 °C", proceedings of *Temperature, Its Measurement and Control in Science and Industry*, vol. 6, edited by J. Schooley, AIP, pp. 1195-1200, 1992
2. P. Castro, P. Bloembergen, Y. Yamada, M. A. Villamañan and G. Machin, "On the Uncertainty in the Temperature Drop across the Backwall of High-Temperature Fixed Points". Acta Metrologica Sinica. Vol. 29. pp 253-260. 200□ Proceedings of International Conference on Temperature and Thermal Measurements, Beijing, 200□
3. Fischer J. and Jung H. J., "Determination of the thermodynamic temperatures of the freezing points of silver and gold by near-infrared pyrometry", Metrologia, **26**, 19□9, pp. 245-252
4. Machin, G., Wright, L., Lowe, D., Pearce J.V., "Optimising the implementation of high temperature fixed-points through the use of thermal modelling", *Int. J. Thermophys.*, 29, 26-2□0, 200□
5. Fischer, J., Sadli, M., Ballico, M., Battuello, M., Park, S. N., Saunders, P., Yuan Zundong, Johnson, B. C., van der Ham, E., Sakuma, F., Machin, G., Fox, N., Wang Li, Ugur, S., Matveyev M., Uncertainty budgets for the realisation of ITS-90 by radiation thermometry, In Proceedings of *Temperature its Measurement and Control in Science and Industry*, Vol. □ ed. Ripple D., AIP Conference Proceedings, Chicago, 2003, pp 631-63□

A DETERMINATION STUDY OF THE CAVITY EMISSIVITY OF THE EUTECTIC FIXED POINTS CO-C, PT-C AND RE-C

(to be published in International Journal of Thermophysics)

P. Bloembergen¹, L. M. Hanssen², S. N. Mekhontsev²,

P. Castro³, Y. Yamada⁴

¹ *NIM, Beijing, China*

² *NIST, Gaithersburg, MD, USA*

³ *University of Valladolid, Valladolid, Spain*

⁴ *NMIJ/AIST, Tsukuba, Japan*

E-mail [corresponding author]: p.bloembergen@xs4all.nl

Abstract

The eutectics Co-C, Pt-C and Re-C, with eutectic temperatures of 1597 K, 2011 K, and 2747K, respectively, are presently investigated for their suitability to serve as reference points for dissemination of T (and T_{90}) within the context of the “Mise en pratique of the definition of the Kelvin” (*MeP-K*) at high temperature. Temperatures are to be measured by means of radiation thermometry of cavity radiators imbedded in the associated eutectic. This paper deals with the determination of the respective spectral effective cavity emissivities, which are influenced by the reflective properties of the graphite constituting the cavity on the one hand, and by the temperature distribution within the cavity and over the radiation-shield structure in front of the cavity, on the other. We have begun a comprehensive effort to determine the effective spectral cavity emissivities at 405 nm and 650 nm. The overall program, taking 7 steps in total, involves diverse measurements on representative graphite samples, furnace-temperature profile measurements, calculations of temperature distributions, and, finally, based upon this information, calculation of the cavity-emissivity dependencies. We report here on the current status of the study, including cavity temperature distributions and Monte Carlo modeling results, associated with steps 5, 6 and 7 of the envisaged overall project. For the time being the modeling assumes current estimates of the graphite emissivity and BRDF, which will be updated as data become available from steps 1 to 4.

Keywords: Emissivity; Eutectics; High temperatures; Fixed Point; Freezing Point;

Blackbody; Monte Carlo Modeling

1. Introduction

With the advent of high-temperature eutectics and peritectics with transition temperatures covering the range from 1427 K (Fe-C) to 3458 K (HfC-C) a new era in temperature measurement at high temperature, i.e. above the silver point, will be entered.[1] Under the auspices of WG-5 of the CCT the eutectics Co-C, Pt-C and Re-C, with eutectic temperatures of 1597 K, 2011 K, 2747 K, respectively, are presently investigated for their suitability to serve as reference points for dissemination of T (and T_{90}),[2] within the context of the '*Mise en pratique of the definition of the kelvin*' (*MeP-K*) at high temperature: *MeP-K-HT*.[3]

Temperatures are to be measured by means of radiation thermometry of cavity radiators imbedded in the associated eutectic. This paper deals with the determination of the spectral effective cavity emissivities for Co-C, Pt-C and Re-C, which are influenced by the reflective properties of the graphite constituting the cavity on the one hand, and by the temperature distribution within the cavity and over the radiation-shield structure in front of the cavity, on the other.

The envisaged overall program to determining the effective spectral emissivities at 405 nm and 650 nm is shortly reviewed in Section 2. It takes 7 steps in total, involving diverse reflectance measurements on representative graphite samples, furnace-temperature profile measurements, calculations of temperature distributions, and, finally, based upon this information, calculation of the cavity-emissivity dependencies.

Section 3 elaborates on the thermal modeling. Modeling of the various systems considered is done by FLUENT[©],[4] a software package utilizing *finite-volume* analysis, usually applied in the study of liquids and gases. Furnace-temperature profiles, carried by eight radiation fields placed ahead of the cell are measured by NMJJ at the Co-C, Pt-C and Re-C eutectic fixed points. This has been reported earlier in Reference [5]. The temperature between measured points is then interpolated and the profile is introduced as a contour condition of the model on the external wall of the blackbody tube, eventually allowing the modeling of the cavity temperature distributions.

Section 4 reviews the current status of the project, including cavity temperature distributions and Monte Carlo modeling results, associated with steps 5, 6 and 7 of the envisaged overall

project, reviewed in Section 2. For the time being the modeling assumes current estimates of the graphite emissivity and BRDF, which will be updated as data become available from steps 1 to 4. The calculations are based upon the General Specular Diffuse (GSD) Model involving the directional-hemispherical reflectance $\rho(\lambda, \theta_i)$, made up of a partial diffuse reflectance (PDR) term complemented by a partial reflectance (PSR) term, the latter in Schlick's approximation. Section 5 shows the results obtained thus far; these are discussed in Section 6. Section 7 concludes the paper.

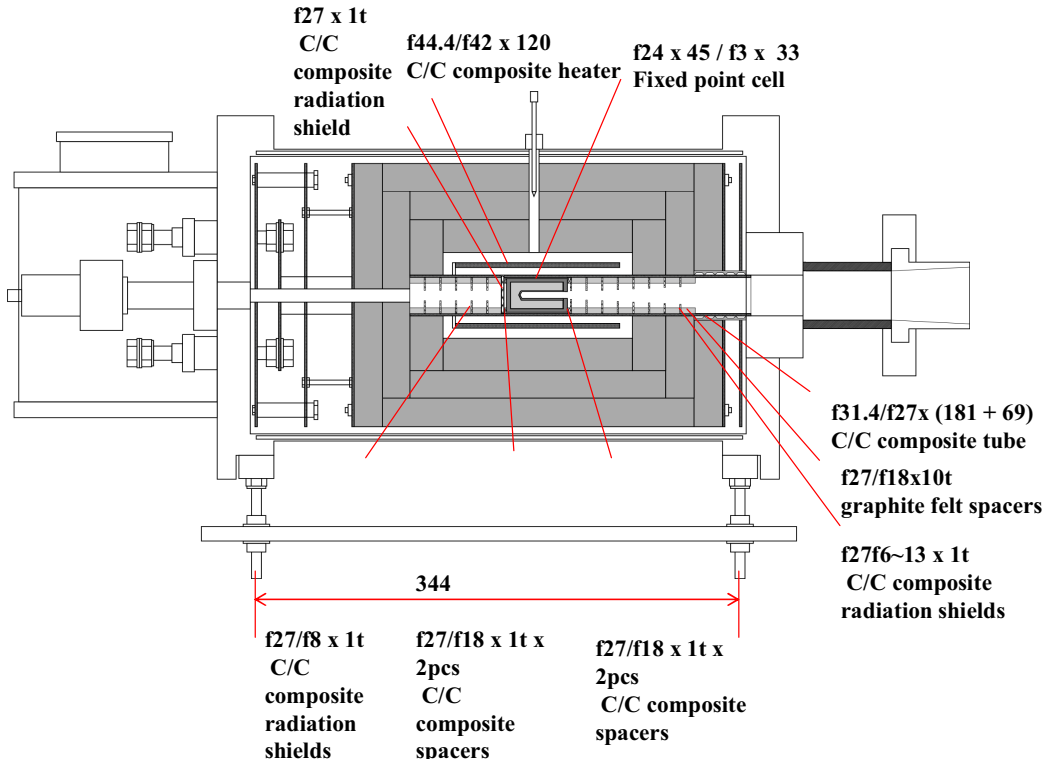


Figure 1. Schematic cross-section view of high temperature furnace with crucible located in the central heating zone.

2. Envisaged overall program

The overall program consists of 7 steps:

- (1) Spectral hemispherical reflectance of graphite samples under neutral gas purge at temperatures above ambient (up to a maximum of about 1200 K). This would provide the near-normal directional emittance.
- (2) Full room-temperature bi-directional reflectance distribution function (BRDF) at 405 nm and 650 nm. These measurements can be validated with hemispherical reflectance at the same wavelengths obtained in step 1. At the same time, the BRDF results can validate the restricted BRDF measurement set in step 3.

- (3) Temperature dependent BRDF samples at a few fixed geometries up to 3000 K. Assuming that the relative BRDF angular distribution does not change with temperature, these measurements will allow scaling the reflectance (from step 2), and hence the near-normal emissivity, up to 3000 K.
- (4) Angle-dependent relative spectral radiance at 405 nm and 650 nm under vacuum at temperatures up to 3000 K in the same setup as step 3 to obtain the angle dependent emittance.
- (5) Furnace-temperature profiles of the radiation-shield structure in front of the cavity measured at the eutectic temperatures of the eutectics in study.
- (6) Calculations of the temperature distributions within the cavity and along its outer environment, using a software package utilizing finite volume analysis, with input from step 5.
- (7) Monte Carlo ray-trace modeling of the effective spectral cavity emissivity with input of the results of all steps 1 to 6.

3. Thermal modeling

Modeling of the various systems to be considered is done by FLUENT[©][4] a software package utilizing finite-volume analysis, commonly applied to the study of liquids and gases.

Several assumptions were necessary in order to simplify the problem of calculating the parameters in question: 1) the model geometry is considered axisymmetric; this allowed us to construct a 2D model; 2) the thermal resistance at contacting elements or screw parts is neglected because of its relatively small influence and the difficulty of estimating it; 3) heat transfer due to convection and conduction in the furnace atmosphere has been taken into account, but these turned out to be negligible; and 4) the model assumes steady-state conditions.

The thermal conductivity of graphite as a function of temperature over the range of interest, is taken from Reference [6]. From this the values 53.6, 45.6, 36.5 in $\text{Wm}^{-1}\text{K}^{-1}$ at the fixed point temperatures of the eutectics Co-C(1597 K), Pt-C (2011 K), Re-C (2747 K), respectively, are derived. The emissivity of graphite, quoted nominally as 0.86, is taken from Reference [7].

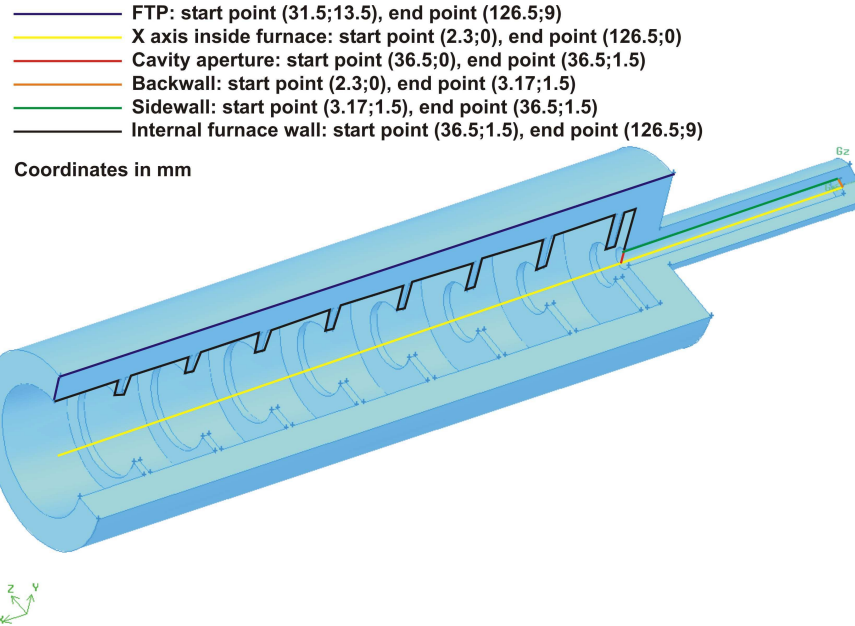


Figure 2. 3D cross-sectional view of the cavity structure including the front furnace baffle structure to present a uniform temperature field to the smaller fixed point crucible section at the right end.

Furnace-temperature profiles, carried by eight radiation fields placed ahead of the cell are measured by NMJ at the Co-C, Pt-C and Re-C eutectic fixed points. The temperature between measured points is then interpolated and the profile is introduced as a contour condition of the model on the external wall of the blackbody tube. The resulting calculated temperature profiles of the inner walls of the crucible and furnace are shown in Figure 3 (a) and (b) in both absolute and relative terms, respectively. These results are used for the radiance calculations in the next Section.

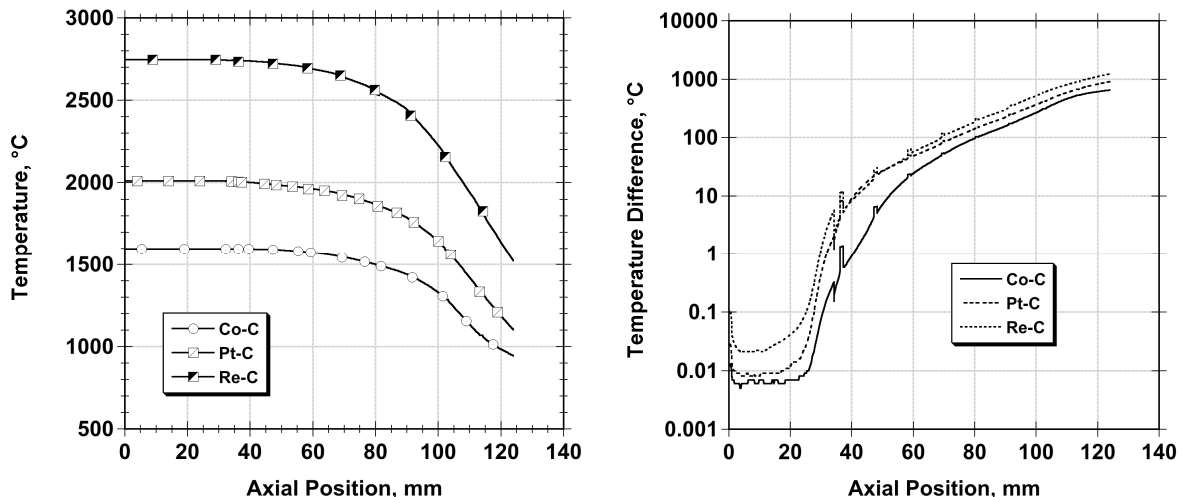


Figure 3. (a) Calculated temperature profiles along the fixed-point crucible and furnace (shown in Figure 2) for the three carbon eutectics. (b) The same profiles shown in terms of the temperature difference relative to the crucible apex temperature.

4. Monte Carlo raytrace analysis model

We have employed a multipurpose custom-developed Monte Carlo raytrace program to perform analysis on the cavity structure shown in Figure 2, with the temperature distribution calculated in Section 3 as input. The paired numbers represent the locations in mm along, and perpendicular to, the primary (X) axis, respectively. The modeling algorithm makes use of reciprocity-based backward ray tracing. It uses the Well Equidistributed Long-period Linear (WELL) pseudorandom number generator.[8] It assumes and incorporates the effects of ambient radiation as isotropic perfectly black background having temperature T_{bg} (assumed to be 300 K). It can take spectral (wavelength dependent) cavity surface reflectance or emittance as input and can produce spectrally dependent cavity emissivity, radiance and radiance temperature as output.

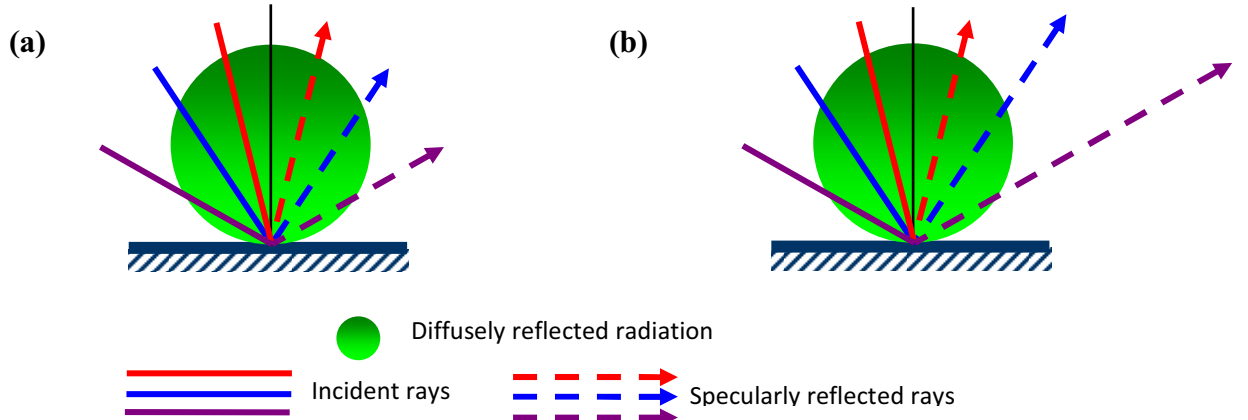


Figure 4. Schematic of the two scattering models used within the Monte Carlo cavity model: (a) the Uniform Specular-Diffuse (USD) model, and (b) the General Specular-Diffuse (GSD) model of reflection.

A schematic comparing the scattering model used for our Monte Carlo cavity model to the simpler more commonly used model, is shown in Figure 4: (a) the Uniform Specular-Diffuse (USD) model, and (b) the General Specular-Diffuse (GSD) model of reflection. The USD is a simple specular-diffuse model widely used in the Monte Carlo modeling of blackbodies (see, e.g. References [9 - 11]), whereas the GSD is a more realistic specular-diffuse model, which takes into consideration the dependence of specular component on incidence angle. The GSD is described by the following equation:

$$\rho(\lambda, \theta_i) = k_d \cdot R_d(\lambda) + (1 - k_d)R_s(\lambda, \theta_i), \quad (1)$$

where

$r(\lambda, \theta_i)$ is the DHR for wavelength and incidence angle ,

$R_d(\lambda)$ is the partial diffuse reflectance (PDR),

$R_i(\lambda, \theta_i)$ is the partial specular reflectance (PSR), and

k_d is the weight of diffuse component.

We use Schlick's approximation [11] of Fresnel's law for the PSR at all wavelengths:

$$R_s(\lambda, \theta_i) = R_s(\lambda, 0) + (1 - R_s(\lambda, 0)) (1 - \cos(\theta_i))^5. \quad (2)$$

From the model output, we calculate the effective emissivity estimate using the expression:

$$\begin{aligned} \varepsilon_e(\lambda, T_{ref}) &= \frac{1}{N} \left[\exp\left(\frac{c_2}{\lambda T_{ref}}\right) - 1 \right]^{-1} \times \\ &\sum_{i=1}^N \left[\left[\exp\left(\frac{c_2}{\lambda T_{bg}}\right) - 1 \right]^{-1} \rho^{M_i}(\lambda, \theta_{i,M_j}) + \sum_{j=1}^{M_i} [1 - \rho(\lambda, \theta_{i,j})] \rho^{j-1}(\lambda, \theta_{i,j}) \left[\exp\left(\frac{c_2}{\lambda T_{i,j}}\right) - 1 \right]^{-1} \right], \end{aligned} \quad (3)$$

where

λ is the wavelength,

T_{ref} is the reference temperature (temperature of cavity bottom center in this case),

T_{bg} is the background temperature,

c_2 is the second radiation constant in Planck's law,

N is the number of rays traced,

M_i is the number of reflections of i^{th} ray until escaping the cavity ,

$\theta_{i,j}$ is the angle of the i^{th} ray incidence at the j^{th} reflection, and

T_{bg} is the temperature of cavity's wall at the point of the j^{th} reflection of the i^{th} ray.

The expression for the radiance temperature T_s is given by:

$$T_s(\lambda) = c_2 \lambda^{-1} \ln \left[1 + \frac{\exp\left(\frac{c_2}{\lambda T_{ref}}\right) - 1}{\varepsilon_e(\lambda, T_{ref})} \right]. \quad (4)$$

Given 10^6 traced rays, the standard deviation of the effective emissivity for a perfectly diffuse cavity will be less than 3×10^{-6} . For 10^7 traced rays, the standard deviation of the effective emissivity for a cavity with the optical properties of its internal surface described by the GSD model, will be approximately 2×10^{-5} .

5. Monte Carlo raytrace results.

Since the actual emittance, reflectance and scattering character of the graphite surface in the crucibles and furnaces during operation are not well known at this point in the study, we have

chosen to examine the modeled system with a range of the key parameters of emittance and the weight of the diffuse component. In Figures 5 (a) and (c), the radiance temperatures of the Co-C and Re-C crucibles are shown for the wavelengths of interest (405 nm and 650 nm), for the isothermal and Lambertian graphite case. Results are shown for graphite emittance values of 0.7 and 0.8, as well as 1.0 (to show the ideal blackbody case for comparison). In Figures 5 (b) and (d), the effective emissivities corresponding to (a) and (b), respectively, are shown, as well as those for the non-isothermal case, with temperature distributions taken from the profiles shown in Figure 3. The effects of non-Lambertian reflectance of the graphite are examined in Figure 6, using the GSD model of reflectance described in Section 4, for Co-C and Re-C cavities. The radiance temperature, shown in (a) and (c), and the effective emissivity shown in (b) and (d), are plotted versus the diffuse component weight, k_d .

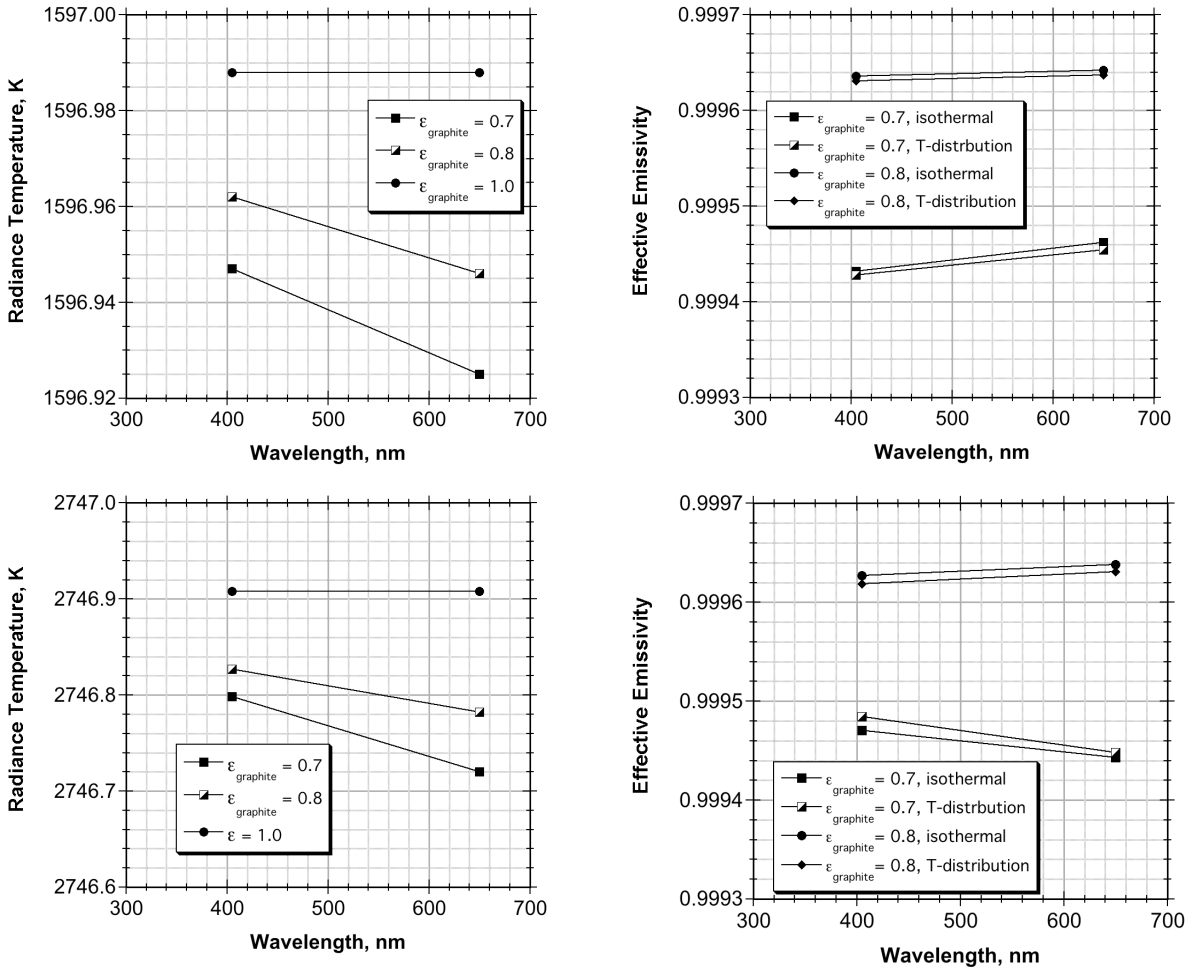


Figure 5. Radiance temperature (a, c) and graphite emittance and wavelength, as the graphite fixed point cavities near the d). The right hand plots include data for both temperature distributions calculated by

effective emissivity (b, d) dependence on determined from Monte Carlo simulations of melting points of Co-C (a, b) and Re-C (c, isothermal cavities as well as for ones with thermal modeling and shown in Figure 2.

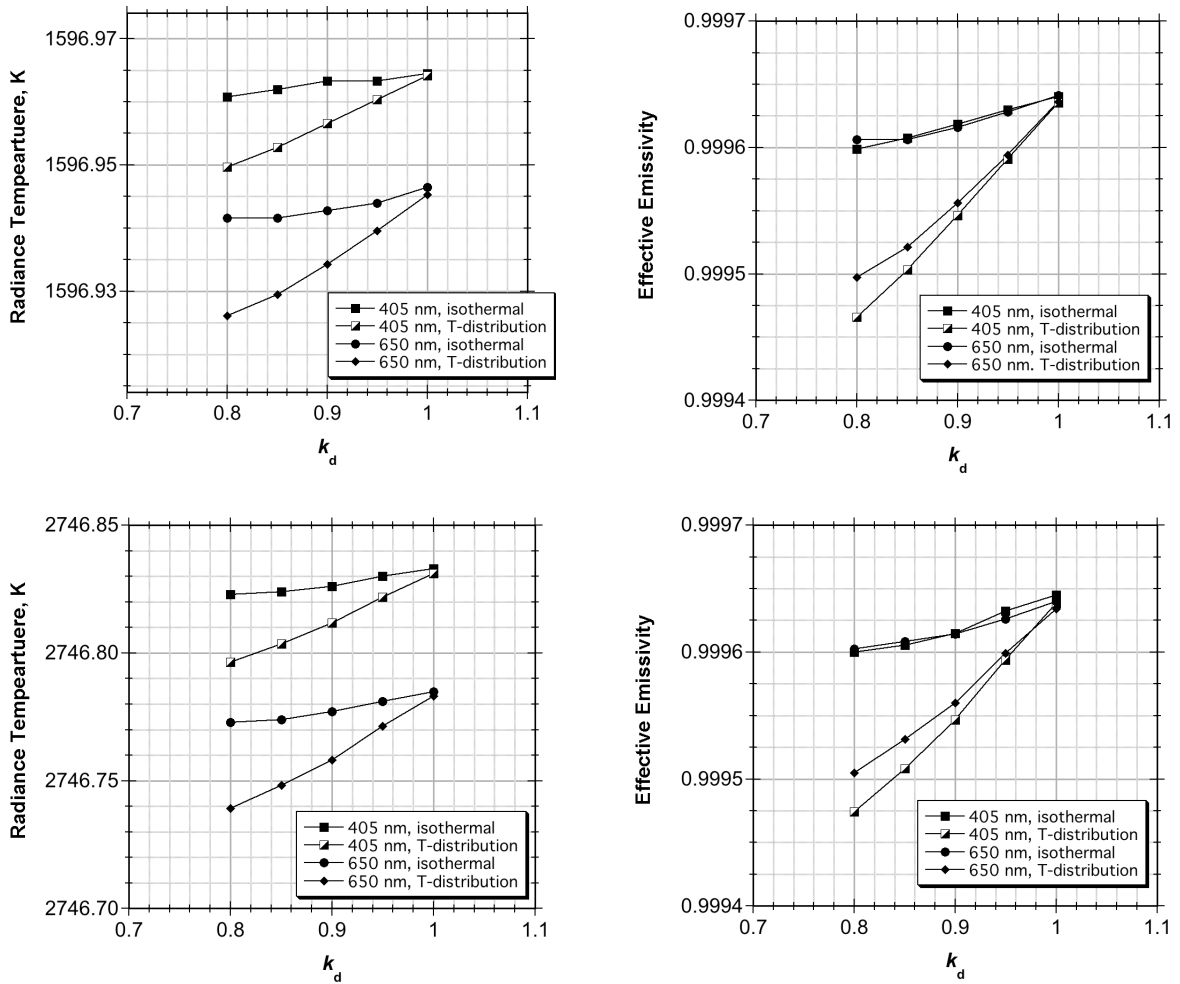


Figure 6. Radiance temperature (a, c) and effective emissivity (b, d) dependence on graphite diffusivity and wavelength, as determined from Monte Carlo simulations of the graphite fixed point cavities near the melting points of Co-C (a, b) and Re-C (c, d). Data are shown for both the isothermal and non-isothermal cases (according to the temperature distributions from Figure 2).

For the Lambertian graphite case, as seen in Figure 5 (b) and (d), there is almost no effect of the calculated non-isothermal temperature distributions on the cavity emissivities. Conversely, the results show that the furnace design would be a sufficient approximation to isothermality, provided the graphite reflectance is Lambertian. On the other hand, as can be seen in the results shown in Figure 6 (a – d), the existence of a specular component of the graphite reflectance leads to a slight decrease of the radiance temperature and cavity effective emissivity, but when a specular component is coupled with the non-uniform temperature distribution, the decrease becomes potentially significant (a change of 10^{-4} in effective emissivity and 10 to 35 mK in radiance temperature for a k_d of 0.8).

6. Summary and conclusions.

We are in the midst of an effort to establish effective emissivity values with minimal uncertainties for fixed-point blackbody cavities using the eutectics Co-C, Pt-C and Re-C. We have studied, by measurement and modeling, the temperature distribution within one cavity design optimized for and presently employed in the operation of existing eutectic blackbodies.[5] The temperature distributions, have, in turn, been used as input data to a custom Monte-Carlo-based ray tracing code to examine the potential variability of the cavity effective emissivity due to the temperature distributions and the graphite reflectance characteristics. Simulating the graphite reflectance by a combination of a Lambertian component and an angle dependent specular component, the modeling results indicate that the combination of a specular component together with a realistic non-uniform cavity temperature can result in a modest change in the cavity effective emissivity.

Although the graphite reflectance model is only an approximation of the actual BRDF, we expect the trends described in this paper to qualitatively represent those of an actual cavity. For more quantitative (accurate) results, we will be measuring the graphite BRDF and upgrading the Monte Carlo code to incorporate the BRDF data in future steps of our planned program.

Acknowledgement.

The authors would like to thank Alexander Prokhorov for his valuable contributions in developing and customizing the Monte Carlo raytracing code, based on the STEEP 3 Program Series from Virial Inc.[4]

References

1. Y. Yamada, “Advances in High-Temperature Standards above 1000 °C”, MAPAN **20**, No. 2, 183-191 (2005).
2. G. Machin, P. Bloembergen, J. Hartmann, M. Sadli, Y. Yamada, “A concerted international project to establish high temperature fixed points for primary thermometry”, Int. J. Thermophys. **28**, 1976-1982 (2007)
3. “Mise en pratique for the definition of the kelvin”
http://www.bipm.org/utils/en/pdf/MeP_K.pdf
4. Certain commercial equipment, instruments, or materials are identified in this paper to specify the experimental procedure adequately. Such identification is not intended to imply recommendation or endorsement by the National Institute of Standards and Technology, nor is it intended to imply that the materials or equipment identified are necessarily the best available for the purpose.
5. P. Castro, P. Bloembergen, Y. Yamada, M.A. Villamanan, G. Machin, “On the uncertainty in the Temperature Drop across the Backwall of High-Temperature Fixed Points”, Acta Metrologica Sinica **29**, 253 – 260 (2008).
6. Y. S. Toulokian, R. W. Poweel, C. Y. Ho, P. G. Klemens, “Thermal conductivity: Nonmetallic Solids, Thermophysical Properties of Matter,” The TPRCX Data Series **2**, New York, Plenum Press, 1978.
7. J. Fischer, H. J. Jung, “Determination of the thermodynamic temperatures of the freezing points of silver and gold by near-infrared pyrometry, Metrologia **26**, 245-252 (1989).
8. P. L'Ecuyer, F. Panneton, M. Matsumoto, “Improved Long-Period Generators Based on Linear Recurrences Modulo 2,” ACM Transactions on Mathematical Software **32**, No. 1, 1–16 (2006).
9. A. Ono, “Calculation of the Directional Emissivities of the Cavities by the Monte Carlo Method,” J. Opt. Soc. Am. **70**, 547-554 (1980).

10. V. I. Sapritsky and A. V. Prokhorov, “Calculation of the Effective Emissivities of Specular- Diffuse Cavities by the Monte Carlo Method,” *Metrologia* **29**, 9-14 (1992).
11. Alexander V Prokhorov and Leonard M Hanssen, “Effective emissivity of a cylindrical cavity with an inclined bottom: II. Non-isothermal cavity,” *Metrologia* **46** 1–14 (2009)
12. Schlick C., “An inexpensive BRDF model for physically-based rendering,” *Computer Graphics Forum (Proc. Eurographics '94)* **13**, No. 3, 233-246 (1994).

MODELLING A HIGH TEMPERATURE FURNACE USING FINITE VOLUME SOFTWARE

P. CASTRO, M. A. VILLAMAÑAN

*Departamento de Ingeniería Energética y Fluidomecánica, Escuela Técnica Superior de
Ingenieros Industriales de Valladolid, Universidad de Valladolid (UVA), Paseo del
Cauce, E-47071 Valladolid, Spain*

M. J. MARTIN, D. DEL CAMPO

*Área de Temperatura, Centro Español de Metrología (CEM), C/ del Alfar 2, Tres Cantos,
28760 Madrid, Spain*

The Spanish National Metrology Institute (CEM) has recently started to develop some equipment and laboratory facilities in the high temperature framework. One of them is a home made horizontal furnace which allows temperatures up to 1600 °C powered by direct current. It has been designed for calibrating noble metal thermocouples and broadband radiation thermometers with reference to a monochromatic radiation thermometer. Because of the measurement of the gradients along the measuring areas are long time consuming, it is been using a finite volume software (FLUENT[®]) in order to simulate the thermal behaviour of this furnace. Different temperature static contours along different dimensions of the furnace will be showed, paying more attention in the results of the temperature gradient from the rear part of the blackbody cavity (thermocouple insertion), which will be compared with experimental measurements.

1. Introduction

The Spanish National Metrology Institute (CEM) has designed and constructed a three zone furnace intended for calibrating noble metal thermocouples and broad band radiation thermometers with reference to a standard monochromatic radiation thermometer up to 1600 °C. This three-zone furnace has been constructed with MoSi₂ heating elements with an interchangeable alumina tube containing a graphite blackbody [1].

It was thought to use some theoretical model in order to simulate its thermal behaviour, because the measurement of the gradients along the measuring areas is long time consuming.

A commercial computational software Fluent[®] was the software chosen to simulate the thermal behaviour, because it has turned out successful in a previous study of simulation in high temperature furnaces [2].

2. Description of the high temperature furnace

A scheme of the high temperature furnace is shown in figure 1. It has three heating zones: the central one, with three heating elements, and the other two, with two heating elements. The heating elements are placed in the air surrounding the measuring tube.

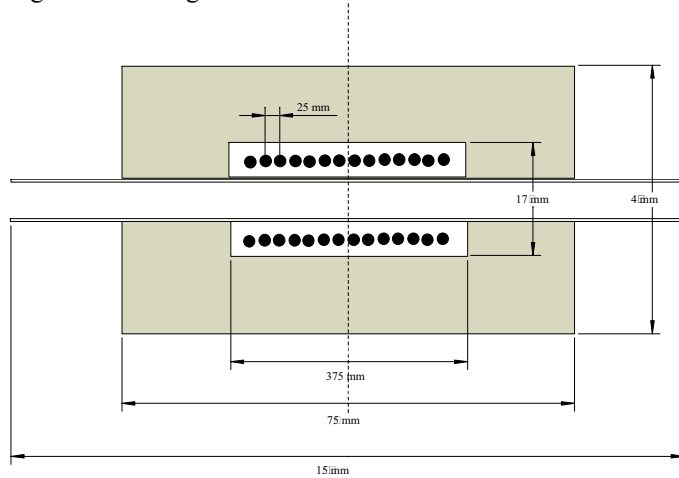


Figure 1. CEM horizontal high temperature furnace. The shadow zone is the insulation of the furnace.

The measuring tube is interchangeable depending on the type of thermometer to be calibrated: thermocouple or broad band radiation thermometer. Figure 2 shows the tube constructed to calibrate thermocouples.

Measuring tubes have four hollow alumina rods to insert different type B thermocouple to measure the homogeneity of the furnace. These alumina rods go across the whole measuring tube.

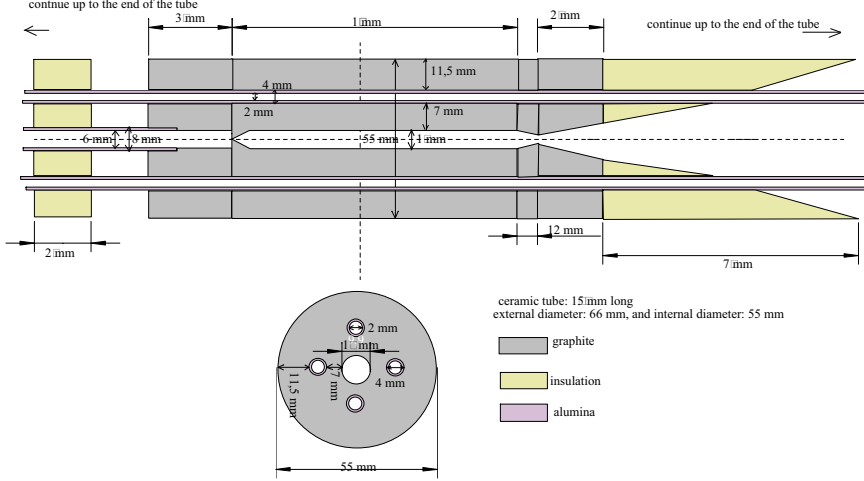


Figure 2. Calibrating thermocouple tube. The thermocouple insertion is in the left part of the drawing. The hot junction of the thermocouple touches the rear part of the black body cavity, whose temperature is measured using a standard radiation thermometer.

3. Finite volume simulations

The software FLUENT[®] [3] has been used to simulate the high temperature furnace described in paragraph 2. It is a general-purpose computational fluid dynamics (CFD) package based on the finite volume method [4]. The domain of study is divided into a finite set of control volumes and the general equations for mass, momentum and energy conservation are discretized into algebraic equations and solved to render flow field values.

A 3D model with a symmetry plane was chosen and material properties used are in table 1.

Table 1. Material properties.

	Density, kg/m ³	C_p , J/kg·K	Thermal conductivity, W/m·K	Viscosity, kg/m·s	Molecular weight, kg/kg·mol
Graphite	1850	810	50		
Alumina	3900	880	35		
Copper	8978	381	387,6		
Insulation	400	880	0,35		
Air	1,225	p1	p2	$1,79 \times 10^{-5}$	28,97

$p1 = 1,9327 \times 10^{10} T^4 - 7,9999 \times 10^7 T^3 + 1,1407 \times 10^3 T^2 - 44997 T + 1057,5$

$p2 = 1,5207 \times 10^{11} T^3 - 4,8574 \times 10^8 T^2 + 1,084 \times 10^4 T - 3,9333 \times 10^4$

Conduction, convection and radiation heat transfer has been simulated with the next boundary conditions:

- heating elements: similar to copper at constant temperature
- external walls: with convection and radiation to the air at 300 K
- caps closing the ceramic tube: similar to air at fixed temperature of 300 K

The thermal behaviour contours obtained for the heating cavity and the measuring tube are shown in figure 3.

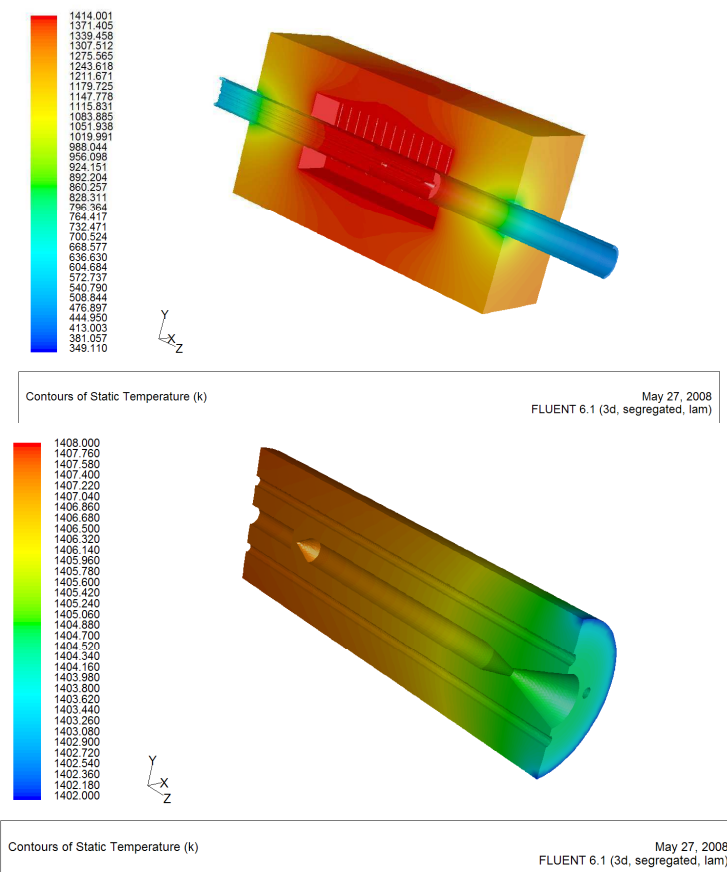


Figure 3. Temperature contours obtained with FLUENT[®] for the high temperature furnace.

4. Results

Based on the thermal simulations performed it is possible to obtain the temperature gradient at the thermocouple location. These theoretical gradients are compared with the experimental data for 1100°C in figure 4.

The agreement between the simulations done and the data measured are pretty good. Presently, we are working in changing some parameters of the model (e. g. set points of the different heating zones, geometry, temperature, etc) and checking if these changes correspond to the actual behaviour of the furnace

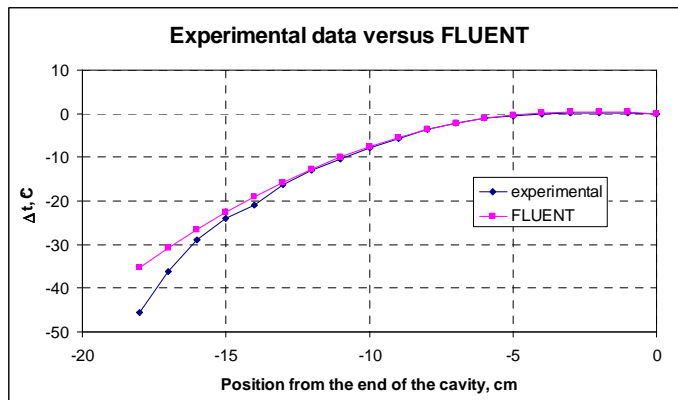


Figure 4. Comparison between the experimental data and the results obtained with FLUENT[®].

References

1. C. García, M. J. Martín, D. del Campo, J. P. Pérez and V. Chimenti, *Proceed. HTFP'2006 International Workshop*, Paris (2006).
2. P. Castro, P. Jimeno-Largo, M. A. Villamañan, J. J. Segovia and C. R. Chamorro, *Proceed. HTFP'2006 International Workshop*, Paris (2006).
3. www.fluent.com
4. M. Y. Kim, S. W. Baek, J.H. Park. *Numerical Heat Transfer, Part B*, Vol 39, 617-635 (2001).

NUMERICAL STUDY OF THE TEMPERATURE DROP IN SET CRUCIBLE-FURNACE FOR EUTECTIC FIXED POINTS USED IN RADIATION THERMOMETRY

P. Castro, P. Jimeno-Largo, M.A. Villamañán, J.J. Segovia and C.R. Chamorro

Laboratorio TERMOCAL, Escuela Técnica Superior de Ingenieros Industriales,
Universidad de Valladolid, E-47071 Valladolid, Spain

Abstract

In the field of thermal modelling and calibration, accurate determination of high temperature eutectic melting is very important. Once these points are determined, they can easily be used in any laboratory that has suitable facilities as reliable high temperature fixed points.

The difference between the ideal fixed point temperature at the liquid-solid interface and the temperature measured by the radiation thermometer is caused by several factors: heat loss to the surroundings, thermal resistance of the crucible walls, temperature profile in the furnace, design of crucible and furnace, nominal temperature of the fixed point and presence of impurities in the alloy.

In this work, calibration uncertainty in radiation thermometry of high-temperature eutectic fixed points is estimated. In particular, it is applied to the melting temperature of the Re-C alloy. This temperature difference has been evaluated by numerical simulation using both FLUENT (finite volume method) and ANSYS (finite element method) computational packages to a specific crucible-furnace set designed by the National Metrology Institute of Japan (NMIJ).

COMPARISON BETWEEN ANALYTICAL AND NUMERICAL SOLUTIONS OF THE TEMPERATURE DROP ACROSS THE CAVITY WALL OF HIGH- TEMPERATURE FIXED POINTS FOR RADIATION THERMOMETRY

P. Castro, P. Jimeno-Largo, M.A. Villamañán, M.C. Martín and R.M. Villamañán

Laboratorio TERMOCAL, Escuela Técnica Superior de Ingenieros Industriales,
Universidad de Valladolid, E-47071 Valladolid, Spain

Abstract

One of the problems that appear when working with high temperature black body fixed points is the difference between the measurements of temperature made with the radiation thermometer and the temperature at the solid-liquid interface, which is the ideal fixed point temperature.

This difference is caused by the cooling of the fixed point cavity wall that sees the colder environment outside the cavity. As a result a temperature drop exists at the cavity walls depending on the cavity wall thickness and its thermal conductivity.

The easiest way to study the temperature drop is to solve a simple schematic model of the system that allows setting up equations with analytical solution. Once solved this way, it is possible to simulate it with commercial computational software, FLUENT, based on a finite volume method, and ANSYS, based on a finite element method, leading to comparison between both simulation methods. A final discussion will show if the analytical solution is enough or if it is necessary to implement the complete system numerically.

PART II

Spanish thesis summary



ÍNDICE

Capítulo 1. Introducción y objetivos

- 1.1. Introducción**
- 1.2. Objetivos**
- 1.3. Referencias del capítulo 1**

Capítulo 2. Fundamentos de termometría: temperatura, termómetros y escalas de temperatura

- 2.1. Notas históricas**
- 2.2. Concepto de temperatura**
- 2.3. Concepto de termómetro y escala de temperatura**
- 2.4. Escala Internacional de Temperatura**
 - 2.4.1. Unidades de Temperatura**
 - 2.4.2. Principios de la Escala Internacional de Temperatura**
 - 2.4.3. Actual desarrollo de la Escala Internacional de Temperatura**
- 2.5. Referencias del capítulo 2**

Capítulo 3. Metodología: Análisis numérico

- 3.1. Introducción**
- 3.2. Generalidades de la Mecánica de Fluidos Computacional**
 - 3.2.1. Introducción**
 - 3.2.2. Ventajas e inconvenientes de la MFC**
 - 3.2.3. Metodología**
- 3.3. Trabajando con FLUENT**
 - 3.3.1. La ecuación de transferencia de calor**
 - 3.3.2. LA ecuación de transferencia d radiación**
 - 3.3.3. Descripción de los distintos modelos de radiación que presenta FLUENT 6.1**
 - 3.3.3.1. Modelo DTRM (discrete to transfer radiation model)**
 - 3.3.3.2. Modelo P-1**

3.3.3.3. Modelo Rosseland
3.3.3.4. Modelo DO (Discrete Ordinates)

3.3.3.5. Modelo S2S (surface to surface)

3.3.4. Elección del modelo de radiación

3.4. Resumen

3.5. Referencias del capítulo 3

Capítulo 4. Estudios preliminares y validación del modelo

4.1. Introducción

4.2. Recinto triangular equilátero

4.3. Recinto cilíndrico axisimétrico con medio participativo

4.4. Horno de alta temperatura de tres zonas

4.4.1. Descripción del horno de alta temperatura

4.4.2. Simulaciones realizadas

4.4.3. Resultados

4.5. Comparación entre los software FLUENT y ANSYS para la resolución numérica de puntos fijos eutécticos de alta temperatura

4.5.1. Descripción del sistema simulado

4.5.2. Modelos numéricos

4.5.3. Resultados

4.5.4. Conclusiones

4.6. Conclusiones

4.7. Referencias del capítulo 4

Capítulo 5. Incertidumbre en la caída de temperatura I: defectos de llenado del crisol

5.1. Introducción

5.2. Construcción e implementación del modelo

5.3. Resultados de la simulación

5.3.1. Resultados del crisol con agujeros

5.3.2. Resultados del crisol con grietas

5.4. Discusión

5.5. Conclusiones

5.6. Referencias del capítulo 5

Capítulo 6. Incertidumbre en la caída de temperatura II: emisividad, conductividad térmica y perfil de temperatura del horno Nagano-M

6.1. Introducción

6.2. Sistemas a modelar

6.3. Cálculos

6.3.1. Estructura del modelo y propiedades de los materiales

6.3.2. Variables calculadas

6.4. Resultados

6.5. Discusión

6.6. Conclusiones

6.7. Referencias del capítulo 6

Capítulo 7. Incertidumbre en la caída de temperatura III: longitud del crisol, espesor de la pared radiante y perfil de temperatura del horno Thermogage

7.1. Introducción

7.2. Descripción del modelo

7.3. Resultados de la simulación

7.3.1. Caída de temperatura

7.3.2. Efecto del espesor de la pared radiante

7.3.3. Efecto de la longitud del crisol

7.4. Discusión

7.4.1. Condiciones del horno

7.4.2. Espesor de la pared radiante

7.4.3. Longitud del crisol

7.4.4. Representación gráfica de los datos

7.5. Conclusiones

7.6 Referencias del capítulo 7

Capítulo 8. Modelado térmico de los puntos fijos Co-C, Pt-C y Re-C como entrada para calcular la emisividad efectiva de la cavidad

8.1. Introducción

- 8.2 Modelado térmico de la distribución de temperaturas en el interior de la cavidad**
- 8.3. Resultados obtenidos para la emisividad efectiva y la temperatura de radiación a partir del modelado térmico**
- 8.4. Resumen y conclusiones**
- 8.5 Referencias del capítulo 8**

Capítulo 9. Estudio de los parámetros de influencia en la termometría de contacto para celdas eutécticas

- 9.1. Introducción**
- 9.2. Descripción del modelo**
- 9.3. Resultado de las simulaciones**
- 9.4. Conclusiones**
- 9.5 Referencias del capítulo 9**

Capítulo 10. Conclusiones finales

- 10.1. Conclusiones**
- 10.2. Líneas futuras de investigación**

Capítulo 1. Introducción y objetivos

1.1. Introducción

En el campo del modelado y calibrado térmico, la determinación de puntos fijos de fusión de materiales es muy importante. Esto es debido a que, una vez determinados dichos puntos, son fácilmente reproducibles en cualquier laboratorio que tenga las instalaciones adecuadas, pudiendo servir de patrón para el calibrado de instrumentos térmicos de medida.

Cuando se trata de caracterizar puntos fijos que se encuentran a muy alta temperatura aparece un problema debido a la diferencia entre la temperatura medida con el termómetro y la temperatura de la interfase líquido-sólido. Esta diferencia es causada por varios factores:

- Las pérdidas de calor al entorno
- La resistencia térmica del metal y de las paredes del crisol
- Las propiedades del material de punto fijo
- La distribución de temperatura en el horno
- El diseño del crisol y del horno
- La temperatura nominal del punto fijo
- La presencia de impurezas en la aleación.

El Comité Consultor de Termometría [CCT] recomendó en 1996 a los Centros Nacionales de Metrología [CNM] el desarrollo de puntos fijos de alta temperatura por encima de los 2300 K con una reproducibilidad mejor de ±1 K. Además, hoy en día, existe una necesidad creciente de exactitud en las medidas a alta temperatura [por ejemplo en las industrias aeroespacial, nuclear, siderúrgica y de materiales]. Por estos motivos se han ido realizando distintos estudios para la construcción de dichos puntos fijos por encima del cobre.

Los puntos fijos de metales puros como el punto de fusión del níquel (1728 K), cobalto (1768 K), hierro (1811 K), paladio (1828 K), platino (2413

K, rodio (2236 K), iridio (2719 K), molibdeno (2895 K) y tungsteno (3687 K) han sido recomendados para temperaturas superiores al punto de fusión del cobre [1]. El problema que se presenta con estos puntos fijos es que no se pueden emplear crisoles de grafito ya que contaminan al metal modificando su temperatura de fusión. Para evitar este problema se han empleado crisoles de alúmina para el níquel [2], platino [3, 4] y paladio [5, 6]. Sin embargo, los crisoles de alúmina son demasiado frágiles para su uso y tienen menor emisividad que los de grafito [7]. En el caso de los termopares, la calibración de alta temperatura puede hacerse con el método del puente de alambre [8] pero llevan a incertidumbres demasiado grandes. Adicionalmente, se ha estudiado la alúmina como posible punto fijo [9], alrededor de los 232 K, empleando tungsteno para construir el crisol.

Más recientemente una nueva serie de puntos fijos de alta temperatura que permitirían el uso de crisoles de grafito ha sido indicada por Yamada *et al.* [1-11] del Instituto Nacional de Metroología de Japón (NMIJ). Esta idea consiste en el uso de metales que tengan una reacción eutéctica con el carbono de tal forma que la aleación eutéctica resultante sea el punto fijo. El uso de estos materiales, eutécticos carbono-metálicos (C-M), evita el problema de la contaminación con los crisoles de grafito. Las ventajas de los crisoles de grafito son su mayor robustez y emisividad. Además, los eutécticos carbono-metálicos presentan otras ventajas aparte de poder usarlos en crisoles de grafito.

Primero, su temperatura de transición es independiente de la cantidad de carbono presente en la aleación, previniendo los excesos de absorción de carbono en la aleación.

Segundo, los eutécticos C-M proveen de un mayor número de posibles puntos fijos eutécticos de alta temperatura, desde el Fe-C (153 °C) hasta el Re-C (2474 °C). Esta temperatura puede incluso superarse por encima de los 2500 °C con el empleo de puntos fijos eutécticos carburo-metálicos (C-MC) [12, 13]. Estos puntos fijos C-MC se basan en reacciones eutécticas de los carburos con el carbono y por tanto tampoco son influenciados por la contaminación del grafito del crisol.

Desde el comienzo de los estudios en eutécticos C-M [1], muchos CNM han empezado estudios en estos materiales para la termometría de contacto y de radiación. Se ha comenzado su desarrollo en el “National Physical Laboratory”

ENPL, Inglaterra, el BNM-“Institut National de Metrologie”/CNAM (BNM-INM, Francia), el BNM-“Laboratoire National D’Essais” (BNM-LNE, Francia) y en “Physikalisch-Technische Bundesanstalt” (PTB, Alemania) en el marco de cooperación del Proyecto Euromet [14]. Los primeros cuerpos negros para termometría de radiación desarrollados en NPL fueron Pd-C y Ir-C. El primer prototipo desarrollado por BNM-LNE para termometría de contacto empleó Pt-C como material de punto fijo.

Más tarde el número de participantes aumentó para incluir participación industrial (Thermocoax y Land Instruments International) y una Universidad (Universidad de Valladolid). Una propuesta fue realizada al “European Commission Fifth Framework “GROWTH” Programme” con la intención de desarrollar el conocimiento de la tecnología de los eutécticos C-M en Europa. Un proyecto de investigación, “Novel, High temperature, Metal-carbon Eutectic fixed points for Radiation Thermometry, Radiometry and Thermocouples (HIMERT)” fue aceptado [15]. Adicionalmente ha habido una importante colaboración entre los miembros del proyecto HIMERT y el NMIIJ.

Otros INM además de los citados con anterioridad han llevado a cabo estudios y han participado en intercomparaciones con eutécticos C-M y C-CM. El “All-Russia Institute for Measurements in Optics and Physics” (VNIIIFI) ha desarrollado puntos fijos eutécticos C-CM para su implementación en radiometría [16]. El VNIIIFI, el “National Institute of Metrology of China” (NIM), el Centro Español de Metroología (CEM), el “National Measurement Laboratory of Australia” (NML), el “Korea Research Institute of Standards and Science” (KRISS), el “Bureau International des Poids et Mesures” (BIPM) y el “National Institute of Standards and Technology of the USA” (NIST) han participado en intercomparaciones con miembros del proyecto HIMERT y del NMIIJ [17-22].

Un buen resumen de mediciones de temperaturas eutécticas C-M y C-CM realizadas por cinco INM (NMIIJ, NPL, BNM-INM, PTB, VNIIIFI y NIST) que han realizado estudios en estos puntos fijos de alta temperatura puede encontrarse en la referencia [23].

Este trabajo es una continuación de los resultados presentados en la tesis de Pablo Jimeno Largo [24], de la Universidad de Valladolid.

1.2. Objetivos

Los objetivos de esta tesis son:

- Encontrar un buen análisis numérico para la simulación de transferencia de calor por radiación dentro de hornos de alta temperatura.
- Entender mejor el comportamiento de los puntos fijos de alta temperatura en el interior del horno, a) el efecto del diseño del crisol y del horno en la temperatura resultante, b) La influencia del perfil de temperatura en el interior del horno.
- Determinar la incertidumbre asociada a las perdidas de calor del horno al entorno, medida como caída de temperatura en la pared de medición.
- Estimar la incertidumbre en la medida de temperatura asociada a la conducción térmica del grafito y la emisividad de las paredes del crisol dentro del horno.

Para realizar estos objetivos, se ha realizado un análisis numérico con el software FLUENT. Se ha empleado el análisis numérico porque la investigación experimental de estos parámetros es demasiado costosa en unos casos e imposible en otros.

1.3. Referencias del capítulo 1

- [1] Bedford R.E., Bonnier G., Maas H. and Pavese F., “Recommended values of temperature on the International Temperature Scale of 1990 for a selected set of secondary reference points”, *Metrologia*, **33**, 1996, pp. 133-154.
- [2] Kim Y.-G., Gam K.S. and Kang K.H., “Fabrication of a nickel freezing-point cell and preliminary study of its behaviour”, *Metrologia*, **37**, 2000, pp. 243-245.
- [3] Quinn T.J. and Chandler T.R.D., “A new determination of the freezing point of platinum”, *Metrologia*, **7**, 1971, pp. 132-133.
- [4] Jones T.P. and Tapping J., “The freezing point of platinum”, *Metrologia*, **12**, 1976, pp. 19-26.
- [5] Jones T.P., “The freezing point of palladium in argon”, *Metrologia*, **25**, 1988, pp. 191-192.
- [6] Kim Y.-G., Gam K.S. and Kang K.H., “Realization of the palladium freezing point for thermocouple calibrations”, *Metrologia*, **36**, 1999, pp. 465-472.
- [7] Machin G., McEvoy H.C. and Boyes S.J., “A realisation of the Pd point at NPL”, *Proceedings of Tempmeko 1996*, Torino, 1996, pp. 31-33.
- [8] Jones T.P. and Hall K.G., “The melting point of palladium and its dependence on oxygen”, *Metrologia*, **15**, 1979, pp. 161-163.
- [9] Sakate H., Sakuma F. and Ono A., “Observation of Al₂O₃ melting and freezing plateaus using a cavity-type tungsten crucible”, *Metrologia*, **32**, 1995, pp. 129-131.
- [10] Yamada Y., Sakate H., Sakuma F. and Ono A., “Radiometric observation of melting and freezing plateaus for a series of metal-carbon eutectic points in the range 133°C to 195°C”, *Metrologia*, **36**, 1999, pp. 207-219.
- [11] Yamada Y., Sakate H., Sakuma F. and Ono A., “A possibility of practical high temperature fixed points above the copper point”, *Proceedings of Tempmeko 1999*, Delft, 1999, pp. 535-540.
- [12] Yamada Y., Sasajima N., Sakuma F. and Ono A., “Realizing fixed points above the copper point up to 250 °C using metal-carbon eutectics”, *Proceedings of Tempmeko 2001*, Berlin, 2001, pp. 19-26.
- [13] Sasajima N., Yamada Y. and Sakuma F., “Investigation of fixed points exceeding 250 °C using metal carbide-carbon eutectics”, *Temperature: Its*

- Measurement and Control in Science and Industry*, 7, edited by Ripple D.C., AIP Conference Proceedings, 2003, pp. 291-296.
- [14] Sadli M., Machin G., Lowe D., Hartmann J. and Morice R., “Realisation and comparison of metal-carbon eutectic points for radiation thermometry applications and W-Re thermocouple calibration”, *Proceedings of Tempmeko 2001*, Berlin, 2001, pp. 507-512.
- [15] Machin G., Beynon G., Edler F., Fourrez S., Hartmann J., Lowe D., Morice R., Sadli M. and Villamanan M., “HIMERT: a pan-European project for the development of metal carbon eutectics as temperature standards”, *Temperature: Its Measurement and Control in Science and Industry*, 7, edited by Ripple D.C., AIP Conference Proceedings, 2003, pp. 285-290.
- [16] Sapritsky V., Ogarev S., Khlevnov B., Samoylov M. and Khromchenko V., “Development of metal-carbon high-temperature fixed-point blackbodies for precision photometry and radiometry”, *Metrologia*, 40, 2003, pp. S128-S131.
- [17] Yamada Y., Duan Y., Ballico M., Park S.N., Sakuma F. and Ono A. “Measurement of Rh-C, Pt-C and Ru-C eutectic points by four national metrology institutes”, *Metrologia*, 38, 2001, pp. 203-211.
- [18] Machin G., Yamada Y., Lowe D., Sasajima N., Anhalt K., Hartmann J., Goebel R., McEvoy M. C. and Bloembergen P., “A comparison of high temperature fixed-points of Pt-C and Re-C constructed by BIPM, NMIJ and NPL”, *Proceedings of Tempmeko 2004*, Cavtat-Dubrovnik, 2004.
- [19] Machin G., Yamada Y., Lowe D., Sasajima N., Sakuma F., and Fan Kai, “A comparison of metal-carbon eutectic blackbody cavities of rhenium, iridium, platinum and palladium between NPL and NMIJ”, *Proceedings of Tempmeko 2001*, Berlin, 2001, pp. 851-856.
- [20] Hartmann J., Anhalt K., Sperfeld P., Hollandt J., Sakharov M., Khlevnov B., Pikalev Yu., Ogarev S. and Sapritsky V., “Thermodynamic temperature measurements of the melting curves of Re-C, TiC-C and ZrC-C eutectics”, *Proceedings of Tempmeko 2004*, Cavtat-Dubrovnik, 2004.
- [21] Goebel R., Yamada Y. and Stock M., “Thermodynamic temperature measurements of metal-carbon eutectic fixed points”, *Proceedings of Tempmeko 2004*, Cavtat-Dubrovnik, 2004.

- [22] Machin G., Gibson C.E., Lowe D., Allen D.W., Yoon H.W. “A comparison of ITS-9 \square and detector based scales between NPL and NIST using metal-carbon eutectics” *Proceedings of Tempmeko 2004*, Cavtat-Dubrovnik, 2 $\square\!4$.
- [23] Sadli M., Fischer J., Yamada Y., Sapritsky V., Lowe D. and Machin G., “Review of metal-carbon eutectic temperatures: proposal for new ITS-9 \square secondary points”, *Proceedings of Tempmeko 2004*, Cavtat-Dubrovnik, 2 $\square\!4$.
- [24] Jimeno Largo P., “novel high temperature metal-carbon eutectic fixed points: influence of impurities and of the temperature distribution at the radiant cavity”. Tesis doctoral. Abril 2 $\square\!5$. Universidad de Valladolid.

Capítulo 2. Fundamentos de termometría: Temperatura, termómetros y escalas de temperatura¹

2.1. Notas históricas

Intuitivamente, al hablar de temperatura, se piensa en que es una magnitud que da idea de cómo de caliente o frío está un cuerpo. Se habla de temperatura al referirse a la fiebre de un ser humano o de la temperatura de un horno para cocinar o del tiempo que hace.

Por tanto, este concepto está íntimamente relacionado con la existencia humana, con el mundo de cada día. Esto también ocurre con otras magnitudes, como la masa, la longitud o el tiempo. Estas cuatro magnitudes son parte de las siete magnitudes fundamentales del SI. Sin embargo, no existió una buena comprensión de la temperatura hasta el siglo XVIII. Y esto es debido a que el establecimiento preciso del concepto de temperatura y su medida está íntimamente ligado con el desarrollo de la termodinámica. De todas formas, a pesar de la existencia de primeras ideas sobre ésta, la cristalización de una apropiada definición y medida costó más de un siglo.

No es tan extraño si se piensa que el concepto intuitivo de temperatura es difícil. Se trata de una magnitud intensiva (es decir, que no depende de la masa), pero que no está directamente relacionada con ninguna magnitud extensiva fácil de percibir (contrariamente al caso de la presión y la fuerza). Además, hay que tener en cuenta que la idea de temperatura viene a través del sentido del tacto el cual no es muy fiable.

Por lo tanto, lo primero que hay que hacer es definir exactamente la magnitud temperatura, lo cual da un punto de partida para medirla. Después se necesitarán aparatos que lo hagan, así como escalas y unidades.

En la vida cotidiana aparecen diferentes escalas, principalmente la Celsius y la Farenheit. Respecto a los aparatos, son familiares los termómetros de mercurio y de alcohol. Se sabe que la longitud de la columna cambia con la temperatura y

¹ Las referencias a gráficas y tablas corresponden al texto original en inglés. No se han incluido en el resumen.

se obtiene una relación. Por tanto, cualquier magnitud que varíe con la temperatura podría servir en principio para construir un termómetro si se conoce la relación.

Los principios de la Termometría se establecieron en Europa en el siglo XVII (Esto no ocurrió por ejemplo en China, donde no hubo un desarrollo independiente de la Física). Antes del siglo XVII se sabía bien poco sobre el calor y la temperatura. Muchas opiniones en ese tiempo todavía se referían a los escritos médicos de Galeno (30-200 d. C.). Su termometría clínica estaba basada en las ideas de Aristóteles, que suponía que las personas diferían en sus proporciones de calor, frío, humedad y sequedad. Él proponía un estándar de temperatura neutra, hecho con cuatro partes de agua hirviendo y cuatro de hielo, correspondiendo a cuatro grados de calor y cuatro de frío.

Más de un milenio después, otro escritor médico en 578 (Hasler de Berne) adscribía diferentes grados de calor y frío a los medicamentos. Estableció una escala de temperatura con los cuatro grados de calor y frío de Galeno, con un cero en medio. Además, estableció una escala de latitudes, postulando que los habitantes de las regiones ecuatoriales tenían cuatro grados de calor y los de las regiones polares cuatro de frío. De manera que se podía calcular la cantidad adecuada de medicamento según el lugar donde el paciente vivía.

Respecto al uso de termómetros, la primera referencia lleva a Santorio Santorre (italiano) que inventó el termómetro de aire (62), aunque normalmente se le atribuye a Galileo. Éste se utilizaba para medir temperaturas, tanto en medicina como en meteorología.

El aire en el bulbo B (figura 2.) se contrae o se expande en proporción a la temperatura y mueve el menisco O del líquido (agua, alcohol o aceite). D es el depósito para el líquido. Evidentemente no era muy preciso y además, la medida dependía de los cambios de presión y temperatura del aire local.

A mediados del siglo XVII empezaron a utilizarse los termómetros de vidrio con líquido en lugar de aire, al principio agua y alcohol ("termómetro de espíritu") y después mercurio (pero el mercurio no se consideró satisfactorio y fue desechado). En el desarrollo de estos termómetros fueron muy importantes los avances en el arte de soplar vidrio en Italia del Norte. Estaban marcados en intervalos iguales de fracciones del volumen del bulbo, por tanto, para obtener

medidas comparables, los termómetros debían ser absolutamente iguales. Eran bastante sensibles, pero todavía no existía una escala universal.

En 1660 Robert Hooke modificó el diseño italiano y demostró que partiendo de los mismos principios, se podían construir termómetros comparables sin necesidad de tener las mismas dimensiones. Se trataba de considerar incrementos iguales de volumen partiendo del punto de congelación del agua. Se introduce por primera vez la idea de un punto fijo, aunque Hooke planteaba dos puntos fijos para la congelación del agua (posiblemente debido a la dilatación anómala del agua a 4°C). Estableció una escala de -7 grados a 3 grados que se utilizó como estándar en la Royal Society hasta 1709 y con la que se registraron muchos datos meteorológicos.

Hasta ahora se tiene el concepto de escala, pero no existe independencia de la escala con la magnitud termométrica, ya que no existe una apreciación de las diferencias entre las propiedades del fluido. Fue Reaumur (1739) quien indicó que las escalas de alcohol y mercurio son diferentes porque los dos líquidos no se dilatan de la misma forma con la temperatura.

A principios del siglo XVIII aparecen las contribuciones de Farenheit y Amontons, los cuales trabajaron en dos aspectos diferentes que ahora se distinguen como termometría primaria y secundaria.

- Farenheit:

Era un vidriero holandés. Fue la primera persona que hizo termómetros de mercurio fiables. Además, después de discusiones con el astrónomo Römer estableció una escala con dos puntos fijos y un conveniente número de divisiones. Él aceptó las calibraciones de Römer y estableció como puntos fijos una mezcla de agua con hielo (32 °F) y la temperatura del cuerpo humano sano a 96°F. (Dividió los grados de Römer en 4 para tener más precisión y aceptó como cero la temperatura del día más frío del año - 7 enero de 1709- en Copenague).

- Amontons:

Desarrolló el termómetro de gas a volumen constante. Usó aire como medio termométrico y concluyó que la temperatura más baja posible era la correspondiente a presión cero de gas (primer paso en la comprensión de la temperatura). Indicó que la temperatura era proporcional a la presión y por tanto sólo era necesario un punto fijo para definir la escala. No fue tenido en cuenta porque a efectos prácticos era muy incómodo.

La historia de la termometría ha seguido desde ese momento dos caminos, que llevan a lo que hoy se considera como termometría primaria y termometría secundaria.

En el primer caso se desarrollan escalas prácticas basadas en puntos fijos arbitrarios y mejores termómetros prácticos. En este sentido, Celsius (1742) estableció una escala en un termómetro de mercurio con dos puntos fijos separados por 100 grados, el punto de hielo y el agua hirviendo. Pero él asignó los 100 grados al agua congelada y los 0 grados al vapor. Fue su discípulo, Strömer quien la invirtió. Además se introdujeron los termómetros de resistencia de platino y el termopar de platino/rodio al final del siglo XIX. La culminación del trabajo en termometría práctica es la adopción de una escala internacional de temperaturas en 1927 (ITS-27).

En la segunda línea, se desarrolla el termómetro de gas y la Termodinámica. Están los trabajos de Boyle, Dalton, Gay-Lussac, Charles, etc. sobre las propiedades de los gases, que llegan a la conclusión de que todos los gases tenían casi el mismo coeficiente de dilatación. Esto hizo posible hablar de una escala independiente de las propiedades del fluido y con un único punto fijo. Todo esto no se aceptó completamente hasta que en 1960 se redefinió el kelvin asignando un único punto fijo.

2.2. Concepto de temperatura

"Temperatura es una magnitud que toma el mismo valor en todos los sistemas que se encuentran en contacto térmico y han llegado al equilibrio térmico".

Esta idea de la existencia de un parámetro que caracteriza el estado interno del sistema proviene del Principio Cero de la Termodinámica, que dice: "Si dos sistemas están separadamente en equilibrio térmico con un tercero, entonces también están en equilibrio entre sí". O lo que es lo mismo: "Si tres o más sistemas están en contacto térmico entre sí y todos juntos en equilibrio, entonces si se toman dos cualesquiera separadamente, también estarán en equilibrio entre sí". Se llamó Principio Cero porque su enunciado fue posterior al del primer principio, pero se consideraba más básico que éste, y por tanto, debía colocarse

antes. También se puede formular el Principio Cero diciendo que "El estado de equilibrio de un sistema queda perfectamente determinado mediante el conocimiento de los parámetros externos y la temperatura".

Esto permite imaginar un sistema, llamado termómetro, que se lleve al contacto térmico con otros sistemas para descubrir si están o no en diferentes estados térmicos. Se sabe que el contacto térmico significa que están separados por paredes diatérmicas, es decir, que permiten el paso de energía característica (calor).

Partiendo de la idea de que existe un equilibrio térmico mutuo y por tanto una relación funcional entre las variables de estado de los sistemas (figura 2.2), $\theta = \theta(x, y)$, se puede justificar matemáticamente la existencia de una función con el mismo valor en todos los sistemas en equilibrio térmico. El lugar geométrico de todos los puntos con el mismo valor de esa función es una isotermia (T constante).

Es interesante recordar que el primer principio da una idea de la ley de transformación de la energía

$$dU = \delta W + \delta Q \quad (2.1)$$

Por convención se establece que el calor se transfiere desde el sistema con temperatura más alta al sistema con temperatura más baja.

Además, el segundo principio permite la definición de otra magnitud muy importante en Termodinámica, la entropía, que está íntimamente ligada con la temperatura, ya que es el factor integrante del calor

$$\delta Q/T = dS \text{ (proceso reversible)} \quad (2.2)$$

Por otra parte, si se analiza el comportamiento microscópico de los sistemas, se ve que en el caso de un gas ideal clásico, la teoría cinética indica que para una molécula de masa m , el valor medio del cuadrado de la velocidad es:

$$\langle v^2 \rangle = 3 k T/m$$

Por lo cual, se podría decir que la temperatura es una medida de la velocidad media de las moléculas de un gas ideal de masa molecular conocida (está relacionada con la energía cinética).

2.3. Concepto de termómetro y escala de temperatura

Habiendo introducido la temperatura, que es magnitud fundamental, se explica ahora la forma de medirla.

Para medir la temperatura se utilizan los termómetros (sistema de referencia) y como tal se puede utilizar cualquier magnitud macroscópica de un sistema que varíe al cambiar la temperatura. A tal magnitud se le denomina propiedad o variable termométrica. Tales pueden ser, por ejemplo, la longitud de un alambre, la resistencia eléctrica de un conductor, la f.e.m. de un par termoeléctrico, el índice de refracción de una sustancia, etc.

En Termometría se suele distinguir entre termómetros primarios y termómetros secundarios.

Termómetros primarios: Son aquellos en los que la ecuación de estado se puede escribir explícitamente sin introducir constantes dependientes de la temperatura.

Ejemplos: Termómetro de gas, termómetro acústico, termómetro de ruido (eléctrico), termómetro de radiación total. (En principio no se puede escribir la ecuación de estado y utilizarla como termómetro, confiando en que la temperatura obtenida esté en acuerdo termodinámico y numérico con otro sistema que tenga una ecuación de estado diferente). La presencia de constantes independientes de la temperatura puede ser resuelta midiendo una temperatura de referencia, T_0 (caso de R en el termómetro de gas).

Termómetros secundarios: Aquellos que no son primarios.

Ejemplos: Termómetro de resistencia de platino (no se puede utilizar como termómetro primario porque no se puede escribir una ecuación explícita de estado). Para utilizar este tipo de termómetros se tienen que calibrar con un termómetro primario, directa o indirectamente, a tantas temperaturas como sea necesario para determinar la forma de los términos dependientes de la temperatura desconocidos. No resulta siempre tan obvio distinguir si un termómetro es primario o secundario.

TERMOMETRÍA PRIMARIA \Rightarrow TEMPERATURA TERMODINÁMICA

(Directamente una variable de la función de estado)

TERMOMETRÍA SECUNDARIA \Rightarrow TEMPERATURA EMPÍRICA

(Ligada a una propiedad termométrica, que varía con la temperatura)

2.4. Escala internacional de temperatura

La Escala Internacional de Temperatura de 1990 fue adoptada por el Comité Internacional de Pesas y Medidas en su reunión de 1989, de acuerdo con la resolución de la Conferencia General de 1987. Esta escala reemplaza la Escala Práctica Internacional de Temperatura de 1968 (edición revisada en 1975) y la Escala Provisional de 1976 entre 0,5 y 30 K [1].

2.4.1. Unidades de Temperatura

La unidad de la magnitud física fundamental conocida como temperatura termodinámica, cuyo símbolo es T , es el kelvin, K, definido como la fracción $1/273,16$ de la temperatura termodinámica del punto triple del agua.

Debido a la forma en que se definieron las escalas anteriores, es común expresar la temperatura a partir de su diferencia respecto al punto de hielo, 273,15 K. Una temperatura termodinámica, T , expresada de esta forma se conoce como temperatura Celsius, cuyo símbolo es t , definida por:

$$t \text{ } (^{\circ}\text{C}) = T(\text{K}) - 273,15 \quad (2.3)$$

La unidad de la temperatura Celsius es el grado Celsius, cuyo símbolo es $^{\circ}\text{C}$, el cual tiene el mismo tamaño por definición. Una diferencia de temperatura se puede expresar en kelvins o en grados Celsius.

La Escala Internacional de Temperatura de 1990 (ITS-90) define tanto las Temperaturas Kelvin Internacionales, T_{90} , como las Temperaturas Celsius Internacionales, t_{90} .

2.4.2. Principios de la Escala Internacional de Temperatura

El propósito de la Escala Internacional de Temperatura es definir procedimientos por los cuales unos determinados termómetros de la calidad requerida puedan ser calibrados de tal manera que los valores de la temperatura obtenidos de ellos sean precisos y reproducibles, y a la vez se aproximen a los correspondientes valores termodinámicos tanto como la tecnología existente lo permita [2].

Existen diferencias numéricas significativas entre los valores de T_{90} y los correspondientes de T_{68} medidos en la Escala Práctica Internacional de 1968 (IPTS-68). La ITS 90 abarca desde 0,65 K hasta la temperatura más alta medible a partir de la ley de radiación de Planck usando radiación monocromática. La ITS-90 comprende un número de intervalos y subintervalos a partir de los cuales se define la T_{90} . Algunos de estos intervalos y subintervalos se solapan y donde se produce este solapamiento, existen diferentes definiciones de T_{90} igualmente válidas.

Para medidas de muy alta precisión puede haber errores numéricos detectables entre medidas realizadas a la misma temperatura, pero con diferentes definiciones. Del mismo modo, incluso usando una única definición, a una temperatura entre dos puntos fijos dos instrumentos de interpolación aceptables (ej. termómetros de resistencia) pueden proporcionar diferentes valores numéricos de T_{90} . En todo caso, estas diferencias tienen una importancia práctica despreciable.

Dispositivos estándar e intervalos de medida

- Entre 0,65 K y 5,0 K, T_{90} se define en términos de las relaciones presión de vapor-temperatura del ^3He y ^4He .
- Entre 3,0 K y el punto triple del neón (24.556 K) T_{90} se define por medio de un termómetro de gas de helio calibrado a tres temperaturas experimentalmente asequibles a las que se les ha asignado valores numéricos (puntos fijos definidos) y usando procedimientos de interpolación específicos.

- Entre el punto triple del hidrógeno (13.8033 K) y el punto de congelación de la plata (96.78°C) T_{90} se define por medio de termómetros de resistencia de platino calibrados con determinados conjuntos de puntos fijos y utilizando unos procedimientos de interpolación específicos.
- Por encima del punto de congelación de la plata (96.78°C), T_{90} se define en función de uno de los puntos fijos adoptados y la ley de radiación de Planck.

Puntos fijos utilizados

Históricamente, en las distintas escalas internacionales aceptadas, se han utilizado distintos puntos de cambio de fase como puntos fijos.

- Puntos triples: Única combinación de presión y temperatura en la cual coexisten las tres fases (sólida, líquida y vapor) de una sustancia pura.
- Puntos de congelación: Temperatura a la cual se empieza a formar el sólido a partir del líquido a 1 atm .
- Puntos de fusión: Temperatura a la cual se funde el sólido a 1 atm .
- Puntos de ebullición: La presión de vapor de una sustancia pura es únicamente función de la temperatura. Se suelen considerar los puntos de ebullición normales, que es la temperatura a la cual la presión de vapor es 1 atm .
- Puntos de transición a superconductor (en la Escala Provisional del 76, para temperaturas muy bajas $< 10\text{ K}$)

Dada la dificultad de los puntos de ebullición por su gran sensibilidad a los cambios de presión, en la ITS-90 se han eliminado todos los puntos de ebullición de escalas anteriores, y han sido sustituidos por puntos triples.

Es interesante resaltar que no se han recogido los puntos de transición a superconductor de 1976, y que en líneas generales, se podría decir que por debajo de 0°C se tiene principalmente puntos triples, mientras que por encima de 0°C son puntos de congelación.

2.4.3. Actual desarrollo de la Escala Internacional de Temperatura

En 2006, motivado por la necesidad de una guía definitiva en la realización práctica del kelvin, El Comité Consultor de Termometría (CCT)

elaboró la “*mise en pratique*” para la definición del kelvin (*MeP-K*) [3]. El Comité Internacional de Pesas y Medidas (CIPM) apuntó que una nueva definición del Kelvin, basada en la determinación más exacta de la constante de Boltzmann, requeriría una *MeP-K* [4]. Por ello, el CCT consideró elaborar una nueva Escala Internacional de Temperatura que remplazara la actual ITS-90 y la Escala Provisional de Baja Temperatura de 0.9 mK a \square K (PLTS-2000). Sin embargo, el CCT decidió no hacerlo porque supondría una pesada carga para la industria, que ha hecho una gran inversión en software y hardware específicos para la ITS-90. En cambio, el CCT elaboró la *MeP-K* para abrir un nuevo y flexible camino para actualizar y expandir el rango de métodos termométricos reconocidos sin cambiar el estatus de la ITS-90. La *MeP-K* incluye obtenciones directas de la temperatura termodinámica, independientes de la ITS-90, donde las técnicas de termometría primaria habían avanzado lo suficiente para asegurar la fiabilidad. Esto se ha realizado tanto para baja como para alta temperatura.

Muy bajas temperaturas (PLTS-2000)

Los requerimientos en la medida de temperatura por debajo de \square K difieren en grado y naturaleza de las medidas de mayor temperatura. Para dichos requerimientos se puede emplear el termómetro de presión de fusión del 3 He propuesto por Scribner y Adams [5].

En \square 996, el CCT impulsó la derivación de la ecuación de presión de fusión del 3 He para que sirviera como base en la ampliación de la ITS-90 hasta la temperatura aproximada de \square mK.

La Escala Provisional de Baja Temperatura del año 2000, PLTS-2000 [6], fue adoptada por el CIPM en octubre de 2000 para extensión de la ITS-90 a bajas temperaturas.

Muy altas temperaturas [7]

Un grupo de trabajo del Comité Consultor de Termometría, CCT-WG5, se estableció en mayo de 2008 para examinar los distintos métodos de medida directa de la temperatura termodinámica por encima del punto de la plata, y en

particular, para elaborar el texto de la *MeP-K* en ese rango de temperatura. A pesar de que la ITS-90 es fácil de implementar, el empleo de otros métodos puede tener ventajas significativas en términos tanto de disminución de incertidumbres como en incremento de robustez y seguridad en la realización. Estos métodos son: (a) Radiometría absoluta ligada a unas unidades radiométricas apropiadas, (b) Los puntos fijos eutécticos de alta temperatura como referencias estándar para la realización de la temperatura termodinámica.

2.□ Referencias del capítulo 2

- [1] Preston-Thomas H., “International Temperature Scale of 1990 (ITS-90)”,
Metrologia, **27(1)**, 1990, pp. 3-10.
- [2] Bureau International des Poids et Mesures, “Supplementary information for the International Temperature Scale of 1990”. 1997.
- [3] Mise en pratique for the definition of the kelvin.
http://www.bipm.org/utils/en/pdf/MeP_K.pdf
- [4] CIPM Recommendation 2(CI-2005).
<http://www.bipm.org/cc/CIPM/Allowed/94/CIPM-RecomCI-2005-EN.pdf>
- [5] Scribner R A and Adams E D 1970 *Rev. Sci. Instrum.* **41** pp. 287-288.
- [6] Rusby R L, Durieux M, Reesink A L, Hudson R P, Schuster G, Kühne M, Fogle W E, Soulen R J, and Adams E D 2002 *Journal of Low Temperature Physics* **126** 633-642.
- [7] Machin G., Bloembergen P., Anhalt K., Hartmann J., Sadli M., Saunders P., Woolliams E., Yamada Y., Yoon H., “Practical Implementation of the *Mise en Pratique* for the Definition of the Kelvin Above the Silver Point”. *Int J Thermophys* **31**, 2010, pp. 779–788.

Capítulo 3. Metodología: Análisis Numérico

3.1. Introducción

Como ya se ha indicado, este proyecto pretende resolver un problema físico en el que están involucrados los fenómenos de transmisión de calor por conducción, convección y radiación, empleando para ello la discretización usada en los métodos numéricos de las ecuaciones que rigen dichos fenómenos.

3.2. Generalidades de la Mecánica de Fluidos Computacional

3.2.1. Introducción

La mecánica de fluidos computacional (MFC) es una técnica que permite hallar una solución numérica de las ecuaciones que gobiernan el movimiento de los fluidos en un dominio espacial y temporal, así como otros fenómenos asociados: transferencia de calor, reacciones químicas, arrastre de sólidos..., permitiendo obtener una descripción completa del campo fluido.

Las ecuaciones que gobiernan la dinámica de fluidos newtonianos, ecuaciones de Navier-Stokes, fueron establecidas hace más de un siglo, pero la resolución numérica era impensable con los medios de cálculo de aquella época. Se sabe que si no se realizan importantes simplificaciones, no existe solución analítica. El área de la experimentación de la Mecánica de Fluidos ha jugado un papel muy importante en la validación de ciertas hipótesis simplificadoras de las ecuaciones que gobiernan el proceso, sin embargo, su coste efectivo incrementa el coste del diseño, y en ocasiones, las medidas a escala real son inviables. El continuo avance en la velocidad de cálculo de los ordenadores y su capacidad de memoria desde 1950, ha permitido afrontar cada vez problemas más complejos. Esto ha originado el nacimiento de la MFC como una rama de la Mecánica de Fluidos complementaria a su rama analítica y experimental.

Hoy en día, la MFC es la forma de encontrar numéricamente una solución a las ecuaciones de Navier-Stokes. La resolución de estas ecuaciones requiere: la implantación de ciertas condiciones de contorno en los límites del dominio, información referente a las propiedades del fluido, como la densidad, viscosidad,..., y además, en los problemas no estacionarios, la implantación de las condiciones iniciales, (campo de presión, velocidad y temperatura inicial en el interior del volumen computacional). Las ecuaciones son las mismas para cualquier situación de flujo de fluidos. La particularización a los casos concretos viene definida por las condiciones de contorno y los valores iniciales. La mejora del potencial de cálculo en la resolución numérica es lo que realmente ha impulsado la Mecánica de Fluidos Computacional (MFC).

La Mecánica de Fluidos Computacional como ciencia está constituida por mucha disciplinas diferentes tales como la física de fluidos, la matemática aplicada y la informática. Los campos de aplicación de la MFC son muy variados, es posible encontrar aplicaciones tan distintas como Aerodinámica, (flujo en torno a coches, aviones, barcos, edificios), Medio Ambiente (humos, dispersión de contaminantes en la atmósfera), Climatización (calefacción, ventilación en sitios cerrados) y Medicina (flujo sanguíneo en venas, simulación de *by pass*). La MFC utiliza los ordenadores como herramienta de trabajo para resolver numéricamente las ecuaciones que gobiernan el movimiento de fluidos. En los paquetes de software existentes, el usuario debe especificar las condiciones del problema que va a resolver, así como proveer al ordenador de ciertos parámetros de resolución para que el programa consiga encontrar una correcta solución del problema.

Las tareas principales a realizar para obtener una simulación del flujo se pueden agrupar en tres etapas:

Preproceso: Es la etapa en la que se discretiza el dominio geométrico, se imponen las propiedades del fluido y se especifican las condiciones iniciales y de contorno. Estas condiciones son las que, junto a la geometría, caracterizan un determinado problema fluidomecánico.

Resolución: En esta etapa se especifican las ecuaciones a resolver, los algoritmos de resolución y sus parámetros, y se genera de forma iterativa la solución al sistema de ecuaciones que gobiernan el proceso.

Postproceso: Finalmente, en esta etapa, los resultados obtenidos se procesan y almacena para facilitar su posterior análisis, es la etapa de visualización y análisis de los resultados con objeto de validar el comportamiento del flujo y obtener conclusiones respecto a su fiabilidad o identificación de posibles errores cometidos.

3.2.2. Ventajas e inconvenientes de la MFC

Las principales ventajas que proporciona la utilización de MFC en la resolución de problemas son:

- Reducción sustancial de tiempos y costes en los nuevos diseños.
- Posibilidad de analizar sistemas o condiciones muy difíciles de simular experimentalmente: velocidades hipersónicas, temperaturas muy altas o bajas, movimientos relativos, etc.
- Capacidad de estudiar sistemas bajo condiciones peligrosas o más allá de sus condiciones límite de funcionamiento.
- Alcanzar una solución que suministra una información más completa y detallada de los campos de velocidad, presión, temperatura..., en el espacio y tiempo, que los métodos experimentales.

Los inconvenientes que podemos encontrar en la utilización de MFC:

- Es una técnica cara, ya que son necesarias máquinas de gran capacidad de cálculo, el software tiene un precio poco accesible al público, y es necesario un personal cualificado para hacer funcionar el programa y analizar adecuadamente los resultados.

- La limitación de los modelos existentes para la turbulencia, flujo bifásico, combustión, etc.

El papel de la MFC en las predicciones de flujos, en el campo de la ingeniería ha alcanzado su apogeo en la actualidad, gracias a la visión tridimensional de los problemas fluido-dinámicos, sobre el análisis bidimensional de la Mecánica de fluidos teórica o experimental.

3.2.3. Metodología

En los paquetes de software de MFC, el usuario debe especificar las condiciones del problema que se va a resolver, así como proveer al código de ciertos parámetros de resolución para que este consiga encontrar una correcta solución del problema. Los pasos en los que esta información es introducida en el ordenador son los siguientes:

1. Especificar la geometría del problema. Es preciso introducir en el programa los contornos del dominio del problema. Este proceso es relativamente sencillo cuando el modelo es bidimensional, porque se trata de definir unas líneas que limitan la zona del problema. Estas líneas pueden ser muy sencillas en el caso de rectas o circunferencias. Si las curvas son de otro tipo, se introducirán mediante puntos. Cuando el modelo es tridimensional, la especificación de la geometría requiere introducir las superficies de contorno del problema, que puede tener mucha complicación si hubiera que definirla por puntos.

2. Creación del mallado o volúmenes en los que van a ser calculadas todas las variables. El mallado puede ser estructurado o no estructurado. El mallado estructurado puede estar compuesto por triángulos o hexaedros, que pueden deformarse para adaptarse a las superficies curvas de la geometría. El mallado estructurado está formado por triángulos o tetraedros, construidos a partir de la división de los contornos de la geometría. Este último tipo de mallado es mucho más sencillo de crear que el anterior, aunque el procedimiento de cálculo converge mejor en las mallas estructuradas.

3. Imposición de las condiciones de contorno, que fijan los valores de ciertas variables en los límites del dominio. Estas condiciones se le imponen a las variables de presión, temperatura, velocidad, o gradiente de las variables. También hay que imponer condiciones para las variables de turbulencia que haya, según el modelo de turbulencia que se está utilizando.

4. Introducción de las condiciones iniciales. En el caso de un problema no estacionario hace falta definir unos valores de las variables para todos los puntos del dominio, desde los cuales empezará el programa a calcular las soluciones de los sucesivos pasos temporales. En el caso de un problema estacionario, es preciso introducirle al programa unos valores iniciales de las variables, de los cuales partirá el proceso iterativo.

5. Especificación de las variables del fluido, tales como la viscosidad y la densidad. Estas magnitudes pueden variar con la temperatura, la presión, etc. Habría que introducirle al programa el modelo matemático de variación, con los coeficientes correspondientes. También pueden considerarse varios tipos de problema, según se tenga en cuenta o no la transferencia de calor. En ese caso, habría que introducirle al programa las propiedades térmicas del fluido de que se trate.

6. Parámetros de control que afectan a la resolución del problema.

3.3. Trabajando con FLUENT

Como se ha dicho anteriormente, el programa FLUENT ha sido elegido para realizar el análisis numérico. Los buenos resultados obtenidos en anteriores estudios [1], la robustez de sus algoritmos y la familiaridad con este software han sido las razones para elegirlo.

3.3.1. La ecuación de transferencia de calor

FLUENT resuelve la ecuación de la energía de la siguiente manera:

$$\frac{\partial}{\partial t}(\rho E) + \nabla \cdot (\vec{v}(\rho E + p)) = \nabla \cdot \left(k_{\text{eff}} \nabla T - \sum_j h_j \vec{J}_j + (\bar{\tau}_{\text{eff}} \cdot \vec{v}) \right) + S_h \quad (3.1)$$

Donde k_{eff} es la conductividad efectiva, y J_j es el flujo de difusión de las especies j . Los tres primeros términos de la parte de la derecha de la ecuación 3.1 representan la transferencia de energía por conducción, difusión de especies y disipación viscosa respectivamente. S_h incluye el calor de las reacciones químicas.

3.3.2. La ecuación de transferencia de radiación

La ecuación de transferencia de radiación (RTE) para un medio participativo es

$$\frac{dI(\vec{r}, \vec{s})}{ds} + (a + \sigma_s)I(\vec{r}, \vec{s}) = an^2 \frac{\sigma T^4}{\pi} + \frac{\sigma_s}{4\pi} \int_0^{4\pi} I(\vec{r}, \vec{s}') \Phi(\vec{s} \cdot \vec{s}') d\Omega' \quad (3.2)$$

donde \vec{r} = Vector posición

\vec{s} = Vector director

s = Longitud del trayecto

a = Coeficiente de absorción

n = Índice de refracción

σ = Constante de Stefan-Boltzmann ($5.672 \times 10^{-8} \text{ W/m}^2 \text{ K}^4$)

I = Intensidad de la radiación

T = Temperatura local

Φ = Función de fase

Ω' = Ángulo sólido

3.3.3. Descripción de los distintos tipos de radiación que presenta FLUENT

6.1

Lo primero es indicar que se trata de una geometría de dimensiones muy reducidas, la zona de estudio mide unos 5 mm donde predomina básicamente la transmisión de calor por radiación frente a la conducción y convección.

Se ha desarrollado un modelo bidimensional axisimétrico para todas las geometrías estudiadas. Para llegar a esta decisión se ha tenido que validar la condición de axisimetría para la transmisión de la radiación a través del eje. Para ello se ha realizado un estudio comparativo entre un modelo 2D axisimétrico, otro 2D sin condición de axisimetría y por último un modelo 3D, obteniendo resultados muy similares en los tres casos en lo que se refiere al transporte de calor por radiación a lo largo de la geometría.

A continuación se ha tenido que escoger el modelo de resolución del transporte por radiación de entre los ofrecidos por el programa. El principal criterio que emplea el programa para decidir que método usar es el de diferenciar los problemas a resolver en dos tipos, dependiendo del valor del llamado espesor óptico, definido por el producto a^*L , donde a es el coeficiente de absorción del

medio y L es una longitud característica de la geometría a estudiar. Así, si el producto a^*L es menor que uno, se trata de problemas de espesor óptico fino, y por tanto será recomendable el uso de un tipo de métodos, y si el producto es mayor que uno serán problemas de espesor óptico grueso y se usará otro tipo.

3.3.3.1. Modelo DTRM (*discrete transfer radiation model*) [2, 3]

La principal hipótesis de este método es que la radiación que emite una superficie en un cierto ángulo sólido puede ser aproximado por un rayo.

En este modelo se resuelven las ecuaciones de conservación de la masa, de cantidad de movimiento, de energía y una ecuación específica de radiación que depende del modelo de radiación seleccionado y que realmente se incorpora a la ecuación de la energía como un término más.

Ventajas del modelo:

- Es un modelo sencillo.
- Se puede incrementar la precisión incrementando en número de rayos.
- Es aplicable en un amplio rango de espesores ópticos.

Desventajas:

- El método asume que todas las superficies son difusas, por lo que la reflexión de la radiación incidente en la superficie es isotrópica respecto al ángulo sólido.
- Los efectos de la dispersión no están contemplados.
- El método supone radiación gris.
- Resolver un problema con un gran número de rayos es computacionalmente costoso.

3.3.3.2. Modelo P-1 [4, 5]

El modelo de radiación P-1 es el caso más simple del modelo P-N, que está basado en la expansión de la intensidad de radiación I en series ortogonales de armónicos esféricos.

Ventajas:

- En este modelo, la ecuación de radiación RTE, se trata como una ecuación de difusión, lo que permite resolverla con escasa demanda de la CPU.
- Permite simular los efectos de la dispersión.
- Es especialmente adecuado para problemas de espesor óptico grueso que involucren combustión y para geometrías complejas con coordenadas curvilíneas.

Desventajas:

- Asunción de superficies grises.
- Simulación únicamente de radiación gris.
- Pérdida de exactitud, dependiendo de la complejidad de la geometría, si el espesor óptico es fino.
- El modelo tiende a sobredimensionar los flujos de radiación de determinadas fuentes o sumideros de calor.

3.3.3.3. Modelo Rosseland [5]

Este modelo es válido para medios de espesor óptico grueso, $a^*L \gg 1$, y en concreto está recomendado para problemas con un espesor óptico mayor de 3. Se deriva del conjunto de ecuaciones del modelo P-1, introduciendo unas modificaciones.

Ventajas:

- No resuelve ecuaciones adicionales para calcular la radiación incidente.
- Es un modelo más rápido y que requiere menos memoria de CPU.

Desventajas:

- Solo puede usarse para geometrías de espesor óptico grueso.
- Únicamente es viable para modelos de resolución con las ecuaciones desligadas.

3.3.3.4. Modelo DO (*Discrete Ordinates*) [6, 7, 8]

Este método resuelve la ecuación de transferencia de radiación para un número discreto de ángulos sólidos, a los que se asocia un vector de dirección s ligado al sistema global de coordenadas cartesianas (x,y,z). La finura de la discretización angular es controlada por el usuario, análogamente a la elección del número de rayos en el modelo DTRM. Sin embargo, este modelo no realiza un trazado de rayos, sino que transforma la ecuación de transferencia de radiación (RTE) (ec 4.1) en una ecuación de transporte de la intensidad de radiación en las coordenadas espaciales (x,y,z). El modelo DO resuelve tantas ecuaciones de transporte como direcciones s existen. El método de resolución es idéntico al usado para resolver las ecuaciones de flujo de fluido y de la energía.

En este modelo se resuelven las ecuaciones de conservación de la masa, de cantidad de movimiento, de energía y una ecuación específica de radiación que depende del modelo de radiación seleccionado y que realmente se incorpora a la ecuación de la energía como un término más.

La implementación en FLUENT usa una variante conservativa del modelo de ordenadas discretas llamado esquema de volúmenes finitos, y su extensión para mallas no estructuradas [3].

Ventajas:

- Permite trabajar en todo el rango de espesores ópticos.
- Es capaz de simular tanto problemas con medios no participativos como con medios participativos.
- Simula medios semitransparentes.
- Los costes computacionales son moderados para las típicas discretizaciones angulares.
- Implementa tanto radiación gris como direccional.

Desventajas:

- El uso de discretizaciones angulares muy finos provoca un gran uso de los recursos de la CPU.

- Para la simulación de radiación direccional, la absorvidad se supone constante para cada longitud de onda.

3.3.3.5. Modelo S2S (*surface to surface*) [5]

Este modelo puede ser usado para calcular el intercambio de radiación en un recinto de superficies grises y con radiación difusa. La energía intercambiada entre dos superficies depende en parte de su tamaño, la distancia de separación y la orientación. Los parámetros son calculados mediante una función geométrica llamada factor de forma.

La principal hipótesis del modelo S2S es que toda la absorción, emisión y dispersión puede ser ignorada, por lo tanto, solo es necesario para el análisis considerar la radiación superficie a superficie.

Ventajas:

- Es ideal para simular cavidades en las que se produzca transferencia de calor por radiación sin que intervengan medios participativos.
- Al realizar las iteraciones, este método es más rápido que los anteriores, aunque el cálculo de la matriz de los factores de forma es costoso computacionalmente.

Desventajas:

- Asume que todas las superficies son difusas.
- Supone radiación gris.
- Los requerimientos de memoria aumentan rápidamente a medida que aumenta el número de caras involucradas en la radiación.
- No puede usarse para problemas que involucren medios participativos.
- No trabaja con mallas deslizantes.
- No permite poner condiciones de simetría ni de periodicidad.

3.3.4. Elección del modelo de radiación

Como primera medida, se pueden descartar para su uso los modelos P-1 y Rosseland ya que ambos son usados para modelar los llamados problemas de espesor óptico grueso $a^*L \geq 1$, y sin embargo el modelo a estudiar presenta un espesor óptico fino, ya que la longitud característica es $L=0.003$ m y la absorbtividad a se supondrá cero o muy próxima a cero, es decir, se tratará el fluido como un medio no participativo al no absorber nada de radiación. Quedan por tanto los otros tres modelos que, en principio serían válidos para resolver este caso.

Han sido probados los tres modelos para un caso y se ha observado que el modelo DTRM no es capaz de detectar correctamente el gradiente de temperaturas, ya que detecta una caída demasiado grande, que refutan los datos experimentales. En cuanto el modelo S2S, al no permitir la condición de axisimetría, se ha implementado un modelo en 3D, que tampoco ha conseguido obtener unos resultados satisfactorios, debido entre otras cosas a la imposibilidad, en cuanto al coste computacional se refiere, de realizar un mallado lo suficientemente fino para satisfacer las condiciones del problema. Por último, se ha probado un modelo DO con varios mallados angulares distintos, llegando a obtenerse unos resultados satisfactorios.

Atendiendo sobre todo a la gran cantidad de información y estudios adicionales disponibles sobre este modelo [6, 9, 10, 11], cosa que no ocurre con ningún otro, se ha decidido continuar la implementación con el modelo DO.

3.4. Resumen

En este capítulo se han explicado las características de la mecánica de fluidos computacional, y en particular el manejo del software FLUENT. A pesar de que este software es generalmente usado para resolver sistemas fluidos, también simula regiones sólidas y su interacción con el campo fluido. Debido a las características de los hornos usados en medidas de alta temperatura, que incluyen partes fluidas (la aleación fundida y la atmósfera de argón en el interior del horno) y sólidas (el crisol, los calentadores, las barreras de radiación...), este software es una buena herramienta para modelarlos. La familiaridad con el software y la robustez de sus algoritmos fueron otras razones para escoger su uso.

Como se ha dicho anteriormente, se emplea el análisis numérico en este estudio porque la investigación experimental de los parámetros en el interior del horno (perfiles de temperatura, pérdidas de calor...) es muy costosa o incluso imposible en algunos casos.

El siguiente capítulo incluye la validación del estudio del modelado térmico con FLUENT, comparándolo con: a) otros estudios sobre transferencia de calor por radiación hechos en el Instituto de Ciencia y Tecnología Avanzadas de Korea por la División de Ingeniería Aeroespacial, b) Algunos resultados experimentales de un horno de tres zonas usado en el Centro Español de Metrología, c) Otro software de análisis numérico llamado ANSYS.

3.5. Referencias del capítulo 3

- [1]. P. Castro. Proyecto Fin de Carrera. “modelado mediante el código fluent de la distribución de temperatura en el conjunto crisol-horno para puntos fijos eutécticos carbono-metálicos a muy alta temperatura”. Abril 2004
- [2]. M. G. Carvalho, T. Farias, and P. Fontes. Predicting Radiative Heat Transfer in Absorbing, Emitting, and Scattering Media Using the Discrete Transfer Method.
In W.A. Fiveland et al., editor, *Fundamentals of Radiation Heat Transfer*, volume 160, pages 17-26. ASME HTD, 1991.
- [3]. N. G. Shah. *A New Method of Computation of Radiant Heat Transfer in Combustion Chambers*. PhD thesis, Imperial College of Science and Technology, London, England, 1979.
- [4]. P. Cheng. Two-Dimensional Radiating Gas Flow by a Moment Method. *AIAA Journal*, 2:1662-1664, 1964.
- [5]. R. Siegel and J. R. Howell. *Thermal Radiation Heat Transfer*. Hemisphere Publishing Corporation, Washington D.C., 1992.
- [6]. E. H. Chui and G. D. Raithby. Computation of Radiant Heat Transfer on a Non-Orthogonal Mesh Using the Finite-Volume Method. *Numerical Heat Transfer, Part B*, 23:269-288, 1993.
- [7]. G. D. Raithby and E. H. Chui. A Finite-Volume Method for Predicting a Radiant Heat Transfer in Enclosures with Participating Media. *J. Heat Transfer*, 112:415-423, 1990.
- [8]. J. Y. Murthy and S. R. Mathur. A Finite Volume Method For Radiative Heat Transfer Using Unstructured Meshes. AIAA-98-0860, January 1998.
- [9]. J. C. Chai, S. V. Patankar. "Finite-Volume Method For Radiation Heat Transfer". *Advances in Numerical Heat Transfer*, pp 109-138 Vol 2, 2000.
- [10]. M. Y. Kim, S. W. Baek, J. H. Park. "Unstructured Finite-Volume Method For Radiative Heat Transfer in a Complex Two-Dimensional Geometry With Obstacles" *Numerical Heat Transfer, Part B*, Vol 39, pp 617-635 , 2001.
- [11]. G. D. Raithby. "Evaluation of Discretization Errors in Finite-Volume Radiant Heat Transfer Predictions". *Numerical Heat Transfer, Part B*, Vol 36, pp 241-264, 1999.

Capítulo 4. Estudios preliminares y validación del modelo¹

4.1. Introducción

La validación del modelo numérico es uno de los principales análisis previos que han de realizarse. Existen muchos estudios sobre el análisis numérico de la transferencia de calor y que algoritmos son mejores para cada tipo de problema. El estudio sobre la sensibilidad del mallado para este tipo de problemas esta ampliamente explicado en [1]. Para validar el cálculo numérico de la transferencia de calor por radiación en hornos de alta temperatura, algunos casos realizados por la División de Ingeniería Aeroespacial del Instituto de Ciencia y Tecnología Avanzadas de Korea [2] se han reproducido mediante FLUENT y han sido comparados.

Otro criterio de validación ha sido el modelado en 3D de un horno de tres zonas para la calibración de termopares y termómetros de radiación empleado en el Centro Español de Metrología (CEM) [3, 4].

4.2. Recinto triangular equilátero [5]

En este caso se trata de reproducir el estudio realizado por los autores M. Y. Kim, S. W. Baek y J. H. Park de la División de Ingeniería Aeroespacial del Instituto de Ciencia y Tecnología Avanzadas de Corea. Se trata de un triángulo equilátero de 1 m de lado cuyas paredes tienen una emisividad de $\epsilon=1$ y se encuentran a 0 K y en cuyo interior se encuentra un fluido a 1000 K con un coeficiente de absorción de 1 m^{-1} . El modelo presentado en su estudio consta de 900 celdas triangulares y 496 nodos.

El modelo realizado en FLUENT consta de 938 celdas y 516 nodos:

¹ Las referencias a gráficas y tablas corresponden al texto original en inglés. No se han incluido en el resumen.

La variable examinada es el flujo de calor en la pared inferior $q_w^R/\sigma T_g^4$ para una discretización angular de $\theta=4$, $\phi=8$ y de $\theta=4$, $\phi=16$ de forma que los resultados son (figuras 4.3 y 4.4)

Las gráficas 4.3 y 4.4 muestran la similitud del parámetro del flujo de calor para ambos modelos.

4.3. Recinto cilíndrico axisimétrico con medio participativo [6]

Acercándose al tipo de geometría implicada en los crisoles de puntos fijos de alta temperatura, se simula ahora un cilindro con configuración axisimétrica. Sus dimensiones son radio $r_c=1$ m y altura $z_c=2$ m. Las paredes están a 0 K con una emisividad de ($\epsilon=1$). El gas encerrado dentro del cilindro es un medio participativo con absorción y emisión a una temperatura de $T_g= 100$ K. Se han estudiado tres coeficientes de absorción distintos($k_a = 0.1, 1, 5 \text{ m}^{-1}$).

Las figuras 4.5 y 4.6 muestran el flujo adimensional de calor ($q_w^R/\sigma T_g^4$) en la pared lateral del cilindro para los tres valores del coeficiente de absorción.

Cuando el coeficiente de absorción es grande, $k_a = 5.0$, la energía de radiación que llega a la pared se acerca la intensidad de cuerpo negro. Cerca de las bases del cilindro en cambio, se observa un descenso brusco del flujo de calor radiante debido a la cercanía de las paredes frías superior e inferior. Cuando el coeficiente de absorción es pequeño $k_a = 0.1$, la emisión del medio es débil y el flujo de calor se reduce significativamente.

En esta comparativa se ve clara la buena coincidencia de ambos modelos con distribución axisimétrica y medios participativos.

4.4. Horno de alta temperatura de tres zonas

El Centro Español de Metroología (CEM) ha diseñado y construido un horno de tres zonas para la calibración de termopares y termómetros de radiación hasta 1600 °C. Este horno ha sido realizado con elementos calefactores de MoSi₂ y un tubo de alumina donde se contiene el cuerpo negro de [3].

Se pensó en la utilización de modelos numéricos para simular el comportamiento en el interior del horno debido a que el tiempo empleado en la

medida de los gradientes de temperatura a lo largo del horno es excesivamente largo.

4.4.1. Descripción del horno de alta temperatura

Un esquema del horno puede verse en la figura 4.7. Tiene tres zonas de calentamiento, la central, con tres elementos calefactores y las dos laterales con dos elementos calefactores cada una. Estos elementos se sitúan en el entorno del tubo de medición.

El tubo de medición es intercambiable dependiendo del tipo de termómetro a calibrar: termopar o termómetro de radiación. La figura 4.8 muestra el tubo diseñado para la calibración de termopares.

Estos tubos tienen cuatro pequeños canales laterales para la medición de la homogeneidad del horno mediante termopares tipo B.

4.4.2. Simulaciones realizadas [4]

Se ha escogido un modelo 3D con un plano de simetría y las propiedades de los materiales empleados se recogen en la tabla 4.1.

Se ha simulado el transporte de calor por conducción, convección y radiación con las siguientes condiciones de contorno:

- Elementos calefactores: Con propiedades similares al cobre y a temperatura constante.
- Paredes exteriores del horno: convección y radiación a la atmósfera a 300 K.
- Tapas de cierre del tubo de medición: Similares al aire y con temperatura de 300 K.

Los contornos de temperatura obtenidos para la cavidad del horno y el tubo de medición se muestran en la figura 4.9.

4.4.3. Resultados

Basados en las simulaciones térmicas es posible obtener el gradiente de temperatura a la altura de los diferentes termopares de control. Estos gradientes

modelados son comparados con los gradientes medidos experimentalmente para 1100 °C en la figura 4.10 y para 1300 °C en la figura 4.11.

Como puede verse, el ajuste entre la simulación y los datos experimentales es altamente satisfactorio.

4.5. Comparación entre los software FLUENT y ANSYS para la resolución numérica de puntos fijos eutécticos de alta temperatura

En este estudio, FLUENT es comparado con resultados previos en el análisis numérico de crisoles y hornos para puntos fijos de alta temperatura hecho por medio del software de elementos finitos ANSYS [7]. En concreto, se calcula la caída de temperatura a través de la pared radiante de un crisol de Re-C. El conjunto crisol-horno ha sido diseñado por el Instituto Nacional de Metrología de Japón (NMIJ).

4.5.1. Descripción del sistema simulado

El horno del NMIJ usado en las simulaciones es el modelo VR10-A19. Una foto y un esquema del horno se pueden ver en la figura 4.12.

La parte del crisol donde se estudia el perfil de temperatura es la pared radiante trasera, que es la que está mirando directamente a la apertura del horno y es donde el termómetro de radiación toma sus medidas. En esta pared se produce una caída de temperatura desde la temperatura nominal, debido principalmente a las pérdidas de calor por radiación al entorno. En la figura 4.13 puede verse un esquema de la posición de esta pared en el interior del horno.

El crisol es el modelo 3S usado en el NMIJ. La cavidad del crisol tiene 62 mm de largo y 3 mm de diámetro interno y la pared radiante tiene un espesor de 2.6 mm y una inclinación de 30°.

4.5.2. Modelos numéricos

Se han realizado dos modelos diferentes y se han comparado con los realizados con ANSYS. El primero es un crisol aislado, sin el horno, y el segundo es el crisol en el interior del horno. Los modelos se ven en la figura 4.14.

Se han hecho las siguientes simplificaciones:

- La geometría es considerada axisimétrica, permitiendo la elaboración de un modelo en 2D.
- La resistencia térmica de las partes roscadas es obviada debido a su escasa influencia.
- Se ha tenido en cuenta la conducción y convección en el interior del horno pero tiene escasa influencia.
- El modelo asume condiciones estacionarias.

4.5.3. Resultados

Los resultados presentados son las caídas de temperatura calculados con FLUENT y con ANSYS en la pared radiante del crisol para la temperatura nominal del Re-C (2748.15 K). Las figuras 4.17 y 4.19 representan los perfiles de temperatura. El eje x (L) de las figuras 4.16 y 4.18 empieza en el vértice del cono de la pared radiante como puede verse en la figura 4.15.

4.5.4. Conclusiones

Ha quedado demostrado que ambos programas obtienen resultados similares en el perfil de la caída de temperatura y en su orden de magnitud, aunque FLUENT calcula una caída mayor que la estimada por ANSYS. Se puede decir que la comparación es satisfactoria, teniendo en cuenta las diferencias estructurales de ambos programas:

<u>FLUENT</u>	<u>ANSYS</u>
Usa volúmenes finitos	Usa elementos finitos
Se simula el argón en el interior del	Se simula vacío en el interior del horno

horno	
El algoritmo para la ecuación de transferencia de radiación se basa en la discretización del ángulo sólido	El algoritmo para la ecuación de transferencia de radiación se basa en los factores de forma

4.6. Conclusiones

La razón principal de estos estudios preliminares era probar y validar la precisión del software FLUENT para resolver problemas de transmisión de calor que incluyeran fenómenos de transferencia de radiación similares a los ocurridos en la termometría de puntos fijos de alta temperatura. Los estudios realizados muestran que FLUENT puede ser usado para modelar los problemas de transferencias por radiación que aparecen en esta tesis.

Los siguientes capítulos se centran en modelar y evaluar los factores de incertidumbre asociados a los puntos fijos de alta temperatura, como la influencia de defectos de llenado de los crisoles, los valores de la emisividad y la conductividad térmica del grafito, la longitud del crisol y el espesor de sus paredes o el uso de distintos hornos y perfiles de temperatura.

4.7. Referencias del capítulo 4

- [1]. P. Castro. “modelado mediante el código fluent de la distribución de temperatura en el conjunto crisol-horno para puntos fijos eutécticos carbono-metálicos a muy alta temperatura”. Master Thesis. Valladolid University. April 2004.
- [2] M. Y. Kim, S. W. Baek, J. H. Park. "Evaluation of the Finite-Volume Solutions of Radiative Heat Transfer in a Complex Two-dimensional Enclosure with Unstructured Polygonal Meshes" *Numerical Heat Transfer, Part B*, Vol 54, pp 116-137 , 2008.
- [3] C. García, M. J. Martín, D. del Campo, J. P. Pérez and V. Chimenti, *Proceed. HTFP'2006 International Workshop*, Paris (2006).
- [4] P. Castro, P. Jimeno-Largo, M. A. Villamañan, J. J. Segovia and C. R. Chamorro, *Proceed. HTFP'2006 International Workshop*, Paris (2006).
- [5] M. Y. Kim, S. W. Baek, J. H. Park. "Unstructured Finite-Volume Method For Radiative Heat Transfer in a Complex Two-Dimensional Geometry With Obstacles" *Numerical Heat Transfer, Part B*, Vol 39, pp 617-635 , 2001.
- [6] M. Y. Kim, S. W. Baek, J. H. Park. "Modelling of Radiative Heat Transfer in an Axisymmetric Cylindrical Enclosure with Participating Medium" *Journal of Quantitative Spectroscopy & Radiative Transfer*, 90, pp 377-388 , 2005.
- [7] Jimeno Largo P., “novel high temperature metal-carbon eutectic fixed points: influence of impurities and of the temperature distribution at the radiant cavity”. Doctoral Thesis. April 2005. Valladolid University.

Capítulo 5. Incertidumbre en la caída de temperatura I: defectos de llenado del crisol¹

5.1. Introducción

El CCT-WG5 (Comité Consultor de Termometría- Grupo de Trabajo en termometría de radiación) ha promovido un programa de investigación para establecer los puntos fijos eutécticos de alta temperatura como estándares de temperatura por encima de 1100 °C para el año 2012 [1]. Estos puntos fijos eutécticos de alta temperatura (HTFPs) se basan en lingotes de materiales eutécticos carbono-metálicos, carburo-metálicos o aleaciones peritécticas contenidas en crisoles de grafito [2]. Sin embargo, el proceso de llenado del crisol no es inmediato y puede provocar defectos en el lingote metálico, con la aparición de agujeros o grietas en el material eutéctico. Parte del plan de investigación del CCT-WG5 es valorar los efectos que este llenado defectuoso puede tener en la temperatura del crisol y por tanto en la medida. Esta influencia no se puede determinar experimentalmente por lo que se ha elaborado un modelo de análisis numérico para el estudio. Se han construido diferentes casos, simulando la presencia de agujeros y grietas en el lingote. A priori, una grieta tendrá mayor influencia al poner en contacto directo para el intercambio térmico por radiación las paredes del crisol y del tubo de cuerpo negro.

Estos modelos han sido implementados mediante software de volúmenes finitos y la temperatura de la pared radiante abarca desde la aleación en estado sólido hasta el momento en que se funde en su totalidad. Los efectos del horno no han sido incluidos en este estudio. El modelo, que se ha realizado en 2D y presenta axisimetría, contempla las siguientes situaciones:

- Agujeros en el lingote metálico situados junto a la pared del crisol, con las dimensiones que se indican en la tabla 5.1. La posición del agujero se ha ido variando a lo largo de la pared.
- Grietas de 1.5 mm y 3 mm de ancho que permiten la vista directa entre la pared

¹ Las referencias a gráficas y tablas corresponden al texto original en inglés. No se han incluido en el resumen.

caliente exterior del crisol y la pared interior del cuerpo negro. La posición de la grieta se ha ido variando igualmente.

Este capítulo describe los resultados de estas simulaciones, en particular el efecto de estos defectos en la duración y calidad de la meseta de fusión del material eutéctico.

5.2. Construcción e implementación del modelo

El modelo térmico ha sido implementado usando el FLUENT 6.1. Para la simulación se ha empleado modelos en 2D axisimétricos. El crisol simulado ha sido diseñado por el NPL [3]. Este crisol ha sido construido con grafito de alta pureza y llenado de la aleación carbono-metálica. La longitud del crisol es de 40 mm y el diámetro externo de 24 mm. Las paredes tienen un espesor de 5 mm. El tubo interior que compone propiamente el cuerpo negro tiene un diámetro exterior de 7 mm e interior de 3 mm, una longitud de 27 mm y acaba con una pared cónica de 120°. El punto fijo modelado ha sido el Re-C (2747 K) pero estos resultados son aplicables para el resto de puntos fijos de alta temperatura. Una fotografía del crisol se puede ver en la figura 1 de [4].

Las propiedades termofísicas más importantes son: emisividad del grafito 0.86, emisividad del Re-C 0.35, conductividad térmica del grafito 36.5 W/m.K, conductividad térmica del Re-C cerca del punto de 55 W/m.K. Para la simulación del Re-C, debido a la falta de datos al respecto, se ha asumido que presenta las mismas propiedades térmicas que el Re puro.

Las condiciones iniciales y de contorno han sido fijadas con temperatura uniforme en la pared exterior del crisol, es decir sin gradientes de temperatura. La apertura al exterior del crisol se ha simulado con una tapa a temperatura ambiente que mira directamente a la pared radiante.

La simulación numérica se ha realizado de la siguiente manera. La condición inicial era que el crisol se encontraba 7 K por debajo de la temperatura de fusión. A continuación, mediante una función de incremento paulatino de temperatura, ésta ha ido aumentando hasta alcanzar en la pared exterior del crisol 20 K más que la temperatura de fusión. La media de la temperatura en la pared radiante ha sido calculada durante todo el proceso de fusión.

Los agujeros y las grietas descritos en la introducción han sido implementados uno a uno. En la figura 5.1 se puede ver uno de los modelos con un agujero y su

correspondiente mallado.

5.3. Resultados de la simulación

5.3.1 Resultados del crisol con agujeros

Los agujeros descritos en la tabla 5.1 fueron simulados en cuatro posiciones distintas a lo largo del crisol. Se han situado siempre en la pared exterior del lingote, mirando a la pared exterior del crisol, como puede verse en la figura 5.2. Estos agujeros se designan (x, y) (ver figura 5.3), donde la x designa la localización y la y sus dimensiones.

Las cuatro posiciones son, $x=1$ en la pared posterior del crisol, la más cercana a la pared radiante. (ver Figura 5.1, el agujero simulado en ese caso se encuentra en la posición 2), $x= 2, 3$ y 4 se encuentran a lo largo de la pared lateral del crisol, siendo la posición 4 la mas alejada de la pared radiante.

Los resultados del modelado térmico para los agujeros de distintos tamaños y en distintas posiciones se muestran en Figuras 5.3 y 5.4. En ellas, la temperatura está representada en el tiempo. La escala temporal es arbitraria al ser función de la conductividad térmica y densidad de la aleación pero lo representativo es la comparación relativa entre los distintos casos.

El modelo muestra que el punto fijo es bastante tolerante con la presencia de agujeros, incluso grandes, y que la posición tiene escasa influencia en la temperatura de fusión y en su duración.

La figura 5.5 muestra el efecto en la temperatura de radiación para agujeros de varios tamaños en la misma posición. De nuevo se observa que el tamaño de los agujeros no influye demasiado en la curva de fusión aunque ésta sí que es un poco menor para los agujeros de mayor tamaño.

5.3.2. Resultados del crisol con grietas

Los dos anchos de grieta 1.5 mm (grieta 1) y 3 mm (grieta 2) se modelaron en tres posiciones distintas a lo largo del crisol todas ellas perpendiculares a la pared del crisol. La posición 1 es la más cercana a la pared radiante y la posición 3 está relativamente cerca de la parte frontal del crisol, como puede verse en la figura 5.6.

Las grietas permiten un visionado directo entre la pared exterior del crisol y la pared del cuerpo negro. En la figura 5.7 se ve el efecto en la temperatura para grietas de distinto tamaño en la misma posición.

En este caso, la grieta más grande y más cercana a la pared radiante afecta significativamente a la temperatura de radiación, incrementándola en 0.1 °C aproximadamente y acortando el tiempo de fusión de la aleación. La grieta mas pequeña en la misma posición ($x=1$) tiene un efecto menor pero también significativo. Sin embargo, es interesante constatar que las grietas lejos de la pared radiante tiene un efecto marginal en la temperatura medida.

5.4. Discusión

Estos resultados fueron inicialmente un poco sorprendentes. Se había anticipado que al ser la radiación un mecanismo de transmisión de calor más eficiente en comparación con la conducción, aquella dominaría sobre ésta en el proceso global. En realidad, en este caso no es así. Esto fue percibido al estudiar el modelo en detalle. Cando se examinaba el modelo dinámico de fusión, se apreciaba que la conducción era mucho más eficiente en la transferencia de calor que la radiación, de tal forma que el frente de fusión del sólido debido a la conducción terminaba por alcanzar al frente de fusión provocado por la radiación.

Este comportamiento puede ser entendido a través de un análisis unidimensional del flujo de calor entre dos paredes paralelas comparando los mecanismos de conducción y de radiación. El factor de flujo por radiación entre flujo por conducción viene dado por la ecuación 5.1.

$$\frac{q_r}{q_c} = \frac{4\sigma T^3 x}{k(\varepsilon_1^{-1} + \varepsilon_2^{-1} - 1)} \quad (5.1)$$

Donde q_r/q_c es el factor entre los flujos de radiación y de conducción, σ es la constante de Stefan Boltzmann, T es la temperatura termodinámica, x es la separación entre las parades paralelas, k es la conductividad térmica del material, ε_1 es la emisividad del material más caliente y ε_2 es la emisividad del material más frío.

Si se emplean los valores para el Re-C (2747 K) dados al comienzo de la sección 2, así como las propiedades del Re y del grafito, entonces para el agujero de 2.5 mm de

ancho y comparando con la conducción a través de 2.5 mm de Re, el factor de flujos de calor es 0.071 mostrando que la conducción domina claramente el proceso. Como ilustración, si el agujero fuera de 25 mm entonces el factor sería 0.71 con la radiación llegando a ser casi igual de eficiente que la conducción.

Está por tanto claro que un pequeño número de agujeros, incluso grandes, en la superficie del lingote puede ser tolerado, a pesar de que se encuentren cerca de la pared radiante. Esta es una consecuencia directa de la mayor eficiencia de la conducción frente a la radiación en las escalas tan pequeñas que se presentan en el crisol. Así, una vez que el frente de fusión ha penetrado lo suficiente en el lingote, el efecto de los agujeros es suavizado enormemente.

Incluso la presencia de grietas en el lingote si están localizadas lejos de la pared radiante tiene un efecto pequeño. Sin embargo, es preciso tener precaución en la formación de grietas cercanas a la pared radiante, que sí pueden tener efectos significativos en la temperatura de radiación medida. Aquí se presenta una interesante implicación de estos resultados. Como la temperatura de radiación no parece verse afectada por pequeñas grietas cuando se encuentran lejos de la pared radiante, puede ser posible reducir el tamaño del lingote sin afectar a las medidas. Esta conclusión está lógicamente supeditada a conseguir una razonable uniformidad de temperaturas en el horno. Esta posibilidad es importante sobre todo para la construcción de lingotes de materiales especialmente caros como el platino.

5.5. Conclusiones

Las conclusiones obtenidas de este capítulo son:

- Incluso con altas temperaturas, para las dimensiones de las estructuras consideradas, la transmisión de calor por conducción es todavía más eficiente que el transporte por radiación.
- Defectos menores en los lingotes, como los agujeros en su superficie, pueden ser obviados.
- Las grietas en el lingote cercanas a la pared radiante tienen un impacto significativo en la temperatura de radiación medida pero son de menor importancia cuando se encuentran lejos de aquella.
- Parece posible, aunque es necesario realizar más estudios al respecto, que la

longitud del crisol en un horno con suficiente uniformidad de temperatura puede ser reducida, cubriendo sólo la parte posterior correspondiente a la pared radiante. Esto afectaría a la duración de la fusión pero no a la temperatura de radiación.

5.6. Referencias del capítulo 5

- [1] <http://www.bipm.org/wg/CCT/CCT-wg5/Allowed/Miscellaneous/CCT-WG5-docs-01.pdf>
- [2]. Woolliams, E., Machin, G., Lowe, D., Winkler, R., “Metal (carbide)-carbon eutectics for thermometry and radiometry: A review of the first seven years”, *Metrologia*, 43, R11-R25, 2006
- [3]. Lowe, D., Machin, G., “Development of metal-carbon eutectic blackbody cavities to 2500 °C at NPL”, In: *Tempmeko 01, The 8th International Symposium on Temperature and Thermal Measurements in Industry and Science*, Berlin, Germany, Eds. B Fellmuth, J. Seidel, G. Scholz, Published: VDE VERLAG GMBH, 519-524, 2002
- [4]. Machin, G., “Realising the benefits of improvements in high temperature metrology”, *Acta Metrologica Sinica*, 29, p. 10-17, 2008.

Capítulo 6. Incertidumbre en la caída de temperatura II: emisividad, conductividad térmica y perfil de temperatura del horno Nagano-M¹

6.1. Introducción

Por debajo del punto de fusión del cobre ($T = 1357.77$ K) la corrección para la caída de temperatura ΔT a través de la pared radiante del crisol es menor que la incertidumbre asociada a la construcción del propio punto fijo. Debido a que el intercambio de calor por radiación se incrementa a la razón de T^4 , esta corrección es mayor para los puntos fijos de alta temperatura, como las aleaciones eutécticas carbono-metálicas y las carburo-metálicas [1]. En este capítulo, la incertidumbre $u(\Delta T)$ en la caída de temperatura ΔT es evaluada para los puntos fijos eutéticos de alta temperatura Co-C, Pt-C y Re-C cuyas temperaturas de fusión T_E son 1597 K, 2011 K y 2747 K, respectivamente, para una variedad de geometrías de crisol y horno.

Los sistemas a modelar se describen en la sección 2. La estructura del modelo y las variables a calcular se presentan en la sección 3. Los resultados se exponen en la sección 4 y se discuten en la sección 5. Las principales conclusiones se presentan en la sección 6.

Este estudio se considera una continuación de [3] y [4]. El modelado de los sistemas se ha realizado mediante FLUENT, un paquete informático basado en volúmenes finitos. Los trabajos sobre la caída de temperatura presentados en [3] y [4] fueron realizados mediante el análisis de elementos finitos implementado con el programa ANSYS. Los resultados obtenidos con FLUENT y con ANSYS, aplicados a casos característicos dentro del ámbito del presente estudio, han mostrado que ambos resultan equivalentes para la resolución de los cálculos.

¹ Las referencias a gráficas y tablas corresponden al texto original en inglés. No se han incluido en el resumen.

6.2. Sistemas a modelar

El sistema utilizado como entorno experimental para los cálculos se muestra en la figura 6.1. Es el horno Nagano ‘VR10-A23’, diseñado por el Instituto Nacional de Metroología Japonés (NMIJ). Un esquema de la celda, tipo 6ST, diseñada igualmente por NMIJ, se puede ver en la figura 6.2C; su geometría se especifica en la tabla 6.1.

El gradiente de temperatura del horno es medido para los puntos fijos Co-C, Pt-C y Re-C en ocho discos bloqueadores de radiación colocados delante del crisol; así se puede ver en la figura 6.3, denominada RP (gradiente real). Los bloqueadores de radiación tienen 1 mm de espesor, separados entre ellos 10 mm y con agujeros cuyo diámetro aumenta 1 mm de uno a otro. Las medidas se han tomado con un termómetro LP-5 con un 1 mm de apertura a una distancia de medición de 760 mm.

Para evaluar la influencia del gradiente de temperatura del horno (FTP) ΔT y su incertidumbre $u(\Delta T)$, los cálculos para el crisol 6ST se han extendido para incluir también otros perfiles de temperatura llamados NF, HP, RP y CP, caracterizados por: NF: el crisol sin horno, RP: el gradiente real, medido en el horno Nagano VR10-23, CP: perfil constante de temperatura a lo largo de todo el horno a la temperatura de fusión del punto fijo en estudio T_E . Respecto al perfil HP, mostrado en la figura 6.3: ha sido obtenido de las medidas realizadas en otro horno de tres zonas, el Nagano ‘VR10-A19’, reajustando las medidas adaptándolas a la longitud del nuevo horno [3].

Finalmente, para evaluar la influencia de la geometría del crisol en la caída de temperatura, se han realizado cálculos para tres geometrías diferentes, llamadas 6ST, 3S, Mk-4; así como 6ST, 3S fueron diseñados en NMIJ, Mk-4 ha sido manufacturado por el Laboratorio Nacional de Física de Inglaterra (NPL). La comparación entre crisoles está realizada para el caso más extremo, aquel que excluye la influencia del horno, simulando únicamente el crisol. Un esquema de cada uno de los crisoles se puede ver en la figura 6.2 y sus especificaciones geométricas en la tabla 6.1.

Como en [3,4] los resultados son comparados con la expresión teórica (6.1) propuesta por Fischer y Jung [5]:

$$\Delta T = \cos\theta \cdot (r/L)^2 \cdot d \cdot (\epsilon_g/K_g) \cdot \sigma \cdot T^4, \quad (6.1)$$

donde θ es el ángulo del cono que configura la pared radiante, r es el radio interno de apertura del crisol, L la longitud de la cavidad radiante, d el espesor de la pared

radiante, ε_g la emisividad del grafito, K_g la conductividad térmica del grafito, σ la constante de Stefan-Boltzmann y T la temperatura de la cavidad en K. En la obtención de esta ecuación, el intercambio de calor por radiación dentro del crisol y entre el crisol y el horno no ha sido tomado en cuenta.

6.3. Cálculos

6.3.1. Estructura del modelo y propiedades de los materiales

Como en [3] han sido necesario asumir varias hipótesis para simplificar el cálculo. Sin estas simplificaciones la resolución hubiera llevado demasiado tiempo de cálculo computacional o bien no se hubiera podido llevar a cabo.

1-La geometría es considerada axisimétrica. Esto permite construir un modelo en 2D.

2-La resistencia térmica de las partes roscadas es despreciada por su escasa influencia y por la dificultad de su estimación.

3-La transmisión de calor por conducción y convección dentro de la atmósfera del horno se ha tenido en cuenta pero su efecto es despreciable frente al intercambio de calor por radiación.

4-El modelo asume un comportamiento estacionario.

La conductividad térmica del grafito como función de la temperatura en todo el rango de interés esta tomada de [8]. De esta referencia se toman los valores de 53.6, 45.6, 36.5 en $\text{Wm}^{-1}\text{K}^{-1}$ par los puntos fijos Co-C(1597 K), Pt-C (2011 K), Re-C (2747 K). La emisividad del grafito, estimada en 0.86 esta tomada de [5].

6.3.2. Variables calculadas

Las variables, calculadas y discutidas en las secciones 4 y 5, son:

(1) Caída de temperatura: ΔT

Es necesario destacar que ΔT se ha calculado con la pared del crisol fijada a la temperatura de fusión T_E . Esto permite simular el final del proceso de fusión y obviar el modelado de la parte correspondiente a la aleación eutéctica.

La caída de temperatura se define como $\Delta T = T_E - T_{\text{cav}}$, donde T_{cav} es obtenida

como la media de la temperatura en la pared de medición a lo largo de la franja de visión del termómetro de radiación.

(2) *Coeficientes de sensibilidad:* $(\partial \Delta T / \partial K_g)_{\varepsilon_g}$ y $(\partial \Delta T / \partial \varepsilon_g)_{K_g}$

Estos coeficientes son llamados ocasionalmente en el texto *SCK* y *SCE*, respectivamente.

Como puede verse en las figuras 6.4.a y 6.4.b para el crisol 6ST, los parámetros *SCK* ó *SCE* se obtienen calculando ΔT en un rango de valores para la variable independiente K_g ó ε_g , respectivamente, y tomando la pendiente de la gráfica de ΔT sobre K_g ó ΔT sobre ε_g a cada correspondiente temperatura nominal.

Hay que mencionar que acorde a la ecuación (6.1) tendremos como una buena aproximación :

$$(\partial \Delta T / \partial K_g)_{\varepsilon_g} = -\Delta T / K_g \quad (6.2a)$$

$$(\partial \Delta T / \partial \varepsilon_g)_{K_g} = \Delta T / \varepsilon_g \quad (6.2b)$$

(3) Incertidumbre estándar en los parámetros K_g y ε_g : $u(K_g)$ y $u(\varepsilon_g)$

(4) *Incertidumbres parciales :*

$u(\Delta T; K_g)$:

Incertidumbre en ΔT debido a la incertidumbre $u(K_g)$ en K_g

$u(\Delta T; \varepsilon_g)$:

Incertidumbre en ΔT debido a la incertidumbre $u(\varepsilon_g)$ en ε_g

$u(\Delta T; K_g, \varepsilon_g)$:

Incertidumbre en ΔT debido a las incertidumbres combinadas $u(K_g)$ en K_g y $u(\varepsilon_g)$ en ε_g

$u(\Delta T; \text{FTP})$:

Incertidumbre en ΔT debido a la incertidumbre del perfil de temperaturas del horno

(5) *Incertidumbre estándar total ΔT : $u(\Delta T)$*

6.4. Resultados

Crisol: 6ST

La tabla 6.2, sección superior, muestra ΔT calculada para los puntos fijos Re-C, Pt-C y Co-C y para los perfiles de temperatura en el horno NF, HP, RP, CP. Los resultados obtenidos aplicando la ecuación (6.1) se muestran en la última columna. Los cálculos han sido hechos para una emisividad de la pared ε_g de 0.86 y para las conductividades térmicas K_g asociadas a los puntos fijos en [5, 8].

Los resultados para los perfiles NF, HP, RP, CP de los distintos puntos fijos pueden verse en los histogramas de las figuras 6.5.a. y 6.5.b. La figura 6.6 representa ΔT , calculada para el perfil CP como función de la temperatura de fusión T_E de los eutécticos Co-C, Pd-C, Pt-C, Ir-C, y Re-C. La línea continua representa el ajuste $\Delta T = 1.50 \cdot 10^{-15} \cdot T_E^4$.

Las secciones media e inferior de la tabla 6.2 recoge los valores de los coeficientes de sensibilidad $(\partial \Delta T / \partial K_g) \varepsilon_g$ y $(\partial \Delta T / \partial \varepsilon_g)_{K_g}$, de los tres puntos fijos, otra vez como función de los distintos perfiles de temperatura del horno y para el crisol 6ST.

Los valores bajo Eq. (6.2a) Eq. (6.2b) se obtienen aplicando las ecuaciones: $\partial \Delta T / \partial K_g = -\Delta T / K_g$ y $\partial \Delta T / \partial \varepsilon_g = \Delta T / \varepsilon_g$, respectivamente, pero con ΔT calculada para el perfil del horno CP, mostrado en la figura 6.6.

Comparación de crisoles, FTP: NF

En la tabla 6.3 se compara ΔT y los coeficientes de sensibilidad $(\partial \Delta T / \partial K_g) \varepsilon_g$ y $(\partial \Delta T / \partial \varepsilon_g)_{K_g}$, calculados para los crisoles 3S, 6ST y Mk-4 con los tres puntos fijos y el perfil NF.

Incertidumbres. Crisol: 6ST, FTP: RP

Finalmente, las tablas 6.4a y 6.4b recogen las incertidumbres que llevan a estimar la incertidumbre estándar $u(\Delta T)$ de ΔT ; todas las incertidumbres representan incertidumbres estándar. La tabla 6.4a muestra las estimaciones para las

incertidumbres $u(\Delta T; K_g)$ y $u(\Delta T; \varepsilon_g)$ y sus valores combinados $u(\Delta T; K_g, \varepsilon_g)$ asociados con las incertidumbres $u(K_g)$ en K_g y $u(\varepsilon_g)$ en ε_g , que se han fijado en 2 y 0.15 unidades, respectivamente. Con esto, $u(\Delta T; K_g) = (\partial \Delta T / \partial K_g) \cdot u(K_g)$ y $u(\Delta T; \varepsilon_g) = (\partial \Delta T / \partial \varepsilon_g) \cdot u(\varepsilon_g)$. Finalmente: $u(\Delta T; K_g, \varepsilon_g) = \{ u(\Delta T; K_g)^2 + u(\Delta T; \varepsilon_g)^2 \}^{1/2}$.

$u(\Delta T; \text{FTP})$ en la tabla 6.4.b representa la incertidumbre en ΔT asociada con la incertidumbre $u(\text{FTP})$ del perfil de temperatura en el horno(FTP) que se ha estimado como $u(\text{FTP}) = [\Delta T(\text{HP}) - \Delta T(\text{CP})]/2$. La razón para esto se aprecia en la figura 6.5.a, el la cual se ve que el ΔT asociado a RP está acotado entre los valores obtenidos para HP y CP. $u(\Delta T)$ se expresa como $u(\Delta T) = \{ u(\Delta T; K_g, \varepsilon_g)^2 + u(\Delta T; \text{FTP})^2 \}^{1/2}$.

6.5. Discusión

Crisol: 6ST

Los valores de ΔT ilustrados en la figura 6.5.a muestran un incremento significativo con el punto fijo, desde Co-C hasta Re-C y un descenso mas gradual con el perfil del horno FTP desde NF hasta CP. Para Co-C los resultados no muestran ninguna dispersión. La figura 6.6 para FTP-CP muestra que para un perfil de temperaturas dado ΔT incrementara según T_E^4 en concordancia con la eq. (6.1).

Los resultados para $(\partial \Delta T / \partial K_g) \varepsilon_g$, SCK y $(\partial \Delta T / \partial \varepsilon_g)_{Kg}$, SCE recogidos para HP, RP y CP el las secciones media e inferior de la tabla 6.2 muestran que los coeficientes de sensibilidad son esencialmente inmunes a las variaciones del perfil de temperatura del horno FTP. (para SCE esta observación se puede ampliar para el perfil NF). Esta es una importante observación porque significa que las incertidumbres asociadas pueden ser calculadas en base a los resultados obtenidos para el perfil CP, es decir, el perfil real no es necesario.

Los resultados bajo Eq. (6.2a) y Eq. (6.2b), de la última columna, calculados como $-\Delta T/K_g$ $\Delta T/\varepsilon_g$, cf. sección 4, se encuentran en un razonable acuerdo con los cálculos directos sobre los perfiles en cuestión para SCK , pero menos para SCE , donde pueden ser considerados como una frontera superior. Los resultados bajo Eqs (6.2a), (6.2b) se pueden obtener de un cálculo de ΔT para una T_E dada para el perfil CP, cf. sección 4. La mayor diferencia para SCE puede entenderse por la interacción entre la pared radiante y las paredes laterales que no está recogida en la eq.(6.1). Para

las eqs (6.2a) y (6.2b), ΔT sigue siendo menos sensible a los cambios en ε_g que lo previsto en la última ecuación. Así, empíricamente se encuentra que $(\partial \Delta T / \partial K_g) \varepsilon_g \approx -\Delta T / K_g$, $(\partial \Delta T / \partial \varepsilon_g)_{K_g} \approx 0.5 \cdot \Delta T / \varepsilon_g$ para el crisol 6ST en combinación con el perfil CP y con cualquier otro perfil considerado.

Comparación de crisoles, FTP: NF

La tabla 6.3 muestra ΔT , $(\partial \Delta T / \partial K_g) \varepsilon_g$, SCK y $(\partial \Delta T / \partial \varepsilon_g)_{K_g}$, SCE respectivamente, calculados para los crisoles 3S, 6ST y Mk-4 y el perfil NF. Las diferencias entre los valores de estos parámetros para el peror caso NF, son interesantes ya que dan un impresión de la influencia de la geometría del crisol.

Como se puede apreciar en la tabla 6.3 las diferencias entre los crisoles 3S y 6ST no son drásticas, los valores para 3S son sistemáticamente mayores (en sentido absoluto) con la excepción de SCE para Co-C. Esto puede deberse en parte por el mayor espesor de la pared radiante d para 3S: 2.6 mm frente 2 mm para 6ST, implicando un mayor ΔT y por tanto mayores valores de SCK y SCE . Los valores obtenidos para Mk-4, calculados por L. Wright [9], en base al software Abaqus, son significativamente las grandes que para 3S, donde también $d = 2.6$ mm. Esto puede ser entendido por las diferencias en la geometría de la cavidad: mientras Mk-4 (a) consiste en un cilindro y cono de of 3 mm de diámetro y una longitud de 27 mm, la cavidad de 3S (b) consiste en un cilindro y cono de of 8 mm de diámetro y una longitud de 62 mm pero con un diafragma de 3 mm de apertura. Esto significa que la cavidad (b) aproxima mejor que la (a) las condiciones ideales de cuerpo negro, implicando menores valores para la caída de temperatura y para SCK y SCE en el caso de (b).

Incertidumbres. Crisol: 6ST, FTP: RP

Finalmente, un comentario sobre las tablas 6.4a y 6.4b. Estos datos deben ser considerados como una primera aproximación cualitativa, especialmente para la derivación del componente $u(\Delta T; \text{FTP})$. También las estimaciones dadas para $u(K_g)$ and $u(\varepsilon_g)$, sección 4, deberán ser reconsideradas teniendo en cuenta las diferencias entre los valores de estos valores recogidos en la literatura especializada. Para un análisis provisional, la incertidumbre $u(\Delta T)$ parece suponer en torno a un 10 % de ΔT .

Esto probablemente representa una frontera superior para $u(\Delta T)$.

6.6. Conclusiones

-Para una geometría de crisol dada, radiando a una temperatura T , y dado un perfil de temperatura del (FTP) la caída de temperatura ΔT a través de la pared radiante varía con T^4 a lo largo del rango de temperaturas considerado. Para el caso específico estudiado en este capítulo, ΔT varía desde 5 mK para el punto del cobre ($T=1357.77$ K) hasta 90 mK para el Re-C ($T_E = 2747$ K). Para el caso en cuestión, a 3500 K tendríamos $\Delta T = 220$ mK.

-Los coeficientes de sensibilidad $(\partial \Delta T / \partial K_g) \varepsilon_g$ y $(\partial \Delta T / \partial \varepsilon_g)_{Kg}$ son esencialmente inmunes al perfil de temperatura. Esta es una importante observación porque significa que las incertidumbres asociadas pueden ser calculadas en base a los resultados obtenidos para el perfil CP, es decir, el perfil real no es necesario.

-Empíricamente se encuentra que $(\partial T_{drop} / \partial K_g) \varepsilon_g \approx -T_{drop}/K_g$, $(\partial T_{drop} / \partial \varepsilon_g)_{Kg} \approx 0.5 \cdot T_{drop}/\varepsilon_g$ para el rango de temperaturas en cuestión y la celda 6ST en combinación con cualquier perfil de temperatura del horno considerado.

-Como primera estimación de la incertidumbre $u(\Delta T)$ para la geometría crisol-horno dada, 6ST/RP, se obtiene $u(\Delta T) \approx 0.1 \cdot \Delta T$ sobre el rango de temperatura considerado.

-Para precisar más $u(\Delta T)$, las incertidumbres en la conductividad térmica $u(K_g)$ del grafito, en la emisividad de la pared $u(\varepsilon_g)$ y en el perfil de temperatura del horno $u(\Delta T; FTP)$ tienen que ser definitivamente fijadas..

-Para una geometría de crisol dada ΔT y $u(\Delta T)$ se puede minimizar minimizando el espesor d de la pared radiante y la apertura de la cavidad a los mínimos valores posibles.

-Cuando se sustituye el perfil real del horno, RP, por un perfil constante a la temperatura nominal del punto fijo, CP, para el crisol 6ST, los errores obtenidos son sólo de 3 mK, 1 mK y cero para las temperaturas de Re-C, Pt-C, Co-C,

respectivamente, correspondiendo con unos errores relativos de 3%, 4% y (virtualmente) cero en ΔT (92, 25 y 12 mK, respectivamente) a estas temperaturas. Desde este punto de vista, el perfil CP es suficientemente bueno para calcular la ΔT .

- En este análisis las incertidumbres asociadas a la incertidumbre de las dimensiones del crisol –influenciadas por la temperatura- y las incertidumbres asociadas a las dimensiones de los bloqueadores de radiación colocados en el horno pueden ser desvinculados.

6.7. Referencias del capítulo 6

- [1]. E.R.Woolliams, G. Machin, D. Lowe, R. Winkler, *Metrologia*. 2006, 43, R11.
- [2]. G. Machin, *Proceedings of International Symposium on Temperature, Humidity, Moisture and Thermal Measurements in Industry and Science*, Slovenia, 2010.
- [3]. P. Jimeno-Largo, Y. Yamada, P. Bloembergen, M.A. Villamanan, G. Machin. Numerical analysis of the temperature drop across the cavity bottom of high-temperature fixed points for radiation thermometry. In *Proceedings of TEMPMEKO 2004*. Edited by D.Zvizdić, L.G. Bermanec, T. Veliki, T.Stašić. Zagreb: FSB/LPM, 2004, 335-340.
- [4]. P.Bloembergen, B.B. Khlevnov, P. Jimeno-Largo, Y.Yamada. Spectral and total effective emissivity of a high-temperature fixed-point radiator considered in relation to the temperature drop across its backwall. *Int. J. Thermophysics*, 2008.
- [5]. J. Fischer, H.J. Jung, Determination of the thermodynamic temperatures of the freezing points of silver and gold by near-infrared pyrometry. *Metrologia*.1989, 26, 245-252.
- [6]. C.K. Ma. Calculation of the distribution of emissivity and temperature for a baffled cylindrical cavity at the freezing points of Ag, Au and Cu. In *Proceedings of TEMPBEIJING 1992* Edited by B. Zhang et al. Beijing: Standard press of China, 1997, 72-77.
- [7]. T.J. Horn and A.N. Abdelmessih. Experimental and numerical characterization of a steady-state cylindrical blackbody cavity at 1100 degrees Celsius. TM-2000-209022, National Aeronautics and Space Administration Dryden Flight Research Centre, 2000.
- [8]. Y.S. Touloukian, R.W. Powell, C.Y. Ho and P.G. Klemens. Thermal conductivity: Nonmetallic Solids, Thermophysical properties of Matter. The TPRC Data Series, 2, New York, Plenum Press, 1978.
- [9]. L.Wright, Optimising the implementation of .high temperature fixed points though the use of thermal modeling, NPL communication

Capítulo 7. Incertidumbre en la caída de temperatura III: longitud del crisol, espesor de la pared radiante y perfil de temperatura del horno Thermogage¹

7.1. Introducción

La caída de temperatura se estima para los siguientes puntos fijos: Co-C (1324 °C), Pd-C (1492 °C), Pt-C (1738 °C), Re-C (2474 °C) y WC-C (2749 °C), empleando un horno de la clase Thermogage. Se modelan los siguientes escenarios:

- Condiciones ideales: El crisol en el horno con uniformidad a la temperatura de fusión del punto fijo.
- Condiciones intermedias: El punto fijo en el horno con un perfil de temperatura senoidal desde el centro hasta la apertura del horno.
- Condiciones extremas: El horno tiene un gradiente lineal de temperatura desde el centro hasta la apertura.
- Condiciones de referencia: Únicamente se simula el crisol, sin el horno. Este caso supone la frontera superior de la caída de temperatura.

También se estudia la influencia del espesor de la pared radiante en la caída de temperatura para los cinco puntos fijos con las condiciones de referencia e ideales. Este espesor es muchas veces desconocido debido a la erosión de la pared durante el proceso de llenado del crisol. Estos cálculos permiten establecer los límites sobre la influencia del espesor de la pared en la caída de temperatura.

Debido a que la longitud de los crisoles usados por los diferentes Centros Nacionales de Temperatura varía de uno a otro, se han simulado también tres tamaños

¹ Las referencias a gráficas y tablas corresponden al texto original en inglés. No se han incluido en el resumen.

de crisol (30, 40 y 50 mm) para los cinco puntos fijos con las condiciones ideales y de referencia.

7.2. Descripción del modelo

Para la simulación se ha empleado el tipo de horno Thermogage de 24 kW (Fig. 1). Está formado por un tubo de grafito de 290 mm de largo y 24 mm de diámetro interno calentado eléctricamente por electrodos cobre. Una descripción más detallada del horno se puede encontrar en [1].

Se ha realizado un modelo axisimétrico en 2D (Fig. 2 and 3) con las siguientes características:

- Dimensiones:

Para investigar el efecto del horno se ha realizado la siguiente configuración:

- Se ha modelado un crisol modelo mark 4 del Laboratorio Nacional de Física de Inglaterra (NPL) [2]. La longitud interna del crisol es de 27 mm, el diámetro interno de 3 mm y el espesor de la pared radiante de 2.6 mm con un ángulo de cono de 120°. El crisol se ha modelado en medio del tubo de grafito del horno, rodeado a ambos lados por seis discos de aislamiento y 5 escudos de radiación. La configuración total mide 110 mm de largo.

□demás, para ver la influencia de la variación del espesor de la pared radiante debido a la erosión y de la longitud del crisol, ha sido modelado lo siguiente:

- El mismo crisol modelo mark 4 pero con cinco espesores distintos para la pared radiante: 0.1, 1, 2, 2.6 y 4 mm. Se han simulado en las condiciones ideales y de referencia.
- El crisol mark 4 con espesor de pared radiante de 2.6 mm y tres longitudes distintas para el tubo interior del crisol: 17, 27 y 37 mm,

que corresponden a unas longitudes externas para el crisol de 30, 40 y 50 mm. Se han simulado en condiciones ideales y de referencia.

Propiedades de los materiales:

La tabla 7.1 muestra las principales propiedades de los materiales empleados en la simulación. Las propiedades son calor específico C_p (J/kg.K), conductividad térmica k (W/m.K), densidad ρ (kg.m $^{-3}$), emisividad y temperatura de fusión (K). Los valores para la conductividad térmica del grafito disminuyen con la temperatura desde 53.6 W/m.K a 1597 K hasta 32.4 W/m.K a 3022 K.

- Condiciones de contorno del modelo:

Se simulan cinco puntos fijos eutécticos de alta temperatura, cada uno de ellos en cuatro condiciones térmicas distintas:

- 1) Condiciones de referencia: El crisol sin el horno con la aleación eutéctica a la temperatura nominal de fusión. La pared exterior del crisol es uniforme en temperatura.
- 2) Condiciones extremas: El horno presenta un gradiente lineal de temperatura desde el centro (a la temperatura nominal de fusión) hasta la apertura (a temperatura ambiente).
- 3) Condiciones intermedias: El crisol en el horno con un gradiente de temperatura senoidal desde el centro hasta la apertura del horno.
- 4) Condiciones ideales: El crisol en el horno estabilizado en su totalidad a la temperatura nominal de fusión.

Los gradientes de temperatura del horno para las condiciones 2, 3 y 4 pueden verse en las figuras Fig. 4, 5 y 6.

7.3. Resultados de la simulación

7.3.1. Caída de temperatura

La caída de temperatura a través de la pared radiante ha sido calculada como la diferencia entre la temperatura nominal de fusión de cada punto fijo y el valor medio de la temperatura en la pared radiante. Los resultados se muestran en la tabla 7.2. El espesor de la pared radiante para este caso ha sido de 2.6 mm

La Fig. 7.7 representa los valores de la caída de temperatura para las distintas condiciones térmicas.

7.3.2. Efecto del espesor de la pared radiante

La caída de temperatura para los cinco puntos fijos en las condiciones ideales y de referencia con los cinco espesores de la pared está recogida en las Tablas 7.3 y 7.4 .

Las curvas de variación de la caída de temperatura con el espesor de la pared se muestran en las Fig. 7.8 y 7.9.

7.3.3. Efecto de la longitud del crisol

La caída de temperatura para los cinco puntos fijos en las condiciones ideales y de referencia con las tres longitudes de crisol está recogida en las Tablas 7.5 y 7.6.

Las curvas de variación de la caída de temperatura con la longitud del crisol se muestran en las Fig. 7.10 y 7.11.

7.4. Discusión

7.4.1. Condiciones del horno

Las pérdidas de calor por radiación incrementan con la cuarta potencia de la temperatura nominal, con el límite superior expresado por la ecuación (1) [3]. Esta expresión puede ser utilizada para representar todos los datos mostrados en la Fig. 12 ya que estos se ajustan a la expresión aT^4 .

$$\Delta T = \cos \theta \cdot \varepsilon \cdot \sigma \cdot \frac{d}{K} \cdot \left(\frac{r}{L} \right)^2 \cdot T^4 \quad (7.1)$$

El coeficiente a de la ecuación exponencial para el modelo teórico (1) y para las cuatro condiciones del horno es (tabla 7.7):

La variación de la caída de temperatura con las respectivas ecuaciones exponenciales ajustadas y con el límite superior de la ecuación (1) está representada en la Fig. 7.12. Se ve claro que el modelo exponencial aT^4 es una buena representación de los datos modelados. Se ve también que ni siquiera el crisol sin el horno sigue la expresión teórica simplificada. Esto es debido a que las paredes laterales mitigan parte de las pérdidas de radiación [4]. Las diferentes condiciones térmicas del horno mitigan en mayor o menor medida estas pérdidas y pueden ser caracterizadas por el coeficiente c , mostrado en la tabla 7.8, como el cociente entre a (distintas condiciones del horno)/ a (ecuación simplificada).

El uso simple de la ecuación 7.1 sobreestima la corrección que debe ser aplicada por las pérdidas debidas a la radiación en un factor de 2 comparado con las condiciones extremas simuladas y en un factor mayor para el resto de las condiciones. Esta ecuación ha sido utilizada para estimar la caída de temperatura en los cálculos de incertidumbre [5] y esta contribución tendría que ser reajustada a hacia menores valores para tener en cuenta el efecto del horno.

La diferencia entre los perfiles del horno lineal y constante es menor de 0.1, indicando que se podría hacer una corrección razonable de la temperatura empleando una contribución a la incertidumbre de tipo B.

7.4.2. Espesor de la pared radiante

La teoría simple (7.1) que presupone la radiación libre de la pared predice que la caída de temperatura debería incrementarse linealmente con el espesor de la pared d , pero como puede verse en las Fig 8 y 9 la influencia del espesor es mayor para los primeros 2 mm.

La incertidumbre estándar asociada al espesor de la pared $u(\Delta T; d)$ se puede expresar como:

$$u(\Delta T; d) = (\delta T / \delta d).u(d) \quad (7.2)$$

El coeficiente de sensibilidad $\delta T / \delta d$ se puede aproximar a:

$$\delta T / \delta d = \Delta T / d \quad (7.3)$$

Y la variación estándar del espesor de la pared $u(d)$ para las distintas configuraciones se puede estimar como $u(d) \approx 0,5 \text{ mm}$.

Con estas aproximaciones, la incertidumbre estándar $u(\Delta T; d)$ expresada en K para las condiciones ideales se muestra en la tabla 7.9. Estudios similares para la emisividad y la conductividad térmica del grafito se pueden ver en [2].

7.4.3. Longitud del crisol

La teoría simple (7.1) predice que las pérdidas por radiación decrecen con la segunda potencia de la longitud interna de la cavidad radiante. Como se puede ver en las Fig. 10 y 11 este comportamiento está bien representado por el modelo y la ecuación simple vuelve a ser una frontera superior.

La incertidumbre estándar asociada al espesor de la pared $u(\Delta T; L)$ se puede expresar como:

$$u(\Delta T; L) = (\delta T / \delta L).u(L) \quad (7.4)$$

El coeficiente de sensibilidad $\delta T / \delta L$ se puede aproximar a:

$$\delta T / \delta L = \Delta T / L \quad (7.5)$$

Y la variación estándar de la longitud del crisol $u(L)$ para las distintas configuraciones se puede estimar como $u(L) \approx 10 \text{ mm}$.

Con estas aproximaciones, la incertidumbre estándar $u(\Delta T; L)$ expresada en K para las condiciones ideales se muestra en la tabla 7.10.

Esta influencia es especialmente importante para el Re-C y WC-C que reducen sus pérdidas a la mitad desde los 30 a los 50 mm de longitud de crisol en condiciones ideales.

7.4.4. Representación gráfica de los datos

Cómo resumen gráfico de las distintas influencias en las pérdidas de calor, se representan las curvas de la caída de temperatura para las diferentes condiciones térmicas del horno (Fig 7.13), los espesores de la pared radiante (Fig 7.14 y 7.15) y las longitudes del crisol (Fig 7.16 y 7.17).

7.5. Conclusiones

El gradiente de temperatura dentro del horno tiene una influencia en la caída de temperatura de la pared radiante que se incrementa con la cuarta potencia de la temperatura nominal de fusión del punto eutéctico. Esta influencia se puede comparar con la ecuación teórica de caída de temperatura de una pared radiando libremente, que supone una frontera superior de las pérdidas por radiación. Se puede hacer una corrección razonable y estimar la incertidumbre para otros puntos fijos eutécticos de diseño similar. Si se emplea otro tipo de horno, se pueden interpolar los datos obtenidos entre las condiciones extremas e ideales, el valor medio puede ser usado como corrección y estimar la diferencia como una incertidumbre de tipo B, es decir, dividiéndola entre $2\sqrt{3}$.

La incertidumbre asociada al espesor de la pared radiante, que puede variar significativamente debido a la erosión, se puede calcular en una primera aproximación y expresarse como $u(\Delta T; d) \approx 0.4 \cdot \Delta T$.

La longitud del crisol, en concreto de la longitud de la cavidad radiante, tiene una fuerte influencia en la caída de temperatura para los puntos fijos de mayor temperatura incluso para las condiciones de horno ideales. Emplear crisoles más largos, siempre que se consiga la homogeneidad del horno, puede ser una buena manera de reducir las pérdidas hasta valores aceptables. La incertidumbre asociada a la longitud del crisol se puede expresar como $u(\Delta T; L) \approx 0.47 \cdot \Delta T$.

7.6 Referencias del capítulo 7

- [1]. C.E. Brookley, W.E. Llewellyn, “Determination of blackbody radiance at temperatures above 2300 °C”, proceedings of *Temperature, Its Measurement and Control in Science and Industry*, vol. 6, edited by J. Schooley, □IP, pp. 1195-1200, 1992
- [2]. P. Castro, P .Bloembergen, Y. Yamada, M. □. Villamañan and G. Machin, “*On the Uncertainty in the Temperature Drop across the Backwall of High-Temperature Fixed Points*”. □cta Metrologica Sinica. Vol. 29. pp 253-260. 2008. Proceedings of International Conference on Temperature and Thermal Measurements, Beijing, 2008
- [3]. Fischer J. and Jung H. J., “Determination of the thermodynamic temperatures of the freezing points of silver and gold by near-infrared pyrometry”, *Metrologia*, **26**, 1989, pp. 245-252
- [4]. Machin, G., Wright, L., Lowe, D., Pearce J.V., “□ptimising the implementation of high temperature fixed-points through the use of thermal modelling”, *Int. J. Thermophys.*, **29**, 26-270, 2008
- [5]. Fischer, J., Sadli, M., Ballico, M., Battuello, M., Park, S. N., Saunders, P., Yuan Zundong, Johnson, B. C., van der Ham, E., Sakuma, F., Machin, G., Fox, N., Wang Li, Ugur, S., Matveyev M., Uncertainty budgets for the realisation of ITS-90 by radiation thermometry, In Proceedings of *Temperature its Measurement and Control in Science and Industry*, Vol. 7, ed. Ripple D., □IP Conference Proceedings, Chicago, 2003, pp 631-638

Capítulo 8. Modelado térmico de los puntos fijos Co-C, Pt-C y Re-C como entrada para calcular la emisividad efectiva de la cavidad¹

8.1. Introducción

En los capítulos anteriores la tesis se ha centrado en los siguientes aspectos sobre la incertidumbre en la realización de puntos fijos de alta temperatura: defectos de llenado en los crisoles [1], los valores de la emisividad y la conductividad térmica del grafito, la longitud del crisol y el espesor de sus paredes y el uso de distintos hornos y perfiles de temperatura [2].

En este capítulo el modelado térmico es empleado como datos de entrada para el cálculo de la emisividad efectiva de la cavidad de cuerpo negro para los puntos fijos Co-C, Pt-C y Re-C medidos a dos longitudes de onda distintas. Esta emisividad efectiva está influenciada por las propiedades de reflexión de la superficie de grafito, la distribución de temperatura dentro del cuerpo negro y la configuración de las barreras de radiación dentro de la cavidad.

El cálculo de la emisividad efectiva implica aquí 7 pasos en total, que incluyen medidas de la reflexión de muestras de grafito representativas (pasos 1 a 3), medidas de la emitancia, el cálculo de la distribución de temperatura dentro de la cavidad mediante el modelado térmico y finalmente, basándose toda esta información, el cálculo de la emisividad efectiva.

La sección 8.2 explica el modelado térmico en el cual se han elaborado varios sistemas mediante FLUENT.

La sección 8.3 muestra los resultados obtenidos y en la sección 8.4 se realiza una discusión de dichos resultados.

8.2. Modelado térmico de la distribución de temperaturas en el interior de la cavidad

¹ Las referencias a gráficas y tablas corresponden al texto original en inglés. No se han incluido en el resumen

El modelado térmico es utilizado para estimar la distribución de temperatura en el interior de la cavidad de cuerpo negro, que incluye el perfil de temperatura en las paredes interiores del horno, a lo largo de la cavidad y en la pared radiante de medición del crisol.

Se han realizado las siguientes simplificaciones: 1) La geometría es considerada axisimétrica. Esto permite construir un modelo en 2D. 2) La resistencia térmica de las partes roscadas es despreciada por su escasa influencia y por la dificultad de su estimación. 3) La transmisión de calor por conducción y convección dentro de la atmósfera del horno se ha tenido en cuenta pero su efecto es despreciable frente al intercambio de calor por radiación. 4) El modelo asume un comportamiento estacionario.

Un corte en 3D de la estructura de la cavidad se puede ver en la figura 8.1. Las parejas de números representan la localización en mm a lo largo y perpendicularmente del eje X.

La conductividad térmica del grafito como función de la temperatura en todo el rango de interés esta tomada de [3]. Des esta referencia se toman los valores de 53.6, 45.6, 36.5 en $\text{Wm}^{-1}\text{K}^{-1}$ par los puntos fijos Co-C(1597 K), Pt-C (2011 K), Re-C (2747 K). La emisividad del grafito, estimada en 0.86 esta tomada de [4].

Los perfiles de temperatura en 8 puntos de las barreras de radiación han sido medidos en el NMIJ para los puntos Co-C, Pt-C y Re-C, usando termometría de radiación. Estas medidas han sido descritas en el capítulo 6 como “perfil real”. El crisol y el horno son los mismos que los descritos en el capítulo 6, un crisol tipo 6ST y en horno Nagano VR10-A23, ambos diseñados por el NMIJ. LA temperatura entre los puntos medidos es luego interpolada e introducida como condición de contorno en el modelo a lo largo de la pared exterior del tubo de cuerpo negro. A continuación, se calcula la distribución de temperatura en las paredes interiores de la cavidad (figura 8.2). El modelo simula el final del proceso de fusión, fijando la temperatura de las paredes exteriores del crisol a la temperatura nominal de fusión.

Los perfiles de temperatura calculados aparecen en la figura 8.3 (a) y (b) en términos absolutos y relativos respectivamente. Una distribución gráfica de la temperatura en el interior del horno puede verse en la figura 8.4. Estos resultados

son empleados en los cálculos de la siguiente sección.

8.3. Resultados obtenidos para la emisividad efectiva y la temperatura de radiación a partir del modelado térmico

Un programa de trazado de rayos basado en el método de Monte-Carlo ha sido empleado por Hanssen y al. [5] para calcular los parámetros de radiación en la cavidad de la figura 8.1 con la distribución de temperatura de la figura 8.2 como entrada. Este método asume e incorpora los efectos de la radiación ambiente a una temperatura T_{bg} de 300 K. El programa puede incluir la reflexión o la emitancia de la superficie como entrada y calcular la emisividad de la cavidad, la radiancia y la temperatura de radiación.

Una explicación detallada del método de Monte-Carlo empleado para el cálculo de las propiedades ópticas del grafito puede encontrarse en [5], como parte de una investigación realizada por NIM, NIST y NMIIJ/AIST en colaboración con la Universidad de Valladolid y que está incluida en el anexo III de esta tesis.

Como la emitancia real de la superficie del grafito durante el proceso no es bien conocida, se ha aplicado un rango de valores para comprender la influencia de este parámetro.

Los valores para la emisividad del grafito fueron 0.7, 0.8 y 1 (para comparar con el caso ideal de cuerpo negro). Los resultados son para estos tres valores de la emisividad del grafito, a dos longitudes de onda distintas 405 nm y 650 nm y calculados para el caso isotermo. En las figuras 8.5 (a), (c) y (e), se muestran las temperaturas de radiación calculadas para los puntos Co-C, Pt-C y Re-C. La temperatura no varía con la longitud de onda para el caso de emisividad 1 pero para los valores de 0.7 y 0.8 la temperatura de radiación disminuye con la longitud de onda. También disminuye a medida que disminuye la emisividad. La emisividad efectiva calculada para los puntos Co-C, Pt-C y Re-C se muestra en las figuras 8.5 (b), (d) y (f) e incluyen los datos tanto para el caso de cavidad isotérmica como para el caso de la cavidad con la distribución de temperatura de la figura 8.3 y calculada mediante modelado térmico.

Como se puede ver en las figuras 8.5 (b), (d) y (f) casi no se aprecia efecto en el valor de la emisividad efectiva en caso de que la cavidad no sea isotérmica.

Por el contrario, los resultados muestran que el diseño del horno se aproxima lo suficiente a las condiciones isotermas, suponiendo que la reflectividad del grafito presenta un comportamiento de Lambertian, es decir, que es isotrópica. La emisividad efectiva tiene también muy poca variación con la longitud de onda y parece que su influencia aumenta para valores más elevados de la emisividad del grafito.

8.4. Resumen y conclusiones

Este trabajo, actualmente en progreso, trata de establecer los valores de la emisividad efectiva de las cavidades de cuerpo negro de los puntos fijos Co-C, Pt-C y Re-C con las mínimas incertidumbres posibles. La distribución de temperaturas dentro de una cavidad de diseño optimizado y en uso actual para los puntos fijos eutécticos existentes [6] ha sido estudiada mediante mediciones y modelado térmico.

La distribución de temperatura ha sido, a su vez, usada como entrada para estudiar la potencial variación de la emisividad efectiva de la cavidad debido a la configuración de la temperatura en su interior y de las características reflexivas del grafito. Suponiendo un comportamiento de Lambertian para la reflectividad, el modelado indica que un perfil real no uniforme dentro del horno implica únicamente pequeños cambios en los valores de la emisividad efectiva.

8.5 Referencias del capítulo 8

- [1]. G. Machin , P. Castro , A. Levick , M. Á. Villamañan, “Quantifying the Temperature Effects of Imperfectly Formed Metal-Ingots in High Temperature Fixed Point Crucibles”. *Proceedings of International Conference on Temperature and Thermal Measurements, Beijing, 2008. Measurement 44* (2011), pp. 738–742.
- [2]. P. Castro, G. Machin, M. A. Villamañan, D. Lowe, “Calculation of the Temperature Drop for High Temperature Fixed Points for Different Furnace Conditions”. *Proceedings of International Symposium on Temperature, Humidity, Moisture and Thermal Measurements in Industry and Science*, Slovenia, 2010. Submitted for publication in International Journal of Thermophysics.
- [3] Y. S. Touloukian, R. W. Poweel, C. Y. Ho, P. G. Klemens, “Thermal conductivity: Nonmetallic Solids, Thermophysical Properties of Matter,” The TPRCX Data Series **2**, New York, Plenum Press, 1978.
- [4] J. Fischer, H. J. Jung, “Determination of the thermodynamic temperatures of the freezing points of silver and gold by near-infrared pyrometry”, *Metrologia* **26**, 245-252 (1989).
- [5] P. Bloembergen, L. M. Hanssen, S. N. Mekhontsev, P. Castro, Y. Yamada, “A determination study of the cavity emissivity of the eutectic fixed points Co-C, Pt-C and Re-C“. *Proceedings of International Symposium on Temperature, Humidity, Moisture and Thermal Measurements in Industry and Science*, Slovenia, 2010. Submitted for publication in International Journal of Thermophysics.
- [6] P. Castro, P. Bloembergen, Y.Yamada, M.A. Villamanan, G. Machin, “On the uncertainty in the Temperature Drop across the Backwall of High-Temperature Fixed Points”, *Acta Metrologica Sinica* **29**, 253 – 260 (2008).

Capítulo 9. Estudio de los parámetros de influencia en la termometría de contacto para celdas eutécticas¹

9.1. Introducción

La técnica de medida de puntos fijos eutécticos de alta temperatura influye en el aspecto de la meseta y en la temperatura nominal medida [1]. La exactitud en el conocimiento de algunas de las propiedades termofísicas de los materiales eutécticos también tiene influencia en la caída de temperatura calculada y la meseta de fusión.

En este capítulo se modela un crisol con el punto fijo Co-C [2] y se estudian las diferencias entre las medidas tomadas con un termopar y con un termómetro de radiación. También se realiza un estudio paramétrico de la densidad, viscosidad, calor de fusión y rango de fusión para el Co-C.

9.2. Descripción del modelo

El crisol estudiado pertenece al Laboratoire National D'Essais (LNE) y es uno de los empleados para termometría de contacto de radiación. La geometría puede verse en la figura 9.1.

El crisol mide 125 mm y tiene unos diámetros exterior e interior de 36 mm y 8 mm respectivamente.

Las propiedades del material usado para la simulación se recogen en la tabla 9.1.

Las condiciones térmicas impuestas en la simulación son:

¹ Las referencias a gráficas y tablas corresponden al texto original en inglés. No se han incluido en el resumen.

- La temperatura del horno se fija 16°C por encima de la temperatura de fusión.
- Temperatura de fusión para el Co-C de 1324°C .
- La distribución de temperatura a lo largo del termopar es tal que a 100 mm de la punta la temperatura es igual a la del horno. Esta condición coincide con los datos experimentales disponibles.

9.3. Resultado de las simulaciones

Para estudiar las diferencias en el comportamiento de la fusión usando termometría de contacto y de radiación, el mismo proceso de fusión ha sido simulado en dos situaciones:

- 1) Con el termopar en el interior del crisol. La temperatura es medida en la punta del termopar, que está situada a 5 mm de la pared radiante
- 2) Con el termómetro de radiación mirando directamente a la pared radiante, en la cual es medida la temperatura.

Las dos situaciones se han modelado en 2D con axisimetría como puede verse en las figuras 9.2 y 9.3.

El proceso de fusión es simulado en régimen transitorio, el cual determina todas las variables dependientes del tiempo.

El primer análisis que ha de realizarse es el estudio paramétrico de las variables de influencia en el proceso: densidad, viscosidad, calor de fusión y rango de fusión del Co-C.

Estudio paramétrico de las variables de influencia

De acuerdo a las dificultades para obtener datos exactos de estas variables a alta temperatura, se ha tomado un rango de valores, como puede verse en la tabla 9.2.

En las figuras 9.4, 9.5 y 9.6, puede observarse que la duración de la fusión está influenciada por los valores de la densidad, calor de fusión y rango de fusión, pero la viscosidad no parece tener una influencia representativa.

Esta influencia se entiende teniendo en cuenta que el calor absorbido por la aleación en el proceso de fusión, Q , viene dado por la expresión:

$$Q=m \cdot L \quad (9.1)$$

Donde m es la masa y L el calor latente de fusión de la aleación.

Teniendo en cuenta que el volumen permanece constante ya que se emplea el mismo crisol para todas las simulaciones, puede verse que el calor necesario para el proceso de fusión aumenta linealmente con la densidad y el calor latente, modificando el tiempo de fusión de la misma manera.

Esta influencia y la incertidumbre acerca de los valores reales explican la diferencia en el tiempo de fusión del proceso real y el simulado.

En este estudio, que es una comparación relativa entre dos técnicas de medición, la exactitud en el tiempo de fusión no es crucial ya que ambas situaciones se ejecutan con los mismos valores para las propiedades del material.

Comparación entre los dos métodos de medida, termómetro de radiación y termopar

Ambos métodos tienen características específicas que afectan de distinta forma a la medida de temperatura durante la fusión.

Los termómetros de radiación empleados en los Laboratorios Nacionales de Metroología tienen un objetivo de medida muy afinado, alrededor de 1 mm a una distancia de 1 m, por lo que en realidad miden la temperatura en una parte de la pared radiante.

Los termopares trabajan de una manera muy distinta. El voltaje es generado por el gradiente de temperatura a lo largo del termopar por lo que la medida se ve afectada por una mayor región dentro del crisol.

No sólo esta diferencia en la región de medida afecta a la temperatura medida, también influye el modo en que el flujo de calor fluye dentro del crisol.

Con el termómetro de radiación, el flujo de calor por radiación fluye directamente hacia el exterior. En el caso del termopar, éste bloquea dicho flujo impidiendo que salga al exterior.

Estas son las razones principales por las que se espera encontrar diferencias entre los dos métodos. La cuestión es si las pérdidas de calor por radiación son mayores que las pérdidas por conducción a través del termopar y por tanto la calibración mediante termómetro de radiación mediría una temperatura inferior a la del termopar. Este efecto incrementa con la temperatura debido a que las pérdidas por radiación aumentan con la cuarta potencia de la temperatura y la conducción presenta un comportamiento lineal.

El principal resultado obtenido en la comparación es la diferencia de unos 25 mK en la temperatura de fusión entre los dos sistemas de medida. Además, el flujo de calor en la pared radiante es más del doble en el caso del termómetro de radiación. Cuando el proceso es medido con el termómetro de radiación, la fusión parece empezar antes y la temperatura de fusión estar unos mK por debajo que en el caso de ser medida con el termopar. Este comportamiento puede verse en figura 9.7.

9.4. Conclusiones

La exactitud en los valores de las propiedades térmicas de los puntos fijos eutécticos a su temperatura de fusión es crucial para la simulación realista del proceso de fusión.

La técnica de medida tiene influencia en la temperatura nominal determinada para los puntos fijos eutécticos de alta temperatura. Como puede pensarse, parece que las pérdidas de calor por radiación cuando se usa un termómetro de radiación son más importantes que aquellas que se producen por conducción a través del termopar cuando se emplea éste en la medición.

Este estudio ha sido hecho a una única temperatura nominal y con el caso más extremo como es el crisol sin el horno. Es recomendable extenderlo a un rango aceptable de temperaturas, sobre todo para el punto Pd-C [3] y evaluar la influencia del entorno del horno.

9.5 Referencias del capítulo 9

- [1] S. G. R. Salim, E. R. Woolliams, M. Dury, D. H. Lowe, J. V. Pearce, G. Machin, N. P. Fox, T. Sun and K.T. V. Grattan. “Furnace uniformity effects on Re–C fixed-point melting plateaux”. *Metrologia*, vol. 46, 2009, pp. 33–42.
- [2] M. Sadli, O. Pehlivan, F. Bourson, A. Diril, K. Ozcan. “Collaboration Between UME and LNE-INM on Co–C Eutectic Fixed-Point Construction and Characterization”. *Int. J. Thermophys.*, 30, 36–46, 2009.
- [3] Pearce J. V., Ogura H., Izuchi, M., Machin G., “Evaluation of the Pd-C eutectic fixed point and the Pt/Pd thermocouple”, *Metrologia*, 46, p.473-479, 2009.

Capítulo 10. Conclusiones finales

10.1. Conclusiones

El modelado térmico mediante FLUENT ha sido probado con éxito convirtiéndose en una herramienta verdaderamente útil para entender el comportamiento de los puntos fijos eutécticos de alta temperatura.

Estas simulaciones han dado la posibilidad de evaluar la influencia del defecto en el llenado de los crisoles, concluyendo que pequeños defectos como agujeros y grietas alejados de la pared de medición se pueden obviar pero las grietas cercanas a la pared de medición tienen una clara influencia en la temperatura nominal medida. Parece posible reducir la cantidad de aleación eutéctica cuando se utiliza un horno adecuado, cubriendo con el metal únicamente la parte trasera de la cavidad.

También se estudió la influencia en la caída de temperatura del espesor de la pared de medición y de la longitud del crisol, de tal manera que se producen mayores caídas con crisoles más cortos y con mayores espesores en la pared de medición.

El modelado térmico ha sido también útil para estimar la incertidumbre en la caída de temperatura debido a los valores de la emisividad y la conductividad térmica del grafito y la temperatura nominal del punto fijo. Las incertidumbres calculadas para estos puntos fijos son muy pequeñas – desde 5mK para el punto del cobre hasta 90 mK para el Re-C – comparadas con la incertidumbre medida para una variación realista de los valores de la emisividad y la conductividad térmica.

La determinación del perfil de temperatura en el interior del horno permitió el estudio del ambiente en su interior y de la emisividad efectiva de la cavidad llegando a la conclusión de que se pueden suponer condiciones isotérmicas en el interior del horno sin perder demasiada exactitud.

Finalmente, el modelado mostró que la técnica de medida tiene pequeña influencia en el valor de la temperatura medida, con pérdidas por radiación ligeramente superiores a las pérdidas por conducción a través del termopar.

10.2. Líneas futuras de investigación

Las próximas líneas de investigación en este campo pueden ser:

- Obtener un único valor para la incertidumbre en las pérdidas de calor asociado al gradiente de temperatura en el horno, las propiedades de los materiales y el intercambio de calor con el ambiente.
- Optimizar la geometría del crisol para mejorar la estabilidad de la meseta de fusión y ahorrar material.
- Recalcular la emisividad efectiva de la cavidad en base a nuevos datos sobre el grafito.
- Extender el estudio de la influencia de la técnica de medida para diferentes temperaturas (e.g. Pd-C) incluyendo la influencia del horno.
- El estudio del modelo en régimen transitorio para ver los efectos en la fusión y su dependencia de la temperatura nominal.